This page intentionally left blank


Trimble


COBRA

Geodesy and Remote Sensing

The renewed eruption of Mount St. Helens provided many opportunities to bring modern geodetic tools—such as radar interferometry and GPS—to bear on monitoring what was, from 2004 to 2008, the only erupting volcano in the conterminous United States. The volume of lava extruded, about 0.1 km^3, proved small enough that geodetic signals associated with ground deformation were subtle and often difficult to interpret.

Surprises? The days and weeks leading to the seismic unrest of September 23, 2004, lacked demonstrable ground deformation. Presumably the volcano was already pressurized, its magma having moved into a position favorable for eruption as early as the late 1980s or early 1990s and awaiting only some incremental change that would initiate the final ascent. The amount of lava extruded between 2004 and 2006 was substantially greater than could be accounted for by reservoir withdrawal, according to models based on the GPS data. Instead, the discrepancy must be accounted for by some combination of magma recharge from greater depth and magma expansion by vesiculation in the shallow magma reservoir and its conduit.

It is this question of recharge by new magma—how much, from how deep, and of what composition?—that remains the inestimable puzzle, addressed partly by chapters in this section but raised again in sections describing modeling and mechanics, gas geochemistry, and petrology.

View southwest across spine 3 on November 29, 2004.
USGS photo by J.W. Vallance.

A Volcano Rekindled: The Renewed Eruption of Mount St. Helens, 2004–2006
Edited by David R. Sherrod, William E. Scott, and Peter H. Stauffer
U.S. Geological Survey Professional Paper 1750, 2008

Chapter 14

Constraints and Conundrums Resulting from Ground-Deformation Measurements Made During the 2004–2005 Dome-Building Eruption of Mount St. Helens, Washington

By Daniel Dzurisin[1], Michael Lisowski[1], Michael P. Poland[2], David R. Sherrod[1], and Richard G. LaHusen[1]

Abstract

A prolonged period of dome growth at Mount St. Helens starting in September–October 2004 provides an opportunity to study how the volcano deforms before, during, and after an eruption by using modern instruments and techniques, such as global positioning system (GPS) receivers and interferometric synthetic aperture radar (InSAR), together with more traditional ones, including tiltmeters, triangulation, photogrammetry, and time-lapse photography. No precursory ground deformation was detected by campaign GPS measurements made in 2000 and 2003, nor by a continuous GPS station (JRO1) operating ~9 km to the north-northwest of the vent area since May 1997. However, JRO1 abruptly began moving downward and southward, toward a source centered about 8 km beneath the volcano, concurrently with the start of a shallow earthquake swarm on September 23, 2004. The JRO1 velocity slowed from ~0.5 millimeters per day (mm/d) in late September–early October 2004 until spring 2005. Thereafter, it was essentially constant at ~0.04 mm/d through December 2005. In similar fashion, the growth rate of the welt on the south crater floor slowed from 8.9 m^3/s during October 4–11 to 6.4 m^3/s during October 11–13, 2004; this trend continued after emergence of the first lava spine on October 11. The volumetric extrusion rate decreased from 5.9 m^3/s during October 13–November 4, 2004, to 2.5 m^3/s during December 11, 2004–January 3, 2005, and for the remainder of 2005, it was in the range 2.0–0.7 m^3/s. Fifteen continuous GPS stations, installed soon after the eruption began, showed radially inward and downward ground motions through December 2005. Likewise, InSAR observations spanning the first year of the eruption indicate broad subsidence centered near the vent. Model-derived estimates of source-volume decrease from September 23, 2004, to October 31, 2006, are $16–24\times10^6$ m^3, substantially less than the volume erupted during the same period (87×10^6 m^3 through October 21, 2006). The discrepancy can be explained by a combination of magma expansion and recharge in the source region.

Lack of precursory deformation at JRO1 suggests that the conduit is poorly coupled to the rest of the edifice, so the rising magma column was able to push ahead older conduit material rather than intruding it. Constraints on conduit length and radius require that reservoir magma (as opposed to conduit-filling magma) reached the surface early during the eruption, probably soon after CO_2 emission rates peaked in early October 2004. If rapid emergence of spine 3 (the first whaleback-shaped extrusion) in late October 2004 marked the arrival of reservoir magma, then the volume of conduit material flushed from the system was about 20×10^6 m^3—the volume of surface deformation plus spines on November 4, 2004. The corresponding radius for a cylinder extending from the surface to depth d = 5 km is 35.7 m, or 28.2 m for d = 8 km. The average ascent rate through the conduit, assuming reservoir magma began its rise on September 23, 2004, was 120 m/d for d = 5 km, or 190 m/d for d = 8 km. Observed lineal extrusion rates were 2–10 m/d, so the conduit must widen considerably near the surface. Equating magma flux through the conduit to that at the surface, we obtain a vent radius of 125 m and an extrusion rate of 5.7 m^3/s—both values representative of the early part of the eruption.

Lack of precursory inflation suggests that the volcano was poised to erupt magma already stored in a crustal reservoir when JRO1 was installed in 1997. Trilateration and campaign GPS data indicate surface dilatation, presumably caused by reservoir expansion between 1982 and 1991, but no measurable deformation between 1991 and 2003. We conclude that all three of the traditionally reliable eruption

[1] U.S. Geological Survey, 1300 SE Cardinal Court, Vancouver, WA 98683

[2] U.S. Geological Survey, PO Box 51, Hawaii National Park, HI 96718

precursors (seismicity, ground deformation, and volcanic gas emission) failed to provide warning that an eruption was imminent until a few days before a visible welt appeared at the surface—a situation reminiscent of the 1980 north-flank bulge at Mount St. Helens.

Introduction

The deformational behavior of active basaltic shield volcanoes and large silicic magmatic systems (restless calderas) can be characterized in a general way by, respectively, (1) repeated inflation-deflation cycles in response to changes in crustal magma storage (for example, Kīlauea, Hawai‘i, U.S.A., Dvorak and Okamura, 1987; Krafla, Iceland, Tryggvason, 1994), and (2) episodes of more gradual surface uplift or subsidence (bradyseisms) caused by magmatic inflation-deflation or hydrothermal system pressurization-depressurization (for example, Long Valley Caldera, Calif., U.S.A., Hill and others, 1985; Yellowstone caldera[3], Wyo., U.S.A., Dzurisin and others, 1999; Wicks and others, 2006; Phlegraean Fields caldera, Italy, Caputo, 1979). Deformation of stratovolcanoes of intermediate composition (andesite–dacite) is more varied and therefore more difficult to understand. Nonetheless, volcanoes of this type are numerous along the Pacific margin and, on short to intermediate time scales, they pose a greater threat to human populations than do basaltic shields or large silicic systems.

The reawakening of Mount St. Helens in 1980 following 123 years of quiescence provided a modern opportunity to study pre-, syn-, and post-eruptive deformation at an accessible and relatively well-studied stratovolcano. However, little was learned about any deep-seated deformation (source depth more than ~2 km) that might have occurred before the eruption because magma rose to shallow depth—as evidenced by the appearance of a bulge on the volcano's north flank by early April 1980 (fig. 1*A*)—before or soon after March 20, 1980, when a swarm of earthquakes caught volcanologists' attention and spurred the start of intensive monitoring (Lipman and others, 1981).

Renewed dome growth at Mount St. Helens starting in September–October 2004 (fig. 1*B*) provides a second opportunity to study how this volcano deforms before, during, and after an eruption—this time by using modern geodetic instruments and techniques, such as Global Positioning System (GPS) receivers (Lisowski and others, this volume, chap. 15; LaHusen and others, this volume, chap. 16) and interferometric synthetic aperture radar (InSAR, Poland and Lu, this volume, chap. 18), together with more traditional instruments and techniques, including tiltmeters, triangulation, photogrammetry, and time-lapse photography (Poland and others, this volume, chap. 11; Major and others, this volume, chap. 12). Deformation data from the first 15 months of the eruption (October 2004–December 2005) help to constrain (1) the depth and geometry of the magma plumbing system and (2) the time history of magma outflow and possible recharge to a crustal magma reservoir (Lisowski and others, this volume, chap. 15; Mastin and others, this volume, chap. 22). The 2004–5 deformation data, especially when considered together with other datasets, also raise several new questions.

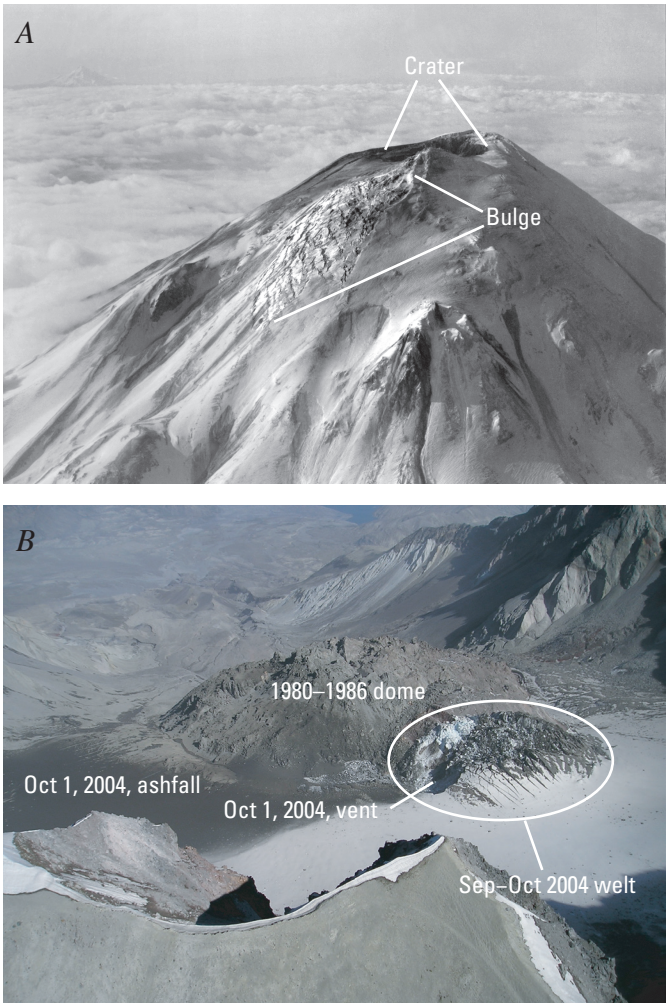

Figure 1. Examples of precursory surface deformation before eruptions at Mount St. Helens, Washington. *A*, Upper north flank on April 7, 1980. Series of phreatic eruptions that began on March 27, 1980, deposited ash and formed summit crater, which had grown to about 500 m west-east and 300 m north-south. Intensely cracked area below and north of crater shows distension of north flank. USGS photograph by R.B. Waitt. *B*, Crater floor as seen from above southwest crater rim on October 3, 2004. Vent for October 1 ash is visible at the west base of the welt of uplifted crater floor and glacial ice first recognized as deforming on September 27, 2004. USGS photograph by S. Konfal.

[3] Capitalization of "Caldera" or "Volcano" indicates adoption of the word as part of the formal geographic name by the host country, as listed in the Geographic Names Information System, a database maintained by the U.S. Board on Geographic Names. Noncapitalized "caldera" or "volcano" is applied informally—eds.

This paper draws freely on datasets and analyses presented elsewhere in this volume. Its main objectives are (1) to present an integrated overview of ground deformation observations, measurements, and results through December 2005 and (2) to explore some implications of these results, together with those from other disciplines, for the mechanism of the eruption and its future course.

Geodetic Techniques Used to Study the Eruption

This section summarizes the techniques used, successfully or unsuccessfully, to measure ground deformation during the 2004–5 eruption. The reader is referred to other papers in this volume for more thorough treatments of some of the techniques, results, and interpretations.

Regional Trilateration and Campaign-Style GPS Measurements

The Helens high-precision trilateration network was established in 1982 to track regional strain accumulation following the 1980 eruption at Mount St. Helens. Line lengths were measured with a Geodolite in 1982 and 1991 and with GPS in 2000. Lisowski and others (this volume, chap. 15) report that line lengths consistently increased by 1–3 cm between 1982 and 1991 but did not change significantly from 1991 to 2000. The line-length increases correspond to areal dilatation at a rate of 144±39 nanostrain/yr, which is an order of magnitude greater and distinctly different than the background tectonic strain. Lisowski and others (this volume, chap. 15) discount possible systematic error in the Geodolite surveys as the sole reason for the observed dilatation and invoke "… some other phenomenon, like recharge of the magma reservoir…" to account for the observations.

During summer 2000, the USGS Cascades Volcano Observatory (CVO) installed and made initial GPS observations at more than 40 benchmarks on and around Mount St. Helens (herein referred to as the large-aperture GPS network). The network is concentrated within 10 km of the volcano, but it extends more than 30 km and covers an area of more than 7,400 km^2 (fig. 2; Dzurisin, 2003). The first repeat survey was made in summer 2003. With effects of rigid-block rotation and regional strain removed, no significant strain was detected, with one exception: a station (DMSH) on the 1980–86 lava dome (fig. 2) moved down and east-northeastward, toward the center of the dome, at average rates of 9.0 cm/yr and 2.9 cm/yr, respectively (Lisowski and others, this volume, chap. 15).

The motion of DMSH is consistent with that seen at several nearby stations on the 1980–86 dome, which were observed each summer from 2000 to 2004 to provide geodetic control for vertical air photos and digital elevation models (Schilling and others, this volume, chap. 8). These stations generally moved down and toward the center of the dome at rates of a few centimeters per year, while stations on the crater floor moved very little (Lisowski and others, this volume, chap. 15). The motion of the stations is attributed to cooling and compaction of the uppermost conduit and dome. The latter consists mainly of stubby, highly deformed, dacite lava flows (lobes) and bouldery talus (Swanson and others, 1987). There is no evidence from the August 2004 control-point survey data of any change in trend that could be associated with the start of the current eruption.

The regional trilateration and campaign GPS data indicate that most of the surface deformation prior to the 2004–5 eruption took place in the decade following the 1980 eruption, and that little or no surface deformation occurred between 1991 and 2003. This is consistent with data from continuous GPS (CGPS) station JRO1, 8 km north-northwest of the volcano, which recorded no volcano-centric deformation from May 1997 to the beginning of seismic unrest on September 23, 2004 (see below). However, there is seismic evidence for pressurization of the magma reservoir and upward fluid intrusion starting in late 1987 and continuing at least until November 2001 (Moran, 1994; Moran and others, this volume, chap. 2). This apparent contradiction and other questions are addressed in the later Discussion section.

Continuous GPS (CGPS)

Johnston Ridge Observatory (JRO1)

Included in the large-aperture GPS network are 17 CGPS stations on or close to the volcano. The first station, JRO1, was installed in May 1997 at the Mount St. Helens National Volcanic Monument's Johnston Ridge Observatory. Lisowski and others (this volume, chap. 15) conclude that, within uncertainties, (1) the velocity of JRO1 was constant from May 1997 through mid-September 2004, and (2) JRO1 abruptly started moving south-southeast and down, toward a source beneath Mount St. Helens, on or about September 23, 2004. The anomalous motion was essentially concurrent (±1 day) with the start of a shallow earthquake swarm beneath the crater floor (Moran and others, this volume, chap. 2). Seismicity was accompanied by the growth of a large welt (fig. 1*B*), which was first visible in photographs taken on September 26. The first of several lava spines emerged from the welt on October 11, and extrusion of a dacite dome continued through the end of 2005 (Dzurisin and others, 2005; Vallance and others, this volume, chap. 9).

Fresh crevasses in glacier ice on the south crater floor, indicating intense deformation of the area that was to become the welt, were first recognized a few days after the start of shallow seismicity and anomalous motion at JRO1. New crevassing and uplift were confirmed by direct observation on September 29, 2004. In hindsight, they were recognized in photographs taken on September 26 by J.S. Pallister during

a fixed-wing observation flight. Helicopter pilot Jeff Linscott (JL Aviation, Inc.) first noticed new cracks in the ice on September 28 while flying with members of the news media. He pointed out the cracks to us (D. Dzurisin and M.P. Poland) the next day, September 29. A photograph taken by a hiker from the south crater rim on September 25 shows no obvious disturbance in the area that became the welt; thus, the first surface cracks probably formed 2–3 days after the start of a shallow earthquake swarm at about 0200 PDT (0900 UTC) on September 23 and within 1 day of an uptick in seismicity on September 25 that culminated with the onset of the eruption.

On August 27, 2004, Linscott landed in the southern part of the crater with USGS–CVO staff; fresh cracks in glacier ice at their customary landing site forced them to use an alternate site nearby. Any significance of those cracks in terms of the impending eruption is undocumented. At the time, the cracks were attributed to summer snowmelt revealing crevasses in the advancing glacier. Similar features had been seen before and were visible at the time on the west arm of the glacier. Any relation to the recognized onset of volcanic unrest nearly a month later is speculative and not supported by the hiker's photograph taken on September 25.

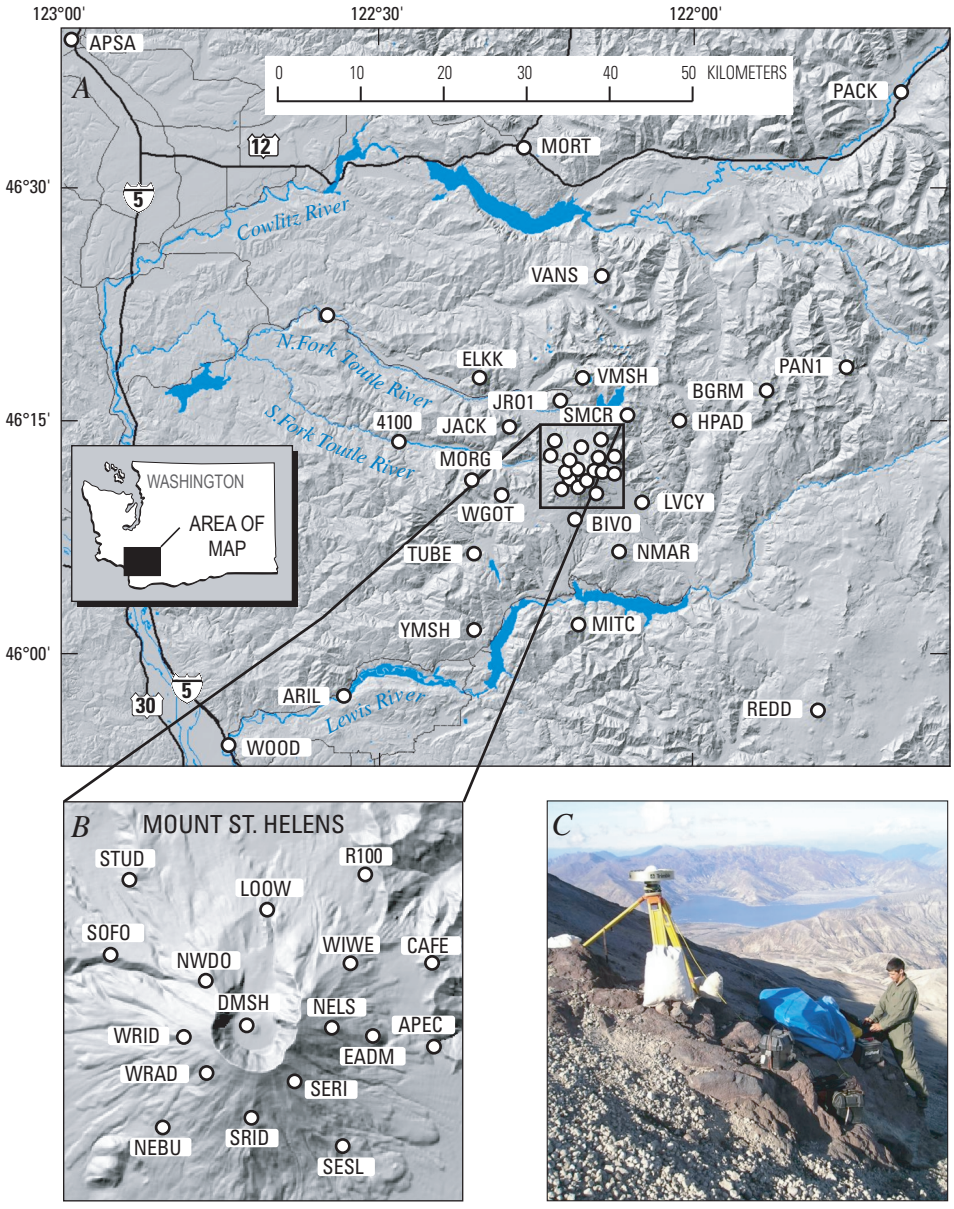

Figure 2. Large-aperture GPS network at Mount St. Helens, Washington. *A*, Location map showing 40 benchmarks observed during summers of 2000 and 2003. Base from shaded relief version of USGS digital elevation model. *B*, Benchmarks on or near the volcano. *C*, GPS receiver deployed at NELS (Nelson Ridge) on upper east flank of Mount St. Helens in October 2004.

Following a period of rapid motion toward a source beneath the volcano at a peak rate of ~0.5 mm/d in late September–early October 2004 (while the growth rate of the welt was as high as 8.9 m^3/s), the movement of JRO1 gradually slowed through December 2004. Meanwhile, the extrusion rate slowed from 5.9 m^3/s (October 13–November 4) to 2.5 m^3/s (December 11, 2004–January 3, 2005; Schilling and others, this volume, chap. 8). During May–December 2005, the velocity of JRO1 was essentially constant at ~0.04 mm/d toward the volcano. During the same interval, the rate of lava extrusion declined from 1.3 m^3/s (April 19–June 15) to 0.7 m^3/s (October 24–December 15), with somewhat higher rates during July 14–August 10 (2.0 m^3/s) and August 10–September 20 (1.6 m^3/s; Schilling and others, this volume, chap. 8).

Mount St. Helens CGPS Cluster

In response to the current eruption, CVO and the EarthScope Plate Boundary Observatory (PBO) installed 13 additional CGPS stations during October–November 2004. Most of the new stations are on the volcano, mounted 3–4 m high on steel tripods that served as EDM stations during the 1980s (fig. 3). Data from all 14 CGPS stations at Mount St. Helens are downloaded automatically to CVO and to the UNAVCO Boulder Facility Archive. The data are processed daily at the USGS Menlo Park facility to produce a 24-hour solution. Five additional stations, mounted on smaller tripods and without telemetry links, have operated intermittently since November 2004. Data from those stations are downloaded manually.

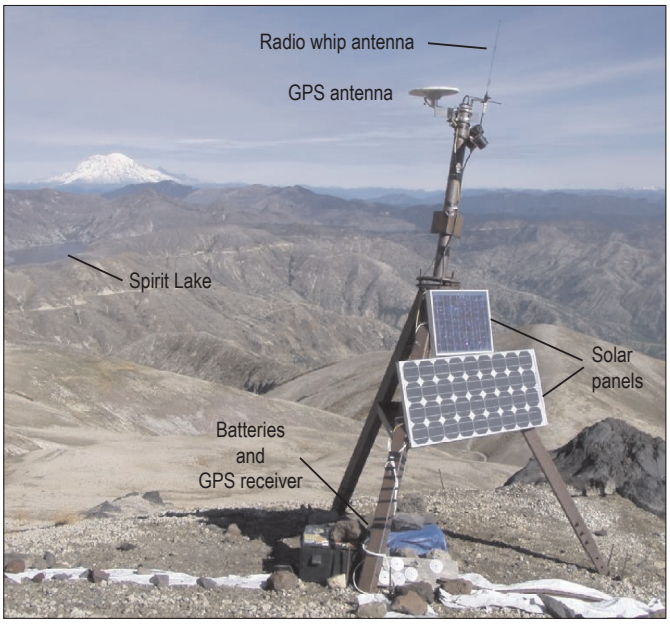

Figure 3. CGPS station WIWE (Windy West) on lower northeast flank of Mount St. Helens, Washington (fig. 2). Station is typical of several installed by CVO. View is to north-northeast. Mount Rainier is visible 77 km in distance.

Time-series plots of CGPS data show that the rate of motion toward the volcano peaked in late September or early October 2004, while the welt was growing rapidly but before the first lava emerged on October 11, 2004 (see figs. 10–13 in Lisowski and others, this volume, chap. 15). Both the far-field (beyond the crater floor) deformation rate and the extrusion rate declined progressively from mid-October through at least December 2004. Perhaps as early as January 2005, and surely by May 2005, the deformation rate and extrusion rate stabilized; both rates were relatively steady through December 2005.

Single-Frequency (L1-Only) GPS "Spiders"

It was clear from the early days of the eruption that extreme deformation of the south crater floor and glacier must attenuate rapidly with distance, because the 1980–86 dome and crater floor to the north remained essentially undisturbed, while the welt, just a few hundred meters to the south, grew to 500 m west-east, 600 m north-south, and 110–120 m high by October 11, 2004. LaHusen and others (this volume, chap. 16) report that a single-frequency CGPS station at SEP, on the 1980–86 dome less than 500 m north of the 2004–5 vent, moved anomalously about 20 cm north, 8 cm west, and 12 cm up during the 9-month period ending on September 27, 2004. This displacement was much less than we expected, given the large size and proximity of the welt. Likewise, all 13 of the CGPS stations that were installed on the volcano's flanks during October–November 2004 moved less than 2 cm during the ensuing 15 months. Therefore, it was necessary to install deformation sensors within a few hundred meters of the vent to monitor the course of the eruption. Conventional CGPS installations were not a reasonable option, because instrumentation in proximal areas had an expected lifetime of only days or weeks during the first few months of the eruption. Instead, we deployed and, in some cases, retrieved and redeployed a series of single-frequency (L1-only) CGPS stations aboard "spiders"—self-contained sensor platforms slung from a helicopter to otherwise inaccessible or hazardous sites (LaHusen and others, this volume, chap. 16). Here we summarize results of three GPS spider deployments to the growing dome, which provided reliable measurements of lineal extrusion rates for spines 3 and 4. See LaHusen and others (this volume, chap. 16) for discussion of additional deployments to the 2004–5 dome, 1980–86 dome, and Crater Glacier.

On November 20, 2004, GPS spider ELEA was set down astride spine 3, which was advancing south-southeastward across the crater floor. During the ensuing six days, before the instrument was destroyed in a rockfall, ELEA traveled 67 m southeast and 8 m up at an average rate of ~10 m/d and an average slope of 5.6° (LaHusen and others, this volume, chap. 16). The GPS spider CDAN was destroyed by a small explosive event starting at 0318 PST on January 16, 2005 (Scott and others, this volume, chap. 1), about 36 hours after it was deployed to spine 4. In the preceding 24 hours, CDAN moved 6.5 m south, 2.2 m east, and 4.7 m up, corresponding

to an average velocity of 8.3 m/d at an average slope of 34.5°. The GPS spider AHAD was deployed to spine 4 on February 8, 2005. By the time it was retrieved on February 16, AHAD had moved 29 m south, 17 m east, and 9 m up, for an average velocity of 6.2 m/day at an average slope of 15.5° (LaHusen and others, this volume, chap. 16).

Velocities measured by ELEA, CDAN, and AHAD are not directly comparable for two reasons: (1) spines 3 and 4 differed in morphology (4 was, for the most part, steeper than 3), and (2) the three spiders occupied different positions with respect to the vent. Nonetheless, slowing of the extrusion velocity between late November 2004 and mid-February 2005, as indicated by the GPS spiders, is consistent with analysis of time-lapse images from the Sugar Bowl camera (Major and others, this volume, chap. 12) and with declining volumetric extrusion rates derived from analysis of digital elevation models (DEMs) for the same period (Schilling and others, this volume, chap. 8).

No additional GPS spiders were deployed to active parts of the growing dome from March to December 2005 because the surface was too steep, too rugged, or too hot. Meanwhile, spiders deployed to older parts of the 2004–5 dome, the 1980–86 dome, and Crater Glacier continued to provide data (LaHusen and others, this volume, chap. 16).

Interferometric Synthetic Aperture Radar (InSAR)

InSAR has been used successfully to study surface deformation at dozens of volcanoes worldwide (for example, Amelung and others, 2000; Zebker and others, 2000; Lu and others, 2007), but at Mount St. Helens three factors have limited its utility. First, EDM and GPS measurements show that any surface displacements that occurred at Mount St. Helens between InSAR's emergence in 1993 (Massonnet and others, 1993) and the start of the 2004–5 eruption were small compared to the resolution of InSAR (2.83 cm/fringe for C-band images; Lisowski and others, this volume, chap. 15). Second, persistent winter snow pack and frequent precipitation destroy coherence, except in small areas above the tree line in summer-to-summer interferograms. Third, the orbital repeat intervals for radar satellites ERS (35 days), RADARSAT (24 days), and ENVISAT (35 days) are too short to capture any slow, preeruption deformation and too long to capture rapid near-vent deformation while an eruption is underway. In the latter case, extreme deformation of the growing dome and displaced glacier make the in-crater part of all interferograms incoherent.

These difficulties with InSAR can be overcome to some extent by "stacking" (averaging) several interferograms for relatively short time periods (so coherence is maintained), which collectively span a period long enough for any deformation signal to emerge from the noise. Stacking works on the premise that a small deformation signal from a fixed source will accumulate with time, while random atmospheric noise sources will tend to cancel. Poland and Lu (this volume, chap. 18) stacked and analyzed hundreds of interferograms of Mount St. Helens acquired by ERS-1/2, ENVISAT, and RADARSAT satellites from 1992 to 2005. Stacks of preeruptive interferograms indicate no sign of volcanowide deformation, which is consistent with trilateration, campaign GPS, and CGPS data for the period from 1992 to 2005 (Lisowski and others, this volume, chap. 15). In contrast, the most reliable stack of coeruptive interferograms shows line-of-sight (LOS) increases (that is, surface subsidence) on the volcano's flanks at rates of 40–50 mm/yr, which is consistent with CGPS results for the coeruptive period.

Time-Lapse Oblique Photography

Several factors contributed to the widespread use of photography, both from aircraft and the ground, to record various aspects of the eruption including (1) growth, deformation, and geomorphic evolution of the lava dome, (2) perturbed motion and deformation of Crater Glacier, and (3) emergence of the lava column from the vent and resulting movement of spines across the crater floor. First, digital cameras are capable of producing high-quality images in near-real time (an advantage over film cameras) that can be shared among colleagues with ease. Second, the perceived level of risk to observers in the crater, especially during early phases of the eruption, was a factor that encouraged remote photo documentation. In hindsight, the 2004–5 eruption has been benign by comparison to most dacite dome eruptions; nonetheless, risks in proximal areas from rockfalls and small explosions were reduced by replacing human observers with cameras, especially for investigations that required repeated observations over long periods of time (for example, time-lapse images of dome growth). Third, it was recognized early in the 2004–5 eruption that cameras were providing a unique and valuable record of the measured pace, longevity, and character of events that transpired in the vent area. An unusual suite of circumstances—gas-poor, crystal-rich magma emerging from an inclined vent on a relatively flat crater floor beneath a newly formed glacier that is contained on three sides by steep crater walls—combined to create an unusual and visually captivating landscape. Over time scales ranging from minutes to months (from drumbeat earthquakes to gouge-covered, laterally mobile, whaleback-shaped spines), the eruption produced a variety of features that are suited to photo documentation and analysis. The following sections summarize two different approaches to time-lapse photo studies of the eruption. More detailed discussions of these and other camera applications can be found in Poland and others (this volume, chap. 11) and Major and others (this volume, chap. 12).

Synoptic Observations of Dome Growth and Glacier Deformation

Mount St. Helens lies 70 km north-northeast of CVO, within sight on a clear day but at a range suitable only for reconnaissance observations. The volcano's 1980 crater opens

to the north, so the view of the current eruption site from CVO is blocked by the volcano's south flank. Continuous surveillance of the eruption by observers within sight of the vent was impractical for logistical reasons, so remote cameras were used instead to track the changing landscape in the crater. Time-lapse photography cannot be construed as deformation monitoring in a classical geodetic sense, but in the 2004–5 eruption, the disruption of the crater floor and glacier was so extreme that cameras became an effective tool for monitoring dramatic changes in the vent area. Elsewhere, CGPS stations and tiltmeters are better suited to measuring strains that are smaller by several orders of magnitude.

The first remote camera station was installed on October 10, 2004, at Sugar Bowl (altitude 1,859 m) on the east side of The Breach (open north end of 1980 crater), 2.3 km north-northeast of the vent. The Sugar Bowl camera recorded the changing morphology of the welt starting one day before emergence of spine 1 on October 11, 2004, followed by development, movement, and disintegration of three prominent whaleback spines (3, 4, and 5). The Sugar Bowl camera was poorly positioned for photographing the disintegration of spine 5 and westward migration of spine 6, which began in early August 2005, because the camera's view was blocked by the 1980–86 dome from August through early October 2005. But by mid-October 2005, spine 7 had grown into the field of view of the Sugar Bowl camera above the profile of the 1980–86 dome, where it remained through the end of 2005. Because the Sugar Bowl camera captured a large part of the dome growth that occurred from mid-October 2004 through December 2005, its images are well suited to systematic quantitative analysis. Major and others (this volume, chap. 12) used the Sugar Bowl images to estimate lineal extrusion rates as a function of time and to infer short-term (days to weeks) variations in the volumetric extrusion rate.

To complement the Sugar Bowl images, two additional camera stations were installed higher on the crater rim in August 2005. Brutus (BRUT) is located at 2,479 m altitude along the northeast rim, 1.1 km east-northeast of the vent. South Rim (SRIM) is located at 2,512 m altitude along the south-southwest crater rim, 0.7 km from the vent. BRUT sees most of the 2004–5 dome and Crater Glacier from the east-northeast; SRIM sees essentially the same area from a reciprocal vantage point.

Camera station Guacamole (GUAC), located at 1,634 m altitude on the floor of The Breach, 2.6 km north of the vent, was added in November 2005. Station GUAC provides a view of the western part of the 2004–5 dome, including spines 6 and 7, and of the deformed east and west arms of Crater Glacier. The lower altitude of GUAC, relative to the other cameras, allows for occasional glimpses under the clouds that obscure views from the higher cameras. See Poland and others (this volume, chap. 11) for additional description of the camera stations and telemetry system, including map locations, equipment used, method of storing and retrieving images, and capability for controlling camera parameters and shooting schedules.

Arguably the greatest value of the remote camera stations lies in the production of time-lapse "movies" (typically one image per day for several days, or all available three-minute images for a 24-hour period) that portray the changing morphology of the dome, deformation of Crater Glacier, rockfall sequences, and patterns of nighttime glow in an intuitive and easy-to-understand format. Several of these sequences are available on the DVD accompanying this volume and on the CVO Web site (http://vulcan.wr.usgs.gov/Volcanoes/MSH/Images/MSH04/repeat_views.html, last accessed January 14, 2008).

High-Resolution, Small Field-of-View Observations of Extrusion Site

In an attempt to capture any short-term (minutes to hours) variations in the lineal extrusion rate and to assess any correlation between these and "drumbeat" earthquakes, we deployed digital cameras with long focal-length lenses and time-lapse controllers at BRUT and on the September 1984 lobe (SEP) of the 1980–86 dome. Drumbeat earthquakes are repetitive, small earthquakes, many with waveforms similar to other drumbeats, that occurred at remarkably constant intervals during the 2004–5 eruption (Moran and others, this volume, chap. 2; Thelen and others, this volume, chap. 4). A correlation between drumbeats and lineal extrusion rate is suggested by a mathematical model that describes the extrusion process in terms of stick-slip motion of a rigid plug under the combined influences of magma pressure, gravity, and friction on the conduit wall (Iverson and others, 2006; Iverson, this volume, chap. 21). To avoid the need for longer-term power and protection from the elements, each of these camera deployments lasted for only a few hours. From BRUT, a Nikon ® CoolPix 990 camera coupled to a 12–36X spotting scope (fig. 4) produces a field of view at the vent (range ~1100 m) of approximately 60×90 m at 12X, or 20×30 m at 36X. From SEP (range ~400 m), the same camera coupled to a Questar ® 700 telephoto lens (3.5-inch diameter, f7.8) fitted with a 24-mm eyepiece (fig. 5) produces a 1.3×1.0 m field of view. Image size of the Nikon ® CoolPix 990 in "fine" resolution mode is 2048×1536 pixels (3.3 megapixels), so using it with the Questar ® 700 from SEP produces an image in which each pixel corresponds to ~0.6 mm on the ground.

Although the Nikon ® CoolPix 990–Questar ® 700 combination deployed at SEP is theoretically capable of millimeter-scale resolution at the vent, two factors combine to degrade the image quality in practice. First is the difficulty in establishing a sufficiently stable base for an imaging system with such high magnification—a problem with two parts. The first, coupling the camera system securely to the ground, can be overcome by mounting the camera and lens to a rigid plate or a short, heavy-duty tripod and by using sandbags to fix the plate or tripod firmly to the ground. The second part of the problem is ground motion associated with incessant drumbeat earthquakes and occasional larger shocks (M_{max} ~3.6).

On five occasions between September 2 and November 18, 2005, we tried frame intervals of 10 s or 30 s for periods of 1–6 hours at times when drumbeats were occurring every 2–3 minutes. Ground shaking is obvious in only a small fraction of the images, as would be expected from the framing interval, shutter speed (0.004–0.5 s), and average time between quakes. Each set of images reveals what appears to be relatively steady motion of the extrusion out of the vent, although any slight displacements of the camera system or underlying ground cannot be distinguished from apparent motion of the extrusion. We tried repeatedly to include in the images some part of the dome or crater wall that was relatively stable, but the camera's limited field of view and depth of field made this difficult and ultimately unproductive.

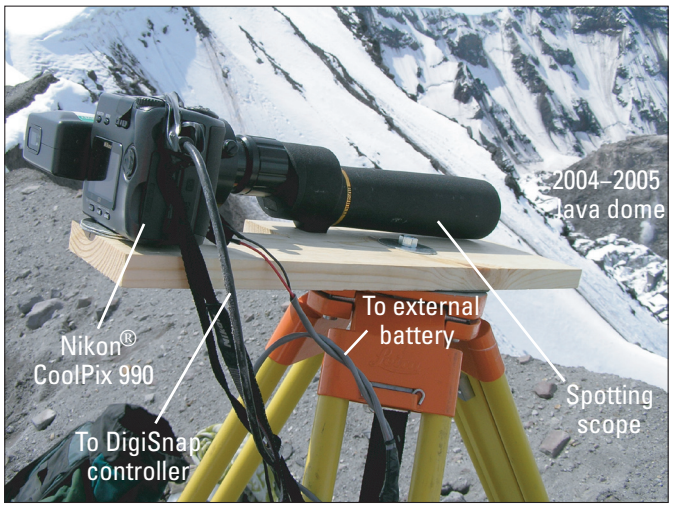

Figure 4. Temporary time-lapse photo station at Brutus (BRUT) on northeast crater rim, Mount St. Helens, Washington. Permanent camera station BRUT is ~100 m north (to the right) of this site.

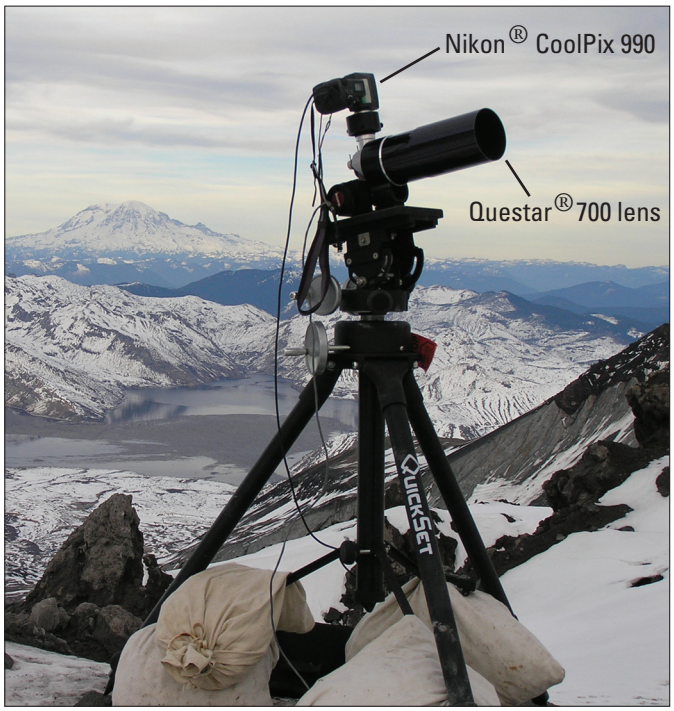

Figure 5. Temporary time-lapse photo station at SEP on September 1984 lobe of 1980–86 dome, ~400 m north of the 2004–5 vent, Mount St. Helens, Washington. Sandbags at base of tripod are for added stability. Spirit Lake near center of photo. Mount Rainier on skyline.

A second factor that contributes to image degradation is heat shimmer caused by uneven refraction of light in unstable air along the camera's line of sight. Heat shimmer is exacerbated by numerous localized heat sources on the 1980–86 and 2004–5 domes and by extensive, hot talus deposits surrounding the active vent. The resulting image degradation can be mitigated to some extent by choosing the line of sight carefully, but this usually comes at the expense of the most desirable framing.

We have been unsuccessful in attempts to capture photographically any jerkiness in the extrusion process that might be associated with drumbeat or larger earthquakes. However, the high-resolution time-lapse images have been useful for another purpose. Because the images are at a known scale (determined empirically by photographing objects of known size with the same camera/lens combination at distances measured using a laser rangefinder), each set of images can be used to measure the average lineal extrusion velocity in the image plane. Motion of the extrusion can be discerned in images acquired only a few minutes apart.

The surface velocity of spine 6 was measured using high-resolution, time-lapse photography from SEP on three occasions from September 2, 2005, to October 18, 2005 (table 1, fig. 6). SEP was due north of the advancing front of spine 6 at the time, so the motion of features through the image frame can be used to measure west and up components of the velocity vector. The resultant velocity (west+up) is a reasonably good indicator of the lineal extrusion rate of spine 6, which was also advancing northward during this period owing to endogenous growth and spreading. The lineal extrusion rate determined in this way declined from 4.51 m/d on September 2 to 4.45 m/d on September 20 and to 2.51 m/d on October 18. Distances from the SEP camera station to the imaged part of spine 6 were measured with a laser rangefinder and are reported as the north component of velocity in table 1. The value for September 2 (>3.3 m/d) is a minimum value because there were no previous rangefinder measurements. The rate was greater than 3.3 m/d, the average value calculated from measurements made on September 2 and September 20, because the extrusion rate and growth rate of spine 6 generally slowed with time.

Figure 6 is based on a subset of 702 images acquired at SEP from 11:14:17 to 17:04:47 PDT (30-s interval) on September 20, 2005. Distance from the camera to the steep, gouge-covered north face of emerging spine 6, measured with a laser rangefinder, was 342±1 m. The camera's field of view included an aluminum target, 46×61 cm in size, for scale. The target was hung by steel cables from an anchor slung by helicopter to the top of the spine. For 58 of the sharpest images, the

pixel coordinates of a distinctive feature on the target relative to a corner of the image were determined by inspection using a PC graphics program. A spreadsheet program was used to convert pixel coordinates to millimeters at the target, using the known image scale, to determine optimal linear fits to the data, to calculate departures from the best-fit line, and to plot the results as a function of time. Average velocity components (that is, slopes of the best-fit lines) are 3.89 m/d west and 2.17 m/d up. Departures from the best-fit lines are irregular and small, on the order of ±10 mm (fig. 6, middle). Therefore, the lineal extrusion rate during a 3.5-hr period on September 20, 2005, was constant within the uncertainty of the measurements. There is no evidence of stick-slip motion of the spine greater than about 10 mm associated with drumbeat earthquakes, which were occurring every 2–3 minutes, nor with two larger shallow quakes at 15:47:19 (M_d 2.9) and 16:05:26 (M_d 1.0) PDT.

Average velocities (west and up) determined from similar observations on September 2, 2005, and October 18, 2005, are 4.51 m/d and 2.51 m/d, respectively (table 1). No comparable measurements were possible from the Sugar Bowl camera on September 2 or September 20, but measurements on October 18, 22, and 24 are in the range 3–4 m/d. In all three cases in which these types of observations were made, the motion of the extruding spine was steady over time scales of a few hours; no evidence of short-term rate variations was seen in any of the photos. However, such variations likely are occurring in the conduit during earthquakes, and variations could also be occurring at the surface in millimeter-scale jerks too small to be resolved by this technique. During the first year of the eruption, drumbeat earthquakes occurred at rates of 0.3–3 per minute, while the lineal extrusion velocity was 1–10 m/d. If all of the motion were associated with drumbeat earthquakes, this would imply an average event size of 2.3 mm/drumbeat at the source. This value for average event size would be smaller if, as seems likely, extrusion is partly aseismic and seismic dislocations are attenuated between the earthquake source area and the surface.

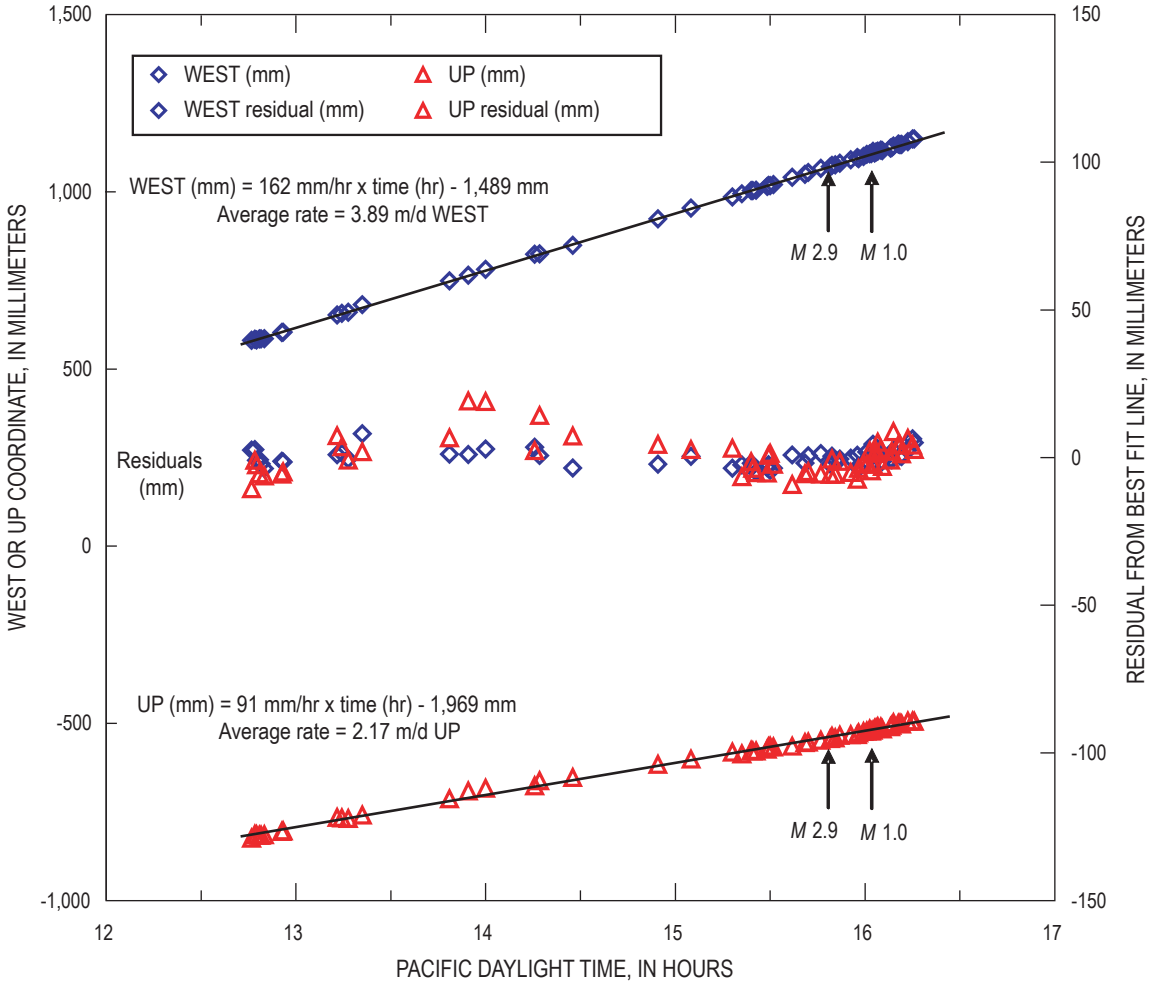

Figure 6. Lineal extrusion velocity of spine 6 for ~3.5-hour period on September 20, 2005, based on analysis of high magnification, small field-of-view, time-lapse (30 s interval) digital images from temporary camera station SEP, Mount St. Helens, Washington. Departures from best-fit lines for west and up components of motion are shown with corresponding symbols in middle ("Residuals").

Table 1. Velocities determined from high-magnification, small field-of-view, time-lapse images at station SEP, Mount St. Helens, Washington.

Date (2005)	West velocity (m/d)	Up velocity (m/d)	Extrusion velocity (west + up) (m/d)	North velocity (m/d)	Distance to target (m)
September 2	4.23	1.55	4.51	>3.3	402
September 20	3.89	2.17	4.45	3.3	342
October 18	2.41	0.69	2.51	1.3	306

Trilateration and Triangulation of Points on the Growing Dome

Classical trilateration and triangulation techniques were adapted with good results to measure changing displacement rates on the growing dome during 1980–86 which, together with changing patterns of seismicity, were used to predict the start of each dome-building episode from a few days to three weeks in advance (Swanson and others, 1983). Measurements were made by affixing prism reflectors to the dome and tracking their motion by using an EDM and theodolite from fixed points on the crater floor or, in some cases, from points on stable parts the dome itself. To increase the number of targets without continuously exposing a large number of reflectors to harsh conditions in the crater, some target points were marked with a survey pin so that a person on foot could accurately position a reflector at the point for a few minutes while a colleague made EDM and theodolite measurements. In this way, more than a dozen survey points distributed across the dome could be surveyed in a few hours.

We tried a similar approach to measure displacement rates on the 2004–5 dome, with lesser success. One difference from the 1980–86 dome is that continuous extrusion, frequent rockfalls, and the deeply crevassed glacier generally precluded foot travel on or around the 2004–5 dome. Instead, five targets, each consisting of a single prism reflector at the center of a painted wooden board attached to a barbell weight as a base, were slung from a helicopter to the 2004–5 dome and Crater Glacier. Three of the targets were set on spine 4, one to the east on rubble of spine 3, and one on the east arm of the glacier. None of the targets could be placed on active spine 5 because it was too steep and hot at the time. All of the targets were observed from BRUT (range ~1,100 m) using a Wild ® TC1000 total station tacheometer on April 21, May 3, and September 20, 2005. The tacheometer can produce surveys with angle measurements accurate to 3 arc seconds at range 1–2.5 km, depending on viewing conditions. Standard deviation of range measurements is 3 mm + 2 ppm, which corresponds to ±5 mm at 1 km range.

Four of the targets survived to the second survey, and three survived to the third survey. However, reflections were obtained from only two targets in the initial survey and from no targets in the second or third surveys, so we lack range measurements for the repeat surveys. The lack of reflections likely resulted from dust clinging to the prisms, etching of the glass by volcanic gases, and (or) changing alignment of the prisms with respect to the sight line as a result of earthquake shaking or slumping. The longest-surviving targets were near the top of spine 4, near the base of spine 3, and on the east arm of the glacier.

For the period May 3 to September 20, 2005, minimum average horizontal velocities of the three surviving targets declined to about one-fourth to one-third of the corresponding values for April 21 to May 3, 2005. For example, the average velocity of a target near the top of spine 4 declined from 0.28 m/d during the early period (April 21 to May 3) to 0.06 m/d during the latter period (May 3 to September 20). For the same periods, the target near the base of spine 3 slowed from 0.09 m/d to 0.02 m/d, and the eastside glacier target slowed from 0.49 m/d to 0.18 m/d. Steep, rugged, and hot terrain on the active dome precluded the use of GPS spiders during this period, so no data are available for comparison. Regardless, the observed slowing trend is consistent with what was happening in the crater at the time. When the first triangulation measurements were made on April 21, 2005, spine 5 was extruding southward, shoving the remnants of spines 3 and 4 southeastward and compressing the east arm of Crater Glacier, which resulted in thickening and increased rate of flow northward (Walder and others, this volume, chap. 13). Spine 6 emerged in early August 2005 and moved westward for the duration of the measurements. The movement of spine 6 eased the stress on spines 3 and 4 and on the glacier's east arm, which caused their velocities to slow.

Total-station surveys made by using helicopter-deployed targets are a feasible, albeit costly and manpower-intensive means to monitor surface displacements on a growing dome. This approach might be cost effective in some situations, but in our case the measurements were abandoned owing to the difficulty of maintaining targets on the dome and the cost of helicopter operations required for each survey. The long sight lines and consequent inability to obtain reflections from the prisms greatly weakened the value of the survey. Although the targets costs less than $200 each, their deployment and initial survey required about one hour of helicopter flight time (~$750/hr), as did each of two repeat surveys spaced 12 days and ~4.5 months apart, resulting in ~1 m accuracy at three

surviving targets. For comparison, a GPS spider costs about $2,500, can be deployed to the dome in about one helicopter flight hour and later retrieved if desired. A spider provides three-dimensional positioning information every few minutes, with an accuracy of a few centimeters, without the need for field personnel, except for deployment and retrieval.

Borehole Tiltmeters

Two Pinnacle 5000 series borehole tiltmeters with tilt resolution of 5×10^{-9} radian (3×10^{-7} angular degree) were installed on the 1980–86 dome to record any transient (seconds to days) ground tilt that might accompany extrusion of the 2004–5 dome and consequent deformation of the crater floor and glacier. The installations were motivated in part by a dynamical model in which stick-slip motion of the plug produces repetitive, reversible strain in host rock near the conduit (Iverson and others, 2006; Iverson, this volume, chap. 21). If each drumbeat earthquake represents an upward "slip" of the plug, followed by a few minutes of increasing magma pressure while the plug remains "stuck," drumbeats should be associated with sudden inward tilt followed by gradual outward tilt between beats.

To test this hypothesis, the first tiltmeter was installed in a 2.3-m-deep hole bored into the September 1984 lobe of the 1980–86 dome (SEP), 480 m N. 16° W. of the 2004–5 vent, on August 5, 2005. A second tiltmeter (REM) was installed in a 1.8-m-deep hole on the northeast sector of the 1980–86 dome, 480 m N. 34° E. of the vent, on November 17, 2004. Both tiltmeters were modified by the manufacturer to enable one-second sampling. Data are telemetered to CVO by way of the U.S. Forest Service's Coldwater Ridge Visitor Center.

Analysis of the tiltmeter records is ongoing, and a complete discussion of results is beyond the scope of this paper. To date, we have seen no evidence of repetitive, reversible tilt events associated with drumbeat earthquakes. It is possible that tilts occur but are too small to be resolved by the tiltmeters, or that the tiltmeters are too far away from the source of the drumbeats. Fractured host rock surrounding the conduit wall or the rubbly interior of the 1980–86 dome might accommodate strains produced by stick-slip motion of the plug without transmitting them to the tiltmeter sites. Without further analysis, this null result should not be interpreted as negative evidence for the occurrence of stick-slip motion as predicted by the model.

Both tiltmeters have recorded tilt changes over time scales of a few minutes to weeks that are likely related to the extrusion process. The azimuths of tilt vectors for many of these events point either toward or away from the extrusion site within a few degrees. Consequently, the vectors from two tiltmeters tend to intersect close to the vent, indicating a shallow pressure source there. It seems plausible that some of the tilt signals are caused by relatively subtle changes in the shallow supply rate or extrusion rate, perhaps related to continual reorganization of the uppermost part of the conduit as the locus of surface activity shifts and the shape of the dome changes. Some of the larger earthquakes (M_d ~2) are associated with tilt events lasting several minutes, but most are not.

A tiltmeter and GPS spider (DOM1), located within 30 m of each other on the September 1984 lobe, responded to some of the same events. For example, the radial tilt component and DOM1 northings increased during September 1–23, 2005, by about 30 microradians and 12 cm, respectively. The instruments are nearly due north of the vent, and both measurements suggest inflation of the vent area. The simplest explanation is that increasing pressure beneath the vent caused the September 1984 lobe to tilt and move northward. At the time, spine 6 was extruding southwestward and migrating westward prior to the emergence of spine 7 in mid-October 2005. Northward tilting and displacement of the September 1984 lobe presaged the emergence of spine 7, possibly during a period of increased extrusion rate. Unfortunately, measurements of the lineal extrusion rate from Sugar Bowl were impossible in September 2005 because the camera's view of spine 6 was blocked by the 1980–86 dome (see earlier section titled Synoptic Observations of Dome Growth and Glacier Deformation).

Discussion

Although some of the techniques discussed above were more successful than others, all of them contributed to our evolving understanding of how Mount St. Helens deformed before and during eruptive activity in 2004–5. Rather than discussing the deformation results separately here, we also consider information from other disciplines (seismology, gas geochemistry, and petrology) and address a few broader issues. Our intent is to characterize current thinking about the eruption and to draw attention to some unresolved questions.

Where, and for how long, was the 2004–5 magma stored before the beginning of unrest on September 23, 2004? What is the nature of the magma reservoir and conduit system? How quickly did the 2004–5 magma rise to the surface? Why was there no inflation at JRO1 prior to September 23, 2004, given that the station clearly responded to deflation and shallow seismicity starting on that date? What are the implications for the future course of this eruption and for anticipating eruptions at similar volcanoes? None of these questions can be answered definitively from the geodetic data alone; however, when combined with other datasets, the geodetic data help to place useful constraints on Mount St. Helens' magma plumbing system and to highlight areas for additional research.

Source Models

The details of various source models fit to the geodetic data are discussed elsewhere in this volume, including Lisowski and others (chap. 15), Poland and Lu (chap. 18), and Mastin and others (chap. 22). Common elements of these source models are (1) depth in the range of 5–12 km (bot-

tom possibly as deep as 20 km), and (2) volume loss through December 2005 in the range 15–30×10^6 m^3, compared to extruded volume of 73×10^6 m^3. Lisowski and others (this volume, chap. 15) modeled and removed the effects of plate motion, regional tectonics, and gravitational loading by the new dome before inverting CGPS data for a best-fit volcanic source model—a point prolate spheroid with its long axis vertical centered near 8 km depth, with a volume loss of 16–24×10^6 m^3 through October 31, 2006. Poland and Lu (this volume, chap. 18) modeled LOS changes from stacked co-eruptive interferograms by using a point source, which best fit the data with a depth of 12 km and a volume loss rate of 27×10^6 m^3/yr. They concluded that a more complicated model is not justified by the InSAR data alone, but they agreed with other authors in the volume that a vertically elongate source is probably more realistic and a better fit to the geodetic dataset as a whole. Mastin and others (this volume, chap. 22) used a vertical ellipsoidal source to fit surface displacements from CGPS data from November 8, 2004, to July 14, 2005. They concluded that the top of the source is 5±1 km deep, but the basal depth is poorly constrained—possibly 10–20 km. Their estimate of source-volume loss during that period is 11–15×10^6 m^3, increasing as the bottom of the source gets deeper. This corresponds to an average volume-loss rate of 16–22×10^6 m^3/yr, which we might double to account for the period of rapid motion at JRO1 from September 23, 2004, to November 8, 2004, which was not included in the model.

These geodetic models generally are consistent with the amount of CO_2 and other volcanic gases emitted during the eruption, which indicate that the erupting magma last equilibrated at 850°C and 130 MPa—conditions corresponding to a reservoir 5.2 km deep (Gerlach and others, this volume, chap. 26). Likewise, samples of the 2004–5 dome indicate that the pressure of last phenocryst growth corresponds to that near the apex of the magma reservoir at a depth of about 5 km (Pallister and others, this volume, chap. 30; Rutherford and Devine, this volume, chap. 31). Pallister and others (this volume, chap. 30) noted the possibility that the 2004–5 magma might be residual from the 1980–86 reservoir and went on to write: "Viewed in the context of seismic, deformation, and gas emission data, the petrologic and geochemical data can be explained by ascent of a geochemically distinct batch of magma into the apex of the [1980–86] reservoir during the period 1987–1997, followed by upward movement of magma into a new conduit, beginning in late September 2004."

In our opinion, the geodetic, gas-emission, and geochemical data from the 2004–5 eruption all point to involvement of magma that was stored in a vertically elongate reservoir centered near 8 km depth and extending upward to about 5 km. We believe this is the same reservoir that fed the plinian eruption of May 18, 1980, smaller explosive eruptions during the summer of 1980, and dome-building eruptions during 1980–86, as inferred by Scandone and Malone (1985) from seismic data (source centered at 9 km, extending from 7 km to 14 km) and Rutherford and others (1985) from the mineral phase assemblage found in May 18 pumice (7.2±1 km). It seems likely that the reservoir was replenished prior to (Moran, 1994; Moran and others, this volume, chap. 2) and possibly during the current eruption (Mastin and others, this volume, chap. 22; Pallister and others, this volume, chap. 30). Data from GPS and InSAR show that most of the surface deformation caused by pre-eruption reservoir inflation occurred prior to 1991, but there is seismic evidence for pressurization of the reservoir and upward fluid intrusion starting in 1987 and continuing at least until 2001. Apparently, reservoir replenishment and surface inflation occurred aseismically until shortly after the extended pause in dome building that began in 1986. Thereafter, increasing strain on rock hosting the reservoir and episodic intrusion of fluids induced microseismicity but no measurable surface deformation.

Implications for the Magma Plumbing System

On September 22, 2004, two things were clear: (1) seismicity at Mount St. Helens was at a low background level characteristic of long periods between sporadic earthquake swarms, and (2) JRO1 was moving northeastward relative to stable North America as part of a tectonic block undergoing clockwise rotation about a pole located either in south-central Oregon (Savage and others, 2000) or along the western part of the Oregon-Washington border where it intersects the Olympic-Wallowa lineament (McCaffrey and others, 2000). The emission rates of volcanic gases probably were low, as they had been each time they were measured after a temporary increase in CO_2 emission was noted during increased seismicity in spring–summer 1998. On four occasions from September 27 to October 2, 2004, measured emission rates of magmatic CO_2 and SO_2 were less than detection thresholds; the first notable increase did not occur until October 3, 2004 (Gerlach and others, this volume, chap. 26).

In hindsight, the September 22 calm belied a volcano poised to erupt. A swarm of small earthquakes, all within 2 km of the crater floor, began around 0200 PDT September 23. By midday on September 28, cracks large enough to be seen from a helicopter flying in the crater appeared in glacier ice on the south crater floor. Rapid uplift and intense seismicity continued for several days, and by October 7, a large welt growing on the south crater floor had approached the height of the 1980–86 dome (fig. 7). The first of several spines emerged from the welt on October 11, less than three weeks after the peaceful dawn of September 22.

Model-derived estimates of source-volume decrease during the first 15 months of the eruption are in the range 15–30×10^6 m^3, compared to an erupted volume of 73±4×10^6 m^3 through December 15, 2005. This suggests, but does not require, that the magma reservoir was partially recharged during the eruption. The lava extrusion rate declined from 5.9 m^3/s to 2.5 m^3/s during the 2.7 months from October 13, 2004, to January 3, 2005, but it varied only between 2.4 m^3/s and 0.7 m^3/s during the ensuing 14 months through the end of 2005 (Schilling and others, this volume, chap. 8). Meanwhile, the

JRO1 displacement rate slowed from a peak value of 0.5 mm/d in late September–early October 2004 to a steady 0.04 mm/d from May through December 2005. These trends suggest that the eruption might be approaching a steady-state condition in which the extrusion rate equals the recharge rate. If so, the situation could persist for years to decades, limited only by the volume of magma available for recharge.

Constraints and Conundrums

The geodetic data help to constrain the depth and geometry of the magma plumbing system and the time history of magma outflow and possible recharge to the reservoir. However, additional questions arise when the geodetic data are considered together with other datasets. For example, why did JRO1 immediately respond to the onset of shallow seismicity, presumably when magma began its ascent, but did not detect any precursory surface deformation during the preceding seven years? The most straightforward answer is that no such deformation occurred because the system was poised to erupt magma stored in the reservoir or conduit system since the 1980–86 eruption, long before JRO1 was installed in May 1997. This idea is consistent with data from trilateration surveys that show surface dilatation, presumably caused by magma accumulation beneath the volcano, between 1982 and 1991. It is also possible that the reservoir inflated during the series of earthquake swarms between 1987 and 2001 by an amount that was too small to cause measurable surface deformation. Mastin and others (this volume, chap. 22) make the point that magma compressibility could have significantly dampened any geodetic signal at Mount St. Helens. Perhaps reservoir magma is compressible enough and the host rock stiff enough that the amount of magma added to the reservoir since 1987 was accommodated without measurably deforming the surface.

How did material that resulted in rapid development of a welt on the south crater floor and subsequent extrusion of highly crystalline, gas-poor magma as gouge-covered spines (Cashman and others, this volume, chap. 19) move through or past the 1980–86 conduit system without substantially deforming more of the volcano and its surroundings? Station JRO1, 9 km north-northwest of the 2004–5 vent, recorded no anoma-

Figure 7. Welt growing on south crater floor, October 7, 2004, as seen from Brutus (BRUT) on northeast crater rim, Mount St. Helens, Washington. South (left) half of the welt is mantled by uplifted glacial ice and ash from small explosions on October 1 and October 5. The north (right) half comprises uplifted crater-floor material and part of the south flank of the 1980–86 dome. The latter was dubbed "Opus area" after 1980s-vintage EDM station Opus, which was located on south side of graben that formed during May 1985 dome-building episode (Swanson and others, 1987).

lous motion at millimeter scale before the eruption. A single-frequency GPS station at SEP on the 1980–86 dome, less than 500 m from the vent, moved anomalously about 20 cm north, 8 cm west, and 12 cm up during the 9-month period ending on September 27, 2004 (LaHusen and others, this volume, chap. 16)—seemingly not enough to accommodate the shallow intrusion of a meters-thick dacite magma body. One possibility is that the conduit is so poorly coupled to the rest of the volcano that the rising magma column was able to push ahead older conduit material, rather than intruding it. Otherwise, the conduit walls and surrounding host rock would have to be implausibly compliant to accommodate an intrusion without causing more widespread deformation.

If the former contents of the conduit were pushed ahead of reservoir magma, when did the latter first reach the surface? If rapid emergence of the first whaleback-shaped extrusion (spine 3) in late October 2004, following the more-labored extrusions of spines 1 and 2, marked the first arrival of reservoir magma, then the volume of conduit material flushed from the system was about 20×10^6 m^3—the volume of surface deformation plus spines on November 4, 2004. The corresponding radius r_c for a cylinder extending from the surface to depth d = 5 km is 35.7 m, or 28.2 m for d = 8 km. Using the volume of material extruded by November 4, 2004 (11.8×10^6 m^3), instead of the volume of surface deformation, we obtain r_c = 27.4 m for d = 5 km, or 21.7 m for d = 8 km. The average ascent rate through the conduit, v_c, assuming reservoir magma began its rise on September 23, 2004, is 120 m/d for d = 5 km, or 190 m/d for d = 8 km. If, instead, reservoir magma arrived at the surface as spine 1 on October 11, 2004, when the volume of the welt was 10.1×10^6 m^3, then r_c = 25.4 m for d = 5 km, or 20.0 m for d = 8 km; and the average ascent rate was 280 m/d (d = 5 km), or 440 m/d (d = 8 km). Thus, for all plausible dimensions of the conduit system, reservoir magma must have reached the surface early in the eruption, probably about the time CO_2 emission rates peaked in October 2004 (Gerlach and others, this volume, chap. 26).

Calculated ascent rates in the conduit exceed observed lineal extrusion rates, v_s = 2–10 m/d, by more than an order of magnitude, so the conduit must widen considerably near the surface. Thornber and others (this volume, chap. 32) reach a similar conclusion (that is, a "wineglass shape" for the conduit) based on their interpretation of amphibole-rim thicknesses in post-November 2004 magma. Equating magma flux through the conduit to that at the surface for d = 8 km, r_c = 28.2 m, v_c = 190 m/d, and v_s = 10 m/d, we obtain a vent radius, r_v, = 125 m and an extrusion rate of 5.7 m^3/s. Using d = 5 km, r_c = 35.7 m, v_c = 120 m/d, and v_s = 10 m/d produces essentially the same results, which are representative of the early part of the eruption. For comparison, Schilling and others (this volume, chap. 8) estimated the vent diameter to be 150–230 m east-west based on partial exposures of the basal perimeters of extruding spines. The north-south vent diameter is unconstrained owing to lack of adequate exposure.

Slowing of the JRO1 displacement rate suggests a corresponding reduction in the net rate at which magma is being withdrawn from the reservoir to a value that might be sustainable for the foreseeable future (0.5–1 m^3/s). If the lesser withdrawal rate is a result of recharge, the eruption could continue indefinitely. On the other hand, in the absence of sufficient recharge, the eruption will end when (1) the reservoir is depleted of eruptible magma, (2) the pressure difference between reservoir and surface falls below some threshold, or (3) friction in the upper part of the conduit chokes off magma flow (that is, stick-slip motion of the plug ceases—the plug stays stuck). In the latter case, increasing magma pressure beneath the plug could eventually result in an explosion; however, the low gas content of the 2004–5 magma makes an explosion less likely than it would be for gas-rich magma.

When gas-saturated magma rises, decreasing lithostatic pressure results in bubble formation. If some of the bubbles rise buoyantly through the magma and escape toward the surface, we might expect an eventual uptick in gas emission rates if, as we suspect, the Mount St. Helens magma reservoir has been recharged during the current eruption. The fact that no such increase was observed through the end of 2005 requires explanation. Emission rates of CO_2, SO_2, and H_2S were negligible during September 27–30, 2004, a period characterized by scrubbing or sealing-in of gases. Several days of wet degassing ensued, when scrubbing by the ground-water system dominated degassing. October 5–6, 2004, marked the beginning of a period of dry degassing when emission rates increased to 800–2,400 metric tons per day (t/d) CO_2, 40–250 t/d SO_2, and 0–10 t/d H_2S (Dzurisin and others, 2005). Throughout 2005, the emission rates of all three gases were near or below the low end of the October 2004 ranges (Gerlach and others, this volume, chap. 26).

It is possible that the 2004–5 eruption was triggered by a recharge event in September 2004 and that gases exsolved from the rising magma made their way to the surface by early October 2004, causing the observed uptick in emission rates; however, this seems unlikely for two reasons. First, the total amount of CO_2 emitted during the eruption is consistent with degassing the volume of magma that reached the surface, assuming the magma last equilibrated at about 5 km depth. In other words, there is no need to invoke recharge to account for the amount of CO_2 emitted. On the contrary, low CO_2 emission rates imply that the reservoir magma is "flat," that is, depleted of any significant exsolved-gas phase that might have accumulated in its upper part (Gerlach and others, this volume, chap. 26). Perhaps the catastrophic landslide and explosive eruptions of 1980 depleted a volatile-rich cap that formed since the end of the Goat Rocks eruptive period in 1857, and any exsolved gases that accumulated since then escaped before the current eruption began.

The second factor that weighs against a recharge event in September 2004 as the cause of increased CO_2 emission in early October is the short time interval involved. If, for example, recharge at 8 km depth beginning on September 23 was responsible for newly-exsolved CO_2 reaching the surface by October 1, the average ascent rate of the gas was ~1 km/d. This ascent rate is far greater than, for example, the

bubble ascent rate of 1.7 m/hr inferred for the 1975 eruption of Mauna Loa volcano, Hawai‘i (Ryan, 1995), even though bubble ascent rates in basalt are likely to be much greater than in dacite. It is possible that the existence of fracture permeability along the margins of the reservoir could allow this constraint to be bypassed. However, it is more straightforward and seems more likely that the source of CO_2 reaching the surface in early October 2004 was the same magma from the conduit or upper part of the reservoir that began extruding shortly thereafter. If so, any volatiles exsolved from magma entering the lower part of the reservoir since the eruption began have not yet fully traversed the length of the reservoir and conduit system. This implies an average rise rate less than about 10 km in 15 months, corresponding to 0.9 m/hr.

The foregoing paragraphs are not meant to imply that a reservoir recharge event could not have occurred during September and October 2004, but rather that such an event, if it did occur, might not have been the source of CO_2 that reached the surface in the next few days. The CO_2 that did reach the surface in early October 2004 could have come from magma previously stored in the conduit or reservoir. Furthermore, the lack of an uptick in CO_2 emission rates since peak values were measured in October 2004 suggests that the path for CO_2 from the base of the reservoir to the surface might be complex and time-consuming to the extent that the CO_2 signature of any recharge that occurred since the 2004–5 eruption began has yet to reach the surface.

Thus, all three of the traditionally reliable eruption precursors (seismicity, ground deformation, and volcanic gas emission) failed to provide warning that an eruption was imminent at Mount St. Helens until a few days before a visible welt appeared at the surface—both in September 2004 and March–April 1980 (the north-flank bulge). Sporadic earthquake swarms beneath the volcano from 1987 to 2003, at least one of which (1998) was accompanied by increased CO_2 emission, provided longer-term but nonspecific forewarning of the current eruption. Data from a single-frequency CGPS station on the 1980–86 dome might have provided several months warning that something anomalous was occurring, but the station was not operational during most of that period, and its data were not analyzed until after the eruption began. Crater-floor deformation might have been hidden beneath thick glacial ice for some time before the first surface cracks were noticed on September 28.

Implications for Volcano Monitoring

One obvious lesson from the 2004–5 eruption is the value of a dense network of CGPS stations operating long before the onset of unrest. The need for CGPS data from proximal stations was addressed at Mount St. Helens only after the 2004–5 eruption began. Most of the ground deformation that accompanied reservoir replenishment following the 1980–86 eruptions had ceased by 1991, before installation of the first CGPS station, JRO1, in 1997. Playing catch-up with a restless volcano is short sighted and dangerous. The best and safest time to install a comprehensive, integrated monitoring system is before unrest begins, when the need for such a system is less apparent.

There is much we do not understand about the 2004–5 eruption of Mount St. Helens, but the challenge does not end there. On January 11, 2006, Augustine Volcano in Cook Inlet, Alaska, began erupting for the first time since 1986. Augustine is a central dome and lava-flow complex surrounded by pyroclastic debris—not unlike Mount St. Helens in several respects. Both volcanoes are relatively young and frequently active. Mount St. Helens is notorious for its debris avalanche and eruption of May 18, 1980; Augustine has produced at least 11 debris avalanches in the past 2,000 years as a result of summit dome collapses (Waitt and Beget, 1996; Beget and Kienle, 1992). Mount St. Helens' eruptive products range from basalt through dacite (dominantly dacite). Augustine's products are dominantly andesite with small amounts of basaltic andesite and dacite. Before their current eruptions, both volcanoes last erupted in 1986, and both eruptions were dome-building events (Mount St. Helens, 1980–86; Augustine, March–September, 1986).

Given these similarities, we might expect that the precursors to Mount St. Helens' and Augustine's most recent eruptions were similar, too, and in several respects they were; however, there were some striking differences. On November 29, 2005, the Alaska Volcano Observatory (AVO) released the following statement (http://www.avo.alaska.edu/activity/avoreport.php?view=info&id=342&type=info&month=November&year=2005, last accessed January 14, 2008):

> Beginning in May 2005, there has been a slow increase in the number of earthquakes located under Augustine Volcano. The earthquakes are generally small (less than magnitude 1.0) and concentrate roughly 1 km below the volcano's summit. These earthquakes have slowly increased from 4–8 earthquakes/day to 20–35 earthquakes/day. Additionally, data from a 6-station Global Positioning System (GPS) network on Augustine Volcano indicate that a slow, steady inflation of the volcano started in mid-summer 2005 and continues at present. The GPS benchmark located nearest the summit has moved a total of 2.5 cm (1 inch). This motion is consistent with a source of inflation or pressure change centered under the volcano. This is the first such deformation detected at Augustine Volcano since measurements began just prior to the 1986 eruption.

Small explosions began on December 9, 2005, and there were reports of unusual "steaming" and sulfur smell downwind of the volcano, as well as a visible, condensed-steam plume extending at least 75 km from the volcano on December 12. The eruption began in earnest on January 11, 2006, characterized by magmatic explosions, pyroclastic flows and lahars, and extrusion of a new lava dome and flow that was first observed on January 16, 2006. Emission rates for SO_2 were about 1,000 t/d in early January and several thousand t/d during the first week of the eruption. Corresponding CO_2 emission rates were 2–3 times greater (Cervelli and others, 2006; Power and others, 2006).

The Augustine and Mount St. Helens eruptions were similar in the following respects:

1. No precursory inflation of a deep (>5 km) source was detected; modeling of GPS data indicates the preeruptive inflation source at Augustine was 1–2 km beneath the volcano's summit, at a depth of approximately sea level (Cervelli and others, 2006),

2. Deep deflation was associated with extrusion,

3. Phreatic explosions preceded the beginning of extrusion,

4. Energetic swarms of shallow earthquakes occurred in the days prior to the first explosion, and

5. Erupted products were predominantly effusive, with only minor tephra.

The eruptions differed in the following ways:

6. There were eight months of elevated seismicity at Augustine versus a few days of elevated seismicity at Mount St. Helens,

7. There were six months of precursory inflation at Augustine versus no precursory inflation at Mount St. Helens (but see below), and

8. There were several thousand tons per day of SO_2 and CO_2 recorded at Augustine versus 40–250 t/d SO_2 and 800–2,400 t/d CO_2 recorded at Mount St. Helens (Gerlach and others, this volume, chap. 26).

The differences in items 6 and 8 are supported by unambiguous seismic and gas emission-rate data, but the apparent lack of precursory inflation at Mount St. Helens (item 7) could be an artifact of inadequate geodetic monitoring. Station JRO1 might have been too distant (9 km) to detect inflation of a shallow source comparable to the one that inflated for months at Augustine. Even so, relatively deep sources at both volcanoes deflated during the eruptions but did not inflate in the years or months beforehand—a pattern unlikely to be sustainable over several eruption cycles. A possible explanation for this observation is that inflation of deep magma sources beneath arc volcanoes occurs mainly early in the eruption cycle, soon after an eruption ends, and slows as the next eruption approaches. This pattern has been observed in InSAR studies of Westdahl and Okmok volcanoes in the Aleutian arc by Lu and others (2003, 2005). Lu and his colleagues suggest that the magma supply rate is governed by the pressure gradient between a deep source and shallow reservoir. The pressure gradient and hence the flow rate are greatest immediately after eruptions. Pressurization of the reservoir decreases both the pressure gradient and flow rate, but eventually the reservoir ruptures, an eruption or intrusion occurs, and the cycle starts anew. This scenario is consistent with trilateration and campaign GPS results for Mount St. Helens that showed dilatation between 1982 and 1991, but no measurable deformation from 1991 to 2000 or from 2000 to 2003.

Given that the latest repose periods at Mount St. Helens and Augustine were similar, and that the magma erupted at Mount St. Helens is more viscous (greater SiO_2 content and crystallinity, lower temperature), why did Mount St. Helens erupt with less precursory seismicity and (perhaps) surface deformation? An important difference between the two eruptions is the higher gas-emission rates at Augustine. Gassy magma suggests a deep source, and the prolonged period of elevated seismicity and surface inflation at Augustine probably reflect the accumulation of rising magma in a shallow reservoir. In contrast, there are indications that gas-poor 2004–5 magma had already accumulated in a crustal reservoir long before the September 2004 earthquake swarm at Mount St. Helens. Inflation might have occurred anytime between 1982 and 1991, as suggested by trilateration and GPS results, episodically during repeated earthquake swarms between 1987 and 2001, or continuously and mostly aseismically.

Conjecture Regarding the Link Between 1980–1986 and 2004–2005 Eruptions

Continued low gas-emission rates at Mount St. Helens more than a year after the eruption began, and after extrusion of more than 73×10^6 m^3 of dacite, suggest that the eruption is being fed from a reservoir of mostly degassed magma. The most likely source is magma left over from the 1980s. The May 18, 1980, eruption was unusual in that it was triggered by a large landslide at 0832 PDT that unloaded the magmatic system suddenly and tapped gas-rich magma from a reservoir at 8 km depth. A devastating lateral blast and debris avalanche produced the most compelling images from the eruption, but an important change in the eruption's character did not occur until midday. Rowley and others (1981, p. 492, 489) reported: "At about noon, the eruption cloud lightened in color from medium gray to dirty white * * * (D.A. Swanson, oral commun., 1980)." and "Pyroclastic flows were first observed being emplaced at 1217 PDT (Pacific Daylight time) on May 18, nearly 4 hr after the start of the eruption, and successive pyroclastic flows continued to form intermittently for about 5 hr thereafter." It seems likely that the change in the eruption cloud at midday corresponded to the first arrival at the surface of gas-rich magma from a deeper source, presumably the 7-km-deep reservoir proposed by Rutherford and others (1985). This idea is consistent with the onset of vigorous harmonic tremor, indicative of magma movement, just before noon, and with its decline at about 1730 PDT (Malone and others, 1981).

If this scenario is correct, the hours-long delay between the initiation of the landslide and the first arrival of reservoir magma at the surface suggests that the latter might not have occurred without the former, that is, that the landslide interrupted a sequence of events that otherwise might not have tapped the reservoir on May 18. Without the landslide trigger, magma intruding the volcano to cause the famous north-flank bulge might have reached the surface in less spectacular fash-

ion and might not have been followed by gas-rich magma from the reservoir. We speculate that catastrophic unloading of the magmatic system by the landslide decreased the reservoir-to-surface distance, thus increasing the pressure gradient abruptly. As a consequence of the greater pressure gradient, rapidly rising magma created and maintained an open conduit to the surface for 9 hours—enough time to release any separate gas phase that might have accumulated near the top of the reservoir. There would have been ample time, since the end of the previous eruption in 1857, for a volatile-rich cap to form by vesiculation and bubble-rise in the reservoir. Magma that rose into the lower-pressure environment of the reservoir prior to 1980 would have been temporarily oversaturated in volatiles. The "excess" volatiles would have exsolved to form bubbles that tend to aggregate and migrate toward the top of the reservoir. Given enough time and low enough permeability to the surface, a volatile-rich cap develops on the reservoir. The physics of this process is beyond the scope of this paper. We suggest only that the May 18, 1980, landslide might have initiated a cascade of events that resulted in, among the more obvious consequences, catastrophic loss of the gas-rich upper part of the reservoir. This set the stage for dome-building eruptions that followed in 1980–86 and 2004–5, which tapped reservoir magma that had been separated from its excess volatiles and only partly replenished during the interim.

The presence in the upper crust of magma remnant from the 1980s and earlier, which was devoid of its excess volatiles as a result of the May 18, 1980, eruption, might explain some aspects of the 2004–5 eruption. For example, the absence of precursory reservoir inflation is consistent with the idea that the magma erupted in 2004–5 was already present in the reservoir and conduit system when JRO1 was installed in 1997. Likewise, the short duration of precursory seismicity and the low gas emission rates throughout the 2004–5 eruption can be explained if the first few days of unrest involved the mobilization of magma that had been stored in the upper part of the conduit since the end of the 1980–86 eruption. This was soon followed by the rise of magma that arrived in the reservoir sometime before 1980, equilibrated to the pressure and temperature conditions in the reservoir, and lost its excess volatiles during the eruption on May 18, 1980. This explanation does not preclude partial recharge of the reservoir prior to or during the 2004–5 eruption. Mastin and others (this volume, chap. 22) conclude from their analysis of the geodetic data that " * * * erupted magma has been replaced in increasing proportions by recharge, but that the recharge rate remains somewhat less than the current effusion rate." Both the velocity of JRO1 and the effusion rate declined throughout 2006–7. During part or all of that period, the recharge rate might have been comparable to the effusion rate (L. Mastin, oral commun., 2008).

Although mostly speculative, we believe the following scenario is consistent with the current state of knowledge concerning the 1980–86 and 2004–5 eruptions. Both eruptions were fed from a reservoir centered near 8 km depth; magma erupted in the 1980s accumulated in the reservoir during an extended period, long enough for gas bubbles to rise and form a volatile-rich cap (Gerlach and McGee, 1994). The May 18, 1980, landslide and plinian eruption depressurized the reservoir catastrophically, releasing the volatile-rich cap and causing additional bubbles to form throughout the reservoir. Most of those bubbles managed to rise to the top of the reservoir at about 5 km depth and escape via the 1980 conduit system prior to the start of the 2004–5 eruption, leaving behind a large volume of gas-poor magma—at least several cubic kilometers according to Mastin and others (this volume, chap. 22). The 2004–5 eruption was preceded by and has been accompanied by reservoir recharge, which is continuing at a rate of ~1 m^3/s (early 2006). Any magmatic gas signature from recharge might be delayed and muted by the large vertical extent of the reservoir and relatively high viscosity of reservoir magma. Factors that will influence the future course of the eruption (for example, slowing and eventual cessation of dome growth, or a transition to either more explosive activity or effusion of more mafic magma) include (1) the recharge rate going forward, (2) bubble-rise rates in the reservoir–conduit system, and (3) the character of magma entering the base of the reservoir (that is, gas content and melt composition).

Volcanoes are complex natural systems. Effective hazards mitigation, even at well-monitored volcanoes such as Mount St. Helens, requires constant vigilance and better understanding of a wide variety of physical, chemical, and hydrologic processes that interact to produce eruptions. The events of late 2004 and 2005 at Mount St. Helens amazed and confounded us as they unfolded, and to some extent they still do. What were the perceived odds on September 22, 2004, that an enormous welt would rise on the crater floor in a matter of days, without producing far-field deformation, deep seismicity, or greatly increased gas emission? Or that the top of a dacite magma column would emerge from the welt in less than three weeks and extrude for more than a year as a series of gouge-covered spines, with older spines shunted aside as newer ones emerged? Or that during the eruption, Crater Glacier would be split in two and crumpled against the crater walls without producing even a trickle of water flow at the crater mouth? Clearly, there is much left to learn at this volcano before we can understand how, when, and why such amazing events occur, and to what extent they might be hazardous.

Acknowledgments

This is an overview and ideas paper, mostly devoid of its own data. The authors make no claim of originality or exclusivity. We accept responsibility for bad or half-baked ideas and credit any good ones to the eruption team at the USGS Cascades Volcano Observatory. We thank L.G. Mastin and P.F. Cervelli for helpful reviews.

References Cited

Amelung, F., Jónsson, S., Zebker, H., and Segall, P., 2000, Widespread uplift and 'trapdoor' faulting on Galápagos volcanoes observed with radar interferometry: Nature, v. 407, no. 6807, p. 993–996.

Beget, J.E., and Kienle, J., 1992, Cyclic formation of debris avalanches at Mount St. Augustine volcano: Nature, v. 356, no. 6371, p. 701–704.

Caputo, M., 1979, Two thousand years of geodetic and geophysical observations in the Phlegraean Fields near Naples: Geophysical Journal of the Royal Astronomical Society, v. 56, p. 319–328.

Cashman, K.V., Thornber, C.R., and Pallister, J.S., 2008, From dome to dust; shallow crystallization and fragmentation of conduit magma during the 2004–2006 dome extrusion of Mount St. Helens, Washington, chap. 19 *of* Sherrod, D.R., Scott, W.E., and Stauffer, P.H., eds., A volcano rekindled; the renewed eruption of Mount St. Helens, 2004–2006: U.S. Geological Survey Professional Paper 1750 (this volume).

Cervelli, P.F., Fournier, T., Freymueller, J., and Power, J.A., 2006, Ground deformation associated with the precursory unrest and early phases of the January 2006 eruption of Augustine Volcano, Alaska: Geophysical Research Letters, v. 33, L18304, doi: 10.1029/2006GL027219.

Dvorak, J.J., and Okamura, A.T., 1987, A hydraulic model to explain variations in summit tilt rate at Kilauea and Mauna Loa volcanoes, chap. 46 *of* Decker, R.W., Wright, T.L., and Stauffer, P.H., eds., Volcanism in Hawaii: U.S. Geological Survey Professional Paper 1350, v. 2, p. 1281–1296.

Dzurisin, D., 2003, A comprehensive approach to monitoring volcano deformation as a window on the eruption cycle: Reviews of Geophysics, v. 41, no. 1, p. 1.1–1.29, doi:10.1029/2001RG000107.

Dzurisin, D., Wicks, C., Jr., and Thatcher, W., 1999, Renewed uplift at the Yellowstone caldera measured by leveling surveys and satellite radar interferometry: Bulletin of Volcanology, v. 61, p. 349–355.

Dzurisin, D., Vallance, J.W., Gerlach, T.M., Moran, S.C., and Malone, S.D., 2005, Mount St. Helens reawakens: Eos (American Geophysical Union Transactions), v. 86, no. 3, p. 25, 29.

Gerlach, T.M., McGee, K.A., and Doukas, M.P., 2008, Emission rates of CO_2, SO_2, and H_2S, scrubbing, and preeruption excess volatiles at Mount St. Helens, 2004–2005, chap. 26 *of* Sherrod, D.R., Scott, W.E., and Stauffer, P.H., eds., A volcano rekindled; the renewed eruption of Mount St. Helens, 2004–2006: U.S. Geological Survey Professional Paper 1750 (this volume).

Herd, R.A., Edmonds, M., and Bass, V.A., 2005, Catastrophic lava dome failure at Soufrière Hills Volcano, Montserrat, 12–13 July 2003: Journal of Volcanology and Geothermal Research, v. 148, nos. 3–4, p. 234–252, doi:10.1016/j.jvolgeores.2005.05.003.

Hill, D.P., Bailey, R.A., and Ryall, A.S., 1985, Active tectonic and magmatic processes beneath Long Valley caldera, eastern California; an overview: Journal of Geophysical Research, v. 90, p. 11111–11120.

Iverson, R.M., 2008, Dynamics of seismogenic volcanic extrusion resisted by a solid surface plug, Mount St. Helens, 2004–2005, chap. 21 *of* Sherrod, D.R., Scott, W.E., and Stauffer, P.H., eds., A volcano rekindled; the renewed eruption of Mount St. Helens, 2004–2006: U.S. Geological Survey Professional Paper 1750 (this volume).

Iverson, R.M., Dzurisin, Daniel, Gardner, C.A., Gerlach, T.M., LaHusen, R.G., Lisowski, Michael, Major, J.J., Malone, S.D., Messerich, J.A., Moran, S.C., Pallister, J.S., Qamar, A.I., Schilling, S.P., and Vallance, J.W., 2006, Dynamics of seismogenic volcanic extrusion at Mount St. Helens in 2004–05: Nature, v. 444, no. 7118, p. 439–443, doi:10.1038/nature05322.

LaHusen, R.G., Swinford, K.J., Logan, M., and Lisowski, M., 2008, Instrumentation in remote and dangerous settings; examples using data from GPS "spider" deployments during the 2004–2005 eruption of Mount St. Helens, Washington, chap. 16 *of* Sherrod, D.R., Scott, W.E., and Stauffer, P.H., eds., A volcano rekindled; the renewed eruption of Mount St. Helens, 2004–2006: U.S. Geological Survey Professional Paper 1750 (this volume).

Lipman, P.W., Moore, J.G., and Swanson, D.A., 1981, Bulging of the north flank before the May 18 eruption—geodetic data, *in* Lipman, P.W., and Mullineaux, D.R., eds., The 1980 eruptions of Mount St. Helens, Washington: U.S. Geological Survey Professional Paper 1250, p. 143–155.

Lisowski, M., Dzurisin, D., Denlinger, R.P., and Iwatsubo, E.Y., 2008, Analysis of GPS-measured deformation associated with the 2004–2006 dome-building eruption of Mount St. Helens, Washington, chap. 15 *of* Sherrod, D.R., Scott, W.E., and Stauffer, P.H., eds., A volcano rekindled; the renewed eruption of Mount St. Helens, 2004–2006: U.S. Geological Survey Professional Paper 1750 (this volume).

Lu, Z., Masterlark, T., Dzurisin, D., Rykhus, R., and Wicks, C., Jr., 2003, Magma supply dynamics at Westdahl volcano, Alaska, modeled from satellite radar interferometry: Journal of Geophysical Research, v. 108, no. B7, 2354, 17 p., doi:10.1029/2002JB002311.

Lu, Z., Masterlark, T., and Dzurisin, D., 2005, Interferometric synthetic aperture radar (InSAR) Study of Okmok Volcano, Alaska, 1992–2003; magma supply dynamics and post-emplacement lava flow deformation: Journal

of Geophysical Research, v. 110, no. B12, B02403, doi: 10.1029/2004JB003148, 18 p.

Lu, Z., Dzurisin, D., Wicks, C., Jr., Power, J., Kwoun, O., and Rykhus, R., 2007, Diverse deformation patterns of Aleutian volcanoes from satellite interferometric synthetic aperture radar (InSAR), *in* Eichelberger, J.C., Gordeev, E., Izbekov, P., Kasahara, M., and Lees, J.M., eds., Volcanism and tectonics of the Kamchatka Peninsula and adjacent arcs: American Geophysical Union Geophysical Monograph 172, p. 249–261.

Major, J.J., Kingsbury, C.G., Poland, M.P., and LaHusen, R.G., 2008, Extrusion rate of the Mount St. Helens lava dome estimated from terrestrial imagery, November 2004–December 2005, chap. 12 *of* Sherrod, D.R., Scott, W.E., and Stauffer, P.H., eds., A volcano rekindled; the renewed eruption of Mount St. Helens, 2004–2006: U.S. Geological Survey Professional Paper 1750 (this volume).

Malone, S.D., Endo, E.T., Weaver, C.S., and Ramey, J.W., 1981, Seismic monitoring for eruption prediction, *in* Lipman, P.W., and Mullineaux, D.R., eds., The 1980 eruptions of Mount St. Helens, Washington: U.S. Geological Survey Professional Paper 1250, p. 803–813.

Mastin, L.G., Roeloffs, E., Beeler, N.M., and Quick, J.E., 2008, Constraints on the size, overpressure, and volatile content of the Mount St. Helens magma system from geodetic and dome-growth measurements during the 2004–2006+ eruption, chap. 22 *of* Sherrod, D.R., Scott, W.E., and Stauffer, P.H., eds., A volcano rekindled; the renewed eruption of Mount St. Helens, 2004–2006: U.S. Geological Survey Professional Paper 1750 (this volume).

Massonnet, D., Rossi, M., Carmona, C., Adragna, F., Peltzer, G., Feigl, K., and Rabaute, T., 1993, The displacement field of the Landers earthquake mapped by radar interferometry: Nature, v. 364, p. 138–142.

McCaffrey, R., Long, M.D., Goldfinger, C., Zwick, P.C., Nabelek, J.L., Johnson, C.K., and Smith, C., 2000, Rotation and plate locking at the southern Cascadia subduction zone: Geophysical Research Letters, v. 27, no. 19, p. 3117–3120.

Moran, S.C., 1994, Seismicity at Mount St. Helens, 1987–1992: Evidence for repressurization of an active magmatic system: Journal of Geophysical Research, v. 99, p. 4341–4354.

Moran, S.C., Malone, S.D., Qamar, A.I., Thelen, W.A., Wright, A.K., and Caplan-Auerbach, J., 2008, Seismicity associated with renewed dome building at Mount St. Helens, 2004–2005, chap. 2 *of* Sherrod, D.R., Scott, W.E., and Stauffer, P.H., eds., A volcano rekindled; the renewed eruption of Mount St. Helens, 2004–2006: U.S. Geological Survey Professional Paper 1750 (this volume).

Pallister, J.S., Thornber, C.R., Cashman, K.V., Clynne, M.A., Lowers, H.A., Mandeville, C.W., Brownfield, I.K., and Meeker, G.P., 2008, Petrology of the 2004–2006 Mount St. Helens lava dome—implications for magmatic plumbing and eruption triggering, chap. 30 *of* Sherrod, D.R., Scott, W.E., and Stauffer, P.H., eds., A volcano rekindled; the renewed eruption of Mount St. Helens, 2004–2006: U.S. Geological Survey Professional Paper 1750 (this volume).

Poland, M.P., and Lu, Z., 2008, Radar interferometry observations of surface displacements during pre- and coeruptive periods at Mount St. Helens, Washington, 1992–2005, chap. 18 *of* Sherrod, D.R., Scott, W.E., and Stauffer, P.H., eds., A volcano rekindled; the renewed eruption of Mount St. Helens, 2004–2006: U.S. Geological Survey Professional Paper 1750 (this volume).

Poland, M.P., Dzurisin, D., LaHusen, R.G., Major, J.J., Lapcewich, D., Endo, E.T., Gooding, D.J., Schilling, S.P., and Janda, C.G., 2008, Remote camera observations of lava dome growth at Mount St. Helens, Washington, October 2004 to February 2006, chap. 11 *of* Sherrod, D.R., Scott, W.E., and Stauffer, P.H., eds., A volcano rekindled; the renewed eruption of Mount St. Helens, 2004–2006: U.S. Geological Survey Professional Paper 1750 (this volume).

Power, J.A., Nye, C.J., Coombs, M.L., Wessels, R.L., Cervelli, P.F., Dehn, J., Wallace, K.L., Freymueller, J.T., and Doukas, M.P., 2006, The reawakening of Alaska's Augustine Volcano [abs.]: Eos (American Geophysical Union Transactions), v. 87, no. 37, p. 373, doi:10.1029/2006EO370002.

Rowley, P.D., Kuntz, M.A., and MacLeod, N.S., 1981, Pyroclastic-flow deposits, *in* Lipman, P.W., and Mullineaux, D.R., eds., The 1980 eruptions of Mount St. Helens, Washington: U.S. Geological Survey Professional Paper 1250, p. 489–512.

Rutherford, M.J., and Devine, J.D., III, 2008, Magmatic conditions and processes in the storage zone of the 2004–2006 Mount St. Helens dacite, chap. 31 *of* Sherrod, D.R., Scott, W.E., and Stauffer, P.H., eds., A volcano rekindled; the renewed eruption of Mount St. Helens, 2004–2006: U.S. Geological Survey Professional Paper 1750 (this volume).

Rutherford, M.J., Sigurdsson, H., Carey, S., and Davis, A., 1985, The May 18, 1980, eruption of Mount St. Helens; 1. melt composition and experimental phase equilibria: Journal of Geophysical Research, v. 90, no. B4, p. 2929–2947.

Ryan, S.C., 1995, Quiescent outgassing of Mauna Loa volcano, 1958–1994, *in* Rhodes, J.M., and Lockwood, J.P., eds., Mauna Loa revealed; structure, composition, history, and hazards: Washington, D.C., American Geophysical Union Geophysical Monograph 92, p. 95–116.

Savage, J.C., Svarc, J.L., Prescott, W.H., and Murray, M.H., 2000, Deformation across the forearc of the Cascadia subduction zone at Cape Blanco, Oregon: Journal of Geophysical Research, v. 105, no. B2, p. 3095–3102.

Scandone, R., and Malone, S.D., 1985, Magma supply, magma discharge and readjustment of the feeding system of Mount St. Helens during 1980: Journal of Volcanology and Geothermal Research, v. 23, nos. 3–4, p. 239–262, doi:10.1016/0377-0273(85)90036-8.

Schilling, S.P., Thompson, R.A., Messerich, J.A., and Iwatsubo, E.Y., 2008, Use of digital aerophotogrammetry to determine rates of lava dome growth, Mount St. Helens, Washington, 2004–2005, chap. 8 *of* Sherrod, D.R., Scott, W.E., and Stauffer, P.H., eds., A volcano rekindled; the renewed eruption of Mount St. Helens, 2004–2006: U.S. Geological Survey Professional Paper 1750 (this volume).

Swanson, D.A., Lipman, P.W., Moore, J.G., Heliker, C.C., and Yamashita, K.M., 1981, Geodetic monitoring after the May 18 eruption, *in* Lipman, P.W., and Mullineaux, D.R., eds., The 1980 eruptions of Mount St. Helens, Washington: U.S. Geological Survey Professional Paper 1250, p. 157–168.

Swanson, D.A., Casadevall, T.J., Dzurisin, D., Malone, S.D., Newhall, C.G., and Weaver, C.S., 1983, Predicting eruptions at Mount St. Helens, June 1980 through December 1982: Science, v. 221, no. 4618, p. 1369–1376.

Swanson, D.A., Dzurisin, D., Holcomb, R.T., Iwatsubo, E.Y., Chadwick, W.W., Jr., Casadevall, T.J., Ewert, J.W., and Heliker, C.C., 1987, Growth of the lava dome at Mount St. Helens, Washington (USA), 1981–1983*, in* Fink, J.H., ed., Emplacement of silicic domes and lava flows: Geological Society of America Special Paper 212, p. 1–16.

Thelen, W.A., Crosson, R.S., and Creager, K.C., 2008, Absolute and relative locations of earthquakes at Mount St. Helens, Washington, using continuous data; implications for magmatic processes, chap. 4 *of* Sherrod, D.R., Scott, W.E., and Stauffer, P.H., eds., A volcano rekindled; the renewed eruption of Mount St. Helens, 2004–2006: U.S. Geological Survey Professional Paper 1750 (this volume).

Tryggvason, E., 1994, Surface deformation at the Krafla volcano, North Iceland, 1982–1992: Bulletin of Volcanology, v. 56, no. 2, p. 98–107.

Vallance, J.W., Schneider, D.J., and Schilling, S.P., 2008, Growth of the 2004–2006 lava-dome complex at Mount St. Helens, Washington, chap. 9 *of* Sherrod, D.R., Scott, W.E., and Stauffer, P.H., eds., A volcano rekindled; the renewed eruption of Mount St. Helens, 2004–2006: U.S. Geological Survey Professional Paper 1750 (this volume).

Waitt, R.B., and Beget, J.E., 1996, Provisional geologic map of Augustine Volcano, Alaska: U.S. Geological Survey Open-File Report 96–0516, 44 p., 1 plate, scale 1:25,000.

Walder, J.S., Schilling, S.P., Vallance, J.W., and LaHusen, R.G., 2008, Effects of lava-dome growth on the Crater Glacier of Mount St. Helens, Washington, chap. 13 *of* Sherrod, D.R., Scott, W.E., and Stauffer, P.H., eds., A volcano rekindled; the renewed eruption of Mount St. Helens, 2004–2006: U.S. Geological Survey Professional Paper 1750 (this volume).

Wicks, C.W., Thatcher, W., Dzurisin, D., and Svarc, J., 2006, Uplift, thermal unrest, and magma intrusion at Yellowstone caldera: Nature, v. 440, no. 7080, p. 72–75, doi:10.1038/nature04507.

Zebker, H.A., Amelung, F., and Jonsson, S., 2000, Remote sensing of volcano surface and internal processes using radar interferometry, *in* Mouginis-Mark, P.J., Crisp, J.A., and Fink, J.H., eds., Remote sensing of active volcanism: American Geophysical Union Geophysical Monograph 116, p. 179–205.

A Volcano Rekindled: The Renewed Eruption of Mount St. Helens, 2004–2006
Edited by David R. Sherrod, William E. Scott, and Peter H. Stauffer
U.S. Geological Survey Professional Paper 1750, 2008

Chapter 15

Analysis of GPS-Measured Deformation Associated with the 2004–2006 Dome-Building Eruption of Mount St. Helens, Washington

By Michael Lisowski[1], Daniel Dzurisin[1], Roger P. Denlinger[1], and Eugene Y. Iwatsubo[1]

Abstract

Detecting far-field deformation at Mount St. Helens since the crater-forming landslide and blast in 1980 has been difficult despite frequent volcanic activity and improved monitoring techniques. Between 1982 and 1991, the systematic extension of line lengths in a regional GPS trilateration network is consistent with recharge of a deep magma chamber during that interval. The rate of extension, however, averages only 3 mm/yr, and some of this apparent deformation may result from systematic scale error in the electronic distance measurements. Subsequent GPS surveys and data from a continuous GPS station, located 9 km north of Mount St. Helens and operating since 1997, show no significant volcanic deformation until the start of unrest on September 23, 2004. The current eruption has been accompanied by subtle but widespread inward and downward movement of GPS monitoring stations, exponentially decreasing with time and totaling as much as 30 mm. The observed deformation is consistent with the predictions of an elastic half-space model of a vertically elongate magma chamber with its center at a depth of around 7 to 8 km and with a total cavity-volume loss of about $16–24\times10^6$ m^3. The discrepancy between the estimated cavity-volume loss and the $>83\times10^6$-m^3 volume of the erupted dome can be explained, for the most part, by exsolution of gas in the stored magma and by minor input of new magma during the eruption.

Introduction

The current episode of volcanic unrest at Mount St. Helens began suddenly with a shallow earthquake swarm on September 23, 2004. Geodetic monitoring of deformation in the months before and days after the start of unrest was limited to data from a single, continuous, dual-frequency GPS (CGPS) station, JRO1 (installed in 1997), having an antenna on the roof of Johnston Ridge Observatory (JRO) (fig. 1). Regional deformation in the years before the start of unrest was measured using campaign-style GPS surveys of a 43-station network during the summers of 2000 and 2003. Annual surveys of background deformation in the crater of Mount St. Helens began in 2000 at six GPS stations on and near the 1980s dome ("old dome") for the purpose of ground control (Schilling and others, this volume, chap. 8). A network of three single-frequency (L1) CGPS stations was installed in 2000 to monitor deformation on the September 1984 lobe of the 1980s dome, relative to two stations just outside of the crater (LaHusen and others, this volume, chap. 16). Only one of these L1 CGPS stations, SFOT (on the west flank), remained operational during most of 2004, and there is no GPS measurement of deformation in the crater until September 28, 2004. In the 1980s and 1990s, deformation of Mount St. Helens was measured by using (1) electronic distance meters (EDM) to track line-length changes, (2) theodolites to track angle changes, and (3) level arrays and electronic tiltmeters to monitor ground tilt (Dvorak and others, 1981; Lipman and others, 1981; Swanson and others, 1981; Ewert and Swanson, 1992).

The observed patterns and rates of deformation in volcanic areas are used to constrain possible sources and mechanisms of volcanic unrest. We did not detect a systematic pattern of deformation, other than secular tectonic motion, between the 2000 and 2003 campaign GPS surveys; nor were there anomalies in the JRO1 CGPS three-dimensional (3D), position-component time series before the start of unrest. By the time of the first phreatic explosion on October 1, 2004, the L1 CGPS network was restored to operational condition (the station on the September 1984

[1]U.S. Geological Survey, 1300 SE Cardinal Court, Vancouver, WA 98683

lobe of the dome was destroyed by ballistics on October 1) and several campaign GPS stations on the volcano's flanks were occupied. Within two weeks, additional CGPS stations were installed by the Cascades Volcano Observatory (CVO) and the Plate Boundary Observatory (PBO). Displacement of these stations during the eruption was small (a few centimeters maximum) and consistently inward toward Mount St. Helens and downward, the pattern of movement expected if a deep magma chamber were being depleted during the eruption. The deformation, however, is small given the volume of lava erupted at the surface. The pressure loss in the deep magma chamber that is feeding the eruption may be compensated by recharge and by exsolution of gas (Mastin and others, this volume, chap. 22).

We begin by discussing our methods of GPS data reduction and analysis, emphasizing the technique used to improve measurement precision by removing common-mode noise. We then use regional GPS surveys and CGPS data to calculate the pattern and rate of background tectonic deformation and to derive a simple tectonic model. Local deformation near Mount St. Helens is then calculated from EDM-measured, line-length data collected during the 1980s and 1990s and from GPS-measured position-change data collected between 2000 and 2003; these results are compared with the predictions indicated in the tectonic model. The time series of deformation at CGPS station JRO1 is examined carefully for anomalies in the years before the start of the current episode of volcanic unrest at Mount St. Helens. Finally, eruption-related deformation is calculated, and an elastic, half-space model of a deflating, spheroidal magma chamber is used to fit the observed deformation.

Figure 1. Radome-covered antenna for CGPS station JRO1, on the roof of the U.S.D.A. Forest Service's Johnston Ridge Observatory, 9 km north of Mount St. Helens, Washington. In the weeks before and days after September 23, 2004, when seismic unrest began, JRO1 was the only GPS station operating within 40 km of the volcano. USGS photo by E.Y. Iwatsubo.

GPS Data Collection and Analysis

Campaign GPS and Continuous Dual-Frequency GPS Networks

Regional and local deformation around Mount St. Helens is measured episodically with campaign GPS surveys and continuously with CGPS stations (fig. 2). The following is a simplified discussion of how GPS positions are determined. The basic principal is that a GPS position can be triangulated from distance measurements to several known locations. The GPS satellites transmit encoded timing signals (pseudoranges) at two carrier frequencies, L1 (1575.42 MHz) and L2 (1227.60 MHz). The orbits of the satellites are predictable, making them reference points from which the ground position can be triangulated. The distance is measured directly by using the travel time of the coded signal, but it is called a pseudorange because the satellite and ground clocks used to measure the travel time of the one-way satellite transmission are not synchronized. The most accurate measurement of distance is obtained from the relatively short-wavelength, continuous L1 and L2 carrier signals and from the so-called "ionospheric free" linear combination of L1 and L2 known as LC or L3. Generally, the LC observable is used to minimize scale error introduced by fluctuations in ionospheric activity. With the carrier signals, the range to the satellite is expressed as the sum of the observed carrier phase plus an ambiguous integer number of carrier wavelengths. Methods have been developed to determine or "fix" the phase ambiguities to their correct integer values, which removes them as an unknown in the solution and improves measurement precision.

The GPS data discussed here are acquired with geodetic-quality receivers that record pseudorange and carrier-phase data at least every 60 s, and most often at rates of 30, 15, or 10 s. During campaign GPS surveys, we collect data for a minimum of 6 hours (usually 24 hours) on multiple days.

Most of the campaign GPS stations around Mount St. Helens were surveyed initially in 2000, with the last complete survey of the network in 2003. Several stations were surveyed after the start of unrest on September 23, 2004, and again in 2005 and 2006. The center-punched, permanent tablets marking the campaign GPS stations generally are set in bedrock to provide a stable, long-term, ground-reference point. The only measure of deformation near Mount St. Helens at the start of unrest was provided by CGPS station JRO1. Other CGPS stations, operated by the Pacific Northwest Geodetic Array (PANGA) and the National Geodetic Survey's Continuous Operating Reference Stations (CORS), are found in the surrounding region and serve as stable local reference stations. Following the initial seismic swarm, a small number of the campaign GPS stations were reoccupied to measure deformation accumulated since 2003 and possible ongoing deformation during the early stages of the eruption.

By mid-October 2004 a new network of CGPS stations, installed by the USGS–CVO and the National Science Foundation's PBO, were tracking deformation associated with the

eruption (table 1). Additional PBO and CVO CGPS stations were added in 2005 and 2006. In order to expedite obtaining site usage permits, and to keep the antennas above the winter snow pack, many of the new CGPS antennas were placed at the top of existing "winterized" 3- to 3.5-m-high steel towers that originally were installed in the fall of 1980 for EDM measurements (Swanson and others, 1981). Burial of the GPS antennas by snow has not been a problem, but ice buildup around the antenna and tower, particularly for stations high on the volcano's flank, has caused pseudodisplacements, two warped towers, and many communication and power failures.

GPS Data Processing: Minimally Constrained Daily Solution

We process GPS data with GIPSY/OASIS II software (Webb and Zumberge, 1995). Daily point-positioning solutions (Zumberge and others, 1997) use satellite orbit and clock

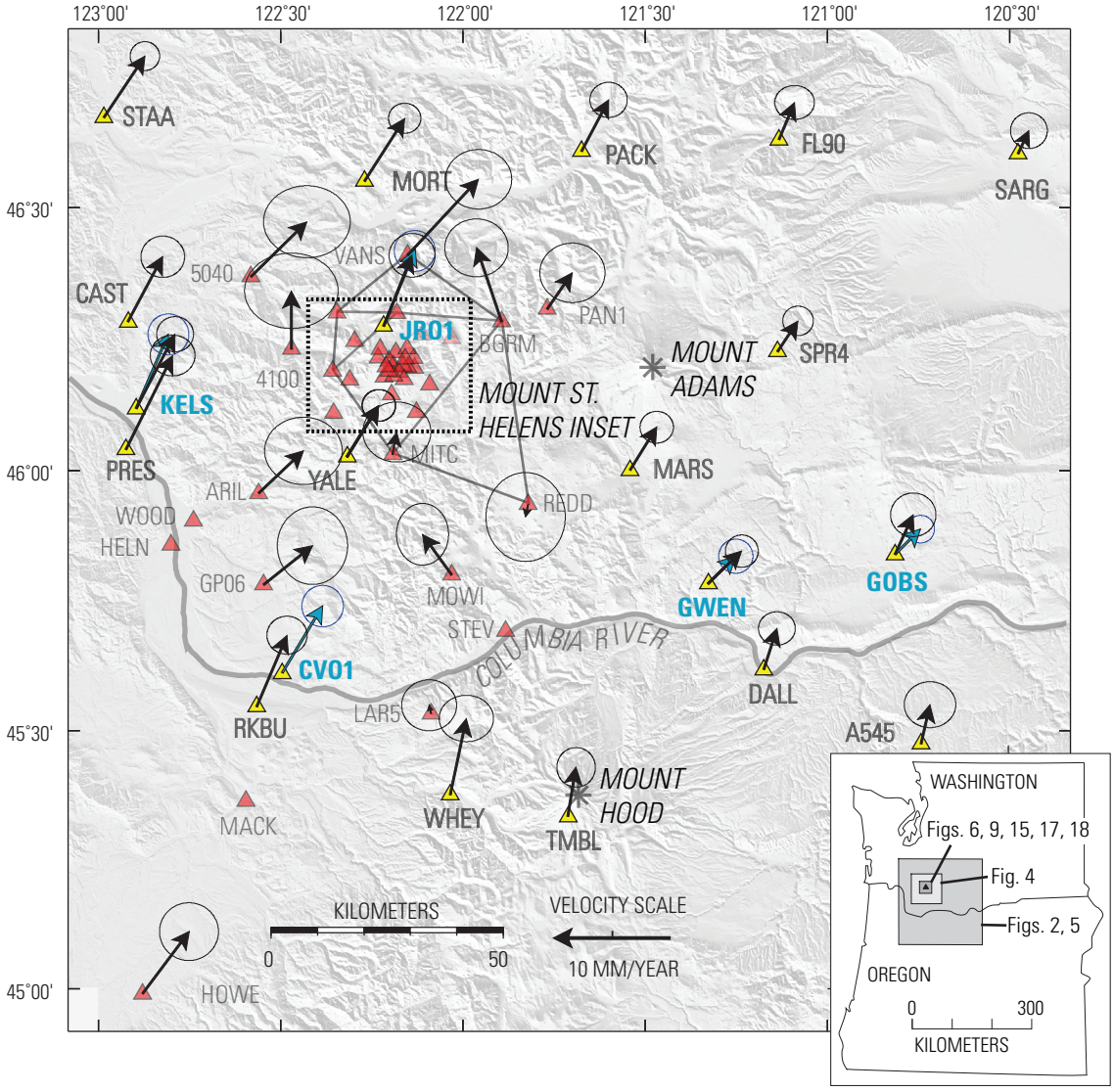

Figure 2. Map showing GPS stations in southwest Washington and northwest Oregon and their average horizontal-velocity vectors relative to stable North America (tipped with 95-percent-confidence error ellipses, vector scale at bottom) through September 2004. CGPS station names and velocity vectors are shown in blue. Black vectors at CGPS stations are calculated only from data coincident with campaign GPS surveys. Velocities at stations marked with yellow triangles are used to calculate background deformation for a tectonic model, which includes rigid-block motion and uniform-strain accumulation. The position of many stations was measured several times using campaign GPS, with some measurements made as early as 1992. However, the positions of most stations near Mount St. Helens (red triangles) were measured only in summers of 2000 and 2003. The Helens trilateration network, measured in 1982 and 1991, is shown here with faint solid lines between stations. The dashed box marks the local area around Mount St. Helens shown in figure 6.

Table 1. Regional and local continuously transmitting GPS (CGPS) stations near Mount St. Helens, Washington.

[Stations are listed in order of installation. PANGA, Pacific Northwest Geodetic Array; CVO, Cascades Volcano Observatory; PBO, Plate Boundary Observatory. See figure 2 for locations of most stations. Station names in bold type are within 20 km of Mount St. Helens.]

Station	Agency	Date operational	Monument type	Latitude (degrees)	Longitude (degrees)	Ellipsoidal elevation (m)
GOBS	PANGA	08/27/1997	Deep-drilled and braced	45.8388	-120.8147	621.49
KELS	PANGA	10/09/1997	Deep-drilled and braced	46.1182	-122.8961	-15.92
JRO1	CVO	05/23/1997	Roof mount	46.2751	-122.2176	1275.61
REDM	PANGA	07/24/1998	Shallow pier	44.2598	-121.1479	919.85
LIND	PANGA	07/28/1998	Roof mount	47.0003	-120.5390	471.93
LINH	PANGA	04/04/2002	Roof mount	47.0000	-120.5390	472.28
CVO1	CVO	01/04/2003	Roof mount	45.6109	-122.4961	66.67
P432	PBO	06/20/2004	Deep-drilled and braced	46.6228	-121.6832	318.88
P420	PBO	06/25/2004	Deep-drilled and braced	46.5886	-122.4961	74.11
P421	PBO	12/15/2004	Deep-drilled and braced	46.5318	-122.4292	220.60
TWRI	CVO	10/06/2004	EDM reflector tower	46.1979	-122.2119	2070.81
TWIW	CVO	10/11/2004	EDM reflector tower	46.2129	-122.1587	1630.55
P697	PBO	10/14/2004	EDM reflector tower	46.1876	-122.1766	2214.61
P693	PBO	10/14/2004	EDM reflector tower	46.2103	-122.2024	2113.00
P695	PBO	10/15/2004	EDM reflector tower	46.1990	-122.1642	2015.68
P696	PBO	10/15/2004	EDM reflector tower	46.1969	-122.1516	1600.03
TSTU	CVO	10/15/2004	EDM instrument tower	46.2369	-122.2241	1248.65
P687	PBO	10/16/2004	Shallow-drilled and braced	46.1096	-122.3546	391.10
TGAU	CVO	10/21/2004	EDM reflector tower	46.2192	-122.1923	1618.28
P698	PBO	11/04/2004	EDM reflector tower	46.1735	-122.1606	1479.39
P702	PBO	11/05/2004	Shallow-drilled and braced	46.3002	-122.3456	1305.70
P690	PBO	02/01/2005	EDM reflector tower	46.1800	-122.1899	2078.91
P699	PBO	02/02/2005	EDM reflector tower	46.1898	-122.2032	2274.11
P689	PBO	10/23/2005	Shallow-drilled and braced	46.1896	-122.3606	1359.46
THAR	CVO	06/28/2006	EDM instrument tower	46.2753	-122.1740	1430.55
P701	PBO	09/22/2006	Shallow-drilled and braced	46.1946	-122.1333	1247.79
P694	PBO	09/24/2006	Shallow-drilled and braced	46.2996	-122.1819	1726.03
P692	PBO	09/25/2006	Shallow-drilled and braced	46.2245	-122.1842	1492.23
P700	PBO	09/26/2006	Shallow-drilled and braced	46.1781	-122.2173	1522.03
P691	PBO	09/29/2006	Shallow-drilled and braced	46.2315	-122.2269	1183.26
P703	PBO	09/30/2006	Shallow-drilled and braced	46.1453	-122.1963	988.75
P705	PBO	09/30/2006	Shallow-drilled and braced	46.1730	-122.3106	1151.23

files obtained from the Jet Propulsion Laboratory (Pasadena, Calif.). The methods described by Blewitt (1989) are applied to the daily solutions of a network of stations, which improves measurement precision by estimating carrier-phase ambiguities within overlapping subsets of stations. The resulting minimally constrained network solution is in the reference frame of the satellite orbits (a nonfiducial reference frame—for example, Helfin and others, 1992). The GPS data processing to this point is standardized by using gp, a set of UNIX scripts and programs developed by Will Prescott and others at the USGS in Menlo Park, Calif. (see http://quake.wr.usgs.gov/research/deformation/gps/gpmanual/index.html).

Transformation of Minimally Constrained Solution to a Terrestrial Reference Frame

The next step in the GPS data-reduction process is experimental and has changed over time. The daily, minimally constrained, fixed-ambiguity network solution is merged with a point-position solution of a global network of CGPS stations (http://quake.wr.usgs.gov/research/deformation/gps/auto/*Track/*) that are in the stable interiors of the Earth's lithospheric plates; their positions and velocities are defined in the ITRF2000 terrestrial reference frame (Altimimi and others, 2002). No ambiguity resolution is attempted for the global network because of the large station separations. Station positions in the ITRF2000 frame station evolve following the no-net-rotation NNR-NUVEL-1A model of DeMets and others (1994). We are interested in deformation relative to the North American plate (NOAM), and for this purpose we created a nominal fixed-NOAM ITRF2000 reference frame using the Euler vector for NOAM given by Altimimi and others (2002, their table 6). We refer herein to this reference frame as "fixed-NOAMgp."

The combined (global and local), minimally constrained daily solution is transformed into ITRF2000 and to the fixed-NOAMgp terrestrial reference system by applying a seven-parameter Helmert transformation (x,y,z translations + rotations about the three axes + a scale change) that minimizes the misfit in the observed positions of the global reference stations with the positions predicted for that day. Misfit residuals from this adjustment are examined automatically to identify outliers, a reference station is removed from the solution if its residual exceeds five times the expected error, and the transformation process is iterated. Finally, the minimally constrained network solution and the combined ITRF and nominal fixed-NOAMgp solutions are archived, and Web-accessible plots of station time series and estimates of station velocities are updated.

GPS Networks Near Mount St. Helens

Campaign GPS and CGPS data from stations near Mount St. Helens are included in three regional groupings (networks): Cascadia includes most regional CGPS stations in the Pacific Northwest; Helens includes Mount St. Helens campaign GPS stations along with a subset of the regional CGPS stations that are processed only on the days campaign GPS data are collected; and HelensMonit includes CGPS stations around Mount St. Helens, a few regional GPS stations, and campaign GPS stations that provide bedrock local ties to the Mount St. Helens CGPS stations (for example, see http://quake.wr.usgs.gov/research/deformation/gps/auto/Helens/). These regional groupings are arbitrary and have resulted from the combination of a rapid increase in the number of stations over time and from the computational efficiency of processing data from networks having a smaller number of stations. New analysis techniques that detect and remove common-mode error in the station positions are most successful when all Mount St. Helens and related reference-station data are processed in a single group.

Local Terrestrial Reference Frames

The precision of regional GPS solutions can be improved by removing spatially correlated noise (Wdowinski and others, 1997). The transformation to a terrestrial reference frame is approximate, and it can be refined by using local stations (within a few hundred kilometers) with well-defined positions and velocities to estimate common-mode daily bias in the local solutions. Common-mode daily bias is estimated by either stacking the position component residuals (after removal of linear trends) of the local reference stations or by the equivalent procedure of estimating origin translations of the daily network solutions. We estimate the local network translations from a subset of CGPS reference stations included in the solutions.

We construct a local reference frame for the Mount St. Helens region to define the position of selected CGPS reference stations at any given time. The reference stations have long measurement histories, daily position measurements, and constant velocities. Starting with the daily combined, fixed-NOAMgp solutions, we remove all but the local reference stations and a subset of NOAM global stations. These solutions are merged to produce weekly averages of positions, outliers are identified and removed, and then the weekly averages for multiple years are adjusted to give an average position at a particular time and average station velocities (see Smith and others, 2004). We include the subset of ITRF2000 NOAM stations to keep the local reference frame aligned with our fixed-NOAMgp reference frame during the adjustment. Thereafter, most NOAM stations are removed from the final local reference frame because they are far from the region of interest.

The daily local solutions, which include several of the local reference stations, are then shifted into the local reference frame by applying a three-parameter Helmert transformation (3D translation), which minimizes the misfit between the observed positions of the local reference stations and those predicted by the local reference frame for that date. Occasionally, one or more of the local reference stations is poorly fit; it is removed from the regional solution and the transformation is iterated.

Removing the common-mode daily bias in the solutions can reduce the scatter in the station-component time series by a factor of 2 to 3 (Williams and others, 2004). Local-station seasonal wander, data offsets, and nonlinear deformation remain in the station-component time series after removing spatially correlated noise common to the reference stations. We use the QOCA (pronounced "coca") software (Quasi-Observation Combination Analysis) (Dong and others, 1998, 2002, 2006), designed and developed at NASA's Jet Propulsion Laboratory, for final analysis of the trends and noise in the GPS solutions. The QOCA software can be used to align the minimally constrained network solutions to any defined terrestrial reference frame, manipulate 3D station-position time series, and calculate spatial and temporal deformation.

Deformation in the Mount St. Helens Region Determined by Using GPS and Trilateration Survey Data

Tectonic interactions between the Pacific, Juan de Fuca, and North American plates displace and deform the ground in the Pacific Northwest (for example, Savage and others, 1991; Murray and Lisowski, 2000; McCaffrey and other, 2000; Savage and others, 2000; Miller and others, 2001; Svarc and others, 2002; Mazzotti and others, 2003). The widespread secular tectonic deformation can mask the more localized background and episodic deformation across the volcanic arc. For example, locking of the shallow interface between the Juan de Fuca and North American plates compresses the adjacent coastal region of the North American plate in the east-northeast direction of relative convergence between the plates. More enigmatic are the rigid-body movements of large continental regions (microplates) and possible strain accumulation or relative motion along their boundaries (for example, Wells and others, 1998; Wells and Simpson, 2001).

We use repeated GPS surveys and data from CGPS stations to derive a model for background tectonic deformation in the Mount St. Helens region. We then compare the modeled background rates of strain accumulation with that determined from line-length changes in an arc-crossing, regional trilateration network that was measured in 1982, 1991, and 2000. Finally, the tectonic model is used to adjust observed GPS station movements to determine the rate and pattern of volcanic deformation around Mount St. Helens since 2000.

Tectonic Rigid-Body Rotation and Strain Accumulation in the Mount St. Helens Region

The Helens GPS network includes several regional campaign stations with well-determined velocities, some occupied as early as 1992 (stations marked with yellow triangles in figs. 2 and 3). In addition, solutions for the Helens and Cascadia networks include several PANGA CGPS stations with well-determined velocities that are situated in the arc and back-arc regions (stations with blue names in figs. 2 and 3).

The GPS station velocities in the fixed-NOAMgp terrestrial reference frame reveal what appears to be a regional, clockwise, rigid-block rotation (figs. 2, 3). This microplate motion is roughly consistent with paleomagnetic studies that suggest widespread Cenozoic rotation in the Cascadia forearc (for example, Simpson and Cox, 1977; Magill and others, 1982; Wells and others, 1998) and is similar to widespread block rotation observed by using GPS to survey much of the Cascadia forearc, arc, and backarc region (McCaffrey and other, 2000; Savage and others, 2000; Svarc and other, 2002). In addition to the obvious block rotation, there may be a small amount of internal deformation (strain accumulation).

We use the method of Savage and others (2001, their appendix A) to simultaneously estimate an Euler vector for the rigid-body rotation and the rate of strain accumulation that best fits the observed regional-station velocities. Our best-fitting tectonic model was obtained by excluding the northern PANGA CGPS stations (CHWK, DRAO, SEDR, BREW) from the model. The resulting Euler vector, principal strain rates, and predicted station velocities are shown in figure 3 and summarized in table 2 (Helens GPS). An independent estimate of the rotation rate and strain was computed using QOCA, which gave similar results (table 2, Helens GPS QOCA). The computed Euler vector is roughly consistent with previous studies of GPS-measured deformation in Cascadia, which show a similar rate of clockwise block rotation (McCaffrey and other, 2000; Savage and others, 2000; Svarc and others, 2002). A small amount of uniaxial contraction (–18.0±1.9 nanostrain/yr, extension reckoned positive) accumulates in the ~N. 60° E. direction of relative convergence between the Juan de Fuca and North American plates. This rate of strain accumulation is equivalent to an average of 3.6 mm/yr of east-northeast-directed contraction across the 200-km-wide zone covered by the regional GPS stations and likely represents penetration of deformation from the locked subduction thrust into this region. The tectonic model does not define possible background vertical deformation, and we assume that there is none because regional studies of historical leveling data show little long-term elevation change across the Cascades (Verdonck, 2006).

Deformation in the 1980s and 1990s Within a Regional High-Precision Trilateration Network

The Helen trilateration network, which straddles the Cascade volcanic arc in southwestern Washington, was established to track regional strain accumulation following the 1980 crater-forming eruption of Mount St. Helens (fig. 4). Line lengths were measured in 1982 and 1991, and they were recovered with GPS in 2000 (EDM-measured line lengths can be downloaded from http://quake.wr.usgs.gov/research/deformation/gps/geodolite/index.html). The GPS-recovered line lengths were corrected for the –0.283 ppm systematic scale bias relative to Geodolite line lengths derived empirically by Savage and others (1996).

Table 2. EDM and GPS network strain and rotation rates.

[Strain rates within entire network assuming uniform strain accumulation. --, data not calculated.]

Network	Averaging interval	ε_1 (nano-strain/yr)	ε_2 (nano-strain /yr)	Azimuth ε_3 (degrees clockwise from north)	Rotation rate (nanoradian/yr)	Euler Pole latitude (degrees)	Euler Pole longitude (degrees)	Correlation latitude-longitude	Standard deviation unit weight
Helens EDM	1982.7–1991.7	82±28	62±27	44 ± 37	--	--	--	--	--
Helens EDM	1991.7–2000.7	11±29	–10±29	70 ± 35	--	--	--	--	--
Helens GPS	1992–2004	2.5±1.7	–18.0±1.9	63.8 ± 3.5	–15.4±1.2	44.476±0.141	–118.526±0.252	–0.804	1.0
Helens GPS (QOCA)	1992–2004	–0.8±2.7	–20.1±2.9	55.0 ± 6.0	–14.3±2.0	45.969±0.31	–117.876±0.540	–0.932	0.84

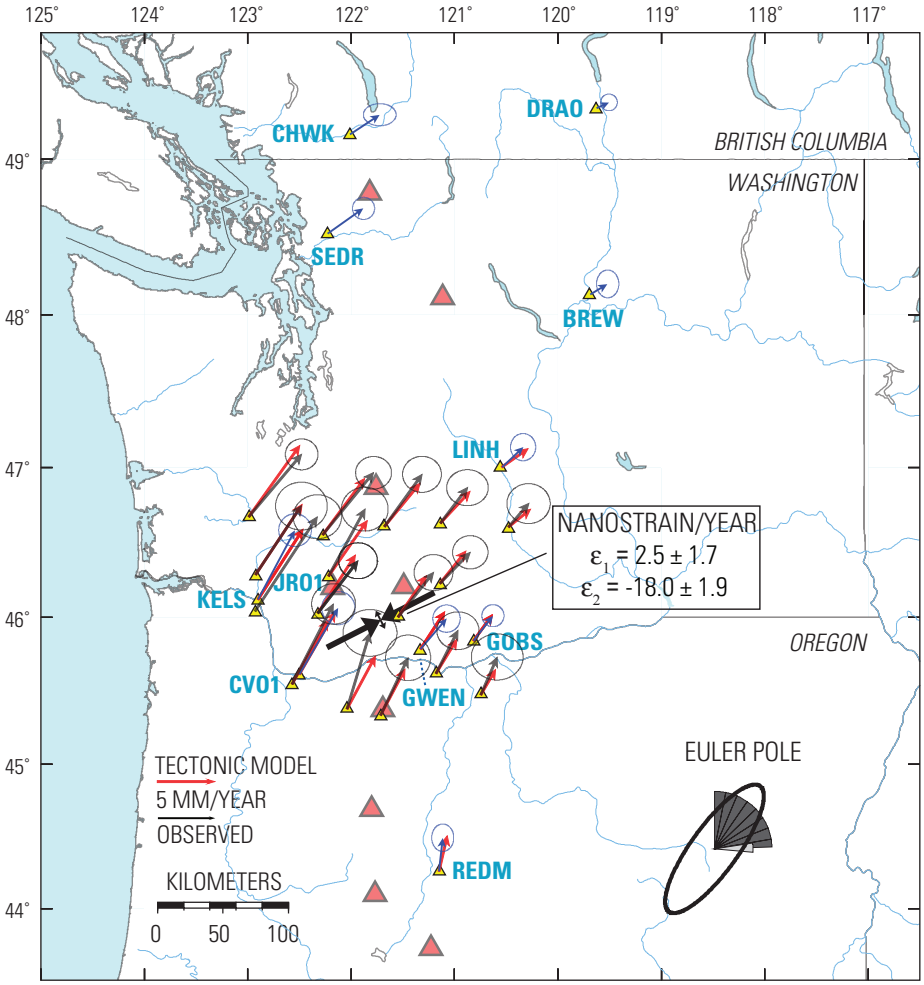

Figure 3. Map of GPS station velocities in Oregon, Washington, and British Columbia used to define the tectonic model of background rigid-block rotation and uniform strain accumulation. Observed station velocity vectors (black or blue arrows tipped with 95-percent-confidence error ellipses) are relative to stable North America. Velocity vectors predicted using the model are shown in red. Region for 95-percent confidence of the computed Euler pole is indicated by dark ellipse in eastern Oregon, rotation rate is indicated by dark wedges, and one-standard-deviation uncertainty in rotation rate is indicated by a light wedge. Large black arrows represent computed directions and rates of principal strains. The four most northerly CGPS stations (CHWK, DRAO, SEDR, BREW) are not included in the tectonic model calculation. Large orange triangles mark locations of major Cascade Range volcanoes.

Line lengths increased consistently by 1 to 3 cm between 1982 and 1991 but showed no significant change between 1991 and 2000. The uncertainty in a Helen line length measured with a Geodolite is between 4 and 8 mm, with the larger value for the longest lines in the network (see Savage and Prescott, 1973). By converting the observed line-length changes to extension rates and assuming that strain accumulates uniformly over the network, we can map variation in the extension rates as a function of line azimuth into surface tensor-strain-rate components. Between 1982 and 1991, areal dilatation ($\varepsilon_1 + \varepsilon_2$, where ε_1 and ε_2 are the principal strains and extension is reckoned positive) accumulated at a rate of 144±39 nanostrain/yr, which is equivalent to a ~3 mm/yr (~70 nanostrain/yr) average increase in the length across the ~40-km-aperture network in any direction. This rate of strain accumulation is distinctly different than the background areal dilatation rate (at –15±3 nanostrain/yr) estimated with the tectonic model (table 2 – note areal dilatation = $\varepsilon_1 + \varepsilon_2$). No significant strain accumulated between 1991 and 2000.

Surficial areal dilatation is expected to accompany recharge of a deep spheroidal magma reservoir. Areal dilatation is also a sensitive measure of possible systematic scale error in the individual EDM surveys because such error is proportional to distance measured and is independent of the direction of the line (Savage and others, 1986, p. 7471–7472). Systematic error in Geodolite line-length measurements is estimated to contribute about 0.14 ppm to the error in a line length, whereas a total systematic error of about 0.6 ppm between the two surveys is needed to reproduce the observed dilatation. The contribution of possible systematic error is included in the uncertainty in the rate of areal dilatation, and we conclude that the observed areal dilatation between 1982 and 1991 is too large for systematic error alone. Some other phenomenon, like recharge of the magma reservoir, contributes to this deformation.

Deformation in the Mount St. Helens GPS Network in the Years before September 23, 2004

The 43-station Helens campaign GPS network, surveyed in 2000 and 2003, extends for more than 50 km around Mount

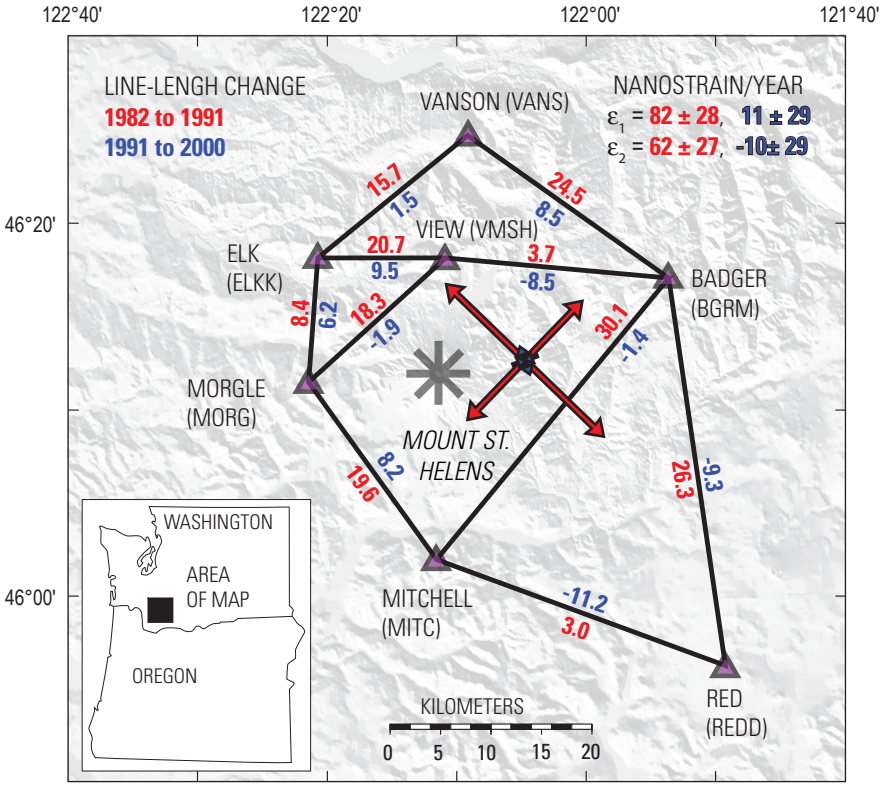

Figure 4. Map of the Helen trilateration network. Measured length changes and calculated uniform principal strain rates from 1982 to 1991 are shown in red. Corresponding values from 1991 to 2000 are shown in blue. EDM station names are given, with four-character GPS station name in parentheses. Line lengths in 2000 were measured with GPS. Directions and relative magnitudes of principal strain rates are shown with large arrows; their values are given in nanostrain per year.

St. Helens (stations marked with red triangles in fig. 2). Network coverage is increased in space and time by incorporating surveys of 13 nearby campaign GPS stations, some of which were measured as early as 1992, in the QOCA adjustment for average station velocities. Several PANGA CGPS stations, most in service since 1997 (table 1), are included in the solutions, and one of these, JRO1, is 9 km north of Mount St. Helens.

We use the predictions of the tectonic model given in table 2 (network Helens GPS) to remove regional secular deformation from the computed average GPS station velocities. We did not propagate uncertainty in the tectonic model into error in the corrected station velocities shown in figure 5 and listed in table 3. At the stations with well-defined velocities—those stations included in the tectonic-model calculation (stations marked with yellow triangles in fig. 5)—we see no significant motion. A few stations near Mount St. Helens have significant velocities, but their movements lack a consistent pattern, so we suspect they result from local instabilities or survey errors.

Examining the station velocities in the local network around Mount St. Helens (fig. 6), we observe no consistent pattern of deformation, but roughly half of the velocities exceed the 95-percent-confidence error ellipses. The highest velocity is found in the crater at station DMSH on the September 1984 lobe of the old dome, which moves to the east-northeast and down. This lobe is west of the old dome's center, and the observed motion is toward the center of the old dome, consistent with the motion expected as the old dome continues to cool and shrink. The westward velocity of stations MORG and WGOT, west of Mount St. Helens, is greater than 5 mm/yr, but other nearby stations show little or no significant motion. With surveys only in 2000 and 2003, it is difficult eliminate local instabilities or survey error, such as instrument setup, as a cause for the anomalous velocities. The daily measurements of position change at CGPS station JRO1 provide the strongest evidence for the lack of anomalous deformation in the years before September 2004. We examine the JRO1 data in the next section.

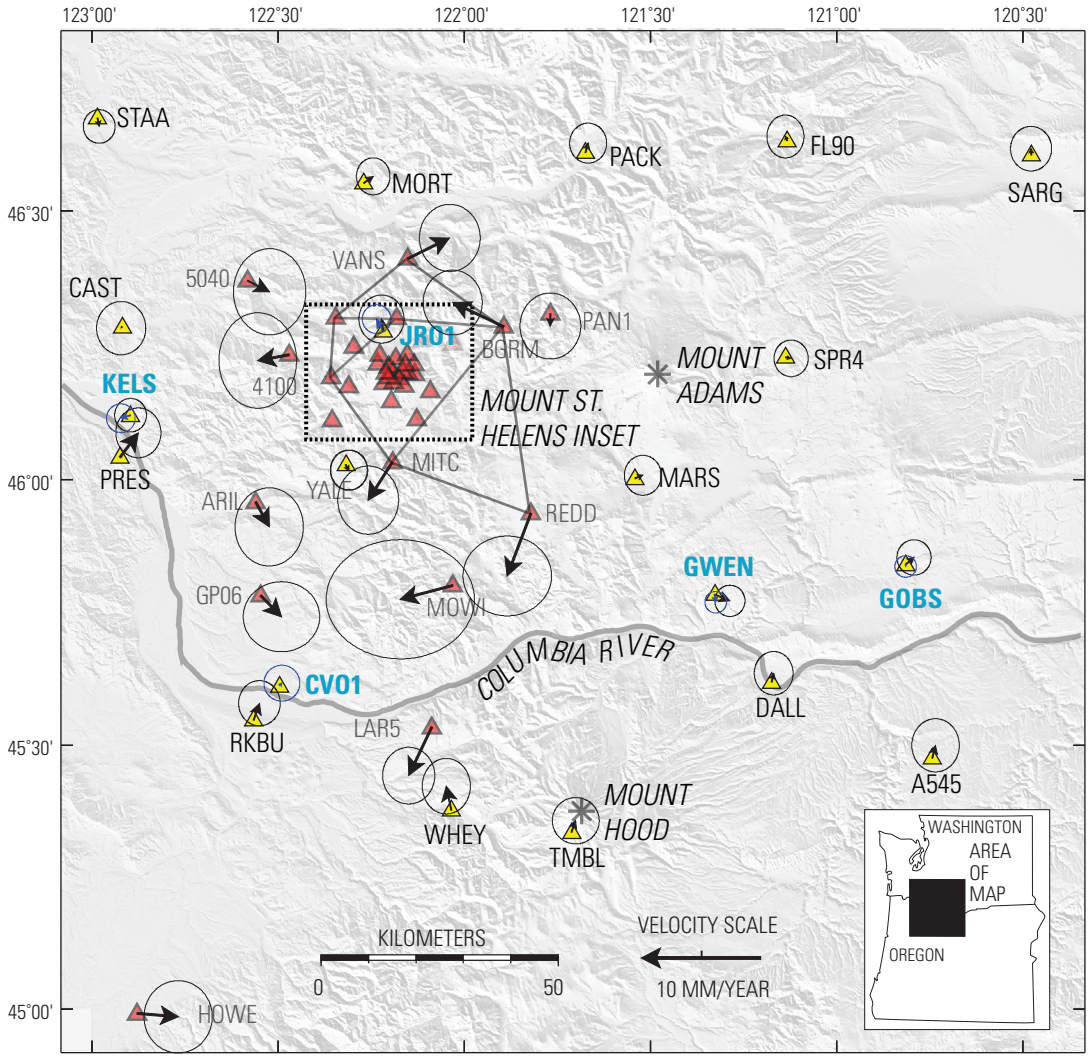

Figure 5. Map showing average GPS station horizontal-velocity vectors (tipped with 95-percent-confidence error ellipses, scale at bottom) for southwest Washington and northwest Oregon through September 2004, corrected for background motion predicted by a tectonic model. None of stations marked with yellow triangles, which were included in calculations for the tectonic model, have significant residual velocity. CGPS station names and velocity vectors are shown in blue. Most stations indicated with red triangles were surveyed only in the summers of 2000 and 2003.

Table 3. Adjusted Helens campaign GPS network average station velocities through September 23, 2004.

[Velocities are in nominal ITRF2000 fixed North American Plate terrestrial reference frame and are corrected for regional rigid-body rotation and strain.]

Station	Longitude (degrees)	Latitude (degrees)	East velocity ± 1σ error (mm/yr)	North velocity ± 1σ error (mm/yr)	E-N correlation	Up velocity ± 1σ error (mm/yr)
4100	-122.4706	46.2316	-2.65 ± 1.34	-0.50 ± 1.65	-0.04	-0.49 ± 6.64
5040	-122.5819	46.3695	1.86 ± 1.25	-0.95 ± 1.49	-0.06	13.87 ± 5.70
A545	-120.7435	45.4745	0.27 ± 0.82	1.08 ± 0.92	0.01	-1.76 ± 3.60
APEC	-122.1330	46.1950	-1.92 ± 1.06	4.00 ± 1.13	-0.01	-1.77 ± 4.93
ARIL	-122.5608	45.9561	1.16 ± 1.18	-2.10 ± 1.35	-0.05	4.29 ± 5.47
BGRM	-121.8943	46.2834	-4.32 ± 1.02	2.05 ± 1.12	0.00	0.14 ± 4.66
BIVO	-122.1962	46.1453	-2.37 ± 1.20	-4.60 ± 1.41	-0.03	11.24 ± 5.63
CAFE	-122.1349	46.2135	-2.56 ± 1.08	-0.39 ± 1.17	-0.03	0.36 ± 5.05
CANN	-123.9603	45.8617	4.29 ± 0.72	0.11 ± 0.77	-0.04	-0.94 ± 2.93
CAST	-122.9188	46.2833	-0.09 ± 0.85	-0.11 ± 0.92	-0.08	3.42 ± 3.30
CVO1	-122.4961	45.6109	-10.76 ± 6.44	1.92 ± 7.12	0.00	17.10 ± 29.68
DALL	-121.1752	45.6178	0.18 ± 0.67	0.76 ± 0.75	0.00	-3.40 ± 2.81
DMSH	-122.1910	46.2000	27.69 ± 1.04	9.39 ± 1.15	-0.01	-90.29 ± 4.86
DRAO	-119.6250	49.3226	-1.78 ± 0.43	1.46 ± 0.44	0.00	1.25 ± 1.39
EADM	-122.1521	46.1973	-1.18 ± 1.04	0.90 ± 1.12	-0.02	-3.54 ± 4.84
ELKK	-122.3452	46.3009	-0.65 ± 1.09	0.94 ± 1.18	-0.02	-0.24 ± 4.95
FL90	-121.1333	46.6288	-0.14 ± 0.64	0.36 ± 0.74	0.05	-6.53 ± 2.90
GOBS	-120.8147	45.8388	0.69 ± 0.59	0.61 ± 0.61	-0.02	0.33 ± 1.68
GP06	-122.5472	45.7810	1.76 ± 1.32	-1.80 ± 1.21	0.06	-5.07 ± 4.49
GWEN	-121.3276	45.7826	1.28 ± 0.52	-0.53 ± 0.54	-0.02	0.51 ± 1.58
HOWE	-122.8797	44.9900	3.50 ± 1.18	-0.29 ± 1.25	-0.07	-4.69 ± 4.57
HPAD	-122.0315	46.2520	-4.97 ± 1.03	1.09 ± 1.16	0.00	2.94 ± 4.70
JARD	-122.2973	46.2469	-1.89 ± 1.10	0.71 ± 1.19	-0.01	-28.35 ± 5.13
JRO1	-122.2176	46.2751	-0.16 ± 0.78	1.03 ± 0.83	-0.01	-2.93 ± 3.53
KELS	-122.8961	46.1182	-0.01 ± 0.55	0.02 ± 0.58	-0.02	-0.05 ± 1.64
LAR5	-122.0876	45.5327	-1.95 ± 0.90	-4.10 ± 0.98	-0.01	-1.77 ± 3.96
LOOW	-122.1843	46.2248	4.03 ± 1.05	0.77 ± 1.13	-0.01	1.29 ± 4.88
LVCY	-122.0912	46.1638	3.52 ± 3.69	2.02 ± 2.82	0.11	2.91 ± 8.44
MARS	-121.5419	46.0001	0.66 ± 0.64	0.28 ± 0.69	-0.02	1.29 ± 2.72
MITC	-122.1931	46.0309	-2.05 ± 1.05	-3.21 ± 1.18	-0.01	4.56 ± 4.73
MORG	-122.3572	46.1893	-7.42 ± 1.00	2.70 ± 1.11	-0.01	-0.66 ± 4.61
MORT	-122.2704	46.5506	0.80 ± 0.58	0.56 ± 0.64	-0.01	-1.76 ± 2.51
MOWI	-122.0308	45.7998	-4.45 ± 2.56	-1.17 ± 2.06	-0.12	-0.15 ± 6.61
NEBU	-122.2173	46.1782	-3.56 ± 1.08	2.41 ± 1.17	0.01	3.49 ± 5.02
NELR	-122.1649	46.1993	-1.33 ± 1.06	-1.07 ± 1.13	-0.03	1.99 ± 4.88
NESK	-123.9662	45.1343	5.07 ± 0.79	1.86 ± 0.83	-0.05	-1.51 ± 3.10
NMAR	-122.1280	46.1112	-1.23 ± 1.06	0.81 ± 1.20	0.03	5.58 ± 4.87

Table 3. Adjusted Helens campaign GPS network average station velocities through September 23, 2004. —Continued

[Velocities are in nominal ITRF2000 fixed North American Plate terrestrial reference frame and are corrected for regional rigid-body rotation and strain.]

Station	Longitude (degrees)	Latitude (degrees)	East velocity ± 1σ error (mm/yr)	North velocity ± 1σ error (mm/yr)	E-N correlation	Up velocity ± 1σ error (mm/yr)
NWDO	-122.2037	46.2096	2.72 ± 1.04	0.10 ± 1.13	-0.01	0.95 ± 4.79
PACK	-121.6752	46.6068	0.23 ± 0.64	0.80 ± 0.69	0.00	-5.60 ± 2.71
PAN1	-121.7685	46.3078	-0.02 ± 1.05	-1.04 ± 1.14	0.00	0.22 ± 4.84
PRES	-122.9245	46.0401	1.54 ± 0.78	2.06 ± 0.86	-0.04	-4.45 ± 3.23
R100	-122.1538	46.2322	1.16 ± 1.01	-1.01 ± 1.12	0.00	-0.64 ± 4.60
REDD	-121.8210	45.9349	-2.01 ± 1.53	-5.29 ± 1.38	-0.04	15.11 ± 5.71
RKBU	-122.5660	45.5467	0.49 ± 0.72	1.41 ± 0.78	-0.03	-5.58 ± 2.96
RS26	-123.4611	45.7968	3.37 ± 0.84	1.31 ± 0.94	-0.04	-2.90 ± 3.46
SARG	-120.4772	46.6024	-0.04 ± 0.71	0.53 ± 0.77	-0.01	-1.67 ± 2.83
SERI	-122.1765	46.1877	-2.81 ± 1.10	-4.41 ± 1.22	-0.05	-5.52 ± 5.07
SESL	-122.1615	46.1737	-1.37 ± 1.06	1.71 ± 1.14	-0.02	0.40 ± 4.94
SMCR	-122.1117	46.2586	-3.83 ± 0.96	2.37 ± 1.05	0.00	0.78 ± 4.33
SOFO	-122.2329	46.2153	0.83 ± 1.09	5.43 ± 1.18	-0.01	-1.88 ± 5.04
SPR4	-121.1371	46.2269	0.46 ± 0.59	-0.11 ± 0.63	-0.02	0.52 ± 2.47
SRID	-122.1899	46.1801	-1.65 ± 1.03	0.36 ± 1.12	-0.01	-5.21 ± 4.78
STAA	-122.9853	46.6708	0.15 ± 0.55	-0.72 ± 0.58	-0.03	1.60 ± 2.33
STUD	-122.2269	46.2314	2.99 ± 1.08	1.89 ± 1.18	0.00	-0.12 ± 5.03
TMBL	-121.7119	45.3340	0.35 ± 0.81	0.98 ± 0.80	-0.07	0.85 ± 3.22
TUBE	-122.3547	46.1095	2.22 ± 1.25	3.59 ± 1.41	-0.06	-2.24 ± 5.88
VANS	-122.1516	46.4101	3.54 ± 1.05	1.75 ± 1.16	0.01	0.47 ± 4.77
VMSH	-122.1820	46.2998	-1.54 ± 1.04	3.07 ± 1.12	-0.01	2.91 ± 4.81
WGOT	-122.3106	46.1730	-8.49 ± 0.88	0.80 ± 0.97	-0.01	-4.27 ± 3.94
WHEY	-122.0349	45.3762	-0.43 ± 0.83	2.02 ± 0.96	0.03	-4.67 ± 3.69
WIWE	-122.1587	46.2129	1.20 ± 1.05	-4.18 ± 1.13	0.00	2.21 ± 4.85
WRAD	-122.2035	46.1897	0.25 ± 1.07	7.46 ± 1.18	0.02	3.44 ± 5.00
WRID	-122.2107	46.1978	1.05 ± 1.05	-2.31 ± 1.13	0.00	0.23 ± 4.87
YALE	-122.3181	46.0262	0.26 ± 0.64	-0.47 ± 0.69	-0.07	1.18 ± 2.61

Time Series of Deformation from CGPS Data Collected at Johnston Ridge Observatory

A detailed history of deformation near Mount St. Helens since 1997 is found in the daily displacement components of CGPS station JRO1. The Cascadia network includes daily solutions in the fixed-NOAMgp reference frame and in a local reference frame that is defined by a subset of 11 CGPS stations in the network (table 4). QOCA's time-series analysis is used to simultaneously compute the component velocities, offsets, and repetitive seasonal displacements of JRO1. We do not include the anomalous data after September 23, 2004, in this analysis for background deformation. Outliers in the time series, found mainly in the winter when ice and snow accumulate around the GPS antenna, are defined as observations where the residual east or north displacement is larger than 5 mm, and the residual vertical displacement is larger than 15 mm. These residual outliers are about three times the weighted root-mean-square (WRMS) scatter observed in the JRO1 time-series analysis (table 4). Of the 2,267 daily observations, 130 (6 percent) were removed from the analysis because one or more of the components was identified as an outlier.

Small vertical offsets (~13 mm) in the time series were introduced on July 8, 1998, when a UNAVCO radome replaced the original Snow radome, and on July 16, 2002, when a SCIGN radome replaced the UNAVCO radome. The vertical offsets are calculated in QOCA by first setting assumed offset values based on estimates from a short span of data around the offset (we use 0.2 year), which is then given a weight of 0.25 times the offset; the final values are estimated simultaneously with other parameters. In our final analysis, only vertical offsets are estimated because initial analysis resulted in horizontal offsets that were small and insignificant. Nevertheless, the long-term trends could be biased slightly by error in the applied vertical offsets and possible small, horizontal offsets related to the antenna-radome changes.

The estimated JRO1 component velocities, offsets, and repetitive seasonal movements are removed to produce a resid-

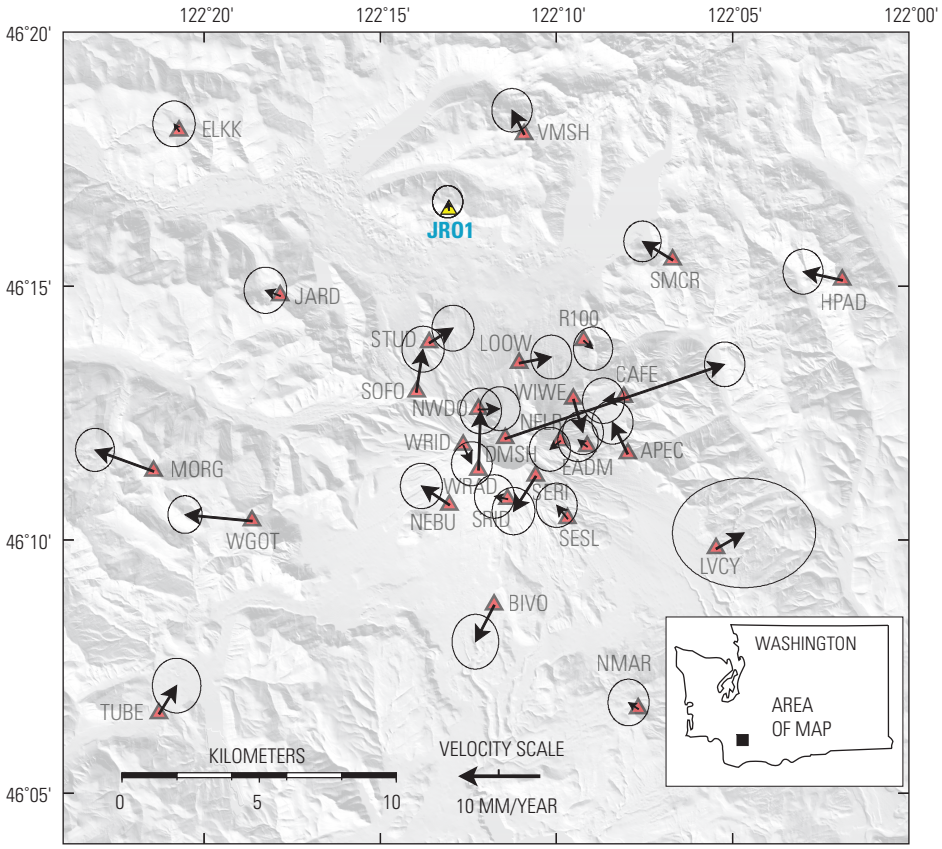

Figure 6. Map showing 2000–2003 corrected average GPS station horizontal-velocity vectors (tipped with 95-percent-confidence error ellipses, scale at bottom) for Mount St. Helens area. Although many stations show significant velocities, there is no systematic pattern that might suggest premonitory deformation before the start of the 2004 eruption. GPS station DMSH, on the 1980–86 lava dome, moved downward 87 mm/yr and east-northeastward 35 mm/yr, presumably as a result of cooling and compaction of the dome.

Table 4. Time-series analysis of Cascadia network local reference frame stations.

[WRMS is weighted root-mean-squared deviation (experimental standard deviation). Phases are relative to start of the calendar year. Data for station KELS are divided into two intervals to calculate velocities; other KELS data, equivalent between columns, are shown by dashes in second KELS column.]

Station	JRO1	KELS	KELS	BREW	CVO1	GOBS	REDM
Start date (year month day)	19970523	19971010	20040923	19971010	20030104	19970827	19980725
End date (year month day)	20040922	20040922	20061013	20061013	20061013	20061013	20061013
Number of daily positions (post-1996)	2,137	2,977	--	1,669	1,308	3,149	2,889
Number of outliers	130	201	--	1	4	30	31
East WRMS (mm)	1.70	1.62	--	0.82	1.13	1.13	1.32
North WRMS (mm)	1.75	1.77	--	0.91	1.19	1.23	1.12
Up WRMS (mm)	5.01	4.62	--	3.23	3.50	3.36	3.25
East velocity (mm/yr)	2.76	3.07	6.14	1.33	3.26	1.52	0.16
North velocity (mm/yr)	5.82	5.84	5.03	0.75	5.63	2.09	2.80
Vertical velocity (mm/yr)	-1.99	-0.45	0.11	0.18	-1.54	-0.73	0.02
East annual amplitude (mm)	2.02	0.84	--	0.35	0.51	1.83	0.35
East annual phase (degrees)	52.35	37.32	--	239.69	288.89	139.06	351.70
North annual amplitude (mm)	1.96	0.98	--	0.10	0.06	1.30	0.62
North annual phase (degrees)	137.86	160.71	--	39.96	161.07	326.93	144.47
Vertical annual amplitude (mm)	1.70	1.10	--	0.35	1.66	0.49	0.97
Vertical annual phase (degrees)	25.41	354.79	--	284.29	356.08	277.76	50.14
East semiannual amplitude (mm)	0.34	0.34	--	0.06	0.12	0.25	0.20
East semiannual phase (degrees)	244.99	109.28	--	316.72	176.88	267.05	220.03
North semiannual amplitude (mm)	0.80	0.22	--	0.11	0.19	0.30	0.27
North semiannual phase (degrees)	263.56	236.34	--	199.17	87.40	85.48	330.50
Vertical semiannual amplitude (mm)	0.64	0.31	--	0.01	0.84	0.40	0.19
Vertical semiannual phase (degrees)	276.03	122.27	--	22.97	84.91	140.26	145.93

Station	LIND	LINH	GWEN	DRAO	CHWK	SEDR
Start date (year month day)	19980728	20020506	19970827	19970827	19981119	19971007
End date (year month day)	20061013	20061013	20061013	20061013	20061013	20061013
Number of daily positions (post 1996)	1,145	1,531	3,138	3,255	2,543	3,209
Number of outliers	13	16	72	12	11	7
East WRMS (mm)	1.3	1.11	1.55	1.00	1.10	1.14
North WRMS (mm)	1.19	1.15	1.50	1.16	1.42	1.33
Up WRMS (mm)	3.95	3.90	4.32	2.97	4.24	3.55
East velocity (mm/yr)	1.70	1.70	2.10	0.93	2.43	2.97
North velocity (mm/yr)	1.69	1.63	2.56	0.41	1.60	2.11
Vertical velocity (mm/yr)	-0.53	0.01	-0.85	1.61	0.25	-0.23
East annual amplitude (mm)	0.26	0.33	0.87	0.42	0.44	0.46
East annual phase (degrees)	90.92	75.29	278.58	73.03	322.68	305.77
North annual amplitude (mm)	0.81	0.48	0.39	0.24	0.37	0.23
North annual phase (degrees)	218.14	209.76	138.47	258.20	85.11	204.89
Vertical annual amplitude (mm)	0.47	1.64	1.69	0.71	0.47	0.09
Vertical annual phase (degrees)	83.08	25.46	229.45	98.87	160.64	279.40
East semiannual amplitude (mm)	0.11	0.37	0.15	0.12	0.02	0.28
East semiannual phase (degrees)	137.32	45.34	349.51	250.97	149.82	77.91
North semiannual amplitude (mm)	0.05	0.25	0.26	0.03	0.17	0.11
North semiannual phase (degrees)	306.59	269.95	232.06	278.87	168.30	30.14
Vertical semiannual amplitude (mm)	0.39	1.33	0.62	0.13	0.61	0.05
Vertical semiannual phase (degrees)	115.22	186.33	357.05	18.87	252.14	117.52

ual-component time series. The horizontal components are then rotated so that one component represents motion radial (N. 13.5° W.), and the other component represents tangential motion (N. 76.5° E.) to Mount St. Helens (fig. 7*A*). Previously identified outliers are included in these plots, but they will be outside the 5-mm (horizontal) and 15-mm (vertical) data-rejection criteria indicated by the yellow bands on figure 7.

Station JRO1 moved at the background rate (no slope in fig. 7*A*) until the start of unrest on September 23, 2004, when anomalous subsidence and movement toward Mount St. Helens began at the station. Intervals of low-level systematic noise remain in the residual-component time series, as do short periods of drift when winter snow and ice accumulate on the GPS antenna and distort its phase center.

The average velocity of station JRO1 derived from the time-series analysis is similar to the velocity estimated from the local reference-frame calculation, but it is 0.9 mm/yr faster in the north component and 0.5 mm/yr slower in the east component than the velocity predicted by the tectonic model. We later use the tectonic model to correct post-September 23, 2004, velocities at JRO1 and at other stations around Mount St. Helens having unknown secular velocities. The observed

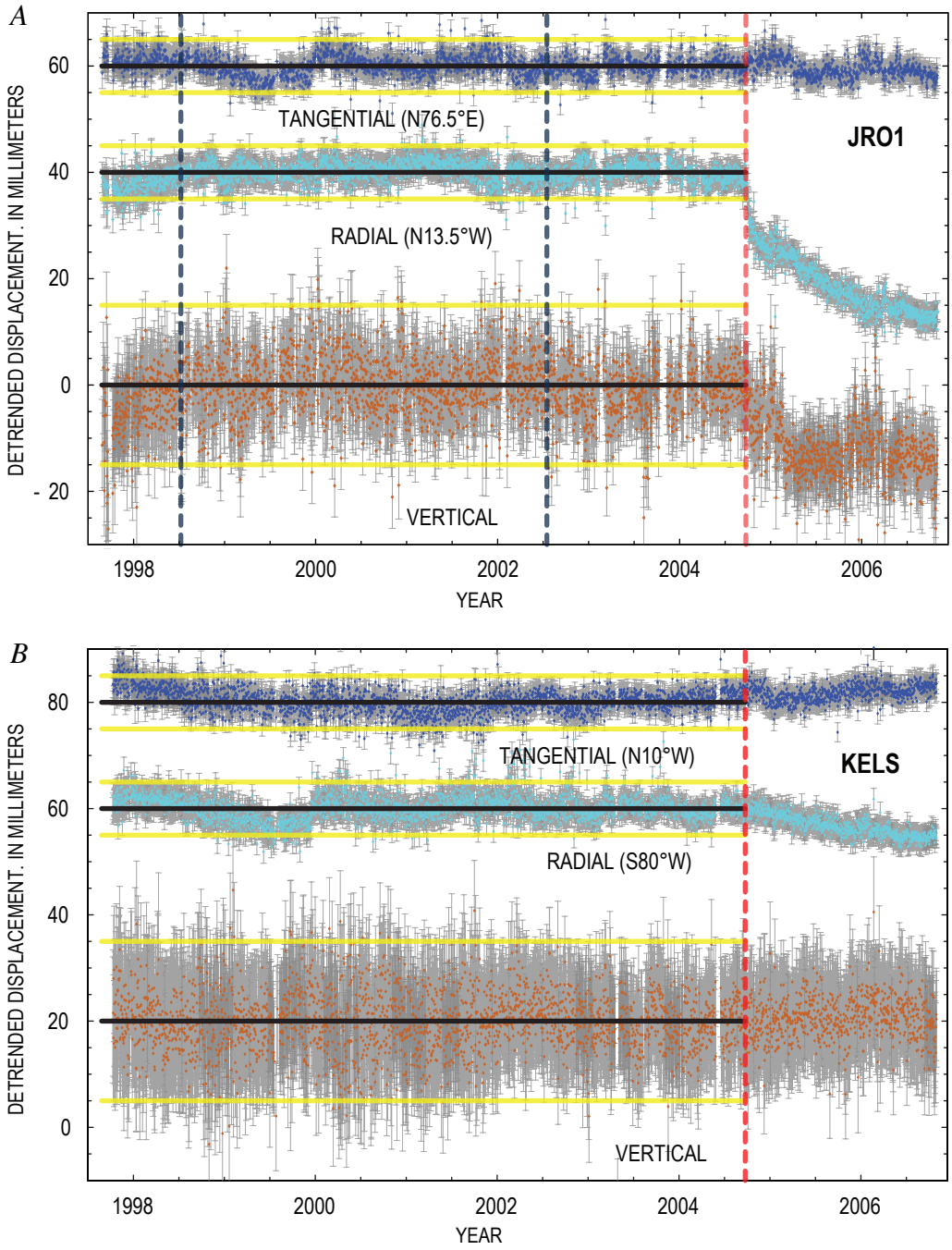

Figure 7. Stacked plots of detrended tangential, radial, and vertical daily average displacement of CGPS stations (*A*) JRO1, located 9 km north-northwest of Mount St. Helens, and (*B*) KELS, located 50 km west-southwest. Displacements are residuals from fitting a station velocity, mean value, cyclical annual and semiannual drift, and offsets from GPS antenna changes as determined by data collected through September 23, 2004. Vertical blue lines mark times that GPS antenna radomes were changed; vertical red line marks start of seismic unrest on September 23, 2004. Yellow horizontal lines are ±5 mm from pre-event tangential and radial mean values (outlier rejection limit) and ±15 mm from pre-event vertical mean value (outlier rejection limit). For station JRO1, one or more displacements were rejected for 130 of a total 2,267 days of data before September 23, 2004. For station KELS, one or more displacement components were rejected for 201 of 2,927 days of data.

discrepancy between the tectonic model and the observed motion at JRO1 is considered in the discussion of eruption-related deformation source models.

A small inward displacement of KELS, one of the PANGA CGPS stations used as a reference station in the local frame, also appears to have initiated at the start of volcanic unrest (fig. 7*B*). Station KELS is in Kelso, Wash., about 50 km west-southwest of Mount St. Helens, and the GPS antenna is mounted on a stable, deep-drilled, braced monument (Langbein and others, 1995) that is anchored at a depth of 10 m and isolated from the topsoil. The time-series analysis at KELS includes an additional term to resolve average velocities for the periods before and after September 23, 2004 (table 4). If deformation from the eruption of Mount St. Helens penetrated as far as station KELS, then it likely is the result of magma chamber pressure changes in a relatively deep (~10 km) source. We later examine data from several PBO CGPS stations located an equivalent distance to the north of Mount St. Helens to determine whether eruption-related deformation could be detected there.

GPS Station Displacements Early in the 2004–2006 Eruption

The only direct measure of deformation associated with the initiation of the eruption was made at JRO1, where slow, relatively steady motion toward Mount St. Helens was observed (fig. 8). The movement of station JRO1 was fastest in the two weeks after September 23, 2004, but even then it averaged only about 0.5 mm/day (inset, fig. 8). The inward movement continued at a nearly linear rate until a few days after the vigorous steam-and-ash explosion on October 5, 2004, when movement began to slow at a time-decaying rate. We later conclude that deformation has gradually slowed at other CGPS stations around Mount St. Helens.

The conduit that fed the eruptions in the 1980s is buried under the dome that developed in the years after the crater formed and that presumably was plugged with cooled magma. Was this plug pushed out at the start of the new dome-building eruption or was it bypassed? If a bypass formed, most likely it would appear as a dike that propagated to the

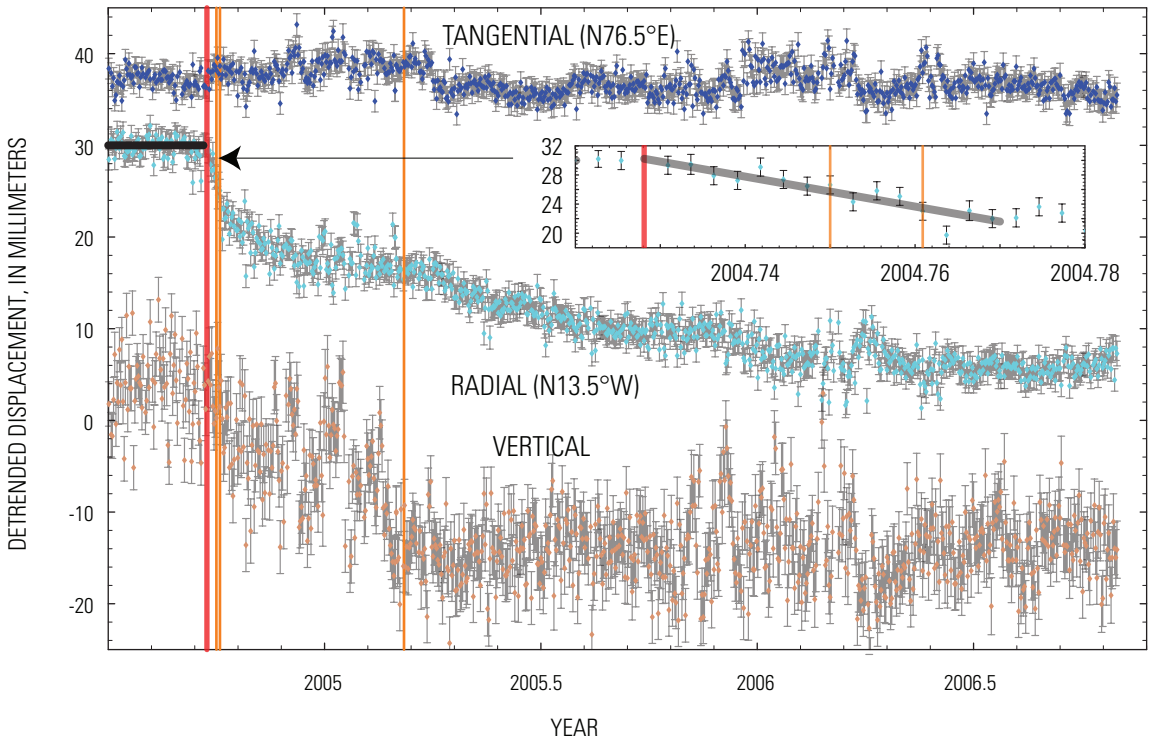

Figure 8. Stacked daily tangential (N. 76.5° E., top), radial (N. 13.5° W., middle), and vertical (bottom) displacements of CGPS station JRO1 from shortly before and during the 2004–2006 dome-building eruption of Mount St. Helens. Error bars are ±1 standard deviation. Bold horizontal black line represents projection of long-term trend in radial displacement, red vertical line marks start of unrest (seismic swarm beginning September 23, 2004), and orange vertical lines show start and end times of a series of phreatic explosions between October 1 and 5, 2004, and the time of last explosion on March 8, 2005. Vertical displacement appears to have ceased shortly after the March 8, 2005, explosion, whereas radial displacement has decayed more slowly. Inset shows a 23-day period at the start of unrest. Winter months show periods of anomalous displacements because of snow and ice accumulation on the GPS antenna radome.

surface, and we would expect associated deformation to be fairly widespread. The propagation of a shallow dike might not produce much deformation at station JRO1, located 9 km from the center of the crater, and we examine data from other stations closer to the newly formed vent for possible offsets at the start of the eruption.

An indirect measure of deformation associated with initial movement of magma to the surface is obtained at the subset of campaign GPS stations that were occupied within a week or two after the start of unrest. Displacement offset of these stations is estimated by projecting the observed 2000 to 2003 position-change trends to the start of unrest (September 23, 2004). We include data from an L1 CGPS station, DOM1, located on the September 1984 lobe of the old dome (see LaHusen and others, this volume, chap. 16). A power failure occurred at DOM1 in January 2004, and the station was not reactivated until September 27, 2004.

The large northward and upward offset at station DOM1 (in the same location as station DMSH) contrasts with the smaller and seemingly random pattern of offsets at surrounding stations (horizontal-displacement offset are shown in fig. 9, and component offsets are listed in table 5). Many of these offsets, though statistically significant on the basis of assumed error estimates, likely result from systematic error in the projected trends. Anomalous 2000 to 2003 velocities (fig. 6) were observed at many of the stations having relatively large event offsets (for example, stations WGOT, BIVO, and SERI, fig.9). These offsets are opposite of the anomalous trends, as might be expected if there were errors in the estimated station velocities. Event deformation appears to be limited to DOM1, which was about 300 m from the newly formed vent. The partially congealed magma plugging the conduit appears to have been pushed to the surface on the south side of the old dome, displacing the old dome slightly to the north and up. Most of the movement at station DOM1 had occurred by the time the station was reactivated (September 27, 2004). In its final days, the station continued moving north until it was destroyed by the first phreatic explosion on October 1, 2004 (LaHusen and others, this volume, chap. 16).

Displacement of GPS Stations During the 2004–2006 Eruption

The inward displacement of CGPS station JRO1 appears to start at about the same time as the first seismic swarm on

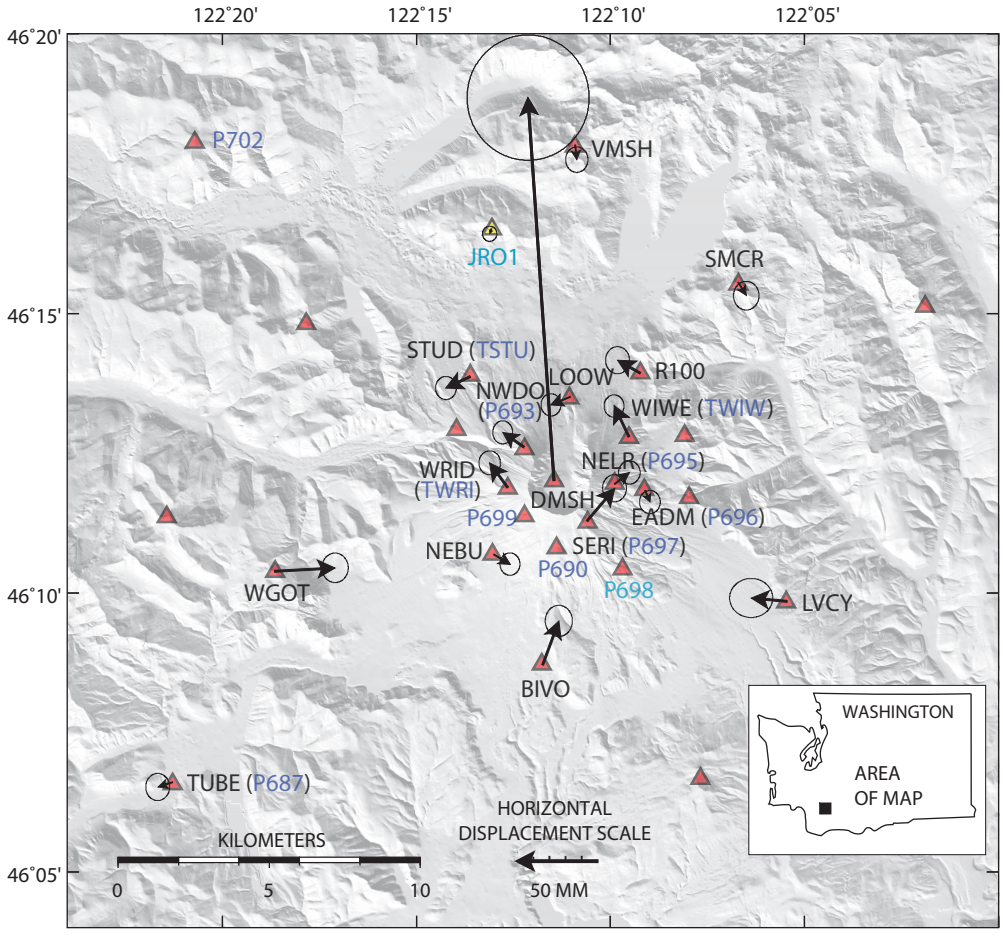

Figure 9. Map showing early event GPS station horizontal-displacement vectors (tipped with 95-percent-confidence error ellipses, vector scale on bottom) in the Mount St. Helens area. Displacements calculated by projecting station velocities to September 23, 2004, and estimating the offset between pre- and post-event positions. Many stations show significant movement, but there is no systematic pattern to suggest intrusion of a new dike to transport magma to the surface. Large displacement on the 1980–86 lava dome is that determined from measurements at DOM1 (same location as DMSH), an L1 CGPS station that was resurrected on September 27, 2004 (LaHusen and other, this volume, chap. 16).

Table 5. Estimated GPS station offsets at start of 2004 seismic unrest.

[Offsets are estimated by projecting 2000–2003 trends to September 23, 2004. Uncertainties are ±1 standard deviation.]

Station	Measurement date (2004)	Longitude (degrees)	Latitude (degrees)	East offset (mm)	North offset (mm)	East-North correlation	Vertical offset (mm)
JRO1	09/28	-122.218	46.275	-1 ± 1.8	-3 ± 1.9	0.004	6 ± 8.7
DOM1	09/28	-122.191	46.200	-16 ± 15.3	235 ± 15.7	0.014	90 ± 40.1
EADM	10/01-10/07	-122.152	46.197	3 ± 2.6	-7 ± 2.9	-0.007	-4 ± 12.2
LOOW	09/28-10/07	-122.184	46.225	-12 ± 2.5	-5 ± 2.8	0.012	-13 ± 11.8
NELR	09/29-10/07	-122.165	46.199	9 ± 2.7	7 ± 2.9	-0.038	3 ± 12.6
NEBU	09/28-10/07	-122.217	46.178	10 ± 2.5	-6 ± 2.8	0.043	-14 ± 12.0
NWDO	09/28-10/07	-122.204	46.210	-13 ± 2.5	9 ± 2.9	-0.002	-3 ± 12.0
SERI	09/30-10/05	-122.177	46.188	17 ± 3.0	20 ± 3.4	-0.070	24 ± 13.7
STUD	09/30-10/07	-122.227	46.231	-15 ± 2.6	-7 ± 2.9	0.016	0 ± 12.1
WIWE	09/29-10/07	-122.159	46.213	-9 ± 2.5	19 ± 2.8	0.021	-7 ± 11.8
WRID	10/01-10/05	-122.211	46.198	-11 ± 2.7	15 ± 3.0	0.024	2 ± 12.9
BIVO	11/03-11/09	-122.196	46.145	10 ± 3.4	27 ± 3.9	0.019	-41 ± 16.1
LVCY	11/04-11/09	-122.091	46.164	-22 ± 5.4	2 ± 4.6	0.057	-3 ± 17.1
R100	11/06 and 11/09	-122.154	46.232	-14 ± 3.0	8 ± 3.4	0.020	-3 ± 14.2
SMCR	11/06 and 11/09	-122.112	46.259	5 ± 3.2	-8 ± 3.6	0.010	-4 ± 14.7
TUBE	11/03-11/07	-122.355	46.110	-9 ± 3.0	-3 ± 3.4	-0.033	-13 ± 13.9
VMSH	11/04-11/09	-122.182	46.300	1 ± 2.8	-9 ± 3.2	0.009	-6 ± 13.3
WGOT	11/04 and 11/05	-122.311	46.173	37 ± 3.3	2 ± 3.7	0.014	-8 ± 15.1

September 23, 2004, and the displacement has continued at a decreasing rate throughout the eruption (fig. 8). The rate of subsidence, however, appears to have leveled off shortly after the March 8, 2005, explosion. Several short periods of anomalous vertical offsets in the winter of 2005, probably the result of snow and ice accumulation on the GPS antenna, make the subsidence appear jerky during the first few months of the eruption. The horizontal components of position change at JRO1 are affected less by winter anomalies, but outliers and short-term variations are apparent in the time series. At the measurement uncertainty of about ±1.7 mm in the horizontal components and ±5 mm in the vertical component of displacement (table 4), there is no apparent deformation anomaly in the months or days before the start of unrest.

The pattern and rate of deformation around Mount St. Helens during all but the first few weeks of the eruption are measured by a network of CGPS stations. Eleven new CGPS stations (seven from PBO and four from CVO) were installed by November 5, 2004 (see table 1 for installation dates and additional information). The PBO stations are part of a planned network of 20 CGPS stations (four with collocated borehole tiltmeters) and four strainmeter stations (each consisting of a borehole tensor strainmeter, a three-component seismometer, and a tiltmeter) in the NSF-funded PBO Mount St. Helens volcanic cluster. The data from new CGPS stations, along with data from JRO1, are processed by CVO as part of the HelensMonit network. Network solutions are transformed into fixed-NOAMgp, ITRF2000, and a local reference frame. The local reference frame for the HelensMonit network consists of five reference stations (GOBS, REDM, KELS, LINH, CVO1).

We use QOCA's time-series analysis to estimate and remove cyclical annual and semiannual seasonal noise from the daily CGPS solutions. We then remove secular tectonic motion predicted by the tectonic model and rotate the resulting cleaned, horizontal-component time series from the east and north geographic components into components that are radial and tangential to Mount St. Helens. At several stations, an eccentric offset correction (table 6) is used to transfer the positions measured at the campaign GPS station early in the eruption to the nearby CGPS station. Then, horizontal and vertical time-series data are stacked to compare position change over time (figs. 10, 11).

The CGPS stations near Mount St. Helens are divided into high- and low-altitude groups for the stacked-component time-series plots. The low-altitude stations have minor winter displacement anomalies, whereas stations at altitudes greater than 2,000 m experience frequent, and sometimes large, winter excursions. The locations of the CGPS stations are shown in figure 9.

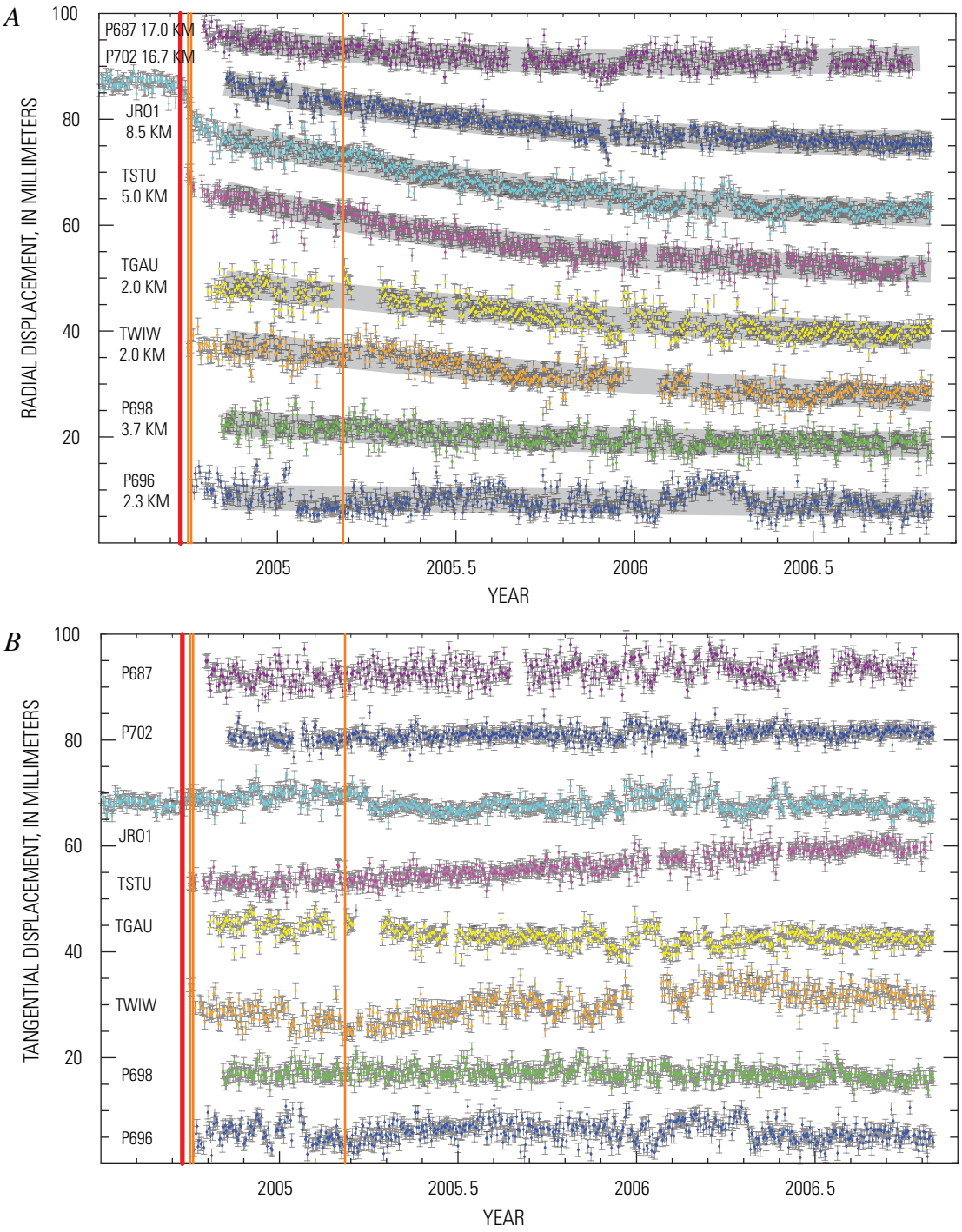

Figure 10. Plots of detrended and stacked time series of daily radial (*A*), tangential (*B*), and vertical (*C*) displacements at eight CGPS stations around Mount St. Helens at altitudes less than 2,000 m. Locations of stations shown in figure 9. Error bars are ±1 standard deviation, and gray bands in radial and vertical displacements are best-fitting rates of exponential decay. The red vertical line marks the start of unrest on September 23, 2004, and the orange vertical lines mark three phreatic explosions. A few of the earliest measurements at TSTU, TWIW, and P696 were made at a nearby campaign GPS station, and an eccentric correction was used to reduce positions to corresponding CGPS station. Tangential displacements at TSTU, TWIW, and TGAU are significantly different than zero. Station distances in *A* and *C* are computed relative to surface projection of modeled source (red cross in fig. 17*A*).

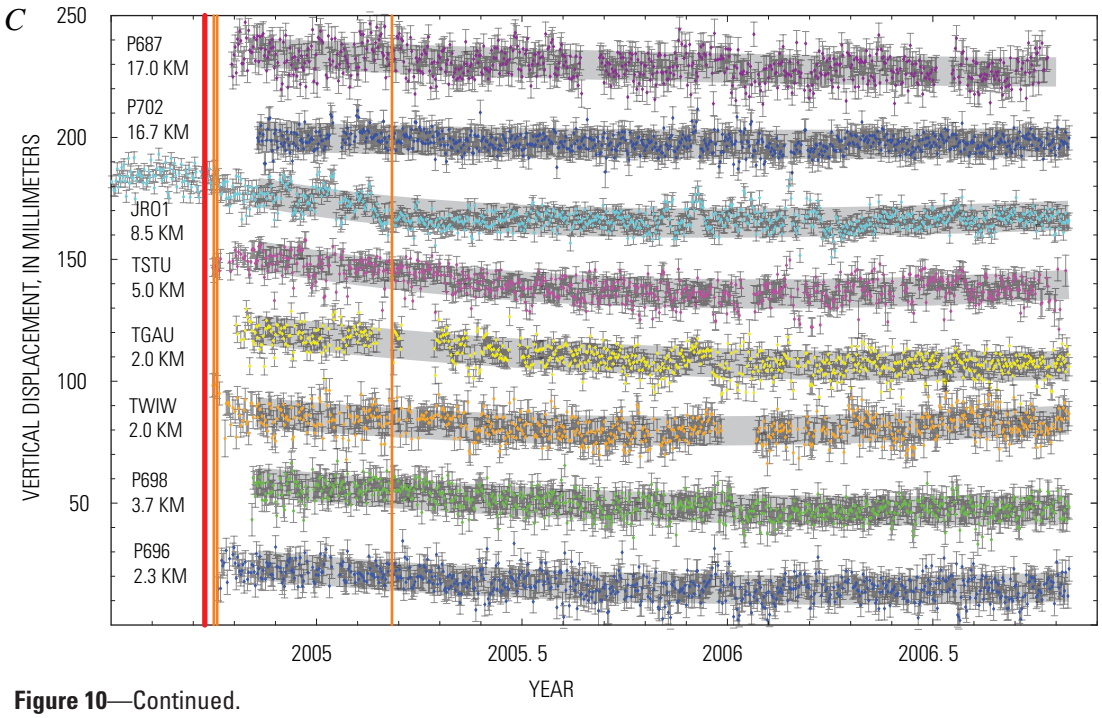

Figure 10—Continued.

The maximum radially inward movement of the low-altitude stations (fig. 10*A*) occurs at stations TSTU and JRO1, located at distances of 5 and 9 km from Mount St. Helens, respectively. Radial movement diminishes at stations located farther (P687, P702) and closer (TGAU, TWIW, P698, P696) to Mount St. Helens. The tangential component of motion is small, except at stations TSTU, TGAU, and TWIW (fig. 10*B*). Subsidence occurs at all stations and reaches its maximum at TSTU, but it diminishes at stations closest to and farthest from Mount St. Helens (fig. 10*C*).

During winter months, CGPS stations installed at altitudes above 2,000 m on Mount St. Helens (P695, P690, TWRI, P693, P697, P699) experience periods of temporary pseudo-displacements (fig. 11) from the accumulation of rime on the GPS antenna (fig. 12). At two high-altitude stations (P690 and P699) where the solar panels were mounted on the south side of the GPS antenna mast, asymmetrical ice loading permanently warped the towers.

The 2004–2005 winter displacements at station P697 were unusually large and constant (fig. 11). Initially we hypothesized that the apparent displacement of this station normal to the south crater wall resulted from the impact of the growing lava spine on that wall. With warming weather in the spring of 2005, the ice covering the GPS antenna melted, and the station returned to its initial position. The winter of 2004–2005 was unusually mild, and large, systematic pseudodisplacements were observed only at the highest stations (P699 and P697), and only the tower for station P699 was warped permanently by ice loading. During the more typical winter of 2005–2006, ice coated the GPS antennas at all high-altitude stations, and the towers at stations P699 and P690 were warped by ice loads on the attached solar panels.

Wintertime pseudodisplacements at the high-altitude CGPS stations complicate analysis of eruption-related deformation there. The application of suitable outlier-rejection criteria in the QOCA time-series analysis minimizes the need for hand-editing data outliers. The calculation of tower offsets at stations P699 (2005 and 2006) and P690 (2006), however, requires careful data editing, and even then the calculated horizontal offsets are poorly determined. The warping of the 3-m-high towers did not appear to cause significant vertical offset. A mechanical offset was introduced at station P699 in September 2006 during site maintenance when a UNAVCO field engineer removed the radome cover and reset the tilted GPS antenna. At the same time, the pole-mounted solar panels at P690 and P699 were removed and replaced with panels mounted on separate frames in an effort to prevent future load-induced offsets.

Time-Decaying Movement of GPS Stations During the 2004–2006 Eruption

The radial and vertical CGPS station displacements have been slowing over time, and the wide, gray bands shown in the stacked radial and vertical displacement plots are best-fitting curves of the form

$$y = ae^{-b(t-t_0)}, \qquad (1)$$

where a and b are constants, t is the observed time, and t_0 is the start time. In the data fit we use October 15, 2004, as the start time and include only data after that date. Our main inter-

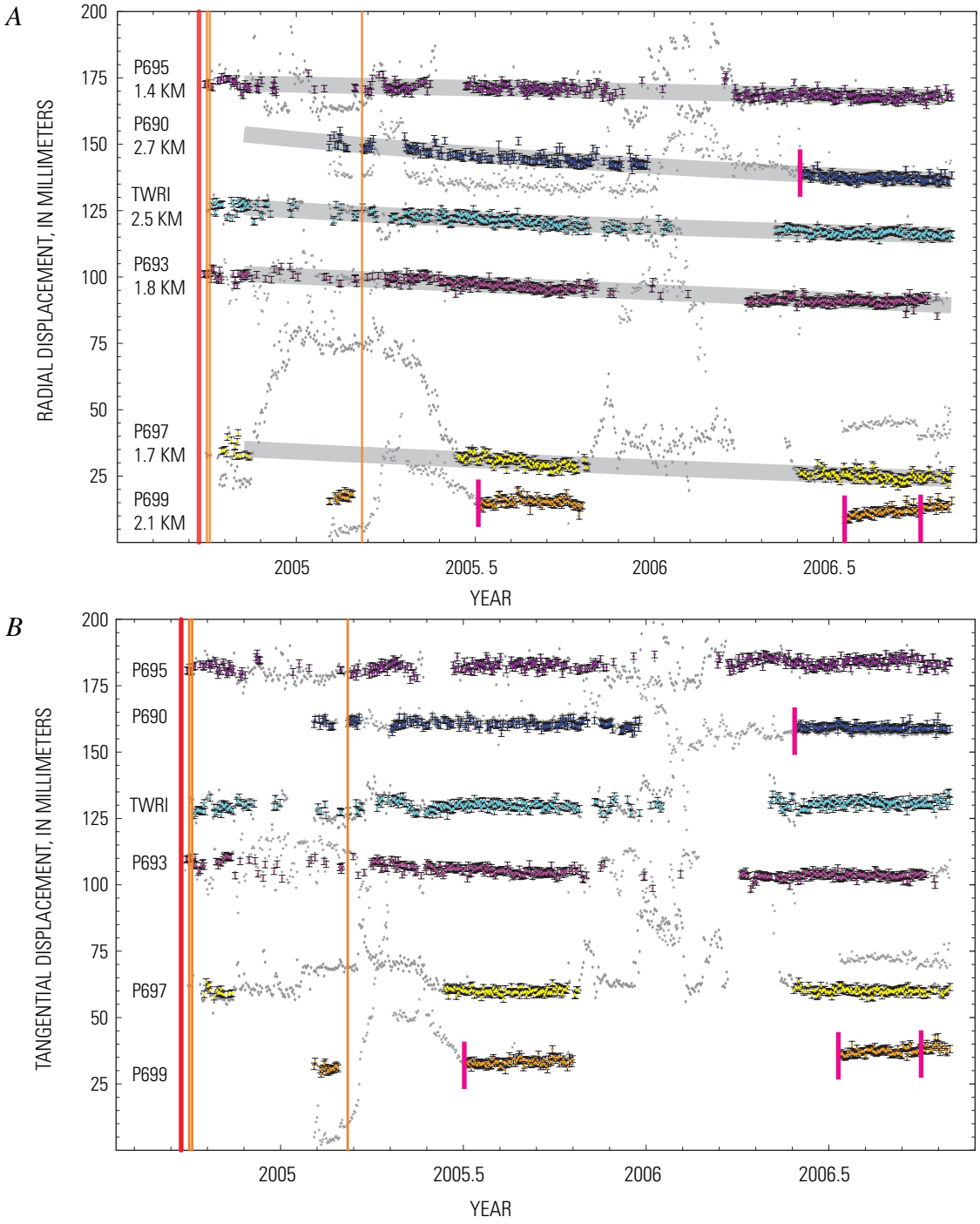

Figure 11. Plots of detrended and stacked time series of daily radial (*A*), tangential (*B*), and vertical (*C*) displacements at six CGPS stations around Mount St. Helens at altitudes greater than 2,000 m. Locations of stations shown in figure 9. Error bars are ±1 standard deviation, and gray bands in radial and vertical displacements are best-fitting rates of exponential decay. Gray dots are outliers (pseudodisplacements) that result from ice coating the GPS antennas, and they are not used in analysis. Short red vertical lines mark time used to calculate an offset for stations P690 and P699 to account for permanent warping of the tower from ice loading. The red vertical line marks the start of unrest on September 23, 2004, and the orange vertical lines mark three phreatic explosions. A few of earliest measurements at P695 and P693 were made at a nearby campaign GPS station, and an eccentric offset correction was used to reduce positions to corresponding CGPS station.

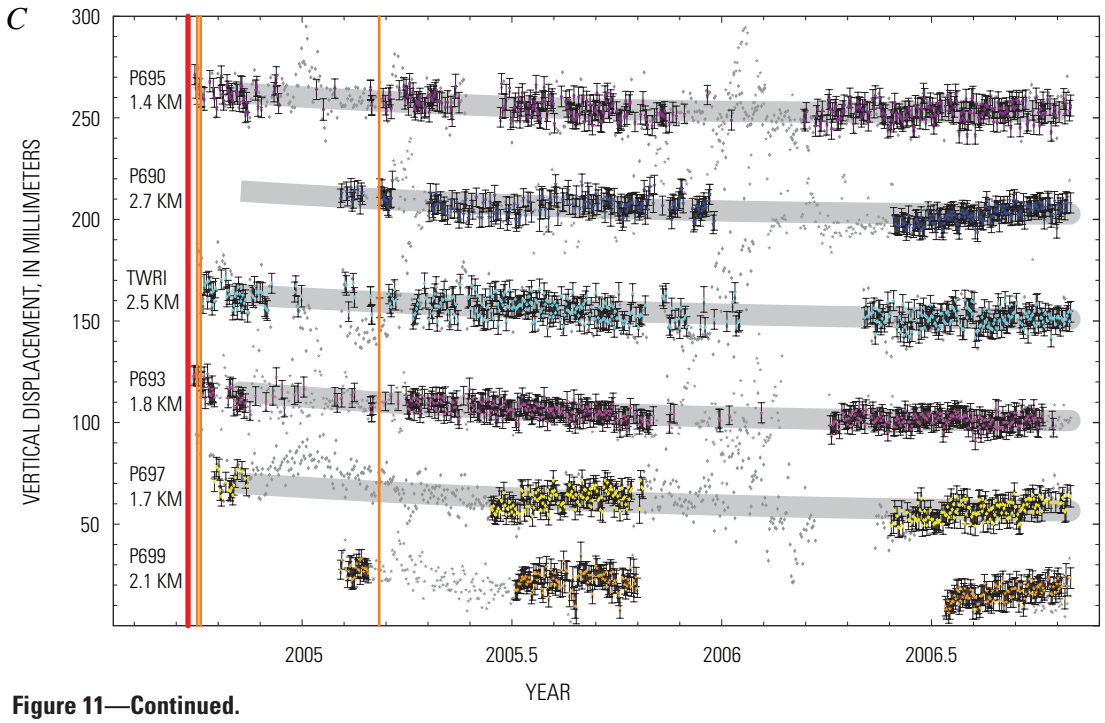

Figure 11—Continued.

Table 6. Surveyed offsets between bedrock campaign GPS stations and nearby tower or braced CGPS stations.

[Offsets may have been surveyed repeatedly and are given in Cartesian coordinates. CGPS, continuously transmitting GPS.]

Bedrock station	CGPS station	Measurement date	X offset (m)	Y offset (m)	Z offset (m)
WIWE	TWIW	2004/10/12	-4.2706	-0.2173	2.2044
WRID	TWRI	2005/08/11-08/18	-71.1883	71.0514	-10.0691
SERI	P697	2005/08/11-08/18	-11.1530	-2.2178	-0.8293
NWDO	P693	2004/10/15-10/19	121.0864	-5.9706	49.7039
STUD	TSTU	2004/10/15	394.1229	211.2114	465.2217
NELR	P695	2004/10/15	36.6088	-37.1623	-30.4480
TUBE	P687	2004/11/03-11/07	1.9623	1.2851	4.3265
SESL	P698	2005/07/13-07/22	50.0780	-53.8675	-15.3364
ELKK	P702	2004/11/05-11/07	-51.9197	-23.0480	-64.4552
EADM	P696	2004/10/15	10.7039	-46.8483	-36.9437
WRAD	P699	2005/08/19	18.1105	-12.8303	19.8468

est is in *b*, which gives the rate of time decay in the displacement components. We add a constant to the residual-component time-series data to make all residual components positive; thus intercept *a* is arbitrary. As discussed previously, the radially inward displacement of JRO1 between September 23 and approximately October 8 averaged 0.5 mm/day (inset, fig. 8). Equation 1 is one of several similar curves derived by Mastin and others (this volume, chap. 22) to fit the volume growth of the dome over time. Changes in the rate of dome growth might be expected to be matched by changes in the rate of volume or mass loss in the magma chamber feeding the eruption. We later test whether the observed deformation can be explained by depressurization of a magma chamber, but first we look for coherent patterns of deformation in the CGPS displacement time series.

Space-Time Correlated Deformation During the 2004–2006 Eruption

The CGPS station-component time series indicate small (total to several centimeters) radially inward and downward movements that appear to have slowed during the eruption. To determine whether these movements are correlated in time, as might be expected if they were in response to pressure loss in a magma reservoir, we apply principal component analysis (PCA; Preisendorfer, 1988). The PCA decomposes the collective station-displacement time series into a number of deformation modes, each of which consists of a common temporal response and a spatial scaling factor that varies between stations but remains constant over time at each station. This method of decomposing space-time data into the superposition of space- and time-separable modes is also called empirical orthogonal-function analysis (Menke, 1984) and eigenanalysis (Aubrey and Emery, 1983). Along with a similar method called Karhunen-Loeve expansion, Dong and others (2006) used PCA to identify and remove common-mode error in daily GPS station-coordinate time series. PCA also has been used to study interseismic deformation (for example, Savage, 1988, 1995).

A mathematical description of the method as applied in QOCA-based PCA analysis is given by Dong and others (2006). Summarizing their discussion, a data matrix X_{ij} is constructed such that each column (subscript i in equation 2) contains a single residual-displacement component (either east, north, or vertical) from a single station in the network. The rows of the matrix (subscript j) include displacement components from all network stations in each period of measurements (daily averages are used here). PCA allows one to represent X_{ij} by

$$X_{ij} = \sum_{k=1}^{N} A_{ik} C_k(t_j), \qquad (2)$$

where the N products $A_{ik}C_k(t_j)$ are the individual modes, with A_{ik} as the spatially varying scale factor and $C_k(t_j)$ as the temporally varying time factor for each mode k. If the PCA-identified deformation modes are ordered by their contribution to the data variance, spatially correlated signals are contained in the first few modes, whereas the higher-order modes usually reflect more local effects.

We apply PCA to the cleaned, residual station-component time series from the 11 Mount St. Helens CGPS stations with the most complete time series (all stations except P690, P697, and P699), three PBO CGPS stations (P420, P421, and P432) located more than 40 km to the north, and the five distant CGPS reference stations (CVO1, KELS, LINH, GOBS, and REDM) included in the solutions. Outliers, predicted tectonic motion, and cyclical annual and semiannual noise are removed from the data. PCA requires observations at all included stations in each epoch. Therefore, Lagrangian interpolation is applied to fill small data gaps, and an iterative process that uses the predictions of the first three PCA modes is used to fill large data gaps (Dong and others, 2006). We examine deformation that occurred after October 15, 2004, when most of the new CGPS stations were operational.

The PCA can identify a single coherent mode of time-varying deformation. The first principal mode (mode 1) accounts for a large percentage (between 40 and 70 percent) of the data variance (fig. 13), particularly in the horizontal components, and only mode 1 temporal components (fig. 14*A*) vary systematically with time. The mode 2 (fig. 14*B*) and higher-order temporal components (not shown) have no long-term changes with time and likely represent random noise and systematic short-term fluctuations at one or more of the analyzed stations.

Mastin and others (this volume, chap. 22) derive logarithmic and exponential functions to fit the time decay in the

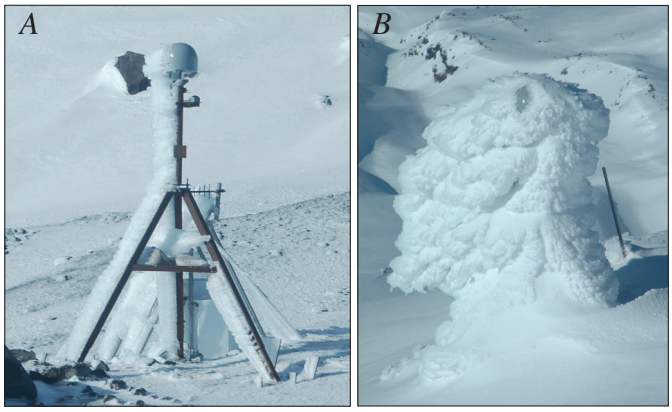

Figure 12. Examples of heavy winter rime on GPS station antennas and tower mounts at altitudes greater than 2,000 m. Locations of stations shown in figure 9. *A*, Station P697. Tower stands 3.5 m above ground, which has been blown free of snow. USGS photo by W.E. Scott. *B*, Station P699. Until September 2006, station P699 had a solar panel mounted on its GPS antenna mast, which exacerbated ice loading and resulted in permanent warping of the tower. USGS photo by M. Lisowski.

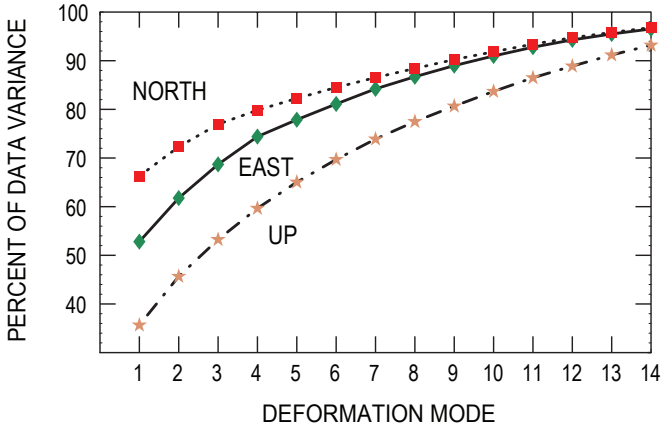

Figure 13. Cumulative percentage of data variance in 14 Mount St. Helens CGPS residual-component time series accounted for by the first 14 PCA deformation modes. North, east, and up spatial components are analyzed independently.

volumetric rate of dome growth and show that a logarithmic decay is expected if flow rate is controlled by frictional sliding of a near-surface plug (provided the coefficient of friction increases with displacement rate), whereas an exponential decay is expected if the effusion rate is a linear function of magma-chamber pressure. Ongoing, constant recharge adds a linear term to the equations of volumetric rate of dome growth.

The mode 1 deformation likely represents the loss of pressure in the magma chamber feeding the eruption, and the mode 1 temporal component can be fit with curves similar to those used by Mastin and others (this volume, chap. 22) to fit dome growth. The mode 1 east and north temporal components are best fit by an exponential decay (equation 1) and by exponential decay with a linear term (table 7). The relatively rapid decrease in the mode 1 vertical component is best fit by

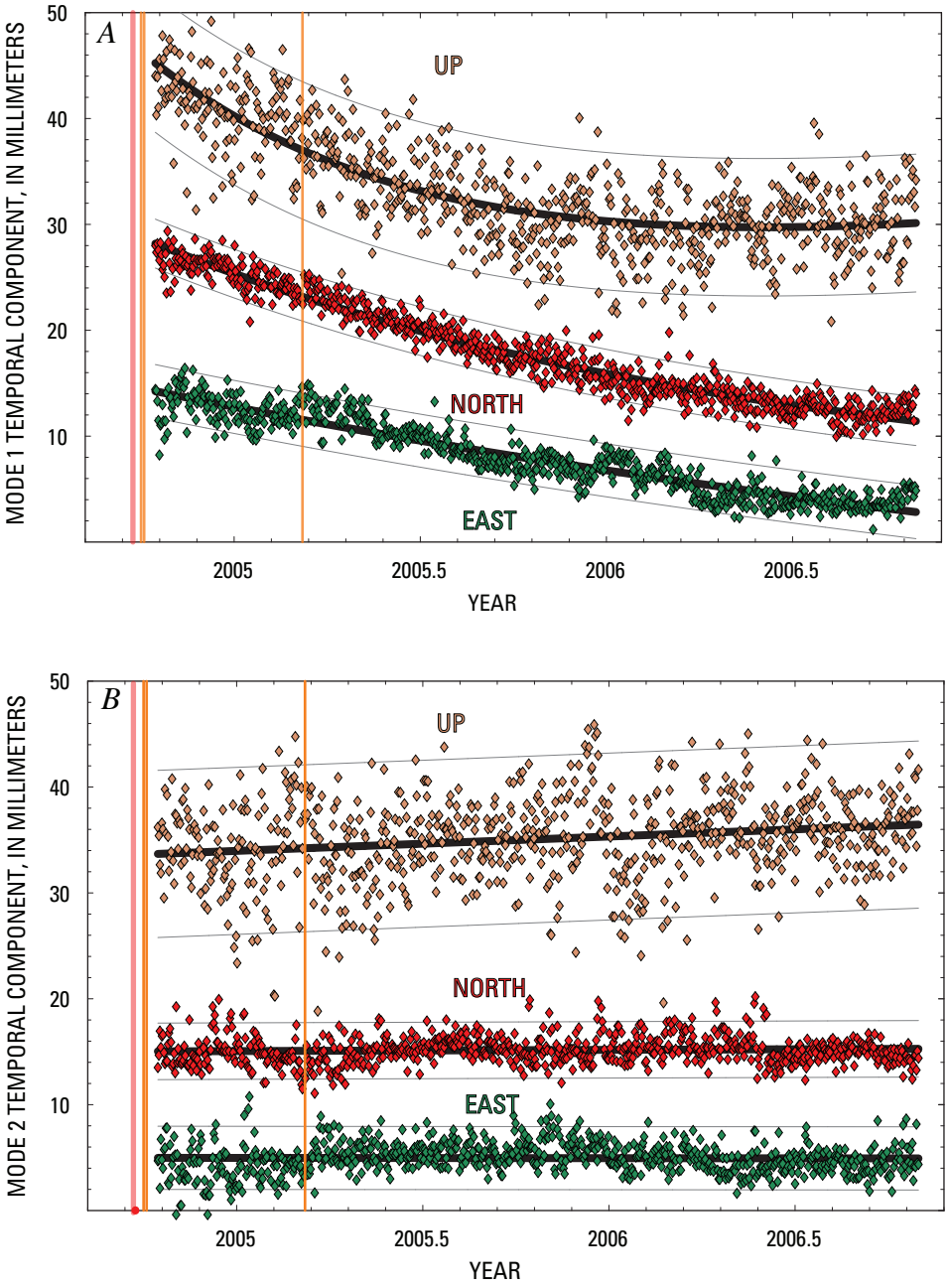

Figure 14. Temporal components from principal component analysis, in millimeters, from the combination of 14 Mount St. Helens CGPS stations and 5 CGPS reference-station residual-component time series. Dark lines are the fits to an exponential decay (equation 1) and light-gray lines are 95-percent-confidence limits of that fit. Vertical orange lines as in figures 10 and 11. *A*, Mode 1. *B*, Mode 2.

an exponential decay with a constant linear increase. The fit of the relatively noisy mode 1 temporal component without a linear term is only slightly worse. In all cases the inverted linear coefficient (*d*) and the exponential time coefficient (*b*) are highly correlated and, therefore, individually poorly determined. The best-fitting curves with the form of equation 1, along with their 95-percent-confidence limits, are shown in figure 14*A*.

So far we have examined only the PCA temporal components $C_k(t_j)$. Scaling the temporal components by the individual station response A_{ik} gives the corresponding station displacement. The scatter in the temporal components, when scaled, will result in scatter in the displacements. To calculate a station displacement for a specified time interval, we need to average or smooth the temporal components. The exponential fit supplies a smoothing that reproduces the data fairly well, and we use it to predict the temporal component and its uncertainty at any given time. The mode 1 horizontal and vertical displacements between October 15, 2004, and October 31, 2006, derived from the exponential fit, are shown in figure 15. Displacements are shown only for close-in stations, so that the map scale remains large enough to display details of deformation near Mount St. Helens, but all displacement values are listed in table 8.

Table 7. Exponential fits to PCA Mode 1 temporal components.

[Constant coefficients for $y=ae^{-b(t-t_0)} + d(t-t_0)$ with $t_0 = 2004.853$.]

Component	a (mm)	b (per yr)	d (mm/yr)	Variance (mm²)
East	22.057	0.366		1.764
East+linear	22.119	0.381	0.163	1.766
North	26.122	0.544		1.432
North+linear	26.077	0.536	-0.075	1.434
Up	24.333	0.471		15.713
Up+linear	29.207	1.171	4.492	13.112

Table 8. PCA Mode 1 station displacements from October 15, 2004, to October 31, 2006.

[Initial and final mode 1 temporal components are scaled by spatial eigenvalue for each station. Estimated 1 standard deviation uncertainty: east, 1.31 mm; north, 1.18 mm; up, 3.59 mm.]

CGPS station	Longitude (degrees)	Latitude (degrees)	East displacement (mm)	North displacement (mm)	Up displacement (mm)
JRO1	237.7824	46.2751	5.0	-14.8	-9.6
TGAU	237.8077	46.2192	4.2	-10.3	-15.3
TSTU	237.7759	46.2369	0.5	-17.2	-14.7
P687	237.6454	46.1096	4.3	-0.4	-8.8
P696	237.8484	46.1969	-0.9	-1.5	-10.3
P698	237.8394	46.1735	-2.7	1.2	-10.2
P702	237.6544	46.3002	6.1	-8.6	-5.5
KELS	237.1039	46.1182	3.7	-2.6	0.8
P693	237.7977	46.2103	8.1	-6.4	-9.3
P695	237.8358	46.1990	-3.2	-1.3	-9.2
TWIW	237.8413	46.2129	-11.5	-3.2	-9.3
P420	237.1337	46.5886	1.4	-3.9	-0.1
P421	237.5708	46.5319	2.4	-5.7	-5.0
P432	238.3168	46.6229	0.1	-3.7	-3.3
GOBS	239.1853	45.8388	-0.7	1.3	-0.8
LINH	239.4615	47.0003	0.3	-1.1	0.7
CVO1	237.5039	45.6109	0.1	-1.5	-1.4
REDM	238.8521	44.2598	0.3	-0.1	-0.7
TWRI	237.7881	46.1979	7.8	-4.5	-9.7

A few general features are apparent in the mode 1 displacements shown in figure 15. Maximum horizontal and vertical displacements are roughly equal, and subsidence is observed everywhere, with maximum values at distances greater than about 3 km and less than about 10 km. Horizontal displacements are toward Mount St. Helens, with maximum values at distances greater than about 5 km and less than about 20 km, and they are larger to the north of Mount St. Helens than to the south. Some of the apparent asymmetry in the deformation could result from the fact that there are more CGPS stations north of Mount St. Helens. Some other possible explanations for the asymmetry include error in the tectonic model that underestimates the background rate of northward motion, a source of deformation that is located to the south of the crater, a dipping source, and a laterally inhomogeneous crust.

The CGPS station displacements can be supplemented with data from a few campaign GPS stations to increase the areal coverage. This combination will be used to constrain possible sources of deformation. When we have a suitable model, we use the PCA mode 1 deformation to estimate the change in time.

Analytical Source Models

By using the PCA, a single mode of time-varying deformation was identified in the cleaned CGPS time series, which consists of an exponentially decaying downward and inward collapse toward Mount St. Helens. Such a collapse can result from pressure loss in the magma chamber feeding the eruption.

A simple model of an erupting volcano includes a magma chamber and a conduit to allow magma to escape to the surface (fig. 16). Magma chambers are idealized as fluid-pressurized, ellipsoidal cavities in an elastic half-space (Mogi, 1958; Davis and others, 1974; Davis, 1986; Yang and others, 1988; Fialko and others, 2001), and conduits are idealized as verti-

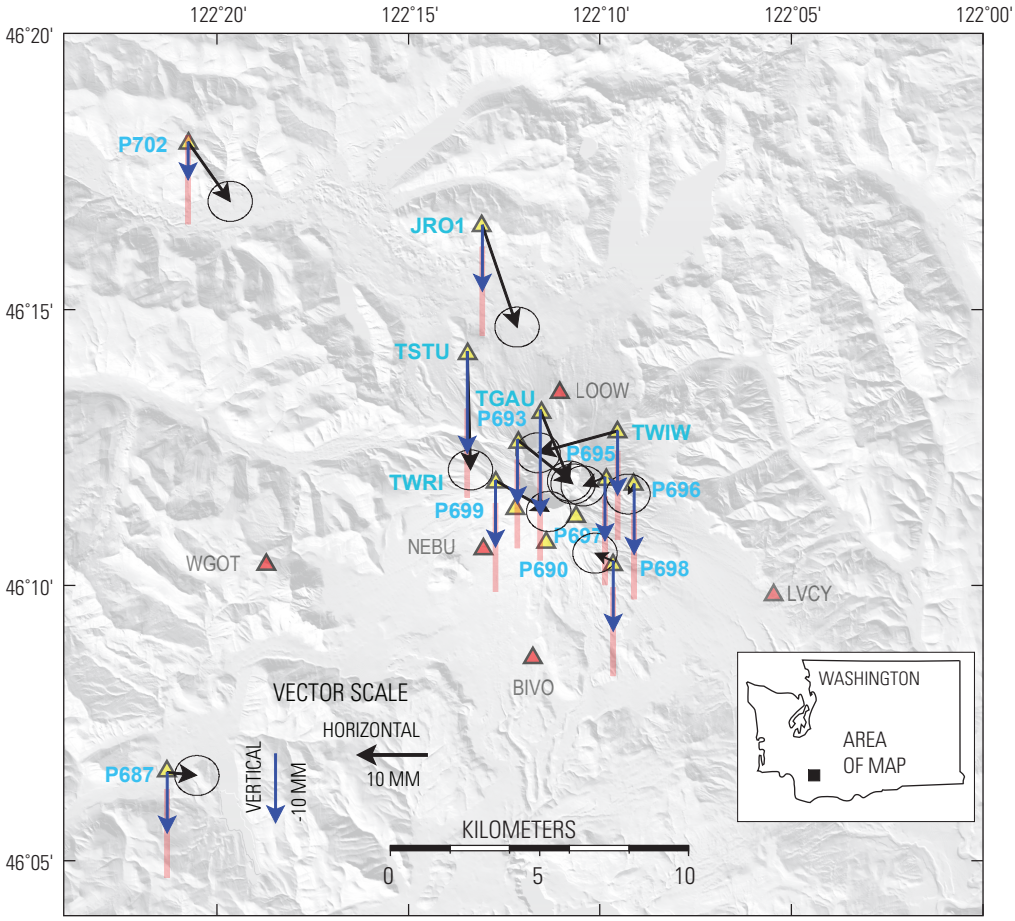

Figure 15. Map showing PCA mode 1 estimated horizontal (black arrows, tipped with 95-percent-confidence error ellipses) and vertical (blue arrows tipped with orange 95-percent-confidence error bars) displacements from October 15, 2004, to October 31, 2006, for the Mount St. Helens area. CGPS stations P699, P690, and P697 are not included in PCA analysis because of offsets and persistent winter excursions.

cal closed or open pipes (Bonaccorso and Davis, 1999). The eruption will continue until overpressure in the magma system drops below that of an equilibrated open magmatic system or until the conduit is blocked by congealing magma. As magma is withdrawn to feed an eruption, the pressure decrease in the magma system can be buffered by exsolution of gas (Mastin and others, this volume, chap. 22) and by input of new magma from depth.

Pressure change in a conduit with a radius of 10–50 m, typical for volcanoes (Bonaccorso and Davis, 1999), contributes little to the surface deformation, except near the vent; for the same reason, we can ignore deformation produced by shear tractions on the wall of the conduit exerted by magma flowing through the conduit. We assume that pressure change in the magma reservoir beneath the conduit is responsible for most of the observed deformation; therefore, we use the data to constrain the approximate limits of source depth, geometry, and the cavity volume change of a pressure source that represents the magma chamber. We limit our search to spheroidal pressure sources, which include spheres and prolate (elongate) and oblate (flattened) spheroids. We assume Poisson's ratio equals 0.25, and that the shear modulus equals 30 GPa in all the models. The pressure change that best reproduces the deformation is not estimated directly; rather, it is combined with the elastic parameters (shear modulus G, and Poisson's ratio ν) and the unknown source volume. Paradoxically, except for very shallow sources (where the chamber size is a large fraction of the depth), a large pressure change in a small source volume is indistinguishable from a small pressure change in a large source volume (McTigue, 1987). The ratio of pressure change to shear modulus must remain within the elastic limits of the surrounding rock.

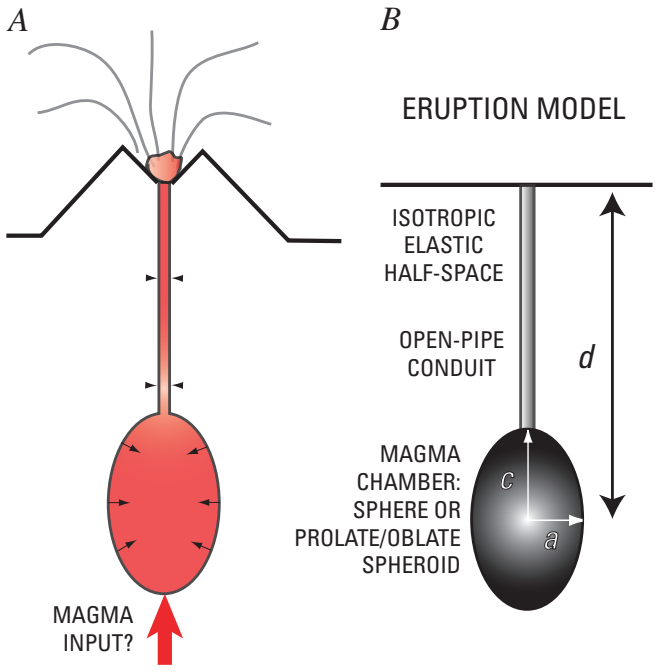

Figure 16. Schematic cross section of erupting volcano (*A*) and pressure sources (*B*) used to model surface deformation. Source depth, d, of magma chamber in half-space is relative to mean elevation of volcano.

Combined CGPS and Campaign GPS Data

Stations in the CGPS network are concentrated around the crater and to the north of Mount St. Helens. To improve spatial coverage of the deformation, we add data from campaign GPS surveys at five stations located at moderate distances from Mount St. Helens (red triangles in fig. 17). These stations were surveyed, at minimum, in late 2004 and again in 2005. We assume that deformation accumulates at a constant rate during the year after October 11, 2004, and obtain average station velocities for CGPS and campaign GPS stations (table 9). Our start and stop dates are arbitrary, but they include surveys of all the key campaign GPS stations. The mode 1 temporal components (fig. 14*A*) decay at approximately a linear rate during this year-long interval, except for the relatively noisy vertical component. The average horizontal (fig. 17) and vertical (fig. 18) station velocities for this one-year period are comparable in direction and relative magnitude to those derived from the PCA for a two-year period. Note that we include velocities for stations P690 and P697, which were excluded from the PCA analysis because of winter anomalies. The uncertainties in the station velocities are those from the QOCA time-series analysis supplemented in quadrature with a random-walk error of 1 mm/yr.

Elastic Half-Space Deformation Source Models

The nearly radial symmetry in the eruption-related deformation is consistent with a spheroidal-source geometry, and we first fit the data to a spherical-point (also called Mogi) pressure source by using a random-cost (Berg, 1993; Murray and others, 1996) search algorithm for the optimal location and depth of the source. Use of a point-source model is justified because the deformation is widespread, and, therefore, consistent with a source that is much deeper than its size (McTigue, 1987). The best-fitting spherical point-source depth (table 10) is deep (13 km), but, as indicated by the data misfit (reduced χ^2) of greater than 2, it is a poor choice when the maximum vertical and horizontal deformation are roughly equal (fig. 19*A*). A spherical source predicts a maximum horizontal deformation that is about 0.4 of the maximum vertical. Some of the misfit of the data to the model may be from the tectonic model used to correct the observed velocities. To account for such systematic error, we solve for a constant horizontal velocity in the data inversion. The point source with a systematic velocity shift fits the data slightly better, having a shallower source depth, and the center of deformation is shifted slightly to the northwest. The components of the translation (1.4 mm/yr west, 2.1 mm/yr north), however, are considerably larger than the misfit of the tectonic model to the pre-event velocity of JRO1 (0.5 mm/yr west, 0.9 mm/yr north).

A prolate spheroidal (cigar-shaped) pressure source predicts roughly equal maximum horizontal and vertical

Table 9. Adjusted Helens CGPS average station velocities from October 11, 2004, to October 11, 2005.

[Velocities are in nominal ITRF2000 fixed North American Plate terrestrial reference frame and are corrected for regional rigid-body rotation and strain.]

Station	Longitude (degrees)	Latitude (degrees)	East velocity ± 1 σ error (mm/yr)	North velocity ± 1 σ error (mm/yr)	Up velocity ± 1σ error (mm/yr)
JRO1	-122.2180	46.2750	5.42 ± 1.09	-10.50 ± 1.10	-13.19 ± 1.45
TSTU	-122.2240	46.2370	2.92 ± 1.09	-11.02 ± 1.10	-15.48 ± 1.46
TGAU	-122.1920	46.2190	3.78 ± 1.10	-5.32 ± 1.11	-12.58 ± 1.51
TWIW	-122.1590	46.2130	-5.53 ± 1.10	-2.24 ± 1.11	-8.49 ± 1.50
TWRI	-122.2120	46.1980	7.03 ± 1.13	-2.46 ± 1.14	-9.21 ± 1.64
P687	-122.3550	46.1100	4.56 ± 1.10	1.69 ± 1.11	-5.75 ± 1.54
P690	-122.1900	46.1800	0.56 ± 1.43	7.88 ± 1.48	-7.63 ± 2.71
P693	-122.2020	46.2100	7.41 ± 1.14	-2.59 ± 1.16	-8.98 ± 1.67
P695	-122.1640	46.1990	-2.08 ± 1.13	0.50 ± 1.14	-8.41 ± 1.66
P696	-122.1520	46.1970	-1.13 ± 1.10	0.32 ± 1.11	-9.11 ± 1.51
P697	-122.1770	46.1880	1.44 ± 1.33	0.58 ± 1.37	-3.30 ± 2.45
P698	-122.1610	46.1730	-1.72 ± 1.11	2.33 ± 1.12	-10.52 ± 1.56
P702	-122.3460	46.3000	5.44 ± 1.12	-7.10 ± 1.13	-3.45 ± 1.57
NEBU	-122.2170	46.1780	5.15 ± 1.77	0.65 ± 1.85	-14.71 ± 3.80
BIVO	-122.1960	46.1450	-1.43 ± 1.19	7.55 ± 1.21	-5.01 ± 1.88
LVCY	-122.0910	46.1640	-5.56 ± 2.16	3.25 ± 2.23	-11.54 ± 4.69
LOOW	-122.1840	46.2250	-0.35 ± 1.84	-7.65 ± 1.91	-10.02 ± 3.91
WGOT	-122.3110	46.1730	5.20 ± 2.40	1.90 ± 2.49	-15.80 ± 5.07
P420	-122.8660	46.5890	1.40 ± 1.08	-1.85 ± 1.09	0.94 ± 1.43
P421	-122.4290	46.5320	2.02 ± 1.17	-3.78 ± 1.19	-1.44 ± 1.79
P432	-121.6830	46.6230	-0.65 ± 1.09	-1.94 ± 1.10	-2.39 ± 1.44
KELS	-122.8960	46.1180	2.07 ± 1.08	-0.81 ± 1.09	-0.23 ± 1.38
GOBS	-120.8150	45.8390	0.86 ± 1.08	-1.55 ± 1.09	-1.10 ± 1.38
CVO1	-122.4960	45.6110	1.41 ± 1.08	0.04 ± 1.09	-0.65 ± 1.38
REDM	-121.1480	44.2600	-0.51 ± 1.08	-0.68 ± 1.09	0.65 ± 1.38
LINH	-120.5390	47.0000	-1.50 ± 1.08	-0.43 ± 1.09	2.26 ± 1.39

deformation. A point source of this type can be constructed by superimposing three collocated orthogonal point cracks (for example, Okada, 1985, 1992), with two of the cracks having equal amplitudes related to the aspect ratio w of the minor radii to the major radius of the spheroid by

$$M_0 = 1/(0.3 - 0.1w), \quad (3)$$

and the third crack having an amplitude

$$M_0 = 1/(0.4w - 0.2). \quad (4)$$

M_0 is the moment, which in this case is equivalent to volume change (the amount of opening times the area affected) multiplied by the shear modulus. If we substitute $w = 1$, then $M_0 = 5$ for the sum of all three cracks, and the source obtained is equivalent to a spherical point pressure source. Decreasing w elongates the spheroid.

A point prolate spheroidal pressure source with its long axis vertical fits the data better than do the spherical point-source models (table 10, fig. 19*B*). The best-fitting aspect ratio (0.66) and depth (7.9 km) is roughly consistent with other models of the Mount St. Helens magma chamber (Pallister and others, 1992). Only a slight improvement in the fit is obtained by adding a systematic horizontal velocity (0.2 mm/yr west, 1.4 mm/yr north), which shifts the center of the source to the southwest. The estimated velocity shift is similar to the misfit of the tectonic model to the pre-event velocity of JRO1.

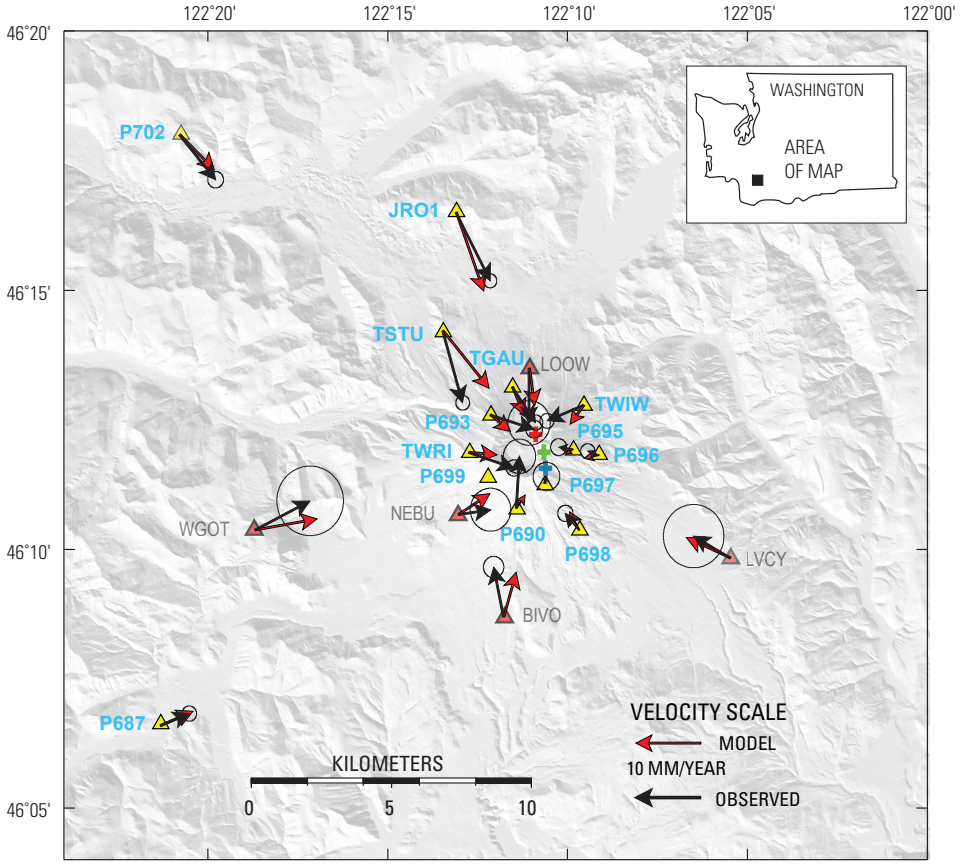

Figure 17. Map showing corrected average GPS station horizontal-velocity vectors (black arrows tipped with 95-percent-confidence error ellipses) and displacements predicted by best-fitting, tilted point prolate spheroid (red arrows, scale at bottom of figure) for the Mount St. Helens area from October 15, 2004, to October 15, 2005. See table 10 for model parameters. Surface projection of center of tilted point prolate spheroid marked by red cross, that of vertical prolate spheroid by blue cross, and that of spherical point pressure source by green cross.

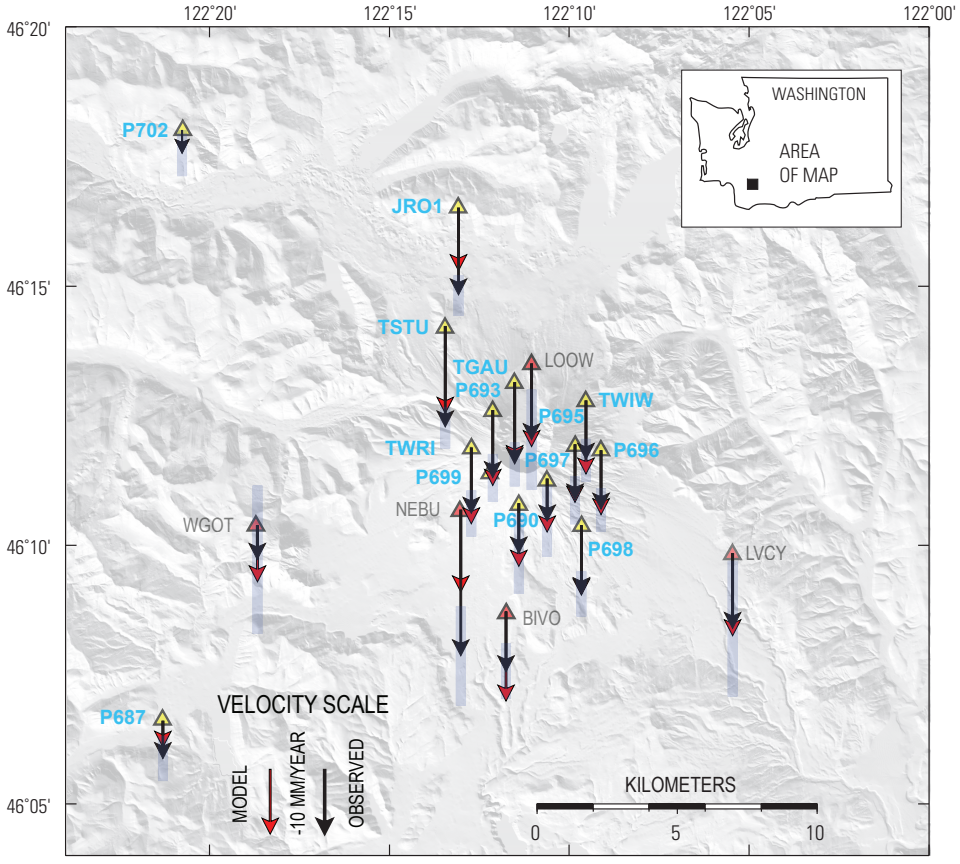

Figure 18. Map showing corrected average GPS station vertical-velocity vectors (black arrows tipped with light blue 95-percent-confidence error bar) and vertical displacements predicted by best-fitting, near-vertical, point-prolate spheroid (red arrows, scale at bottom) for Mount St. Helens area from October 15, 2004, to October 15, 2005. See table 10 for model parameters.

Another way for the model to account for asymmetry in the deformation is to allow the source to plunge at an angle less than 90º and to allow the azimuth of this axis to vary. If we do not allow for a systematic rate of translation, the parameter search returns a vertical optimal plunge. If we allow for a systematic velocity error, the best-fitting, plunging prolate source is nearly vertical (83º) with azimuth N. 37º W. (fig. 19*C*). The systematic velocity is again similar to the misfit of the tectonic model to the pre-event velocity of JRO1.

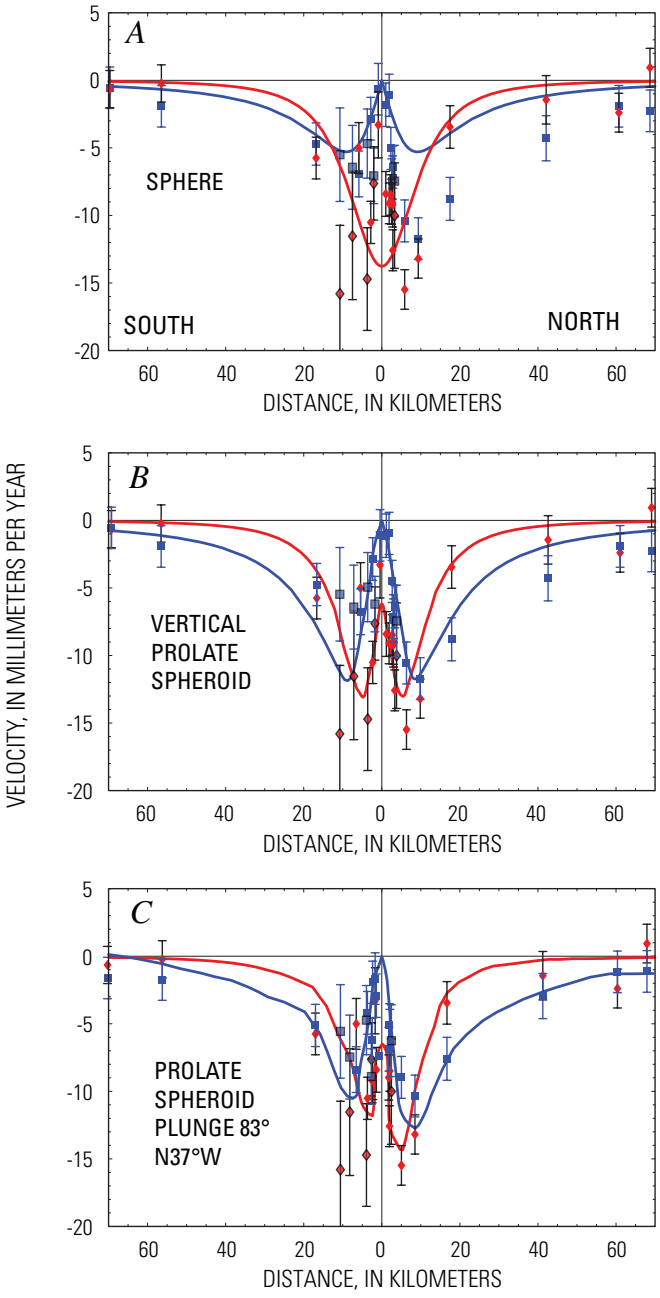

Figure 19. Observed radial (blue squares) and vertical (red diamonds) velocities for deformation of Mount St. Helens from October 15, 2004, to October 15, 2005, projected onto north-south profile and compared with predicted radial (solid blue curve) and vertical (red curve) velocities from best-fitting point sources. Error bars are ±1 standard deviation. Details of models given in table 9. *A*, spherical point pressure source; *B*, vertical point prolate spheroid; *C*, tilted or dipping point prolate spheroid with a small velocity correction.

To calculate the volume change consistent with the source strength, we assume that the spherical source has a radius of 1 km and the prolate spheroid has a minor radius of 1 km. Once the model geometry is fixed to the values obtained by the parameter search, the radius change (equivalent to strength of the source) is inverted directly. The equivalent source cavity-volume decrease for the one-year period covered by the data is in the range 8–12×10^6 m^3 in the various prolate spheroid models.

Only JRO1 recorded the relatively rapid deformation that occurred during the first two weeks of the eruption, and we use its motion as a proxy to estimate the total cavity-volume loss. The predicted 12.8 mm/yr of radially inward motion at JRO1 from the dipping prolate spheroid model with a systematic velocity correction is about half of the total movement of JRO1 from September 23, 2004, to October 31, 2006. A total cavity-volume loss of 16–24×10^6 m^3 is consistent with the JRO1 displacements, and it is a fraction of the >83×10^6 m^3 dome volume as of August 2006. Mastin and others (this volume, chap. 22) explain this discrepancy as a combination of exsolution of gas, which buffers pressure loss in the magma chamber, and recharge by new magma (recharge estimated to be only about one-tenth of the erupted volume). The recharge, if it is occurring, has thus far not increased the flux of volcanic gases (Gerlach and others, this volume, chap. 26).

Conclusions

Remarkably little far-field volcanic deformation has occurred around Mount St. Helens since shortly after the crater-forming collapse and eruption in 1980. Data collected in 1982 and 1991 for surveys of a regional high-precision trilateration network provide the clearest evidence for recharge of the volcano's magma system. During that interval, areal dilatation accumulated at an average rate of 144±39 nanostrain/yr, an order of magnitude greater than and opposite in sign to the estimated background rate of −15±3 nanostrain/yr. No significant deformation occurred in the same network between 1991 and 2000.

GPS surveys conducted since the 1990s reveal background deformation, which is used to define a tectonic model that includes a rigid-body clockwise rotation and a small amount of strain accumulation. The background strain accumulation within the network (in the absence of volcano deformation) is essentially a uniaxal contraction in the east-northeast direction, a possible effect of a locked Cascadia subduction-zone thrust fault. After removing this secular deformation, we find no coherent pattern of volcanic deformation around Mount St. Helens between 2000 and 2003. Furthermore, daily position measurements made at a CGPS

Table 10. Elastic half-space deformation source models.

[ΔEast and ΔNorth data show estimates for rigid-body translation rate that account for possible error in tectonic model. --, elements not part of solution; n.a., not applicable to long-axis trend because model is of vertical prolate geometry.]

Source description	Longitude (degrees)	Latitude (degrees)	Depth (km)	ΔRadius (m/yr)	ΔEast (m/yr)	ΔNorth (m/yr)	Aspect ratio	Long axis plunge (degrees)	Long axis (trend)	Model parameters	Reduced χ^2	ΔVolume (10^6 m^3/yr)
Spherical point pressure (Mogi)	-122.1765	46.1961	12.93	-0.7653	--	--	1.00 (fixed)	--	--	4	2.17	9.7
Spherical point pressure + translation rate	-122.1926	46.2119	10.39	-0.5028	-0.0014	0.0021	1.00 (fixed)	--	--	6	1.95	6.3
Vertical prolate spheroid	-122.1746	46.2133	7.99	-1.1485	--	--	0.66	90 (fixed)	n.a.	5	1.59	11.9
Vertical prolate spheroid + translation rate	-122.1758	46.2000	7.60	-0.9651	-0.0002	0.0014	0.673	--	n.a.	7	1.54	9.6
Tilted prolate spheroid	-122.1748	46.2133	7.94	-1.1356	--	--	0.660	90 (fixed)	n.a.	7	1.60	11.9
Tilted prolate spheroid + translation rate	-122.1811	46.2133	7.14	-0.7927	-0.0004	0.0013	0.676	82.4	N36°W	9	1.49	7.9

station 9 km north of Mount St. Helens show no anomalous deformation from 1997 until the start of seismic unrest on September 23, 2004.

The movement of magma to the surface at the start of unrest did not systematically displace GPS stations on the volcano's flanks, but it did displace station DOM1 on the September 1984 lobe of the old dome by more than 0.2 m to the north. The lack of systematic deformation around the crater suggests that solidified magma plugging the top of the conduit was pushed out, rather than being bypassed. Much of the movement of the L1 CGPS station DOM1 occurred by September 28, well before the first phreatic explosion, suggesting that the movement of magma began with the start of seismic unrest. At the same time, CGPS station JRO1 moved toward Mount St. Helens an average of about 0.5 mm/day from September 23 until a few days after the phreatic explosion on October 5, 2004, when its motion slowed and began to decay.

Analysis of eruption-related deformation data reveals a single space- and time-coherent mode of time-varying deformation, which has been decaying exponentially since the start of unrest. All GPS stations are moving toward Mount St. Helens and downward in a manner consistent with the predictions of an elastic half-space model that represents pressure loss in a vertically elongate magma chamber. The center of Mount St. Helens' magma chamber is estimated to be at a depth of 7 to 8 km, and the chamber's long axis, which is vertical or near vertical, is estimated to be approximately three times longer than its diameter. The actual dimensions of the magma chamber are poorly constrained by the deformation data. The source-cavity volume loss, which is proportional to the strength of the source, is about $16–24\times10^6$ m^3, about one-third of the erupted volume. This discrepancy can be accounted for mostly by buffering of pressure loss in the magma chamber through exsolution of gas and with a small amount of recharge (Mastin and others, this volume, chap. 22).

Acknowledgments

We thank the NSF-sponsored Plate Boundary Observatory for rapid installation of CGPS monitoring stations in October 2004 in response to renewed unrest at Mount St. Helens. In particular, we are grateful for the timely efforts of Katrin Hafner and other field engineers from UNAVCO, Inc., the contractor responsible for installing PBO stations.

We thank the CVO staff, temporary staff, and volunteers who helped with the field surveys and permanent CGPS station construction. We are grateful that Elliot Endo had the foresight to install a CGPS station at the Johnston Ridge Observatory. Richard LaHusen established telecommunications at the U.S. Forest Service's Coldwater Ridge maintenance shed in order to download CVO GPS data, and he provided L1 CGPS data. We used computer code from John Langbein of the USGS Earthquake Hazards Team to invert for best-fitting source-model parameters. The original code was developed by James C. Savage; Mark H. Murray added random-cost extensions and the Okada dislocation routines, and John Langbein added code for the ellipsoidal pressure sources. John Langbein and Larry Mastin provided constructive reviews of this paper.

References Cited

Aubrey, D.G., and Emery, K.O., 1983, Eigenanalysis of recent United States sea levels: Continental Shelf Research, v. 2, p. 21–33.

Altimimi, Z., Sillard, P., and Boucher, C., 2002, ITRF2000: A new release of the International Terrestrial Reference Frame for earth science applications: Journal of Geophysical Research, v. 107, no. B10, 2214, doi:10.1029/2001JB000561.

Berg, B., 1993, Locating global minima in optimization problems by a random-cost approach: Nature, v. 361, p. 708–710.

Blewitt, G., 1989, Carrier phase ambiguity resolution for the Global Positioning System applied to geodetic baselines up to 2000 km: Journal of Geophysical Research, v. 94, no. B8, p. 10187–10203.

Bonaccorso, A., and Davis, P.M., 1999, Models of ground deformation from vertical volcanic conduits with application to eruptions of Mount St. Helens and Mount Etna: Journal of Geophysical Research, v. 104, no. B5, p. 10531–10542.

Davis, P.M., 1986, Surface deformation due to inflation of an arbitrarily oriented triaxial ellipsoidal cavity in an elastic half-space, with reference to Kilauea volcano: Journal of Geophysical Research, v. 91, p. 7429–7438.

Davis, P.M., Hastie, L.M., and Stacey, F.D., 1974, Stresses within an active volcano, with particular reference to Kilauea: Tectonophysics, v. 22, p. 363–7438.

Demets, C., Gordon, R.G., Argus, D.F., and Stein, S., 1994, Effect of recent revisions of the geomagnetic reversal timescale on estimates of current plate motions: Geophysical Research Letters, v. 21, p. 2191–2194.

Dong, D., Herring, T.A., and King, R.W., 1998, Estimating regional deformation from a combination of space and terrestrial geodetic data: Journal of Geodesy, v. 72, p. 200–214.

Dong, D., Fang, P., Bock, Y., Cheng, M.K., and Miyazaki, S., 2002, Anatomy of apparent seasonal variations from GPS-derived site position time series: Journal of Geophysical Research, v. 107, no. B4, p. ETG 9-1–ETG 9-16.

Dong, D., Fang, P., Bock, Y., Webb, F., Prawirodirdjo, L., Kedar, S., and Jamason, P., 2006, Spatiotemporal filtering using principal component analysis and Karhunen-Loeve expansion approaches for regional GPS network analysis: Journal of Geophysical Research, v. 111, no. B03405, doi:10.1029/2005JB003806.

Dvorak, J., Okamura, A., Mortensen, C., and Johnston, M.J.S., 1981, Summary of electronic tilt studies at Mount St. Helens, *in* Lipman, P.W., and Mullineaux, D.R., eds., The 1980 eruptions of Mount St. Helens, Washington: U.S. Geological Survey Professional Paper 1250, p. 169–174.

Ewert, J.W., and Swanson, D.A., 1992, Monitoring volcanoes; techniques and strategies used by the staff of the Cascades Volcano Observatory, 1980–90: U.S. Geological Survey Bulletin 1966, 223 p.

Fialko, Y., Khazan, Y., and Simons, M., 2001, Deformation due to a pressurized horizontal circular crack in an elastic half-space, with applications to volcano geodesy: Geophysical Journal International, v. 146, p. 181–190.

Gerlach, T.M., McGee, K.A., and Doukas, M.P., 2008, Emission rates of CO_2, SO_2, and H_2S, scrubbing, and preeruption excess volatiles at Mount St. Helens, 2004–2005, chap. 26 *of* Sherrod, D.R., Scott, W.E., and Stauffer, P.H., eds., A volcano rekindled; the renewed eruption of Mount St. Helens, 2004–2006: U.S. Geological Survey Professional Paper 1750 (this volume).

Heflin, M., Bertiger, W., Blewitt, G., Freedman, A., Hurst, K., Licten, S., Lindqwister, U., Vigue, Y., Webb, F., Yunck, T., and Zumberge, J., 1992, Global geodesy using GPS without fiducial sites: Geophysical Research Letters, v. 19, no. 2, p. 131–134.

LaHusen, R.G., Swinford, K.J., Logan, M., and Lisowski, M., 2008, Instrumentation in remote and dangerous settings; examples using data from GPS "spider" deployments during the 2004–2005 eruption of Mount St. Helens, Washington, chap. 16 *of* Sherrod, D.R., Scott, W.E., and Stauffer, P.H., eds., A volcano rekindled; the renewed eruption of Mount St. Helens, 2004–2006: U.S. Geological Survey Professional Paper 1750 (this volume).

Langbein, J., Wyatt, F., Johnson, H., Hamann, D., and Zimmer, P., 1995, Improved stability of a deeply anchored geodetic monument for deformation monitoring: Geophysical Research Letters, v. 22, p. 3533–3536.

Lipman, P.W., Moore, J.G., and Swanson, D.A., 1981, Bulging of the north flank before the May 18 eruption—geodetic data, *in* Lipman, P.W., and Mullineaux, D.R., eds., The 1980 eruptions of Mount St. Helens, Washington: U.S. Geological Survey Professional Paper 1250, p. 143–155.

Magill, J., Wells, R.E., Simpson, R.W., and Cox, A.V., 1982, Post 12 m.y. rotations of southwestern Washington: Journal of Geophysical Research, v. 87, p. 3761–3776.

Mastin, L.G., Roeloffs, E., Beeler, N.M., and Quick, J.E., 2008, Constraints on the size, overpressure, and volatile content of the Mount St. Helens magma system from geodetic and dome-growth measurements during the 2004–2006+ eruption, chap. 22 *of* Sherrod, D.R., Scott, W.E., and Stauffer, P.H., eds., A volcano rekindled; the renewed

eruption of Mount St. Helens, 2004–2006: U.S. Geological Survey Professional Paper 1750 (this volume).

Mazzotti, S., Dragert, H., Henton, J., Schmidt, M., Hyndman, R., James, T., Lu, Y., and Craymer, M., 2003, Current tectonics of northern Cascadia from a decade of GPS measurements: Journal of Geophysical Research, v. 108, no. B12, 2554, doi:10.1029/2003JB002653.

McCaffrey, R., Long, M.D., Goldfinger, C., Zwick, P.C., Nabelek, J.L., Johnson, C.K., and Smith, C., 2000, Rotation and plate locking at the southern Cascadia subduction zone: Geophysical Research Letters, v. 27, no. 19, p. 3117–3120.

McTigue, D.F., 1987, Elastic stress and deformation near a finite spherical magma body; resolution of the point source paradox: Journal of Geophysical Research, v. 92, no. B12, p. 12931–12940.

Menke, W., 1984, Geophysical data analysis; discrete inverse theory: New York, Elsevier, 260 p.

Miller, M.M., Johnson, D.J., Rubin, C.M., Dragert, H., Wang, K., Qamar, A., and Goldfinger, C., 2001, GPS determination of alongstrike variation in Cascadia margin kinematics; implications for relative plate motion, subduction zone coupling, and permanent deformation: Tectonics, v. 20, p. 161–176.

Mogi, K., 1958, Relations between the eruptions of various volcanoes and the deformations of the ground surfaces around them: Bulletin of the Earthquake Research Institute of University of Tokyo, v. 36, p. 99–134.

Murray, M., and Lisowski, M., 2000, Strain accumulation along the Cascadia subduction zone; Cape Mendocino to the Straits of Juan de Fuca: Geophysical Research Letters, v. 27, p. 3631–3634.

Murray, M.H., Marshall, G.A., Lisowski, M., and Stein, R.S., 1996, The 1992 M=7 Cape Mendocino, California, earthquake; coseismic deformation at the south end of the Cascadia megathrust: Journal of Geophysical Research, v. 101, no. B8, p. 17707–17725.

Okada, Y., 1985, Surface deformation due to shear and tensile faults in a half-space: Bulletin of the Seismological Society of America, v. 75, no. 4, p. 1135–1154.

Okada, Y., 1992, Internal deformation due to shear and tensile faults in a half-space: Bulletin of the Seismological Society of America, v. 82, no. 2, p. 1018–1040.

Pallister, J.S., Hoblitt, R.P., Crandell, D.R., and Mullineaux, D.R., 1992, Mount St. Helens a decade after the 1980 eruptions; magmatic models, chemical cycles, and a revised hazards assessment: Bulletin of Volcanology, v. 54, no. 2, p. 126–146, doi: 10.1007/BF00278003.

Preisendorfer, R.W., 1988, Principal component analysis in meteorology and oceanography, *in* Mobley, C.D., ed., Developments in Atmospheric Science 17: New York, Elsevier, 425 p.

Savage, J.C., 1988, Principal component analysis of geodetically measured deformation in Long Valley caldera, eastern California: Journal of Geophysical Research, v. 93, p. 1983–1987.

Savage, J.C., 1995, Principal component analysis of interseismic deformation in southern California: Journal of Geophysical Research, v. 100, p. 12691–12701.

Savage, J.C., and Prescott, W.H., 1973, Precision of Geodolite distance measurements for determining fault movements: Journal of Geophysical Research, v. 78, p. 6001–6008.

Savage, J.C., Prescott, W.H., and Gu, G., 1986, Strain accumulation in southern California, 1973–1984: Journal of Geophysical Research, v. 91, p. 7455–7473.

Savage, J.C., Lisowski, M., and Prescott, W.H., 1991, Strain accumulation in western Washington: Journal of Geophysical Research, v. 96, p. 14493–14507.

Savage, J.C., Lisowski, M., and Prescott, W.H., 1996, Observed discrepancy between Geodolite and GPS distance measurements: Journal of Geophysical Research, v. 101, p. 25547–25552.

Savage, J.C., Svarc, J.L., Prescott, W.H., and Murray, M.H., 2000, Deformation across the forearc of the Cascadia subduction zone at Cape Blanco, Oregon: Journal of Geophysical Research, v. 105, no. B2, p. 3095–3102.

Savage, J.C., Gan, W., and Svarc, J.L., 2001, Strain accumulation and rotation in the Eastern California Shear Zone: Journal of Geophysical Research, v. 106, no. B10, p. 21995–22007.

Schilling, S.P., Thompson, R.A., Messerich, J.A., and Iwatsubo, E.Y., 2008, Use of digital aerophotogrammetry to determine rates of lava dome growth, Mount St. Helens, Washington, 2004–2005, chap. 8 *of* Sherrod, D.R., Scott, W.E., and Stauffer, P.H., eds., A volcano rekindled; the renewed eruption of Mount St. Helens, 2004–2006: U.S. Geological Survey Professional Paper 1750 (this volume).

Simpson, R.W., and Cox, A.V., 1977, Paleomagnetic evidence for tectonic rotation of the Oregon Coast Range: Geology, v. 5, p. 585–598.

Smith, K.D., von Seggern, D., Blewitt, G., Preston, L., Anderson, J.G., Wernicke, B.P., and Davis, J.L., 2004, Evidence for deep magma injection beneath Lake Tahoe, Nevada–California: Science, v. 305, no. 5688, p. 1277–1280.

Svarc, J.L., Savage, J.C., Prescott, W.H., and Murray, M.H., 2002, Strain accumulation and rotation in western Oregon and southwestern Washington: Journal of Geophysical

Research, v. 107, no. B5, 2087, doi:10.1029/2000JB000033.

Swanson, D.A., Lipman, P.W., Moore, J.G., Heliker, C.C., and Yamashita, K.M., 1981, Geodetic monitoring after the May 18 eruption, *in* Lipman, P.W., and Mullineaux, D.R., eds., The 1980 eruptions of Mount St. Helens, Washington: U.S. Geological Survey Professional Paper 1250, p. 157–168.

Verdonck, D., 2006, Contemporary vertical crustal deformation in Cascadia: Tectonophysics, v. 417, nos. 3–4, p. 221–230.

Wdowinski, S., Bock, Y., Zhang, J., Fang, R., and Genrich, J.F., 1997, Southern California Permanent GPS Geodetic Array; spatial filtering of daily positions for estimating coseismic and postseismic displacements induced by the 1992 Landers earthquake: Journal of Geophysical Research, v. 102, no. B8, p. 18057–18070.

Webb, F.H., and Zumberge, J.F., 1995, An introduction to GIPSY/OASIS-II: Pasadena, Calif., Jet Propulsion Laboratory Publication No. JPL D-11088.

Wells, R.E., and Simpson, R.W., 2001, Northward migration of the Cascadia forearc in the northwestern U.S. and implications for the subduction deformation: Earth, Planets and Space, v. 53, p. 275–283.

Wells, R.E., Weaver, C.S., and Blakely, R.J., 1998, Fore-arc migration in Cascadia and its neotectonic significance: Geology, v. 26, no. 8, p. 759–762.

Williams, S.D., Bock, Y., Fang, P., Jamason, P., Nikolaidis, R.M., Prawirodirdjo, L., Miller, M., and Johnson, D.J., 2004, Error analysis of continuous GPS position time series: Journal of Geophysical Research, v. 109, no. B03412, doi:10.1029/2003JB00274.

Yang, X., Davis, P.M., and Dieterich, J.H., 1988, Deformation from inflation of a dipping finite prolate spheroid in an elastic half-space as a model for volcanic stressing: Journal of Geophysical Research, v. 93, no. B5, p. 4289–4257.

Zumberge, J.F., Heflin, M.B., Jefferson, D.C., Watkins, M.M., and Webb, F.H., 1997, Precise point positioning for the efficient and robust analysis of GPS data from large networks: Journal of Geophysical Research, v. 102, no. B3, p. 5005–5017.

This page intentionally left blank

A Volcano Rekindled: The Renewed Eruption of Mount St. Helens, 2004–2006
Edited by David R. Sherrod, William E. Scott, and Peter H. Stauffer
U.S. Geological Survey Professional Paper 1750, 2008

Chapter 16

Instrumentation in Remote and Dangerous Settings; Examples Using Data from GPS "Spider" Deployments During the 2004–2005 Eruption of Mount St. Helens, Washington

By Richard G. LaHusen[1], Kelly J. Swinford[1], Matthew Logan[1], and Michael Lisowski[1]

Abstract

Self-contained, single-frequency GPS instruments fitted on lightweight stations suitable for helicopter-sling payloads became a critical part of volcano monitoring during the September 2004 unrest and subsequent eruption of Mount St. Helens. Known as "spiders" because of their spindly frames, the stations were slung into the crater 29 times from September 2004 to December 2005 when conditions at the volcano were too dangerous for crews to install conventional equipment. Data were transmitted in near-real time to the Cascades Volcano Observatory in Vancouver, Washington. Each fully equipped unit cost about $2,500 in materials and, if not destroyed by natural events, was retrieved and redeployed as needed. The GPS spiders have been used to track the growth and decay of extruding dacite lava (meters per day), thickening and accelerated flow of Crater Glacier (meters per month), and movement of the 1980–86 dome from pressure and relaxation of the newly extruding lava dome (centimeters per day).

Introduction

Typically, volcano monitoring and associated eruption forecasting relies on several disciplines of volcanology, principally seismology, gas geochemistry, and geodesy (Dzurisin, 2006). No single tool or technique can adequately monitor or predict the range of volcanic behaviors—from aseismic deformation to relatively benign dome building to major explosive eruptions. Accordingly, volcanologists rely on an assortment of instruments and techniques to monitor volcanic unrest. Sensors and related instrumentation have been developed in attempts to accommodate the needs of each particular discipline. However, even when an instrument is available that is capable of making a desired measurement, use of the instrument may be limited by expense or by an inability to deploy it in dangerous or inaccessible sites close to volcanic vents. New techniques and instruments are notable to volcanologists when they are affordable and minimize exposure of personnel to hazards. This paper describes the rapid development and application of a self-contained instrument package that was used successfully to monitor deformation close to the vent during the renewed eruption of Mount St. Helens in 2004–2005.

Prior Near-Vent Geodesy at Mount St. Helens

Pioneering geodetic work done during the 1980–86 eruptions of Mount St. Helens demonstrated that some eruptions could be predicted by monitoring accelerating deformation on localized parts of the dome (fig. 1; Swanson and others, 1983; Dzurisin and others, 1983). The 1980s geodetic work demonstrated that substantial preeruptive dome deformation typically was limited to areas near the active vent. The geodetic-deformation measurements commonly required the repeated and prolonged presence of personnel working close to the vent to bury electronic tiltmeters or to measure distances between fixed monuments by using electronic distance meters. Fortunately, with the subsequent availability of commercial GPS instruments, it is now possible to make repeated high-precision geodetic measurements on the volcano without exposing personnel to prolonged periods of work in hazardous areas.

Prototype GPS Instrument

For 4 years prior to the September 2004 seismic unrest at Mount St. Helens, an automated L1 GPS system was intermittently operated as a prototype monitoring tool. The system was

[1] U.S. Geological Survey, 1300 SE Cardinal Court, Vancouver, WA 98683

being developed by the U.S. Geological Survey's Cascades Volcano Observatory (CVO) as an inexpensive, near-real-time, ground-deformation monitoring tool with design emphasis on low cost, power conservation, and telemetered data integrity (LaHusen and Reid, 2000). Station DOM1 was installed on the 1980–86 dome within the crater of Mount St. Helens, and stations SFT2 and POA3 were installed outside the crater about 4 km to the west and east of DOM1, respectively. Each station was powered by a 20-W solar panel and a rechargeable lead-acid battery. Within each was a USGS microcontroller controlled remotely from a desktop computer at CVO using a 100-km multi-hop 900-MHz radio link. The operational scheme conserves power at the remote stations by alternately powering the GPS receivers and radio-telemetry components. During data-acquisition cycles, a CMC Allstar model L1 GPS receiver coupled with a Micropulse model 1372 survey-grade GPS antenna is powered for 20 minutes while raw GPS data at 10-s epochs are logged to the microcontroller. At the end of each data-logging session, the GPS receiver is switched off to conserve power, and the radio is switched on to relay data packets to CVO. Each data-transmission session lasts several minutes and includes error checking and retransmission to achieve error-free blocks of raw GPS data. The operational duty cycle is adjustable to balance power conservation, frequency of measurement, and station longevity.

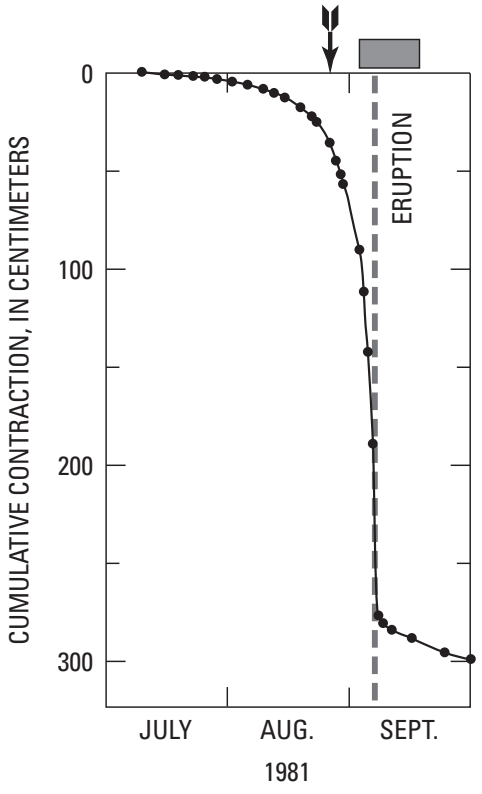

Figure 1. Movement of monument on lava dome in 1981 as determined by sequential EDM measurements, Mount St. Helens, Washington. Arrow indicates issuance of eruption prediction for time window shown by rectangular bar. Vertical dashed line shows time that dome eruption began (from Swanson and others, 1983).

Fixed, static, double-differential solutions between stations were calculated automatically using USGS control and scheduling software that applied a commercial software module, Waypoint Precise DLL. An independent position solution was calculated for every 20-minute data-acquisition period. Although GPS data acquisition within the crater posed substantial challenges owing to obscured views of the sky, mantling by rime ice, and noise from multipath reflections, this monitoring scheme typically transferred data reliably and repeatedly. The accuracy of each single solution was 1 cm plus 1 ppm of the differential baseline length (4 km), or 1.4 cm for the horizontal components. Vertical accuracy was found to be about double the horizontal value. This noise, inherent to single-frequency GPS solutions, was reduced greatly by applying a moving median filter that allowed discrimination of more subtle motions of less than a centimeter over longer time periods. Between 2002 and February 2004, the system measured dome subsidence that possibly reflected contractive cooling of the dome interior. The subsidence was at an annual rate of about 8 cm/yr downward and 2 cm/yr eastward, toward the center of the dome (fig. 2). Batteries at DOM1 failed in February 2004 and were not replaced until September.

When the GPS system was reactivated on September 27, 2004, following initiation of seismicity at Mount St. Helens, station DOM1 was in a location significantly different from what would have been predicted based on the subsidence trend of the preceding years. It was about 20 cm north and 12 cm higher than the predicted location (fig. 2). These location changes occurred between February 2004 and September 27, 2004, but we cannot further constrain the rate and timing of this deformation. Automated measurements on September 27 showed that DOM1 was moving northward at 2 cm per day. This station and a companion seismometer, the only stations on the old dome, were destroyed 4 days later, on October 1, by ballistic fragments ejected during the first phreatic explosion of the 2004 eruption (fig. 3).

GPS Spider Deployments

Loss of the only GPS station in the crater presented a dilemma because near-vent deformation could no longer be monitored. The time-consuming task of reinstalling a solar-powered GPS station onsite was considered unsafe because of the risk of additional, unpredictable phreatic explosions. Other challenges for deformation monitoring in the crater included the likelihood of additional ashfall from explosions and the impending onset of winter snowfall.

As an alternative to installing a permanent, monumented station, we assembled three GPS stations electronically similar in design to the original DOM1. However, unlike DOM1, which

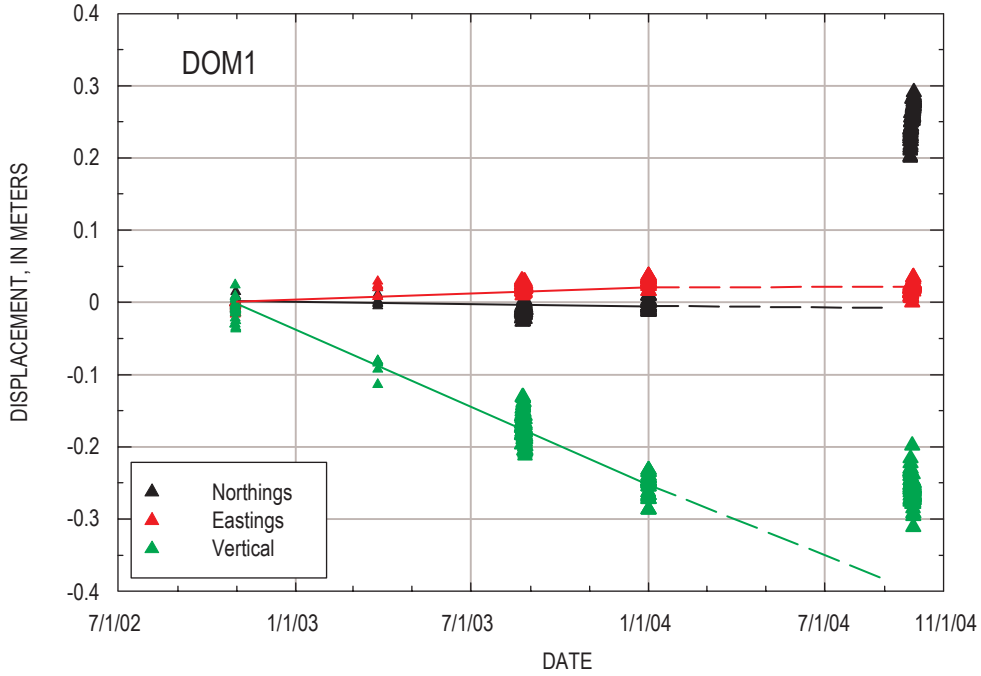

Figure 2. Time series of preeruptive deformation at GPS station DOM1, Mount St. Helens, Washington. Prior to February 2004, the 1980–86 dome was subsiding, possibly due to contraction of cooling interior. When DOM1 was reactivated on September 27, 2004, it was 20 cm north and 12 cm above its predicted location based on its previous trend (dashed lines).

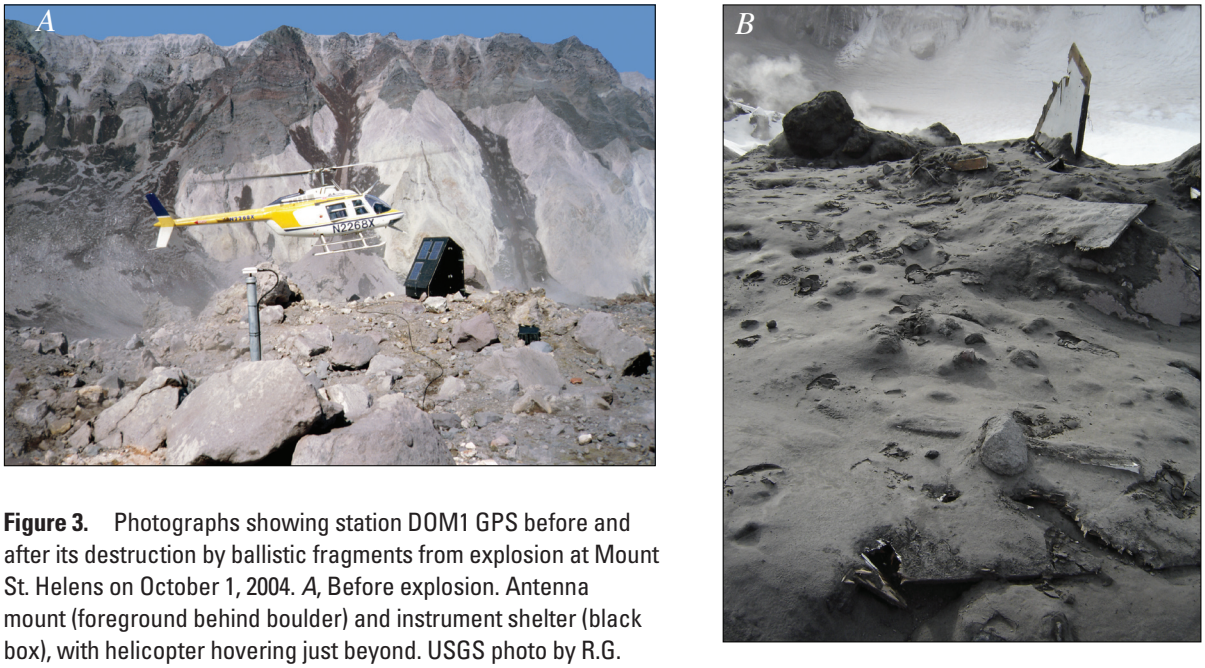

Figure 3. Photographs showing station DOM1 GPS before and after its destruction by ballistic fragments from explosion at Mount St. Helens on October 1, 2004. *A*, Before explosion. Antenna mount (foreground behind boulder) and instrument shelter (black box), with helicopter hovering just beyond. USGS photo by R.G. LaHusen. *B*, After explosion, from slightly closer viewpoint. White jagged sheet of plywood is the only side of instrument box still erect. USGS photo by S.C. Moran, November 5, 2004.

was pieced together on site, these new stations were constructed as self-contained portable units. Each unit consisted of an aluminum case that housed a 1,200-Ah supply of nonrechargeable air-alkaline batteries and a weatherproof ABS plastic case enclosing the electronic components. A GPS antenna was attached to a 1.5-m-long steel pipe mast on one end of the aluminum case, and a similar mast on the other end supported a radio antenna. A rope sling with a swivel eye was bolted to the outer metal case for attachment to a helicopter sling-cable remote-release hook. Each of these three stations weighed approximately 70 kg, and parts for each unit cost about $2,500, making it practical to deploy several stations and constituting an acceptable loss if a station were destroyed. With this design, stations could be set in the crater near the source of the recent explosion, and personnel would be exposed only briefly to potential hazards. Initial results from these portable installations were promising, demonstrating that GPS stations could be installed quickly to provide repeatable results at centimeter accuracy in near-real time. One unit toppled shortly after deployment, so we redesigned the frame with three widely spaced legs for better stability on rocky, uneven terrain.

Spider Frame Design

Field tests of several frame prototypes helped to determine design requirements and constraints. These included the need for a frame that was: (1) strong and rigid for its weight, (2) corrosion resistant, (3) relatively inexpensive and simple to build, (4) capable of accommodating various onboard electronic instruments and antennas, (5) capable of being slung safely beneath a helicopter, (6) capable of deployment by helicopter sling cable onto uneven and rocky terrain, (7) stable when placed on uneven and rocky terrain, and (8) capable of being retrieved by grappling hook from a helicopter for redeployment to another site or transport to a safe location to replace batteries.

Using these design considerations, we constructed 18 frames at CVO (fig. 4). The frames were built of type 6061 stainless steel square tubing with 1.6-mm-thick walls and a 38×38-mm cross section. The tubing was cut with a horizontal band saw and welded using stainless steel welding wire.

The large leg span (1.4 m) of the three-legged frames and the low center of gravity of the welded aluminum battery and electronics box (0.34 m above ground surface) provided a stable platform for the onboard batteries and electronics. The GPS antenna was mounted to one of the three framing legs that extended higher than the other two, 1.7 m from the ground. A short leg served as a mount for a 1-m-long omnidirectional antenna for the data transceiver.

A pyramidal stainless steel tripod canopy of the same tubular material was welded to the legs, culminating 1.8 m above the ground where a lifting eye, cable, and swivel were attached. In addition to strengthening the frame, this canopy provided a centered attachment point for airborne transport and presented a large, open target for helicopter retrieval using a grappling hook. With the addition of the spindly-legged framework, these self-contained stations took on the appearance and nickname of "spiders."

The spider is stable when in flight beneath a helicopter, and the low center of gravity and wide leg span make the station resistant to tipping during deployment and retrieval, as well as resistant to toppling by high winds after deployment. Over the first 18 months of use, the stainless steel frames did not deteriorate in the harsh volcanic environment except for damage from direct ballistic impact. During 2004–5, we experimented with additional instruments on board some spiders including tiltmeters, cameras, gas sensors, and seismic accelerometers (McChesney and others, this volume, chap. 7).

Examples of GPS Spiders at Mount St. Helens, 2004–2005

GPS Spiders on the 1980–86 Dome

Remotely placed GPS spiders have occupied five sites on the 1980–86 dome. These sites were about 400–500 m from

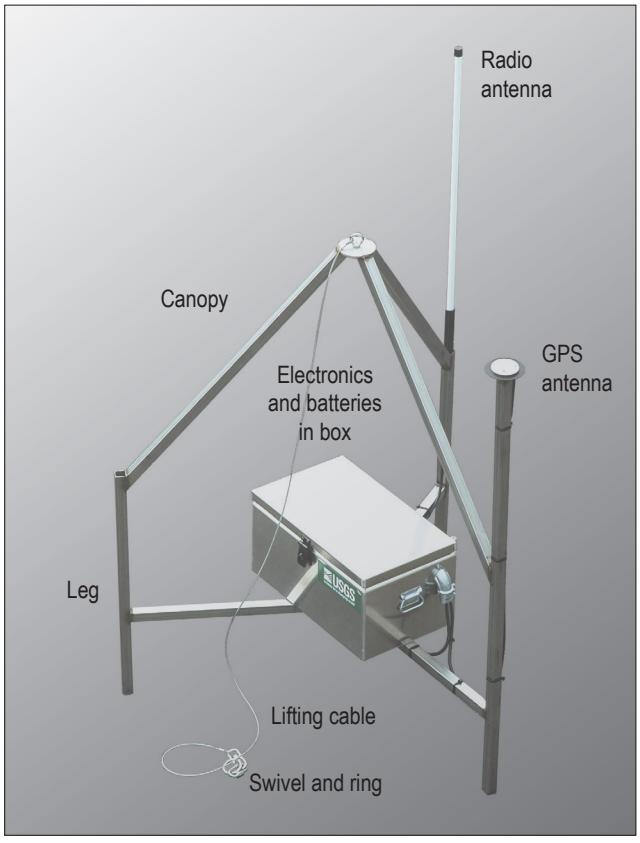

Figure 4. Photograph of GPS spider with stainless steel leg and canopy framework (leg span, 1.4 m) and aluminum box housing the unit's electronics and batteries. GPS antenna is located on extended leg in right foreground, and data radio antenna is attached to right rear leg. Stainless steel lifting cable with swivel and ring is attached to top of canopy. USGS photo by M. Logan.

Table 1. History of GPS spider deployments in the crater of Mount St. Helens, Washington, 2004–2005.

Station	Start date	End date	Displacement (m)	Fate
1980–86 dome				
DOM1.0 [1]	9/27/04	10/1/04	--	Explosion October 1, 2004
NDM5	10/3/04	1/2/05	0.15	Toppled, recovered
NRM6	10/4/04	11/20/04	--	Toppled, recovered
TOP7	10/4/04	3/8/05	--	Explosion March 8, 2005
DOM1.1	11/6/04	3/8/05	0.4	Explosion March 8, 2005
NEDB	11/20/04	3/8/05	0.16	Explosion March 8, 2005
DOM1.2	3/10/05	8/5/05	0.1	Moved
NEDB.1	4/6/05	3/2/06	0.1	Batteries expired
DOM1.3	8/5/05	12/25/05	0.05	Batteries expired
HIE5.2	9/21/05	12/31/05+	0.05	Continued operating into 2006
Middle zone				
MID9.0	10/27/04	2/3/05	1.4	Explosion damage Jan. 16, 2005
MIDE.0	2/11/05	3/8/05	0.22	Explosion March 8, 2005
MID9.1	4/6/05	6/29/05	2.3	Removed
MID9.2	11/17/05	12/16/05	0.17	Buried by talus
New dome				
CLF4	10/27/04	1/21/05	48	Rockfall
ELEA.0	11/20/04	11/27/04	67	Rockfall
HNY0	1/3/05	1/29/05	78	Rockfall
CDAN	1/15/05	1/16/05	8	Explosion Jan. 16, 2005
AHAD	2/8/05	2/16/05	41	Removed
ELE4.0	4/19/05	4/21/05	2	Moved
SEV7	5/24/05	3/24/06	10	Batteries expired
East Crater Glacier				
ICY4	2/16/05	4/8/05	22	Lost in crevasse
ICY5.0	2/16/05	3/8/05	28	Explosion March 8, 2005
ELE4.1	4/21/05	6/30/05	26	Moved
ELE4.2	6/30/05	7/28/05	6.7	Moved
HIE5.0	7/18/05	8/19/05	8.5	Moved
ELE4.3	7/28/05	8/19/05	7.8	Moved
West Crater Glacier				
WES6	7/14/05	9/14/05	70	Removed
ELE4.4	8/19/05	11/9/05	122	Batteries expired
HIE5.1	8/19/05	9/14/05	24	Moved

[1] Permanent monumented station; restarted Sept. 27, 2004.

the center of September 2004 deformation, ensuing phreatic explosions, and lava-spine extrusion. The history of emplacement and subsequent life is summarized in table 1; distribution and mapped progression is shown in figure 5.

The first three portable GPS stations were set on the north, east, and approximate center of the 1980–86 dome on October 3 and 4, 2004; station designations were NDM5, NRM6, and TOP7, respectively. Results from these installations showed that (1) motion of the three stations was similar, indicating the relative stability of the remotely deployed packages, and (2) the northward movement of the 1980–86 dome was continuing and was not restricted to the area of DOM1 on the west side of the dome. The 1980–86 dome lay north of the vent, so these spiders typically moved slightly northward. It appeared that the entire 1980–86 dome was moving to the north, away from the vent area, as if it were being shouldered aside in response to the growing mass beneath its south flank. Consequently, the northing component of the GPS solution best depicts the predominant motion. Magnitude of total motion during this period was less than 1 m (fig. 6). Rates were as much as 2 cm per day northward. Vertical displacement was typically within the noise of the analysis.

The 1980–86 dome appeared to behave as a semicoherent block so that, with few exceptions, spiders at different sites responded similarly (fig. 6). The rate of displacement varied with time. The limited evidence suggests that the rate of old-dome movement varied directly with the linear extrusion rate of the new dome, as shown by the coincidence of highest 1980–86 dome displacement rates with the greatest velocity for spiders riding on the extruding spine (fig. 6). We were

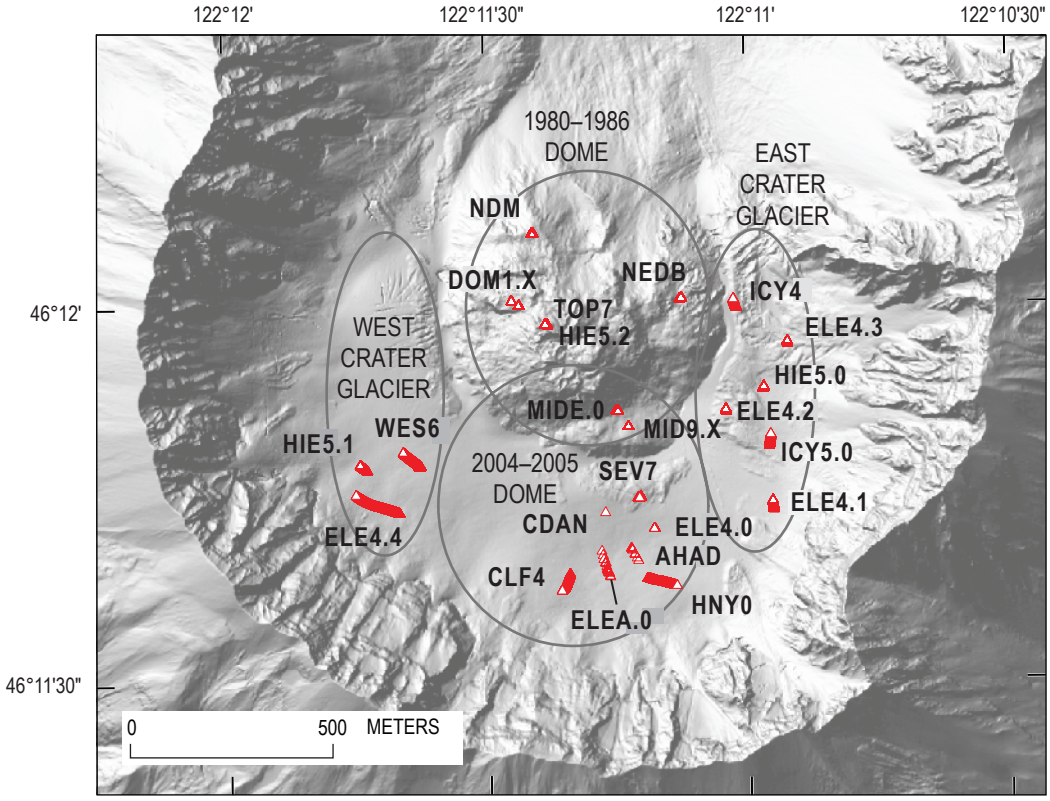

Figure 5. Shaded-relief digital elevation model (2003) showing GPS spider deployments (red triangles) in crater of Mount St. Helens, Washington. Tracks of triangles indicate total movement of stations (table 1).

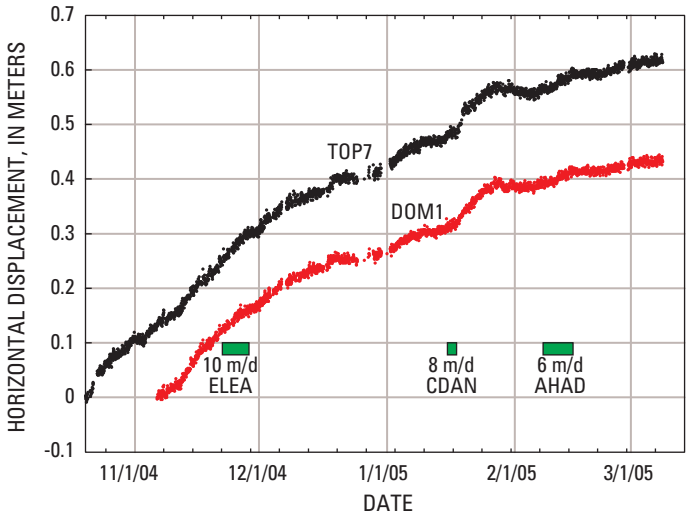

Figure 6. Graph showing movement of two GPS spiders on 1980–86 dome (DOM1, TOP7) and three GPS spiders on 2004–5 dome (ELEA, CDAN, and AHAD) during first 5 months of eruption. Location of stations shown in figure 5. The green boxes show duration of new-dome spiders, each labeled with elapsed horizontal velocity, which was nearly halved from November 2004 to March 2005. These three spiders had substantial displacements (as much as 67 m over a 7-day period for ELEA), which makes it difficult to portray their data in a manner comparable to the old-dome spiders TOP7 and DOM1.

unable to maintain a spider on the extruding spine long enough to demonstrate this relation more convincingly.

Intermittently, velocity of GPS spiders on the old dome increased as the rate of seismicity increased, as measured by real-time seismic amplitude measurements, or RSAM (Endo and Murray, 1991; Moran and others, this volume, chap. 2). One example of this correlation occurred on January 15, 2005, when TOP7 and other near-vent stations accelerated away from the vent as RSAM values started to increase (fig. 7). An explosion the following day destroyed several spiders (table 1).

GPS Spiders on the New Dome

Measurements of extrusive rates are the most effective way to monitor the progress of effusive eruptions. The best day-to-day proxy for extrusive rate at Mount St. Helens was the linear rate at which lava emerged from the vent; thus, we first targeted sites on and immediately adjacent to the actively extruding dome. Prior to new lava appearing at the surface on October 11, 2004, intense surface deformation created an uplift of part of the 1980–86 dome, deformed glacier ice, and crater-floor debris, or the "welt," through which the first lava spines emerged (Vallance and others, this volume, chap. 9). Sites on the welt had the advantage of longevity compared to placement directly on the active lava spines and were used first in October 2004. Although not directly on the extruding lava, these spiders were useful as proxies of eruption vigor because they were being actively pushed away from the vent. By late November 2004, we began placing spiders directly astride the actively extruding lava spine.

The first spider was set on the welt adjacent to the northeast side of the new dome on October 12, 2004, but its GPS antenna was damaged on deployment, rendering it geodetically useless. The spider also had seismic instrumentation on board that continued to function (McChesney and others, this volume, chap. 7). The next GPS spider, station CLF4, was installed on October 27, adjacent to the south flank of newly emergent spine 3, on uplifted crater-floor debris of the welt (fig. 5; table 1). Station CLF4 moved downward and to the south, traveling 10 m in the first three days as spine 3 plowed across the crater floor. Station CLF4 was pushed away from the growing spine as if riding the bow wave of a ship. It operated for 85 days, outliving the growth period of spine 3 and persisting into the first third of spine 4's life before succumbing to rockfall.

Some of the most interesting correlations between eruptive phenomena and movement of GPS spiders came from site MID9, which was on the saddle midway between the new and old domes (figs. 5, 8). On November 12, November 22, and December 8, 2004, MID9.0, the first of the MID9 spiders (table 1), accelerated away from the vent (fig. 9) coincident with increased RSAM counts. These velocity changes appeared as surge-pause-surge phases that lasted several days. The correlation with RSAM was masked for some other events that occurred in stormy weather, owing to heightened seismic noise that accompanied high wind.

On December 21, MID9.0 stalled and slowly reversed direction, heading back toward the vent and downward (figs. 9, 10). This change may have been in response to depressurization within the conduit and relaxation at the surface. Other crater GPS stations also slowed or stopped moving away from the vent. This event coincided with a change in seismicity, during which several large earthquakes had downward first motions as opposed to the typical pattern of upward first motions (S. Malone, written commun., 2004). But station MID9.0 continued its southward and down motion into 2005 while extrusion continued, so a more likely explanation for the ventward motion is that vent-adjacent bedrock was shifting in response to some other factor. Because this area between the

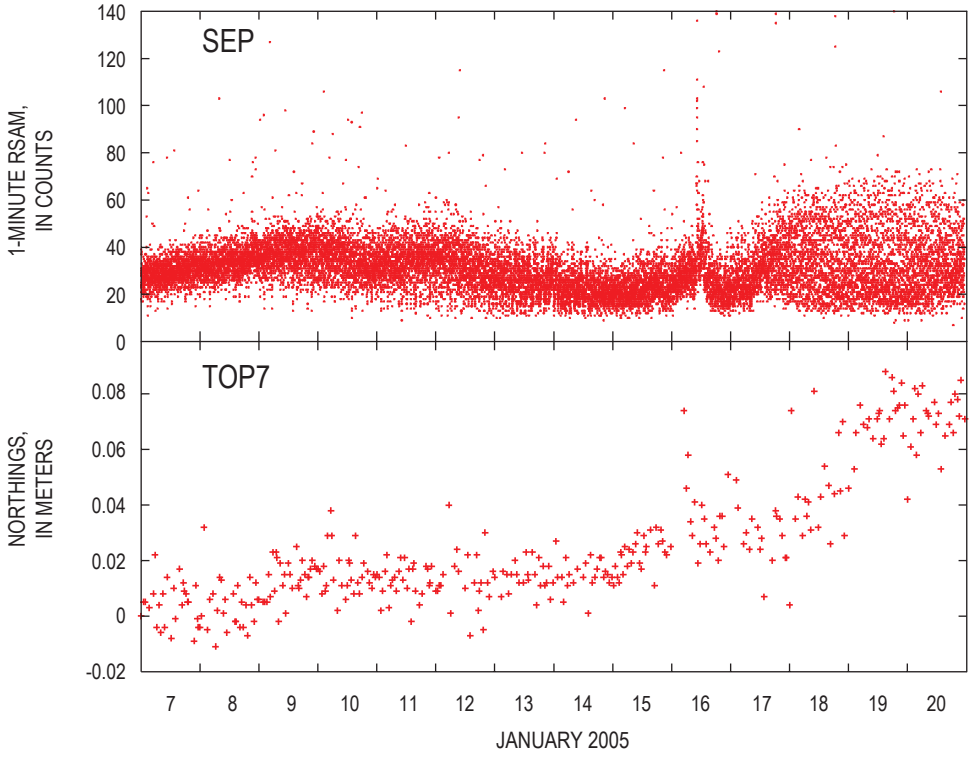

Figure 7. Graphs showing relation between increases in real-time seismic amplitude (RSAM) and northward motion of station TOP7 in mid-January 2005. Seismic station SEP is located 100 m northwest of TOP7, on the September lobe of the 1980–86 dome.

domes was so responsive to changes in eruption dynamics, we tried to keep a functioning GPS spider near the original MID9.0 location. Accordingly, after MID9.0 suffered antenna damage in an explosion on January 16, it was replaced by MIDE.0 followed by MID9.1 and MID9.2 (table 1).

On November 20, spider ELEA.0 was placed on the highest point of spine 3 (fig. 5). Its initial motion was an astonishing 10 m per day. Before it was destroyed by a rockfall 6 days later, ELEA.0 had moved 67 m south-southeastward and 8 m up.

The remarkable record of ELEA.0 reinforced our decision to keep a GPS spider on the actively growing spine of the new dome. A GPS spider, especially one carrying an accelerometer (seismometer), could add substantially to the amount of data available for evaluating steady-state extrusion models and for locating seismic sources more precisely. The task of slinging spiders onto hot lava spines proved more difficult than expected, owing to turbulence and decreased lift in heated air. Thermal surveys showed surface temperatures of spines away from the vent typically were less than 50°C, but cracks exposed interior lava as hot as 700°C (Vallance and others, chap. 9; Schneider and others, this volume, chap. 17) and created strong hot updrafts. A successful installation on January 3, 2005, deployed spider HNY0 (Happy New Year) on a large block near the south end of spine 4 (fig. 5). For more than 3 weeks, spider HNY0 moved 2–2.5 m/day east-southeastward, consistent with eastward spreading as the south end of the spine broke apart.

Figure 8. January 2005 photograph of station MID9 site (red box) between 1980–86 dome on the right and snow-free spine 4 on the left. Vent is marked by smooth emergent lava spine. Ground on which MID spiders were deployed was warm and was chosen to reduce burial by snow. USGS photo by D. Dzurisin, January 3, 2005.

Because spine 4's surface rose steeply from the vent, we built a spider with legs of differing length, cut appropriately to match the spine's 32° slope. This spider, CDAN, held fast in the soft fault gouge that mantled the spine (fig. 11). However, station CDAN was toppled and buried in talus during an explosion on the day after its installation, but not before it had moved about 8 m southward and upward (table 1).

Spiders were sited on the active spine sporadically into 2006 (table 1). Spines 5–7 grew more vertically than their recumbent predecessors and became increasingly mantled by talus, preventing us from finding sites suitable for setting a spider. Sites in talus were notably perilous, owing not only to instability of blocks on which spiders could be placed, but also to destruction by rockfalls from upslope debris. Summits of spines were free of risk from rockfall, but unlike the earlier recumbent spines that extended hundreds of meters from the vent—the site of greatest heat discharge—spines 5–7 grew more steeply, formed smooth surfaces for relatively short distances, and produced mostly rubble and large flanking talus aprons. Consequently, the summits of spines 5–7 were too hot and the air there too turbulent to safely deploy the instruments.

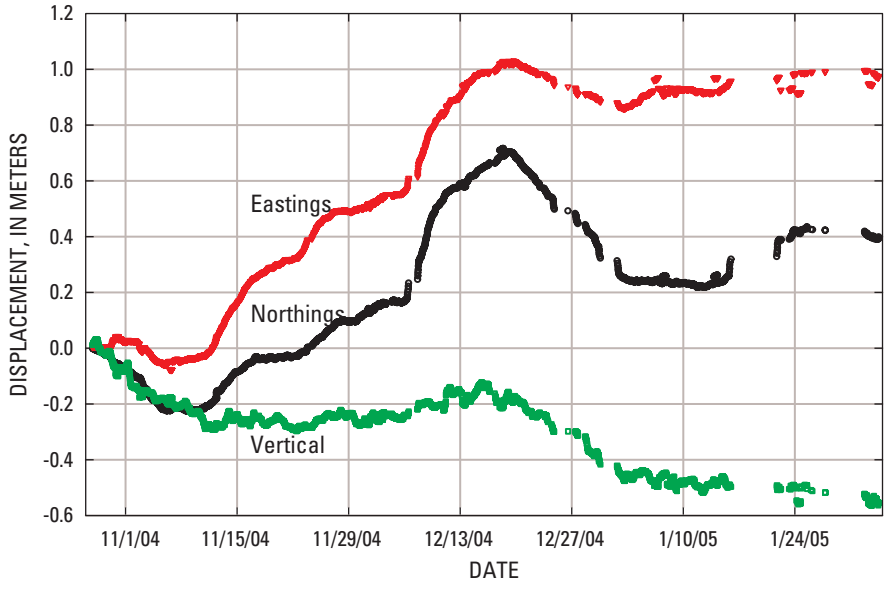

Spiders on Crater Glacier

Throughout the 2004–5 eruption, lava-dome growth through formerly horseshoe-shaped Crater Glacier has caused dramatic disruption and deformation (Walder and others, this volume, chap. 13). This remarkable process was documented with intermittent aerial photographs and creation of digital elevation models (Schilling and others, this volume, chap. 8), albeit with some

Figure 9. Graph of displacement of MID9.0 GPS spider, indicating accelerations, decelerations, and reversals as this near-vent station responded to subtle changes in eruption dynamics.

difficulty owing to the lack of persistently identifiable features on the glacier surface. Those GPS spiders placed on the glacier provided a more continuous record of glacial deformation that allowed detailed examination of glacier compression, thickening, and increased rate of flow. Initially, growth of the welt and lava extrusions affected the southeastern part of the crater, cleaving Crater Glacier into east and west arms and compressing the east arm against the crater wall. Visual observations of this process indicated that the east arm was being greatly thickened. In response, the flow rate appeared to accelerate as a bulging lobe advanced northward toward the glacier's terminus east of the old lava dome. This deformation was accompanied by pervasive fracturing of the glacier with the formation of deep crevasses and, ultimately, extensive fields of seracs. In order to quantify these phenomena, several spiders were deployed temporarily on the glacier in nine locations between February and August 2005 (table 1).

Spiders ICY4 and ICY5.0 were installed on the east arm of Crater Glacier on February 16, 2005. Spider ICY5.0 was placed on the thickened and bulging part of the glacier, and ICY4 was placed on the relatively undisrupted part downslope of the bulge. Resultant velocity measurements from ICY4 showed the upper part of the glacier was moving 1.4 m/d and the lower undisturbed part was moving only 0.4 m/d. Of particular interest was the lack of diurnal velocity changes that typify temperate glaciers, indicating that Crater Glacier has a permeable bed that precludes basal slip resulting from meltwater accumulation (Walder and others, this volume, chap. 13). Additional spiders placed on the east and west arms confirmed these observations (table 1).

When dome growth shifted westward in midsummer 2005, the west arm of Crater Glacier started to show signs of bulging and crevassing, so in July and August 2005 a series of spider deployments was begun in order to collect data necessary to track changes. Stations WES6, ELE4.4 and HIE5.1 showed velocities of 1 m/d or more (fig. 12). Of particular interest was the stations' utility as an indirect confirmation of continuing lava extrusion because their instruments indicated continued upward motion as the advancing lava compressed the glacier against the crater wall. In times of limited visibility when remote cameras were ineffective, these spiders were our only means of confirming continuing dome growth. Their utility was limited by the occasional need to move them away from widening crevasses in the summer and by their inability to function under accumulation of several meters of snow during winter months.

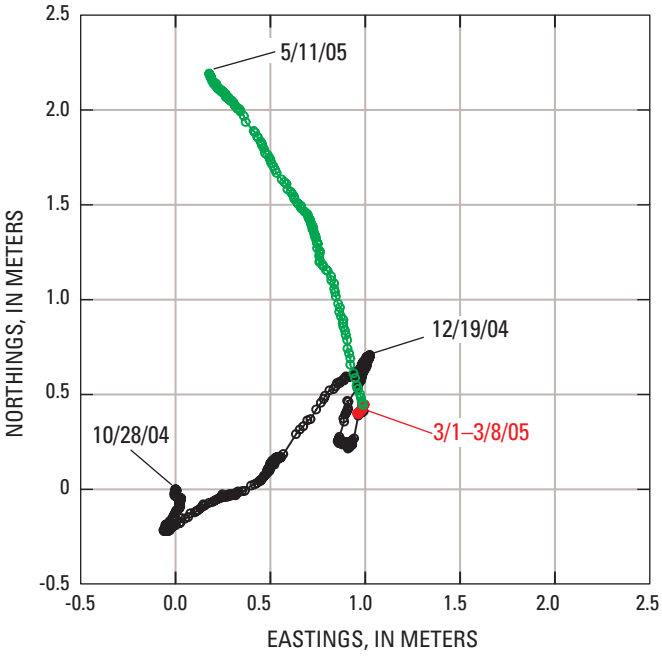

Figure 10. Schematic map showing horizontal path of three sequentially placed GPS spiders as they moved from the initial MID site. Site was alternately pushed away or relaxed toward the vent area during the course of deployment. Vent lay about 200 m southwest of MID. Change of symbol colors is solely to clarify the trace of displacement path.

Conclusions

During the 2004–5 eruption of Mount St. Helens, portable GPS stations, nicknamed spiders, installed by helicopter-sling operations proved to be an invaluable volcano-monitoring tool at sites in hazardous settings or where landing a helicopter was not possible. With real-time telemetry of data, spiders transmitted day and night. Cloudy weather that obscured camera images had no effect on the monitoring capability of GPS spiders. Although seismicity has become the most widely used real-time tool to detect explosive eruptions, real-time deformation monitoring may be equally or

Figure 11. Mid-January 2005 photograph of station CDAN GPS spider on extruding spine 4. Legs of differing lengths permitted level deployment on 32° slope. Legs are embedded several centimeters into soft gouge that mantles spine. USGS photo by J.S. Pallister, January 14, 2005.

more valuable to track dome-building eruptions. At present, nothing demonstrates ongoing extrusion of lava as directly as a GPS receiver riding on an active spine. Costing about $2,500 each in materials, spiders can be built relatively quickly and deployed in numbers needed to obtain data that provide a detailed record of near-vent deformation, lava extrusion, and effects on adjacent glaciers.

Acknowledgments

Our success with spiders stems in part from highly skilled helicopter pilots. In particular Jeff Linscott of JL Aviation and Morgan Kozloski of Hillsboro Aviation have carried greatest responsibility for installing and retrieving equipment. We gratefully acknowledge manuscript reviews by Tom Murray and Mark Reid.

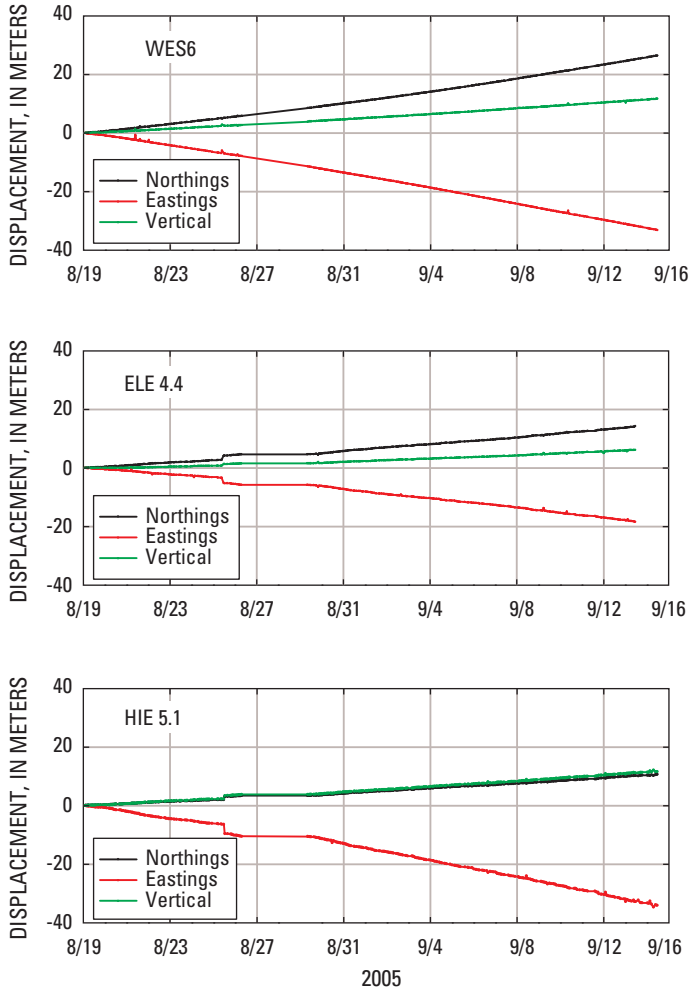

Figure 12. Plot of three GPS spiders on west arm of Crater Glacier during summer 2005, showing similar uplift and motion away from the advancing lava dome as the glacier was compressed against crater wall. Site locations shown in figure 5.

References Cited

Dzurisin, D., ed., 2006, Volcano deformation—geodetic monitoring techniques: Berlin, Springer, Springer-Praxis Books in Geophysical Sciences, 441 p.

Dzurisin, D., Westphal, J.A., and Johnson, D.J., 1983, Eruption prediction aided by electronic tiltmeter data at Mount St. Helens: Science, v. 221, no. 4618, p. 1381–1383.

Endo, E.T., and Murray, T., 1991, Real-time seismic amplitude measurement (RSAM); a volcano monitoring tool: Bulletin of Volcanology, v. 53, no. 7, p. 533–545.

LaHusen, R.G., and Reid, M.E., 2000, A versatile GPS system for monitoring deformation of active landslides and volcanoes [abs.]: Eos (American Geophysical Union Transactions), v. 81, no. 48, p. F320.

McChesney, P.J., Couchman, M.R., Moran, S.C., Lockhart, A.B., Swinford, K.J., and LaHusen, R.G., 2008, Seismic-monitoring changes and the remote deployment of seismic stations (seismic spider) at Mount St. Helens, 2004–2005, chap. 7 *of* Sherrod, D.R., Scott, W.E., and Stauffer, P.H., eds., A volcano rekindled; the renewed eruption of Mount St. Helens, 2004–2006: U.S. Geological Survey Professional Paper 1750 (this volume).

Moran, S.C., Malone, S.D., Qamar, A.I., Thelen, W.A., Wright, A.K., and Caplan-Auerbach, J., 2008, Seismicity associated with renewed dome building at Mount St. Helens, 2004–2005, chap. 2 *of* Sherrod, D.R., Scott, W.E., and Stauffer, P.H., eds., A volcano rekindled; the renewed eruption of Mount St. Helens, 2004–2006: U.S. Geological Survey Professional Paper 1750 (this volume).

Schilling, S.P., Thompson, R.A., Messerich, J.A., and Iwatsubo, E.Y., 2008, Use of digital aerophotogrammetry to determine rates of lava dome growth, Mount St. Helens, Washington, 2004–2005, chap. 8 *of* Sherrod, D.R., Scott, W.E., and Stauffer, P.H., eds., A volcano rekindled; the renewed eruption of Mount St. Helens, 2004–2006: U.S. Geological Survey Professional Paper 1750 (this volume).

Schneider, D.J., Vallance, J.W., Wessels, R.L., Logan, M., and Ramsey, M.S., 2008, Use of thermal infrared imaging for monitoring renewed dome growth at Mount St. Helens, 2004, chap. 17 *of* Sherrod, D.R., Scott, W.E., and Stauffer, P.H., eds., A volcano rekindled; the renewed eruption of Mount St. Helens, 2004–2006: U.S. Geological Survey Professional Paper 1750 (this volume).

Swanson, D.A., Casadevall, T.J., Dzurisin, D., Malone, S.D.,

Newhall, C.G., and Weaver, C.S., 1983, Predicting eruptions at Mount St. Helens, June 1980 through December 1982: Science, v. 221, no. 4618, p. 1369–1376.

Vallance, J.W., Schneider, D.J., and Schilling, S.P., 2008, Growth of the 2004–2006 lava-dome complex at Mount St. Helens, Washington, chap. 9 *of* Sherrod, D.R., Scott, W.E., and Stauffer, P.H., eds., A volcano rekindled; the renewed eruption of Mount St. Helens, 2004–2006: U.S. Geological Survey Professional Paper 1750 (this volume).

Walder, J.S., Schilling, S.P., Vallance, J.W., and LaHusen, R.G., 2008, Effects of lava-dome growth on the Crater Glacier of Mount St. Helens, Washington, chap. 13 *of* Sherrod, D.R., Scott, W.E., and Stauffer, P.H., eds., A volcano rekindled; the renewed eruption of Mount St. Helens, 2004–2006: U.S. Geological Survey Professional Paper 1750 (this volume).

This page intentionally left blank

A Volcano Rekindled: The Renewed Eruption of Mount St. Helens, 2004–2006
Edited by David R. Sherrod, William E. Scott, and Peter H. Stauffer
U.S. Geological Survey Professional Paper 1750, 2008

Chapter 17

Use of Thermal Infrared Imaging for Monitoring Renewed Dome Growth at Mount St. Helens, 2004

By David J. Schneider[1], James W. Vallance[2], Rick L. Wessels[1], Matthew Logan[2], and Michael S. Ramsey[3]

Abstract

A helicopter-mounted thermal imaging radiometer documented the explosive vent-clearing and effusive phases of the eruption of Mount St. Helens in 2004. A gyrostabilized gimbal controlled by a crew member housed the radiometer and an optical video camera attached to the nose of the helicopter. Since October 1, 2004, the system has provided thermal and video observations of dome growth. Flights conducted as frequently as twice daily during the initial month of the eruption monitored rapid changes in the crater and 1980–86 lava dome. Thermal monitoring decreased to several times per week once dome extrusion began. The thermal imaging system provided unique observations, including timely recognition that the early explosive phase was phreatic, location of structures controlling thermal emissions and active faults, detection of increased heat flow prior to the extrusion of lava, and recognition of new lava extrusion. The first spines, 1 and 2, were hotter when they emerged (maximum temperature 700–730°C) than subsequent spines insulated by as much as several meters of fault gouge. Temperature of gouge-covered spines was about 200°C where they emerged from the vent, and it decreased rapidly with distance from the vent. The hottest parts of these spines were as high as 500–730°C in fractured and broken-up regions. Such temperature variation needs to be accounted for in the retrieval of eruption parameters using satellite-based techniques, as such features are smaller than pixels in satellite images.

Introduction

Detection and measurement of elevated temperature can play an important role in understanding the processes involved with active volcanic processes. As magma moves into a volcano, an increase in surface heat flow may occur that is manifested by various phenomena, such as increases in fumarole temperatures, opening of new fumaroles, development of hot faults and fractures, increases in hot spring and crater lake temperatures, and melting of snow and ice. Once an eruption begins there are numerous potential heat sources such as eruption columns, lava lakes, lava domes, lava flows, and pyroclastic-flow deposits. Analysis of thermal data can provide a means to detect unrest, observe phenomena not discernible at visible wavelengths, see through thin cloud cover and steam, and track changes in eruption style and eruption volume.

Thermal data are acquired at a variety of spatial and temporal resolutions: (1) low spatial resolution (kilometer scale) from high temporal resolution (multiple images per day) satellite sensors such as GOES, AVHRR, and MODIS (Dehn and others, 2002; Harris and others, 1997; Wright and others, 2002); (2) moderate spatial resolution (tens of meters) from low temporal resolution (weekly or greater) satellite sensors such as ASTER and Landsat TM/ETM+ (Flynn and others, 2001; Ramsey and Dehn, 2004; Vaughan and others, 2005); and (3) high spatial resolution (meter scale) from airborne or ground-based thermal imaging radiometers deployed on a tactical basis. This study focuses on an application of the latter—high-resolution thermal monitoring of eruptive activity at Mount St. Helens during October and November 2004.

The use of thermal imaging radiometers for monitoring volcanic activity has increased greatly over the past 5 years. A new generation of instruments that has entered the commercial marketplace utilizes detector arrays without external cooling (such as liquid nitrogen), thereby simplifying field logistics and increasing portability. These instruments provide calibrated temperature images and are useful in such applications

[1] U.S. Geological Survey, 4200 University Drive, Anchorage, AK 99508

[2] U.S. Geological Survey, 1300 SE Cardinal Court, Vancouver, WA 98683

[3] Department of Geology and Planetary Science, University of Pittsburgh, 200 SRCC Building, Pittsburgh, PA 15260

as detecting heated fractures prior to lava eruption (Andronico and others, 2005) or flank collapse (Calvari and others, 2005), estimation of lava effusion rate (Harris and others, 2005a), and study of eruption dynamics (Harris and others, 2005b; Patrick and others, 2007).

The reawakening of Mount St. Helens in September 2004 began with a swarm of shallow earthquakes on September 23 (Moran and others, this volume, chap. 2) and progressed to deformation and cracking of glacier ice on the crater floor south of the 1980–86 dome to form the so-called welt, which was first observed on September 26 (Dzurisin and others, this volume, chap. 14). In response to this unrest, thermal-image monitoring began on October 1, 2004, to establish baseline thermal imagery and to examine the 1980–86 dome for signs of deformation. This paper reports results of the thermal surveys conducted during the first 2 months of activity during vent clearing and early stages of dome extrusion from October to December 2004. Thermal monitoring has continued throughout the eruption and has aided in the analysis of subsequent dome growth (Vallance and others, this volume, chap. 9).

Instrumentation and Methodology

The imaging system used in this study comprises a FLIR Systems ThermaCAM™ PM595 infrared camera and a Sony EVI-370 (visual-wavelength) video camera housed in a four-axis gyrostabilized gimbal that is mounted to the nose of a Bell-206 helicopter (fig. 1*A*). Although these types of thermal imaging cameras are generally referred to as FLIR, for Forward Looking Infrared, the gimbal can rotate in any direction. A crew member controls gimbal orientation and camera operation with a remote control (fig. 1*B*). The infrared camera utilizes a 320×240 microbolometer array that detects long-wave thermal radiation in the 7.5–13-µm atmospheric window and converts these values to brightness temperature. A 12°-wide telephoto lens provides a horizontal field of view of 210 m and a pixel resolution of 1.5 m at a distance of 1,000 m. Temperature is measured in three ranges: –40–200ºC, 30–800ºC, and 350–1,500ºC. An internal flash memory card stores data from the infrared camera at 14-bit resolution and maximum frequency of 1 Hz. The visual video camera has a resolution of 720×480 pixels and a 12x auto-focus zoom lens. Analog video signals from the infrared and visual cameras are recorded simultaneously. These data are used to provide context and geographical reference for the individually calibrated thermal images.

The total radiant emittance measured by the infrared camera is

$$W_{tot} = \varepsilon\tau W_{obj} + (1-\varepsilon)\,\tau W_{refl} + (1-\tau)W_{atm}, \qquad (1)$$

where ε is the emissivity of the object (a measure of how much radiation is emitted from an object compared to a perfect blackbody emitter, see discussion), τ is the atmospheric transmission, W_{obj} is the emission from the object, W_{refl} is the reflected emission from ambient sources, and W_{atm} is the emission from the atmosphere. The camera system converts radiant emittance (as measured by camera detector voltage) to brightness temperature internally using factory-defined calibration coefficients. We use an average emissivity value of 0.96 based on laboratory measurements of a dacite reference (Vaughan and others, 2005). We use ThermaCAM™ Researcher software to calculate atmospheric transmissivity using measured values of the ambient air temperature, relative humidity, and atmospheric path length (from the object to the camera).

The telephoto capabilities of the infrared camera allowed for safe helicopter operations from outside the 1980 crater at a typical altitude of 3,000 m above sea level (600 m above the crater rim) and a horizontal distance of 1,000 m from the

Figure 1. Forward Looking Infrared (FLIR) thermal and visual video imaging system used during airborne observations of Mount St. Helens, 2004–2007. *A*, FLIR instrument mounted on nose of Bell 206-L helicopter. Inset shows infrared (top) and visual video (bottom) lenses. *B*, Remote control panel used to display infrared and visual video streams, to control orientation of sensors using a joystick, and to capture data.

welt on the south crater floor. This was especially important for flights conducted during the first week of October 2004 when there was a high level of uncertainty regarding eruption prognosis and associated hazard. Infrared images, digital still photographs, and infrared and visual video were collected primarily at an oblique perspective, in many cases allowing for observation under steam and gas plumes that would have been impossible from a vertical viewing perspective. The thermal infrared and visual video collected using this system also provided striking graphical images for distribution to the media (Driedger and others, this volume, chap. 24).

In this study, thermal images are displayed in pseudocolor. Minimum and maximum temperature values (shown by a scale bar) are selected to provide optimal image enhancement. In some cases, the maximum temperature value reported in the text is higher than the maximum value shown by the scale bar.

Observations

Vent Clearing

We began thermal infrared monitoring on October 1, 2004, to develop baseline thermal images of the 1980–86 dome, to investigate the uplifted welt on the south crater floor, and to determine whether there was any thermal evidence for fracturing or faulting in the 1980–86 dome in response to ongoing uplift. Imaging began at 1156 PDT and showed several warm fumarolic regions with temperatures of 40ºC to 65ºC, primarily on the north flank of the dome, as well as the influence of solar heating on the south flank. The region of the dome and the south crater floor adjacent to the welt (an area of visible deformation and faulting) was near ambient temperature (0–15ºC) except for a t-shaped thermal lineament (figs. 2*A*, 2*B*) at the west end of the graben that formed during dome extrusion in 1985 near the area of the dome informally known as Opus. This lineament had temperatures of 30ºC to 38ºC.

At approximately 1202 PDT an ash-rich explosion ruptured ice at the west end of the welt. This event began without recognizable precursory seismicity (Moran and others, this volume, chap. 6) and without any observable thermal change in images collected 15 seconds prior to onset. The eruption column comprised ballistic projectiles, jetting, ash-rich projections inclined northward, and a convecting steam-rich cloud (figs. 2*C*, 2*D*). The maximum temperature, 160ºC, recorded from the base the column, indicated a phreatic rather than a magmatic mechanism. Infrared video shows that ballistic blocks were ejected primarily northward, where they destroyed seismic station SEP and GPS station DOM1 on the 1980–86 dome, located about 400 m north of the vent. Within 5 minutes of the eruption onset, a horizontally convecting ash-rich cloud developed and moved westward from the vent until it encountered the crater wall (figs. 2*E*, 2*F*). The steam-and-ash cloud ultimately reached an altitude of ~4,500 m above sea level. Ash emissions ended abruptly at 1220 PDT, and images collected several minutes later once the residual steam dispersed revealed a vent with a diameter of ~20 m in ice of the welt and a broad area of ash deposits on the west crater floor (fig. 2*G*). Vent temperatures were only slightly above freezing (2 –6ºC). Deposits adjacent to the vent had temperatures that ranged from 45ºC to 50ºC, and ballistic blocks with similar temperatures lay in small areas on the south and west flank of the 1980–86 dome (fig. 2*H*). The relatively low temperatures of the vent and deposits provide further evidence for a phreatic rather than magmatic eruption mechanism. A minor amount of snow and ice was melted, generating a small channelized flow that extended several hundred meters west from the vent.

Rapid deformation and uplift of the welt continued following the explosion, and thermal images tracked increasing temperatures of certain features (figs. 3, 4). Uplift of Opus (south of the 1985 graben) began to expose warmer interior rocks primarily on its eastern margin. Images of the Opus area collected on October 1, 2004 (figs. 3*A*, 3*B*), show several areas of elevated surface temperatures that ranged from 40ºC to 50ºC. Thermal images taken the following day showed that this area had been uplifted further and was the source of nearly constant warm rockfalls. By October 3, a broad region of oxidized rock from the interior of the dome was exposed (fig. 3*C*), and warm rockfalls and streaks of elevated temperature were more pronounced (fig. 3*D*). An elongate region of elevated temperature, detected at the north margin of the welt, trended east to west along the axis of the 1985 graben and intersected the October 1 vent (figs. 4*A*, 4*B*). Areas of enhanced heat flow along normal faults appeared in images as shorter lineaments perpendicular to the 1985 graben (fig. 4*B*).

Three additional phreatic explosions on October 3, 4, and 5 (Moran and others this volume, chap. 6) indicated the presence of a shallow heat source. These events reamed out a small basin on the west end of the welt, wherein water and ice collected (fig. 5*A*). On October 4, small ash-rich geysers (less than 50 m high) erupted through the lake, after which hot upwelling gas bubbles with temperatures as high as 200ºC appeared (fig. 5*B*). The last phreatic explosion on October 5 produced a new vent north of the earlier one. Over the next several days, new fumaroles developed near these vent regions, with temperatures as high as 55ºC observed on October 7.

On October 10, after 2 days of poor weather, thermal imagery detected a broad steaming area of ice- and snow-free rock at the west end of the welt (fig. 6*A*). Elevated temperatures that ranged from 30ºC to 50ºC characterized this broad area, and numerous hot point sources within it ranged from 100ºC to more than 270ºC (fig. 6*B*). This marked increase in temperature was the greatest yet observed and presented strong evidence that magma was nearing the surface.

Lava Extrusion Begins

Lava, first observed on October 11, extruded from the northern part of the zone of elevated temperatures shown in

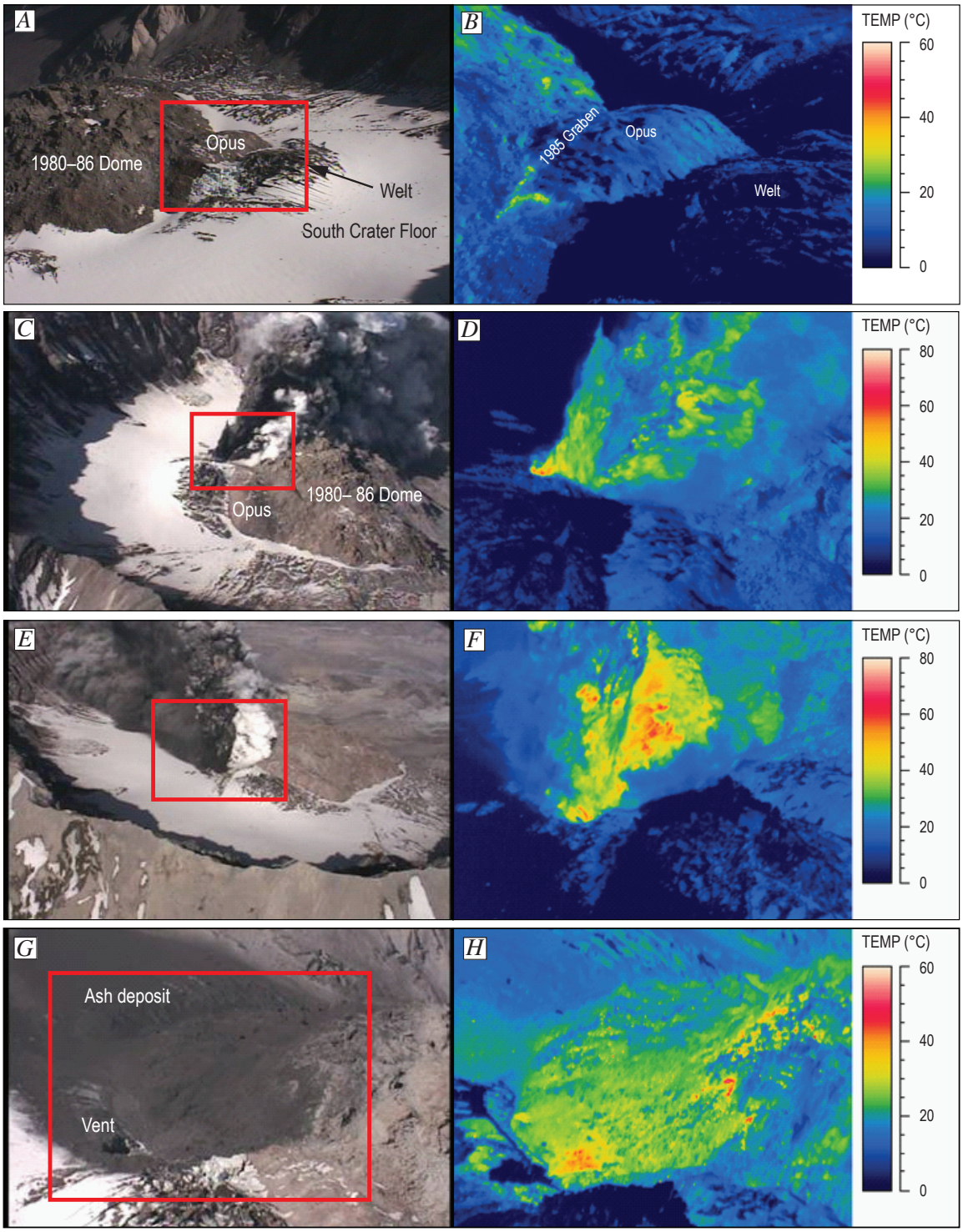

Figure 2. Comparisons between visual and infrared images of Mount St. Helens collected on October 1, 2004. Red rectangles in visual images show approximate boundaries of contemporaneous infrared images. *A*, Visual view from southwest of south crater floor and deforming welt collected at 11:56:30 PDT. *B*, Infrared image of area shown in *A*. *C*, Visual image from east showing phreatic eruption column collected at 12:05:50 PDT. *D*, Infrared image of area in *C*. *E*, Visual image from south showing phreatic eruption column collected at 12:07:07 PDT. *F*, Infrared image of area in *E*. *G*, Visual image from southeast showing vent region of phreatic explosion and associated ashfall deposits. *H*, Infrared image of area in *G*.

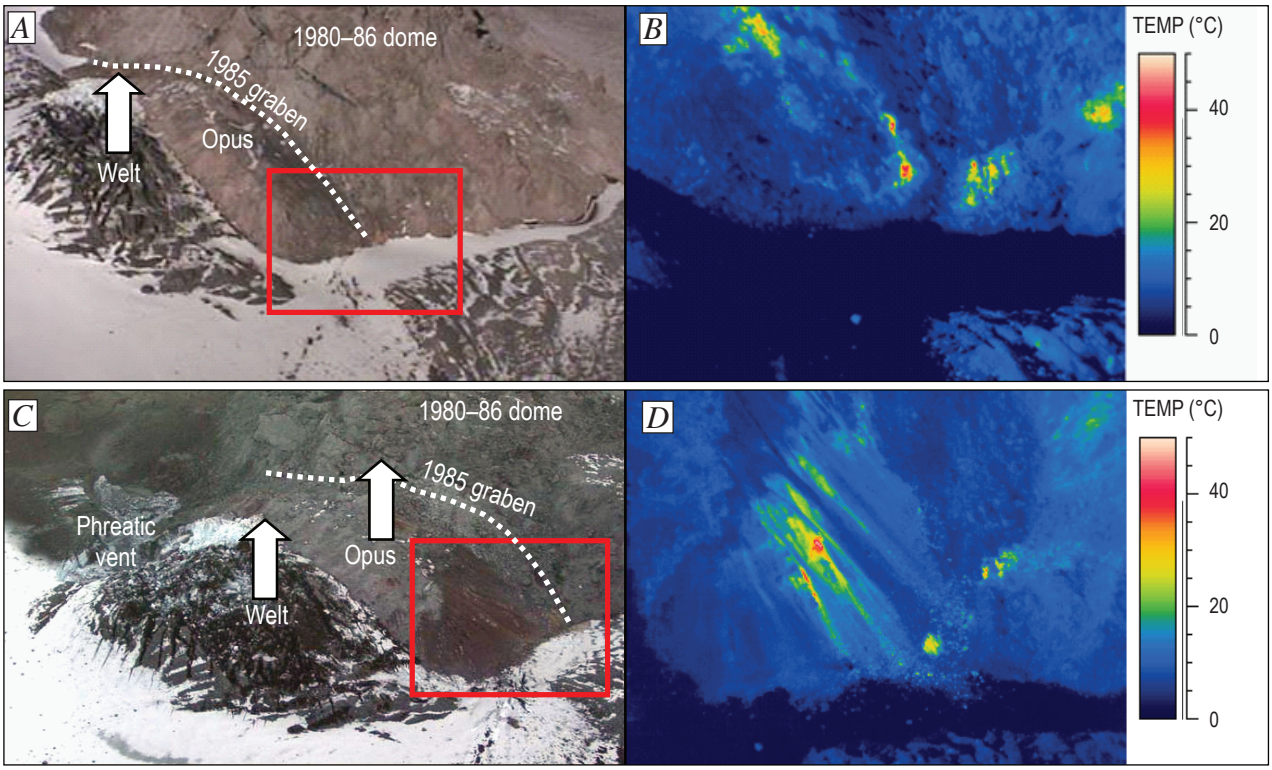

Figure 3. Comparisons between visual and infrared images of southeast part of 1980–86 dome and welt at Mount St. Helens. View from southeast. Red rectangles in visual images show approximate boundaries of contemporaneous infrared images. *A*, Visual image collected on October 1, 2004. *B*, Infrared image of area in *A*. *C*, Visual image collected on October 3, 2004. *D*, Infrared image of area in *C*.

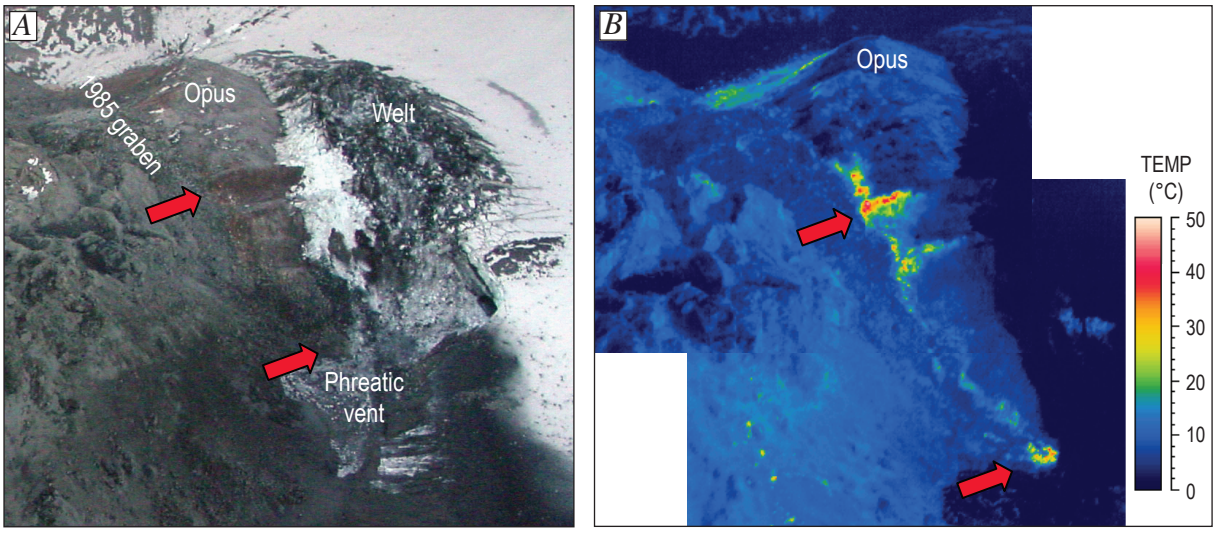

Figure 4. Comparison between visual and infrared images collected on October 3, 2004, of southern part of 1980–86 dome and welt at Mount St. Helens, showing thermal lineaments related to deformation. Red arrows indicate similar features between images. *A*, Visual image, view from the west. *B*, Contemporaneous infrared image.

figure 6. Following the usage of Cascades Volcano Observatory scientists, this and all subsequent lava extrusions are referred to as "spines," with a number assigned based on order of appearance. Spine 1 emerged as a fin-shaped slab approximately 80 m wide, 40 m high, and 10 m thick (fig. 7). Although the spine was partially obscured by steam during thermal observation (figs. 7*A*, 7*C*), temperatures as high as 580ºC were measured at its base (figs. 7*B*, 7*D*). A small warm debris fan extended from spine 1, but there was little melting evident on adjacent snow and ice. Extrusion of spine 1 continued through at least October 14, with the hottest temperatures of the entire eruption sequence, 730ºC, measured in cracks and fractures on that date.

Poor weather prevented thermal imaging flights from October 15 to 20, at which time extrusion of spine 2 had extended southward from spine 1 across the south crater floor. By October 24, spine 2 encountered the south crater wall (fig. 8). Spine 1 had cooled considerably since observation on October 14, with temperatures that ranged from 40ºC to 60ºC where it emerged from the ground, whereas the temperature of spine 2 ranged as high as 430ºC within fractured and fragmented rock near the likely zone of extrusion (fig. 8*B*). Intense steaming, caused by high relative humidity on this day (~80 percent), attenuated measured temperatures. The surfaces of spines 1 and 2 were rough, fractured, and blocky. Hot rockfalls on their west sides caused minor melting of snow and ice. An overflight on October 27 detected temperatures as hot as 700ºC where spine 2 emerged, as well as a broad warm area in the debris cover southeast of spine 1. Observations were hampered by thick steam, but retrospective analysis suggests that extrusion of spine 3 had begun by this time.

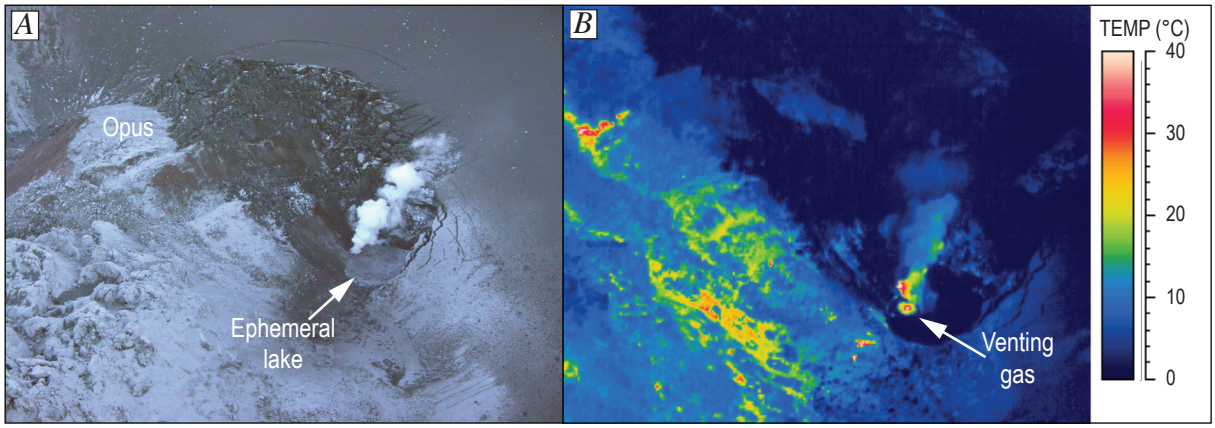

Figure 5. Comparison between visual and infrared images collected on October 4, 2004, of southern part of 1980–86 dome and phreatic vent on welt at Mount St. Helens, showing hot gas venting through ephemeral lake. *A*, Visual image, view from west. *B*, Contemporaneous infrared image.

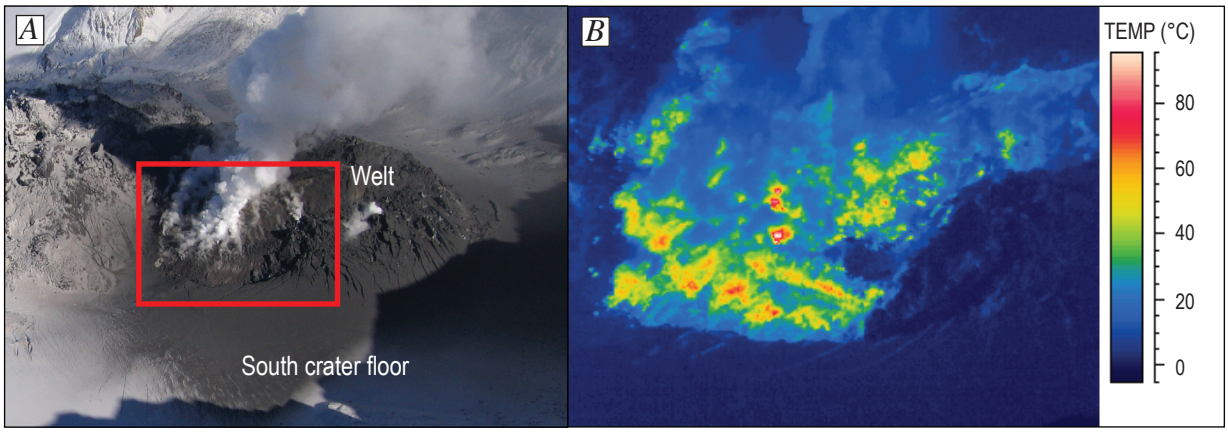

Figure 6. Comparison between visual and infrared images collected on October 10, 2004, of welt at Mount St. Helens, showing increased heat flow due to magma nearing surface. View from west. Red rectangle in visual image shows approximate boundary of contemporaneous infrared image. *A*, Visual image. *B*, Infrared image.

By November 4, spine 3 had grown considerably. Its surface was smooth with a few large cracks (fig. 9*A*), but its west and south sides were blocky and fractured. As much as several meters of fault gouge covering spine 3 formed as largely crystallized magma ascended the upper part of the conduit (Cashman and others, this volume, chap. 19). Its smooth surface and recumbent attitude gave spine 3 a whaleback-like morphology. The fault gouge served as an effective insulator so that surface temperatures where it emerged from the vent on its north end ranged from 150ºC to 200ºC and decreased exponentially to typical values of 25ºC to 50ºC within 50 to 75 m (fig. 9*B*). The hottest temperature observed in small regions of collapse and fractures was 625ºC.

Spine 3 moved toward the south as it was extruded and encountered the south crater wall by November 12 (Vallance and others, this volume, chap. 9). By late November, continued southward compression against the crater wall resulted in crumbling of spine 3 at its south end (fig 10*A*). Large open fractures in the fault-gouge carapace observed in thermal images (fig. 10*B*) suggested tensional cracking caused by bending of the solid spine as the extrusion continued southward. A typical temperature profile during this time period is shown in figure 11 along a line parallel to direction of extrusion. Temperature at the vent was typically 200ºC and decreased abruptly southward, but was as high as 700ºC in fractures.

Thermal infrared images continue to be used as a monitoring tool to observe dome growth and have documented the thermal characteristics of recumbent (whaleback) extrusion from November 2004 to April 2005, vertical spine extrusion from April to July 2005, and composite spine growth (composed of massive rock and disintegrating rock debris) from July 2005 to present (April 2007) (Vallance and others, this volume, chap. 9).

Discussion

Sources of Temperature Measurement Error

Accurate measurement of temperature using a thermal radiometer depends on several factors including viewing angle, characteristics of the atmospheric path, absorption by volcanic gases (water and SO_2), and the emissivity of the

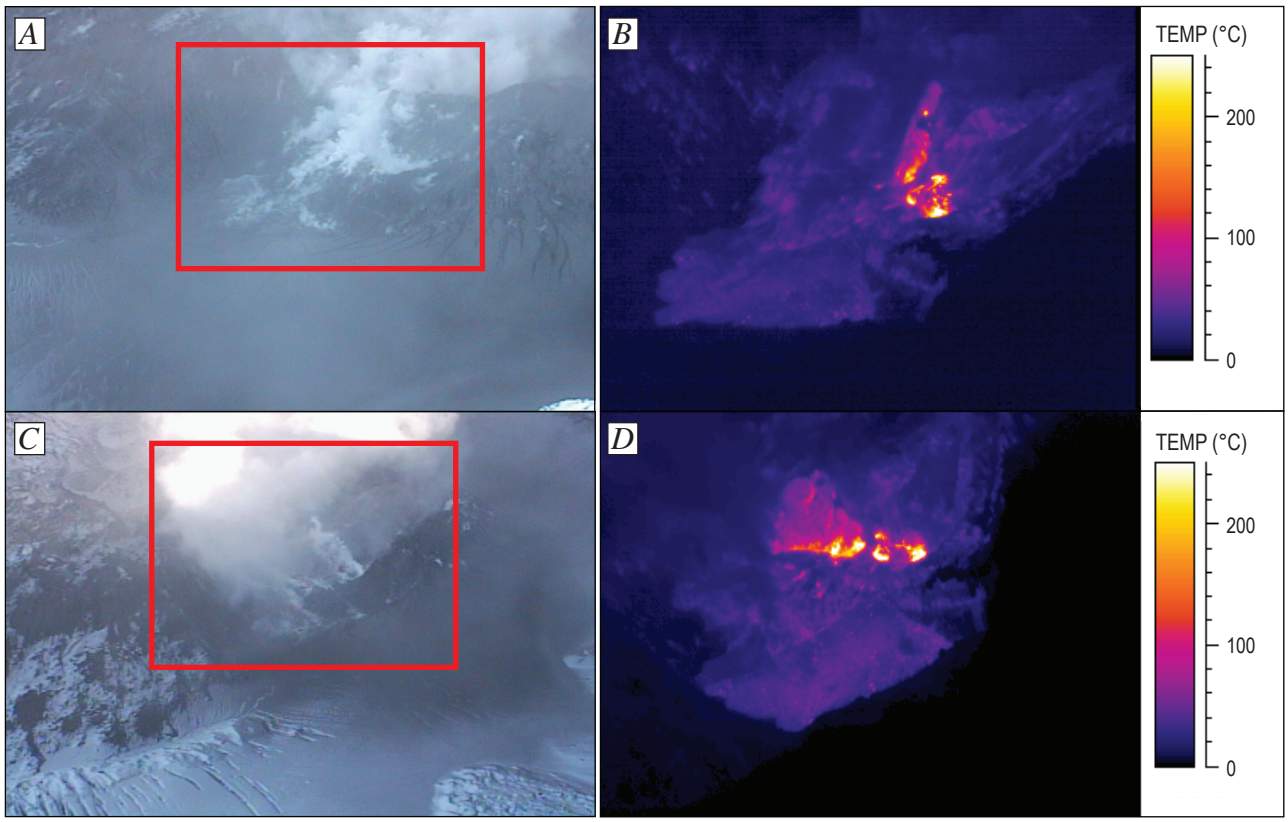

Figure 7. Comparison between visual and infrared images of Mount St. Helens collected on October 11, 2004, showing the first views of lava at the surface. Red rectangle in visual image shows approximate boundary of contemporaneous infrared image. *A*, Visual image, view from southwest. *B*, Infrared image, view from southwest. *C*, Visual image, view from northwest. *D*, Infrared image, view from northwest.

target (Ball and Pinkerton, 2006). The maximum temperature values reported herein are most strongly affected by viewing angle, because the source of heat typically was a fracture or fissure. In these cases, physical blockage of the source(s) of thermal emission occurred, and imaging of the target from multiple viewing angles was required to detect the maximum values. In other cases, opaque steam clouds completely obscured the source, making it impossible to measure the temperature accurately.

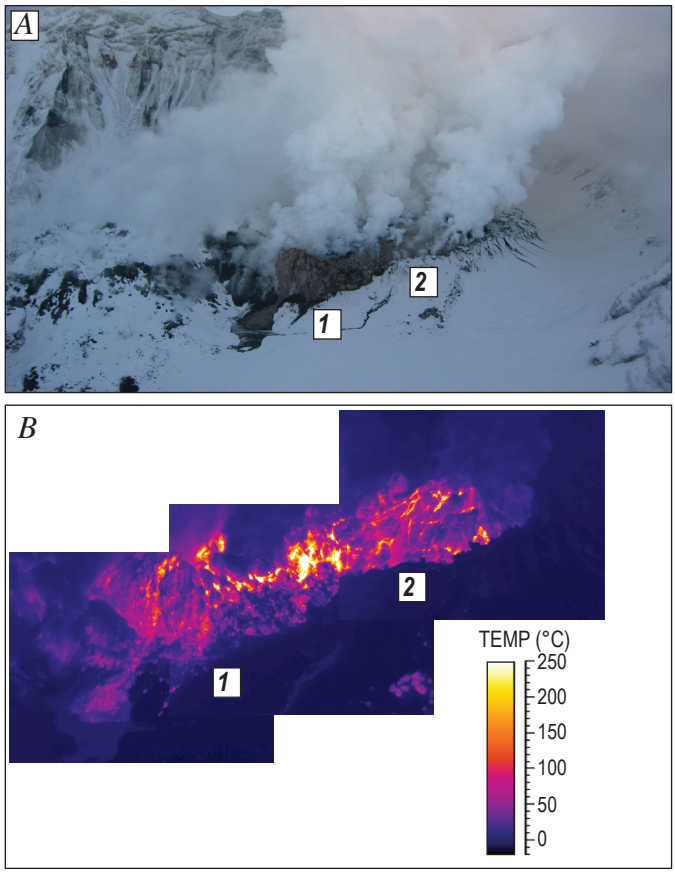

Figure 8. Comparison between visual and infrared images of Mount St. Helens collected on October 24, 2004, showing the development of spines 1 and 2 (as labeled). *A*, Visual image, view from the west. *B*, Composite infrared image.

Corrections for atmospheric-path absorption were made using ThermaCAM™ Researcher software and estimates of atmospheric temperature, relative humidity, and path length. For each mission, temperature and humidity values for Mount St. Helens were estimated using archived EDAS40 model sounding data provided by the NOAA Air Resources Laboratory (http//www.arl.noaa.gov/ready/amet.html). These values were used to compute the atmospheric transmission; the relation between these parameters is shown in figure 12 for a typical range of values. Uncertainty in estimating a representative relative humidity will contribute to a larger error in calculating transmission as the temperature of the atmosphere increases; the error will be compounded as the path length increases. Many of the thermal imaging missions were conducted at atmospheric temperatures near 0ºC, the relative humidity values varied by a maximum of ±15 percent, and variation in path length was ±250 m. This results in a variation in atmospheric transmission of about ±2 percent. For an object with a temperature of 500ºC, this results in a variation of ±10ºC.

Although water is the dominant volcanic gas that absorbs infrared radiation, SO_2 has two strong absorption features (centered at wavelengths of 7.3 and 8.5 μm) within the spectral range of the thermal radiometer. Although techniques to quantify the systematic error in ground-based thermal infrared measurements caused by gas absorption are still being developed, it may be a significant issue in situations where gas concentrations are high (Sawyer and others, 2005). The SO_2 emission rates during the time period of this study were low, ranging from values at the lower detection limit of 1 metric ton per day (t/d) through October 4 and increasing to an average value of approximately 100 t/d thereafter (Gerlach and others, this volume, chap. 26). Thus, absorption of infrared emissions by SO_2 is likely to be a relatively small source of error.

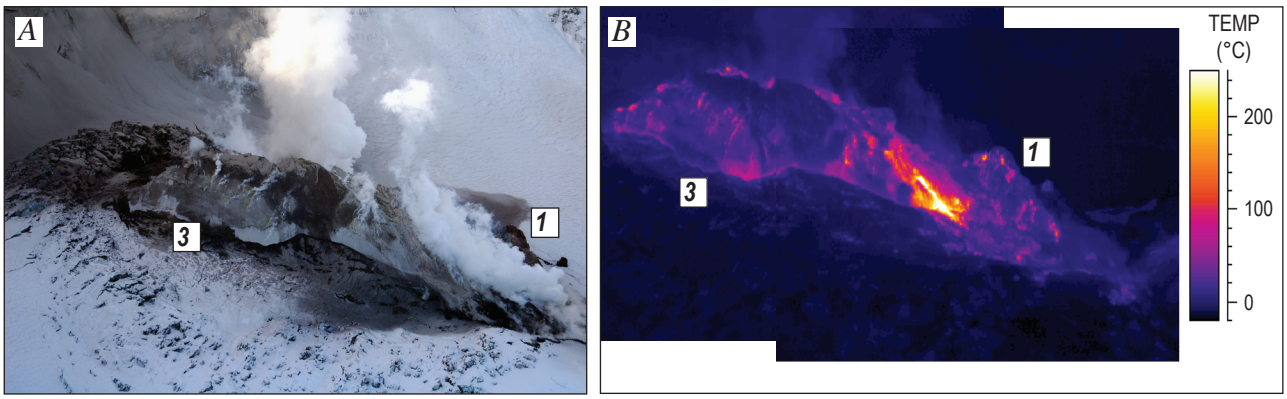

Figure 9. Comparison between visual and infrared images of Mount St. Helens collected on November 4, 2004, showing the development of spines 1 and 3 (as labeled). *A*, Visual image, view from the northeast. *B*, Composite infrared image.

Emissivity is a measure of how much energy is emitted from an object compared to a theoretical perfect emitter known as a blackbody. In nature, all materials emit less energy than a blackbody, because energy is absorbed by the vibration of molecular bonds. They are referred to as selective radiators wherein emissivity varies as a function of wavelength. Although the emissivity of silicate rocks has a characteristic decrease in emissivity at a wavelength range of 8 to 10 μm, an average value over the broader range of 7.5 to 13 μm is used where measuring temperatures with a broadband radiometer. Variations in emissivity can also occur for a given rock type as a result of vesicularity and particle size. In general, emissivity decreases as vesicularity decreases (Ramsey and Fink, 1999). The 2004 lava was largely degassed and dense (Pallister and others, this volume, chap. 30), suggesting that the actual emissivity may be lower than a laboratory reference. Furthermore, very fine grained silicates (<60 μm) exhibit a decrease in emissivity of the primary absorption band between 8 and 10 μm owing to the scattering of radiant energy (Ramsey and Christensen, 1998). It is possible that ash fallout and (or) the cover of the chalky fault-gouge carapace served to reduce the effective emissivity of the extruded lava (compared to the dacite reference value). The effect of an overestimated emissivity would be an increase in the temperatures above those reported herein. The result of a variation in emissivity was tested by changing the value by a factor of 0.1 within the ThermaCAM™ Researcher software, which resulted in a change in temperature on the order of 20ºC for an area with a temperature of 450ºC. Thus, variations in emissivity may account for changes on the order of 5 percent in the absolute temperature recorded.

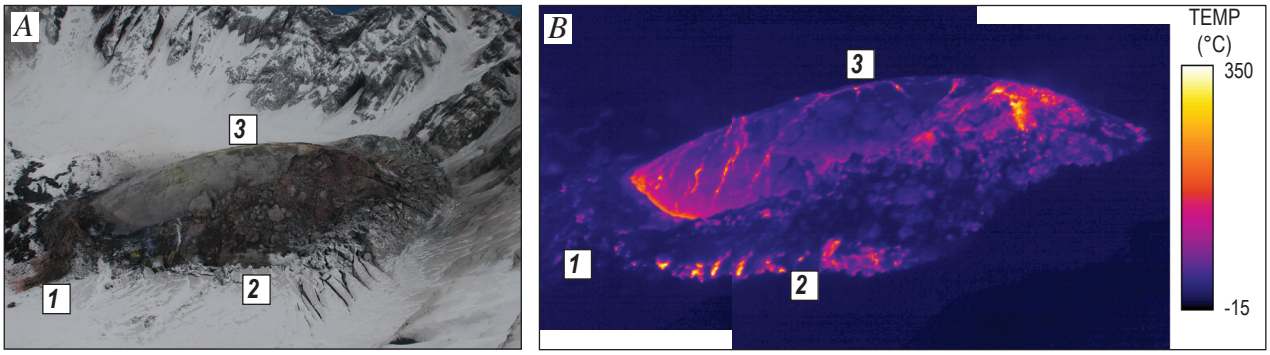

Figure 10. Comparison between visual and infrared images of Mount St. Helens collected on November 29, 2004, showing the development of spines 1 to 3. Spine 3 (as labeled) is actively being extruded and is crumbling as it encounters the south crater wall. *A*, Visual image, view from the west. *B*, Composite infrared image.

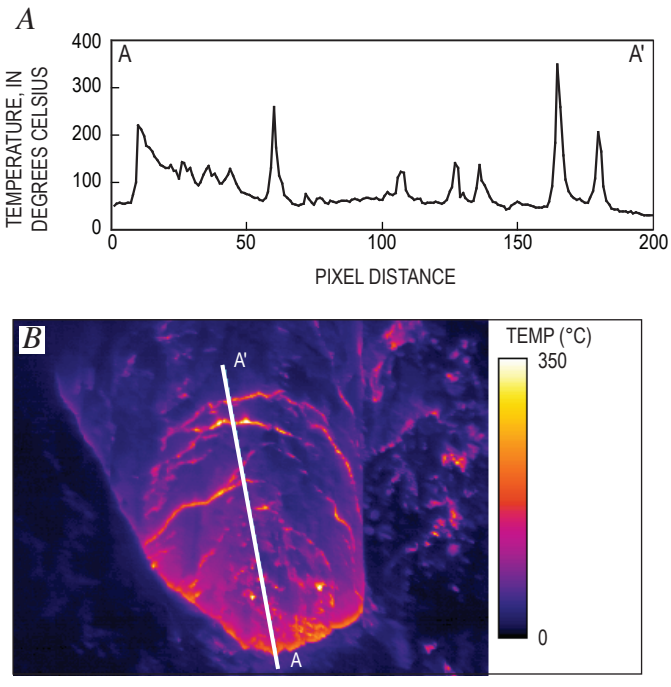

Figure 11. Temperature profile along north end of spine 3 at Mount St. Helens on November 29, 2004, showing typical temperatures observed during extrusion of whaleback spines. *A*, Temperature profile A–A'; profile length approximately 125 m, north toward left. *B*, Infrared image of spine 3 viewed from the north showing the location of the north-south profile, A–A'.

Thermal Imaging as a Response Tool

The rapid pace of unrest associated with the reawakening of Mount St. Helens in September 2004 resulted in an intense monitoring response by the Cascades Volcano Observatory (CVO) and the broader U.S. Geological Survey Volcano Hazards Program (VHP). Although handheld thermal imaging cameras have been used successfully in eruption response by other volcano observatories worldwide (Kauahikaua and others, 2003; Andronico and others, 2005; Calvari and others, 2005; Harris and others, 2005a), the gimbal-mounted system used during this response was a relatively new tool for VHP scientists. It had been flown on several missions at the Alaska Volcano Observatory (AVO) to collect baseline thermal data and on one flight in response to unrest at Mount Spurr (Power, 2004). Thus, the gimbal-mounted instrument was largely untested for eruption response by the USGS when first flown at Mount St. Helens on October 1, 2004, arriving only 6 minutes prior to the initial phreatic explosion. The utility of the instrument was quickly recognized as it was determined rapidly that the initial explosion was of phreatic origin. This information was quickly radioed to the operations center at CVO and used to apprise land management and emergency response personnel. In addition, the thermal and visual video imagery was made available to the media and was broadcast widely. The ability to control the gimbal and shoot video in a wide range of orientations was extremely useful as the helicopter maneuvered in response to the eruption cloud, topographic barriers, and wind. The telephoto capabilities were also vital, allowing for observation at a safe distance beyond the crater rim.

In addition to documenting thermal features on the crater floor and dome, use of the instrument during the first 2 weeks of October provided opportunities to test thermal-observation strategies and to determine what kinds of useful information could be obtained. The stability of the 1980–86 dome in response to the deformation on the south crater floor was initially of great concern, as potential eruption scenarios were evaluated involving (1) large-scale collapse of the 1980s dome toward the northern open end of the 1980 crater and (2) potential hazards to the public who had come to view the volcano. Thus, an important early use of the system was to look for the thermal expression of faults or fractures on the northern flank of the dome. Observations made throughout the eruption have shown no significant change in thermal response of the 1980–86 dome and thus have eased concerns about its stability.

Structural Control of Heat Emissions

The south flank of the 1980–86 dome, which formed the northern part of the welt, showed several examples of structural control of heat emissions during a time of rapid uplift, faulting, and deformation (figs. 3, 4) along a graben formed during an episode of dome growth in 1985. Between flights on October 1 and 2, rapid uplift of tens of meters on the east end of the graben caused warm rockfalls from the newly exposed interior of the dome. Over the next several days, the thermal imaging system was able to record continued uplift in this region as expressed by displacement of thermal features and nearly continuous warm rockfalls. On the west end of the graben (fig. 4), the thermal expression of normal faulting was observed, suggesting that this area was not moving upward as rapidly as the east end. Although these features can be seen in visible images, the advantage of the thermal system was to highlight areas of interest during a time period of very rapid changes in surface topography. Similar phenomena (on a larger scale) were observed at Mount St. Helens in April and May 1980 during development of the bulge. For example, Kieffer and others (1981) documented increased heat flow from several faults, fractures, and brecciated zones using a variety of thermal imaging devices, and they reported

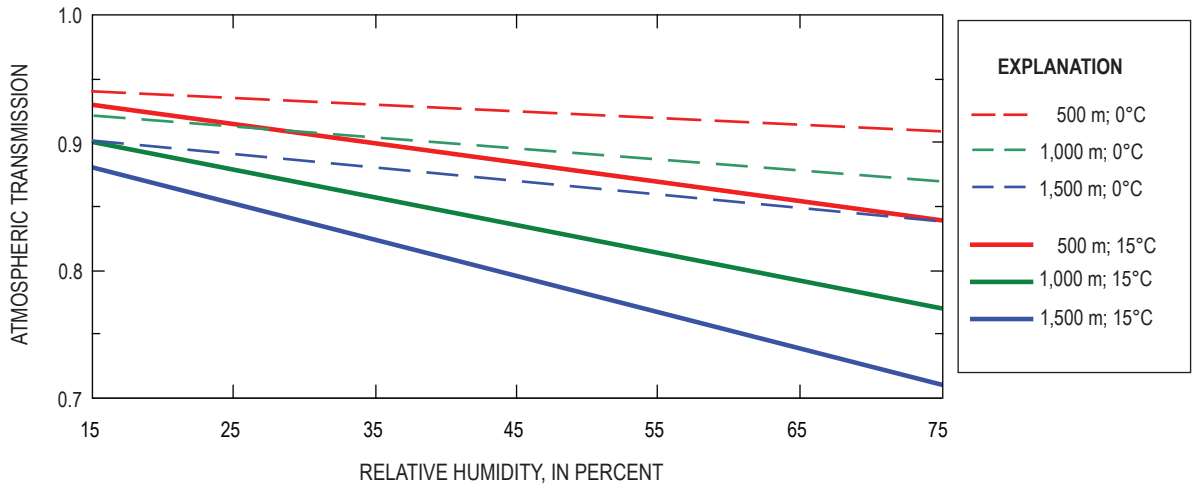

Figure 12. Atmospheric transmission as a function of relative humidity, atmospheric temperature, and path length.

temperature values in these regions of 15ºC to >25ºC above background, similar to those observed in October 2004. Structural control of heat emissions have also been noted at Mt. Etna in 2002 where hot fractures were observed several weeks prior to the eruption of a lava flow (Andronico and others, 2005), at Stromboli in 2002 where fractures were observed several hours prior to a major slope failure (Calvari and others, 2005), and at Augustine Volcano in 2006 where hot fractures and fissures were observed in the weeks preceding vulcanian explosions (D. Schneider, unpub. data). These studies suggest the broad utility of thermal imaging systems for detecting and monitoring deformation in the weeks and months prior to eruption.

The thermal measurements at Mount St. Helens documented an increase in heat flow on October 10 as magma neared the surface. On October 11, they provided unambiguous confirmation that lava (rather than uplifted crater floor) was being extruded. The imaging capabilities provided better viewing conditions at times when steam otherwise obscured observation (fig. 7) and allowed for an estimate of the volume of spine 1. The maximum temperature observed in fractures and regions of collapse during the eruption sequence was 730ºC, well below the solidus temperature of dacite. Although the thermal measurements may underestimate the maximum temperature as a result of thermal stratification due to radiative cooling, the observations are consistent with the petrologic (Pallister and others, this volume, chap. 30; Cashman and others, this volume, chap. 19) and seismic observations (Moran and others, this volume, chap. 2) that suggest a viscous to solid transition at a depth of approximately 1 km.

Comparisons to Satellite Methods

The detection limit of satellite-based measurements of thermal emissions is largely a matter of spatial resolution. With the exception of large thermal features (such as lava lakes, crater lakes, and pyroclastic-flow deposits), most sources of volcanogenic heat are subpixel in size when viewed with moderate-resolution sensors such as ASTER (90-m pixels) or coarse-resolution sensors such as AVHRR or MODIS (1-km pixels). Thus, the signal detected by the satellite is a pixel-integrated value of (at least) a hot and a cold (background) component. In order for a thermal anomaly to be detected, the proportion of hot material within a pixel, or the temperature of the hot component, needs to increase to the point where the integrated temperature exceeds a threshold (compared to neighboring pixels). So it follows that the smaller the spatial resolution of a sensor, the more sensitive it will be to detecting anomalous pixels.

Vaughan and Hook (2006) examined nighttime (to eliminate the solar reflected radiance) ASTER thermal infrared data for Mount St. Helens and reported that a single-pixel, weak (10°C) thermal feature was observed on the evening of October 1 approximately 11 hours after the first phreatic explosion. They noted that this value was within the range of typical ASTER-derived temperatures observed over the previous 5 years and would likely have not been viewed as significant without knowledge of the explosion. The next clear nighttime ASTER image was collected in February 2005 and showed an unambiguous maximum temperature of about 50°C. Although this instrument has been used successfully to monitor eruptive activity at many other volcanoes, the long period of time between successful, cloud-free nighttime images illustrates that significant eruptive activity can occur without being observed.

Manual analyses conducted by AVO of mid-infrared data from the AVHRR and MODIS sensors (1-km spatial resolution with multiple image collections per day) were not able to detect any unusual thermal (or volcanic ash) emissions during the precursory and vent-clearing phases of the eruption. The first weak thermal anomaly of 10°C (above background) was observed in data collected on the evening of October 11, shortly after the first observations of lava extrusion using the thermal imaging system (Alaska Volcano Observatory, unpub. data). It is unclear whether this level of activity would have been observed or reported without the knowledge of lava being extruded, as thermal anomalies of this magnitude can be masked by noise or other environmental factors. Thermal anomalies of 10°C to 20°C above background were reported by AVO throughout most of October during times of clear weather and increased to a one-pixel anomaly of 32°C above background in nighttime data on November 8 (Alaska Volcano Observatory, unpub. data). This observation corresponds most closely with the thermal image shown in figure 9 and occurred about 2 weeks after the start of the extrusion of spine 3. By comparison, MODVOLC, an automated global system designed to detect volcanic activity (with a rather high threshold to reduce false alarms) (Wright and others, 2004), did not trigger until December 18. By this time, spine 3 had encountered the south crater wall and started to disintegrate. Undoubtedly the detection of thermal activity by satellite techniques was greatly reduced by the insulating properties of the relatively cool fault-gouge carapace. Once the spines grew large and began to break apart, detection was more apparent. Still, lava extrusion was ongoing for a least a month before satellite methods utilizing 1-km-resolution data were able to unambiguously detect it.

Conclusions

The use of airborne thermal imaging to document eruptive activity at Mount St. Helens began in October 2004 to develop baseline thermal images of the 1980–86 dome and to investigate the rising welt on the south crater floor. Since that time, it has become a routine monitoring tool for tracking evolution of the lava dome (Vallance and others, this volume, chap. 9). Some of the unique information that has been derived from these data to date include (1) rapid identification of the phreatic nature of the early vent-clearing explosive phase; (2)

observation of the structural control of heat flow during times of large-scale deformation of the south flank of the 1980–86 dome, which was part of the welt; (3) observations of the venting of hot gas through an ephemeral crater lake and increased heat flow through the welt, indicative of a shallow magma source; (4) confirmation of new lava reaching the surface; (5) characterization of the change in surface temperature of the lava spines, from the initial, hotter spines 1 and 2 that were free of fault gouge, to the cooler gouge-covered whaleback spines (beginning with spine 3); (6) documentation that the relatively low maximum temperature of 730°C agreed with petrologic and seismic data suggesting a viscous-to-solid transition at shallow depth; and (7) identification of the source of active lava extrusion, dome collapse, and large variation in surface temperatures. Such temperature variation needs to be accounted for in the retrieval of eruption parameters using satellite-based techniques, because the thermal features are of subpixel size in satellite images.

Acknowledgments

We would like to thank Matthew Patrick and Cynthia Werner, who provided thoughtful and helpful reviews, and helicopter pilot Jeff Linscott of JL Aviation for his skillful, safe, and enthusiastic flying.

References Cited

Andronico, D., Branca, S., Calvari, S., Burton, M., Caltabiano, T., Corsaro, R.A., Del Carlo, P., Garfì, G., Lodato, L., Miraglia, L., Murè, F., Neri, M., Pecora, E., Pompilio, M., Salerno, G., and Spampinato, L., 2005, A multi-disciplinary study of the 2002–03 Etna eruption; insights into a complex plumbing system: Bulletin of Volcanology, v. 67, no. 4, p. 314–330, doi:10.1007/s00445-004-0372-8.

Ball, M., and Pinkerton, H., 2006, Factors affecting the accuracy of thermal imaging cameras in volcanology: Journal of Geophysical Research, v. 111, no. B11, B11203, 14 p., doi:10.1029/2005JB003829.

Calvari, S., Spampinato, L., Lodato, L., Harris, A.J.L., Patrick, M.R., Dehn, J., Burton, M.R., and Andronico, D., 2005, Chronology and complex volcanic processes during the 2002–2003 flank eruption at Stromboli volcano (Italy) reconstructed from direct observations and surveys with a handheld thermal camera: Journal of Geophysical Research, v. 110, no. B2, p. 1–23, doi:10.1029/2004JB003129.

Cashman, K.V., Thornber, C.R., and Pallister, J.S., 2008, From dome to dust; shallow crystallization and fragmentation of conduit magma during the 2004–2006 dome extrusion of Mount St. Helens, Washington, chap. 19 *of* Sherrod, D.R., Scott, W.E., and Stauffer, P.H., eds., A volcano rekindled; the renewed eruption of Mount St. Helens, 2004–2006: U.S. Geological Survey Professional Paper 1750 (this volume).

Dehn, J., Dean, K.G., Engle, K., and Izbekov, P., 2002, Thermal precursors in satellite images of the 1999 eruption of Shishaldin Volcano: Bulletin of Volcanology, v. 64, no. 8, p. 525–534, doi:10.1007/s00445-002-0227-0.

Driedger, C.L., Neal, C.A., Knappenberger, T.H., Needham, D.H., Harper, R.B., and Steele, W.P., 2008, Hazard information management during the autumn 2004 reawakening of Mount St. Helens volcano, Washington, chap. 24 *of* Sherrod, D.R., Scott, W.E., and Stauffer, P.H., eds., A volcano rekindled; the renewed eruption of Mount St. Helens, 2004–2006: U.S. Geological Survey Professional Paper 1750 (this volume).

Dzurisin, D., Lisowski, M., Poland, M.P., Sherrod, D.R., and LaHusen, R.G., 2008, Constraints and conundrums resulting from ground-deformation measurements made during the 2004–2005 dome-building eruption of Mount St. Helens, Washington, chap. 14 *of* Sherrod, D.R., Scott, W.E., and Stauffer, P.H., eds., A volcano rekindled; the renewed eruption of Mount St. Helens, 2004–2006: U.S. Geological Survey Professional Paper 1750 (this volume).

Flynn, L.P., Harris, A.J.L., and Wright, R., 2001, Improved identification of volcanic features using Landsat 7 ETM+: Remote Sensing of Environment, v. 78, nos. 1–2, p. 180–193.

Gerlach, T.M., McGee, K.A., and Doukas, M.P., 2008, Emission rates of CO_2, SO_2, and H_2S, scrubbing, and preeruption excess volatiles at Mount St. Helens, 2004–2005, chap. 26 *of* Sherrod, D.R., Scott, W.E., and Stauffer, P.H., eds., A volcano rekindled; the renewed eruption of Mount St. Helens, 2004–2006: U.S. Geological Survey Professional Paper 1750 (this volume).

Harris, A.J.L., Keszthelyi, L., Flynn, L.P., Mouginis-Mark, P.J., Thornber, C., Kauahikaua, J., Sherrod, D., Trusdell, F., Sawyer, M.W., and Flament, P., 1997, Chronology of the episode 54 eruption at Kilauea Volcano, Hawaii, from GOES-9 satellite data: Geophysical Research Letters, v. 24, no. 24, p. 3281–3284.

Harris, A., Dehn, J., Patrick, M., Calvari, S., Ripepe, M., and Lodato, L., 2005a, Lava effusion rates from hand-held thermal infrared imagery: an example from the June 2003 effusive activity at Stromboli: Bulletin of Volcanology, v. 68, no. 2, p. 107–117, doi:10.1007/s00445-005-0425-7.

Harris, A., Ripepe, M., Sahetapy-Engel, S., Marchetti, E., and Patrick, M., 2005b, Plume ascent velocities measured during explosive eruptions using thermal infrared thermometers [abs.]: Eos (American Geophysical Union Transactions), v. 86, no. 52, Fall Meeting Supplement, Abstract V24A-06.

Kauahikaua, J., Sherrod, D.R., Cashman, K.V., Heliker, C.,

Hon, K., Mattox, T.N., and Johnson, J.A., 2003, Hawaiian lava-flow dynamics during the Pu‘u ‘Ō‘ō-Kūpaianaha eruption; a tale of two decades, *in* Heliker, C., Swanson, D.A., and Takahashi, T.J., eds., The Pu‘u ‘Ō‘ō-Kūpaianaha eruption of Kīlauea Volcano, Hawai‘i; the first 20 years: U.S. Geological Survey Professional Paper 1676, p. 63–87.

Kiefer, H.H., Frank, D., and Friedman, J.D., 1981, Thermal infrared surveys at Mount St. Helens—observations prior to the eruption of May 18, *in* Lipman, P.W., and Mullineaux, D.R., eds., The 1980 eruptions of Mount St. Helens, Washington: U.S. Geological Survey Professional Paper 1250, p. 257–277.

Moran, S.C., Malone, S.D., Qamar, A.I., Thelen, W.A., Wright, A.K., and Caplan-Auerbach, J., 2008a, Seismicity associated with renewed dome building at Mount St. Helens, 2004–2005, chap. 2 *of* Sherrod, D.R., Scott, W.E., and Stauffer, P.H., eds., A volcano rekindled; the renewed eruption of Mount St. Helens, 2004–2006: U.S. Geological Survey Professional Paper 1750 (this volume).

Moran, S.C., McChesney, P.J., and Lockhart, A.B., 2008b, Seismicity and infrasound associated with explosions at Mount St. Helens, 2004–2005, chap. 6 *of* Sherrod, D.R., Scott, W.E., and Stauffer, P.H., eds., A volcano rekindled; the renewed eruption of Mount St. Helens, 2004–2006: U.S. Geological Survey Professional Paper 1750 (this volume).

Pallister, J.S., Thornber, C.R., Cashman, K.V., Clynne, M.A., Lowers, H.A., Mandeville, C.W., Brownfield, I.K., and Meeker, G.P., 2008, Petrology of the 2004–2006 Mount St. Helens lava dome—implications for magmatic plumbing and eruption triggering, chap. 30 *of* Sherrod, D.R., Scott, W.E., and Stauffer, P.H., eds., A volcano rekindled; the renewed eruption of Mount St. Helens, 2004–2006: U.S. Geological Survey Professional Paper 1750 (this volume).

Patrick M.R., Harris, A.J.L., Ripepe, M., Dehn, J., Rothery, D.A., and Calvari, S., 2007, Strombolian explosive styles and source conditions; insights from thermal (FLIR) video: Bulletin of Volcanology, v. 69, no. 7, p. 769–784, doi:10.1007/s00445-006-0107-0.

Power, J., 2004, Renewed unrest at Mount Spurr volcano, Alaska [abs.]: Eos (American Geophysical Union Transactions), v. 85, no. 43, p. 434.

Ramsey, M.S., and Christensen, P.R., 1998, Mineral abundance determination; Quantitative deconvolution of thermal emission spectra: Journal of Geophysical Research, v. 103, no. B1, p. 577–596.

Ramsey, M., and Dehn, J., 2004, Spaceborne observations of the 2000 Bezymianny, Kamchatka, eruption; the integration of high-resolution ASTER data into near real-time monitoring using AVHRR: Journal of Volcanology and Geothermal Research, v. 135, nos. 1–2, p. 127–146, doi:10.1016/j.jvolgeores.2003.12.014.

Ramsey, M.S., and Fink, J.H., 1999, Estimating silicic lava vesicularity with thermal remote sensing; a new technique for volcanic mapping and monitoring: Bulletin of Volcanology, v. 61, no. 1, p. 32–39.

Sawyer, G., Burton, M., and Oppenheimer, C., 2005, The effect of volcanic gases on quantitative temperature measurements using the FLIR thermal camera [abs.]: Eos (American Geophysical Union Transactions), v. 86, no. 52, Fall Meeting Supplement, Abstract V24A-08.

Vallance, J.W., Schneider, D.J., and Schilling, S.P., 2008, Growth of the 2004–2006 lava-dome complex at Mount St. Helens, Washington, chap. 9 *of* Sherrod, D.R., Scott, W.E., and Stauffer, P.H., eds., A volcano rekindled; the renewed eruption of Mount St. Helens, 2004–2006: U.S. Geological Survey Professional Paper 1750 (this volume).

Vaughan, R.G., and Hook, S.J., 2006, Using satellite data to characterize the temporal thermal behavior of an active volcano; Mount St. Helens, WA: Geophysical Research Letters, v. 33, L20303, doi:10.1029/2006GL027957.

Vaughan, R.G., Hook, S.J., Ramsey, M.S., Realmuto, V.J., and Schneider, D.J., 2005, Monitoring eruptive activity at Mount St. Helens with TIR image data: Geophysical Research Letters, v. 32, L19305, doi:10.1029/2005GL024112.

Wright, R., Flynn, L., Garbeil, H., Harris, A., and Pilger, E., 2002, Automated volcanic eruption detection using MODIS: Remote Sensing of Environment, v. 82, no. 1, p. 135–155.

Wright, R., Flynn, L.P., Garbeil, H., Harris, A.J.L., and Pilger, E., 2004, MODVOLC: Near-real-time thermal monitoring of global volcanism: Journal of Volcanology and Geothermal Research, v. 135, nos. 1–2, p. 29–49.

This page intentionally left blank

A Volcano Rekindled: The Renewed Eruption of Mount St. Helens, 2004–2006
Edited by David R. Sherrod, William E. Scott, and Peter H. Stauffer
U.S. Geological Survey Professional Paper 1750, 2008

Chapter 18

Radar Interferometry Observations of Surface Displacements During Pre- and Coeruptive Periods at Mount St. Helens, Washington, 1992–2005

By Michael P. Poland[1] and Zhong Lu[2]

Abstract

We analyzed hundreds of interferograms of Mount St. Helens produced from radar images acquired by the ERS-1/2, ENVISAT, and RADARSAT satellites during the 1992–2004 preeruptive and 2004–2005 coeruptive periods for signs of deformation associated with magmatic activity at depth. Individual interferograms were often contaminated by atmospheric delay anomalies; therefore, we employed stacking to amplify any deformation patterns that might exist while minimizing random noise. Preeruptive interferograms show no signs of volcanowide deformation between 1992 and the onset of eruptive activity in 2004. Several patches of subsidence in the 1980 debris-avalanche deposit were identified, however, and are thought to be caused by viscoelastic relaxation of loosely consolidated substrate, consolidation of water-saturated sediment, or melting of buried ice. Coeruptive interferometric stacks are dominated by atmospheric noise, probably because individual interferograms span only short time intervals in 2004 and 2005. Nevertheless, we are confident that at least one of the seven coeruptive stacks we constructed is reliable at about the 1-cm level. This stack suggests deflation of Mount St. Helens driven by contraction of a source beneath the volcano.

Introduction

Continuous Global Positioning System (GPS) measurements at Mount St. Helens have provided unequivocal evidence of coeruptive deflation that started in 2004, coincident with the onset of seismicity in late September of that year (Lisowski and others, this volume, chap. 15). These data have been used to model an ellipsoidal source of volume loss between 6 and 12 km depth beneath the volcano (Lisowski and others, this volume, chap. 15; Mastin and others, this volume, chap. 22). In addition, GPS results from in and around the crater, including single-frequency instruments deployed on the growing lava dome, have recorded surface displacements associated with dome extrusion (LaHusen and others, this volume, chap. 16). Interferometric synthetic aperture radar (InSAR) data provide an excellent complement to these GPS data. Though lacking the high temporal resolution of continuous GPS or tiltmeter data, InSAR has the potential to provide much greater spatial resolution of deformation, which is useful both for identifying localized deformation sources and modeling complex source geometries. Further, radar images of Mount St. Helens are available from 1992 onward, making it possible to quantify surface displacements during the 1992–2004 preeruption period, when few other geodetic measurements were collected.

Although InSAR characterizations of surface deformation at shield volcanoes (for example, Amelung and others, 2000a) and calderas (for example, Hooper and others, 2004; Wicks and others, 1998; Wicks and others, 2006) have been quite successful, studies of stratovolcanoes have proven more challenging. This is largely due to the fact that most stratovolcanoes are steep sided and covered to varying degrees by vegetation, snow, and ice, leading to a loss of coherent interferometric signal on and around the volcano, especially for C-band radar wavelengths (Zebker and others, 2000; Lu and others, 2005b; Moran and others, 2006). The great height of many stratovolcanoes, relative to the surrounding terrain, can also create atmospheric conditions that introduce significant artifacts into InSAR results (Beaudecel and others, 2000; Wadge and others, 2006). The combined effects of these conditions prevented the use of coeruptive InSAR data for the analysis of deformation at numerous stratovolcanoes, includ-

[1] U.S. Geological Survey, PO Box 51, Hawaii National Park, HI 96718

[2] U.S. Geological Survey, 1300 SE Cardinal Court, Vancouver, WA 98683

ing Galeras, Colombia; Rincon de la Vieja, Costa Rica; Unzen, Japan; and Merapi, Indonesia (Zebker and others, 2000). Even when coeruptive data for a stratovolcano are coherent, there is no guarantee that deformation will be observed, as demonstrated by results from Fuego and Pacaya, Guatemala; Popocatepetl, Mexico; Sakurajima, Japan (Zebker and others, 2000); Irruputuncu (Zebker and others, 2000; Pritchard and Simons, 2004b) and Lascar (Pritchard and Simons, 2002; Pritchard and Simons, 2004a), Chile; and Shishaldin (Moran and others, 2006), Pavlof, Cleveland, and Korovin, Alaska (Lu and others, 2003b). Lu and others (2003b) and Moran and others (2006) suggested that, at least in the case of Shishaldin, the lack of observed line-of-sight displacements in coeruptive InSAR data may be caused by (1) posteruption motion that balanced preeruption displacements, resulting in no net deformation across the time spanned by the interferograms, (2) the occurrence of deformation in "blind zones" where InSAR data are not coherent, or (3) the lack of any significant deformation associated with the eruption. Pritchard and Simons (2004a; 2004b) suggest similar reasons for the lack of observed deformation in InSAR data from Cerro Irruputuncu and Volcán Lascar, two volcanoes in Chile, in addition to the possibility that the magma reservoir may be too deep to produce surface displacements detectable by InSAR.

Poor coherence at a volcano does not necessarily imply that surface displacements cannot be observed by InSAR. Cerro Hudson is a 10-km-diameter, ice-filled caldera in southern Chile. Despite a complete lack of coherence within and limited coherence outside the caldera, displacements were of sufficient magnitude (15-cm line-of-sight inflation over 3 years) to be detected and distinguished from atmospheric noise (Pritchard and Simons, 2004b). Although large displacements were not observed in individual coeruptive interferograms of Soufrière Hills volcano[1], Montserrat, Wadge and others (2006) identified deformation caused by a variety of processes once they stacked (averaged) multiple interferograms. At stratovolcanoes where coherence is excellent, InSAR studies have resulted in important discoveries of aseismic magma accumulation, including Peulik, Alaska (Lu and others, 2002b) and South Sister, Oregon (Dzurisin and others, 2006; Wicks and others, 2002). In addition, InSAR has been critical for characterizing deformation at many composite volcanoes that have experienced unrest or eruptions, including Westdahl (Lu and others, 2003a), Makushin (Lu and others, 2002a), Akutan (Lu and others, 2000; Lu and others, 2005b), Augustine (Masterlark and others, 2006), and Seguam (Masterlark and Lu, 2004), Alaska; Gada 'Ale, Ethiopia (Amelung and others, 2000b); and several volcanoes in the central and southern Andes (Pritchard and Simons, 2002; 2004a; 2004b). Clearly, the potential for advancing the understanding of pre- and coeruptive activity at Mount St. Helens through InSAR studies is substantial.

We completed an exhaustive analysis of InSAR data collected from Mount St. Helens between 1992 and 2005 from a variety of satellites, ground tracks, time spans, and satellite viewing geometries. Our goals were to (1) obtain high-spatial-resolution coeruptive surface displacement data of the known volcanowide deflation (Lisowski and others, this volume, chap. 15) for input into deformation source models, (2) identify any localized displacements that might not be detectable by GPS or other terrestrial measurements, and (3) identify any displacements precursory to the onset of eruptive activity in 2004. Coherence was poor and atmospheric artifacts were significant in most interferograms; nevertheless, we recognized localized displacements unrelated to volcanic activity and modeled coeruptive subsidence (although poor coherence prevented the use of complex model geometries). Preeruptive interferograms showed no evidence of precursory deformation; however, displacements localized within the crater cannot be ruled out, owing to poor coherence and atmospheric distortions.

Methodology

Traditional InSAR studies combine two radar images of the same area on the ground acquired at different times from nearly the same point in space to determine the deformation over the time spanned along the radar's line-of-sight (LOS). This procedure, unfortunately, does not produce satisfactory results at Mount St. Helens for three reasons: (1) atmospheric path delays, which often correlate with topography, can introduce artifacts that amount to several centimeters of apparent LOS displacement (fig. 1), (2) interferograms that include scenes acquired during nonsummer months are generally incoherent due to seasonal snow cover, and (3) coherence breaks down quickly over time, causing interferograms that span more than one or two years to be mostly incoherent. In fact, in interferograms spanning several months or more, coherence was generally maintained only on deposits that were emplaced during the explosive eruptions of 1980 (for example, May 18, May 25, June 12, July 22), especially north of the volcano and in the upper North Fork Toutle River. As a result, we relied on interferometric stacks to study deformation of Mount St. Helens.

Stacking is a procedure that adds the LOS displacements from multiple interferograms (which may or may not be overlapping in time) acquired along the same look angle. Dividing the summed displacements by the cumulative time spanned results in an average displacement rate (for example, Fialko and Simons, 2001; Peltzer and others, 2001). The technique decreases the magnitude of random noise (primarily atmospheric artifacts) by $N/u^{0.5}$, where N is the error in a single interferogram and u is the number of interferograms in the stack (Bevington and Robinson, 1992, p. 39–40). For

[1] Capitalization of "Volcano" indicates adoption of the word as part of the formal geographic name by the host country, as listed in the Geographic Names Information System, a database maintained by the U.S. Board on Geographic Names. Noncapitalized "volcano" is applied informally—eds.

example, if atmospheric variations typically result in an error of 10 mm/yr, a stack of 25 interferograms would reduce the noise level to about 2 mm/yr (assuming atmospheric path delay errors have similar magnitudes in all interferograms). In contrast, signals that persist over time—including steady deformation due to volcanic or tectonic activity—are emphasized because the signal is manifested in all interferograms in the stack. InSAR stacks have been able to distinguish displacement rates as low as a few millimeters per year (Wright and others, 2001, 2004) but are useful only when the strength and geometry of the deformation source do not vary significantly over time, meaning that nonlinear deformation rates or changes in source location or geometry are not easily recovered in interferometric stacks.

We do not expect changes in source geometry over time to bias the interferometric stacks. The geometry of the magmatic system of Mount St. Helens has been investigated using both petrologic (for example, Rutherford and others, 1985; Cashman, 1988; Cashman, 1992; Pallister and others, 1992) and seismic (Scandone and Malone, 1985; Barker and Malone, 1991; Lees, 1992; Moran, 1994; Musumeci and others, 2002) techniques and includes a reservoir at around 6–10 km depth connected to the surface by a near-vertical conduit. The conduit appears to have been sealed at a depth of about 2 km following the end of the 1980–86 eruptive period (Moran, 1994). Any pre- or coeruptive deformation associated with unrest beginning in 2004 will likely have a source within this system (especially at the levels around the 6–10-km-depth reservoir or 2-km-depth seal).

Similarly, deformation rates during both the pre- and coeruptive periods appear to be approximately linear, so time-variable displacements will not bias deformation rates derived by stacking. Electronic Distance Measurement (EDM) and campaign GPS measurements in the inter-eruptive period, from late 1986 through the first half of 2004, indicate that little deformation occurred, especially after 1991 (Lisowski and others, this volume, chap. 15). In addition, individual interferograms that span time periods before

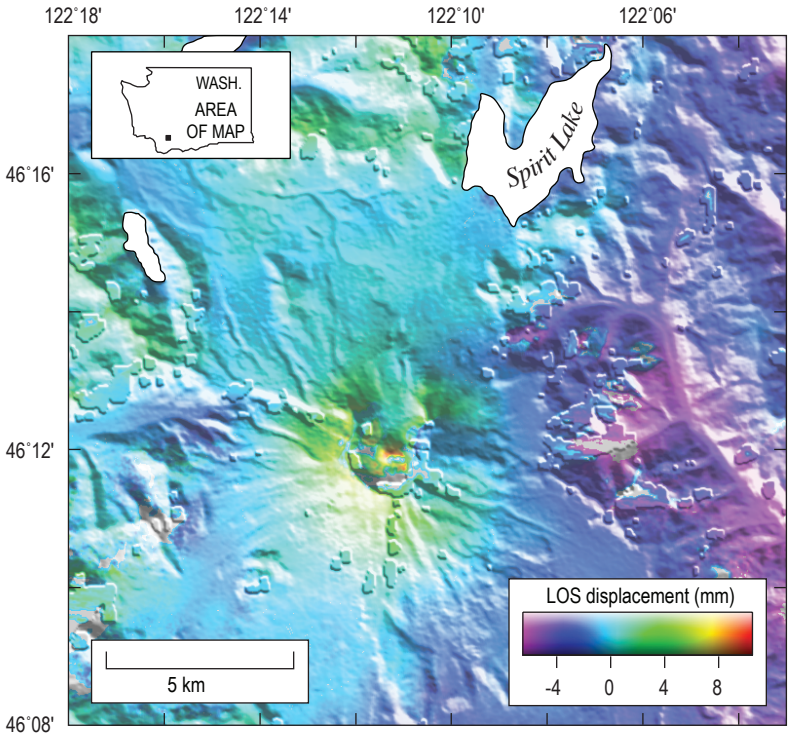

Figure 1. Interferogram of Mount St. Helens, Washington, formed from ERS-1 orbit 21415 (August 19, 1995) and ERS-2 orbit 2243 (September 24, 1995). Interferogram spans only 36 days during summer months, hence high level of coherence. Phase correlates strongly with topography, so Mount St. Helens shows apparent line-of-sight (LOS) lengthening, while lower valleys to east show LOS shortening. Such behavior is characteristic of strong atmospheric influence. Topographic irregularities caused by areas of no data in SRTM DEM.

the start of the unrest in September 2004 show no unambiguous signs of volcanowide deformation. If preeruptive surface displacements occurred, the motion must therefore have been small in magnitude but may have accumulated over time. Coeruptive displacements, measured by continuous GPS starting on September 23, 2004, are generally linear after the first few weeks of the activity (Lisowski and others, this volume, chap. 15) and suggest only minor temporal or spatial variations in the contraction of a source at depth beneath Mount St. Helens.

An unusually large InSAR data set, summarized in table 1, is available for Mount St. Helens, including multiple satellites with a variety of imaging geometries. For preeruptive time periods, we analyzed data from ERS-1, ERS-2, and ENVISAT. Usable data from the first two satellites span 1992–2001 and are available for four orbital tracks, whereas a sufficiently large archive of ENVISAT data is available from one track to allow an assessment of the surface displacement field in 2003–4. Our coeruptive InSAR data set includes five ENVISAT and two RADARSAT tracks. All possible interferograms from each independent track with perpendicular baselines of less than 300 m were created.

Topographic corrections to interferograms utilized the 30-m resolution Shuttle Radar Topography Mission (SRTM) digital elevation model (DEM), which was generated in 2000 (Farr and Kobrick, 2000). The older National Elevation Dataset (NED) 30-m DEM, created before 1986, contains fewer holes than the SRTM data, but its use resulted in deformation artifacts in interferograms in the area of Mount St. Helens crater. Significant topographic changes have occurred in the crater since the end of the 1980–86 eruptive period, most notably the growth of a glacier that had reached a maximum thickness of 200 m by the time eruptive activity resumed in 2004 (Schilling and others, 2004; Walder and others, this volume, chap. 13). The more recent SRTM DEM accounts for growth of the glacier and other changes since 1986 and does not introduce significant artifacts related to topographic change. Interferograms were smoothed using the filtering strategy of Goldstein and Werner (1998) and unwrapped following Chen and Zebker (2001).

From this collection of interferograms, we omitted all images that spanned less than 100 days (except for coeruptive ENVISAT mode 2, track 385, where the only interferograms with perpendicular baselines less than 300 m spanned 70 days or less), because images that span such short times have a low signal-to-noise ratio given the low displacement rates known from GPS (Lisowski and others, this volume, chap. 15). There is no upper limit on the time spanned, although interferograms that showed no or very limited coherence, including nearly all images that span more than two years, were omitted from the analysis. Stacks of each independent track were computed from this modified data set, and only pixels that are coherent in 60 percent of the input images are included in the final stack. Five preeruption and seven coeruption stacks were created, with 3 to 38 input interferograms each (table 1).

Preeruptive Stacks

Results

In preeruptive stacks (figs. 2–6), the range of displacements for each track is generally small, suggesting that the random atmospheric signal has been mostly removed. The lack of significant topography-correlated phase at Mount Adams (which we assume to be undeforming, based on the absence of other signs of unrest) in tracks that both cover and are coherent around both volcanoes (figs. 4, 5) further supports our assertion that atmospheric noise has been mostly suppressed by stacking.

None of the preeruption stacks show any signs of volcanowide deformation, suggesting that no significant surface displacements accumulated over the times spanned by the stacks. Unfortunately there are no InSAR results available between late 2001 and early 2003, so we cannot rule out deformation during this time period. No volcanowide displacements are apparent in the one stack that covers the early 2003 to September 2004 epoch (up to the start of the eruption), suggesting that no centimeter-level displacements on the flanks of the volcano occurred in the months immediately preceding the start of the eruption.

Despite this lack of signal, the five preeruption stacks do reveal at least three localized areas of surface displacement that are unrelated to the magmatic system of Mount St. Helens. All three regions are patches of subsidence located on the May 18, 1980, debris-avalanche deposit (fig. 2). The area with the highest subsidence rate, as much as 15 mm/yr (LOS), is directly north of the crater (site 1 in fig. 2), near the base of Johnston Ridge, and had been recognized previously in individual interferograms by Diefenbach and Poland (2003). A second, less distinct area located near the outlet of Coldwater Lake (site 2 in fig. 2) is subsiding at a rate of slightly less than 5 mm/yr (LOS). The third patch of subsidence, which is sinking at an LOS rate of approximately 6 mm/yr, is in the North Fork Toutle River valley, just southeast of Elk Rock and immediately upstream from a valley constriction (site 3 in fig. 2). The latter two patches had not been recognized previously.

The stacks presented in figures 2 through 6 give average deformation rates. To assess whether or not the subsidence rates of the three localized patches changed during 1992–2005, we used the individual unwrapped interferograms to reconstruct the temporal evolution of the deformation following the method of Berardino and others (2002). At Mount St. Helens, all five preeruption stacks suggest a constant subsidence rate of the area near the base of Johnston Ridge (fig. 7*A*). The four ERS-1/2 tracks are directly comparable in these time series, because they have similar look angles (table 1), and we assume that the deformation is dominated by vertical motion. In addition, the ENVISAT mode 2, track 156, time series confirms that the subsidence was continuing at least into 2004 at a similar rate. Subsidence near the mouth of Coldwater Lake (fig. 7*B*) and below Elk Rock (fig. 7*C*) may have decayed

Table 1. Characteristics of SAR data from Mount St. Helens, Washington, used in stacks and corresponding figures.

[Mode not shown for ERS-1/2 satellite data, which have only one mode. RADARSAT does not use track numbers. A, ascending; D, descending. Incidence angle is measured in degrees from vertical. Number of interferograms (igrams) indicates those used to construct the stack. Figure numbers correspond to this chapter.]

Satellite	Mode	Track	A or D	Incidence angle (deg)	Years spanned	Number of igrams	Figure No.
Preeruptive SAR data							
ERS-1/2	-	156	D	23.2	1992–2001	36	2
ERS-1/2	-	163	A	23.2	1993–2000	7	3
ERS-1/2	-	385	D	23.2	1992–2001	38	4
ERS-1/2	-	392	A	23.2	1995–2000	7	5
ENVISAT	IS 2	156	D	22.8	2003–2004	6	6
Coeruptive SAR data							
ENVISAT	IS 2	156	D	22.8	2004–2005	7	8
ENVISAT	IS 2	163	A	22.8	2004–2005	13	9
ENVISAT	IS 2	385	D	22.8	2004–2005	3[1]	10
ENVISAT	IS 2	392	A	22.8	2004–2005	6	11
ENVISAT	IS 6	20	A	40.9	2004–2005	13	12
RADARSAT	S 2	-	A	27.6	2004–2005	9	13
RADARSAT	S 5	-	A	39.1	2004–2005	6	14

[1] Note that all three input interferograms span 70 days or less.

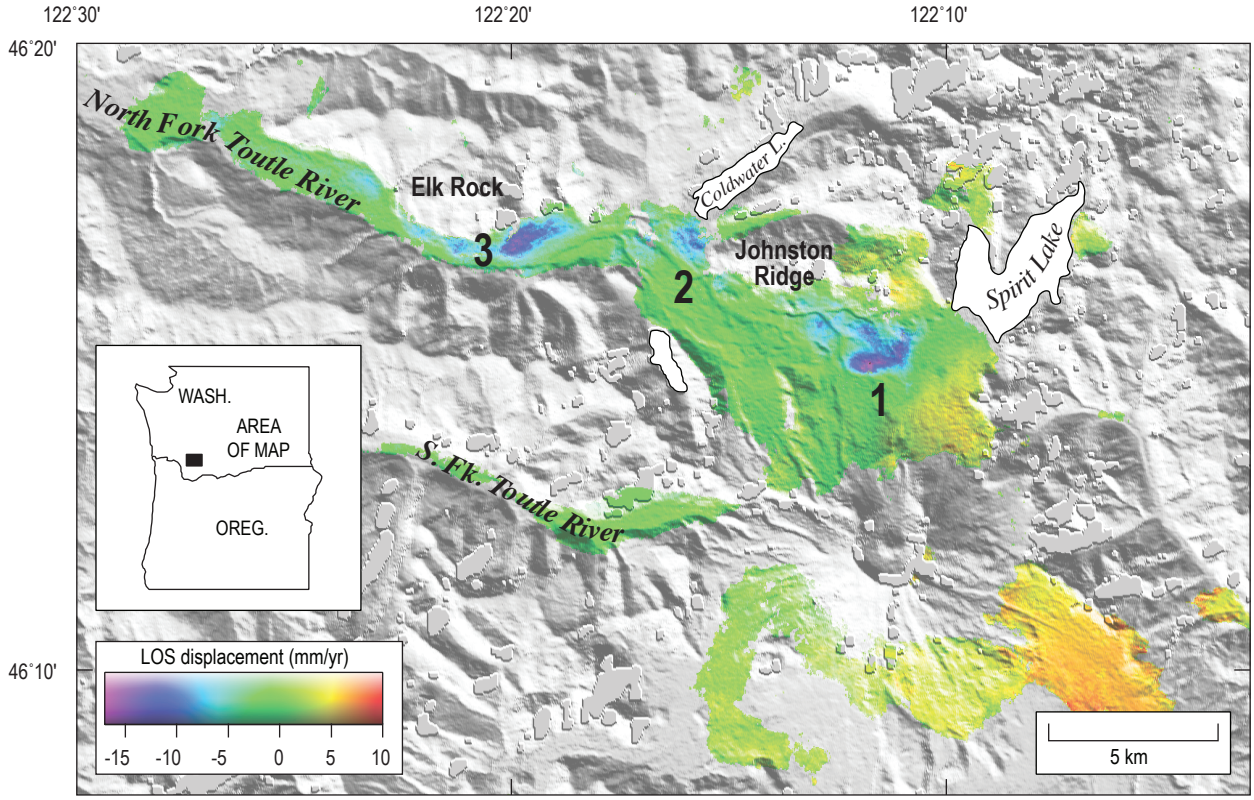

Figure 2. ERS-1/2, track 156, interferometric stack of Mount St. Helens, Washington, composed of 36 interferograms spanning preeruptive 1992–2001 period. Inset shows location of stack. Locations of major features referred to in the text are labeled. Image shows three areas of subsidence in debris-avalanche deposit—1 (Johnston Ridge), 2 (Coldwater), and 3 (Elk Rock).

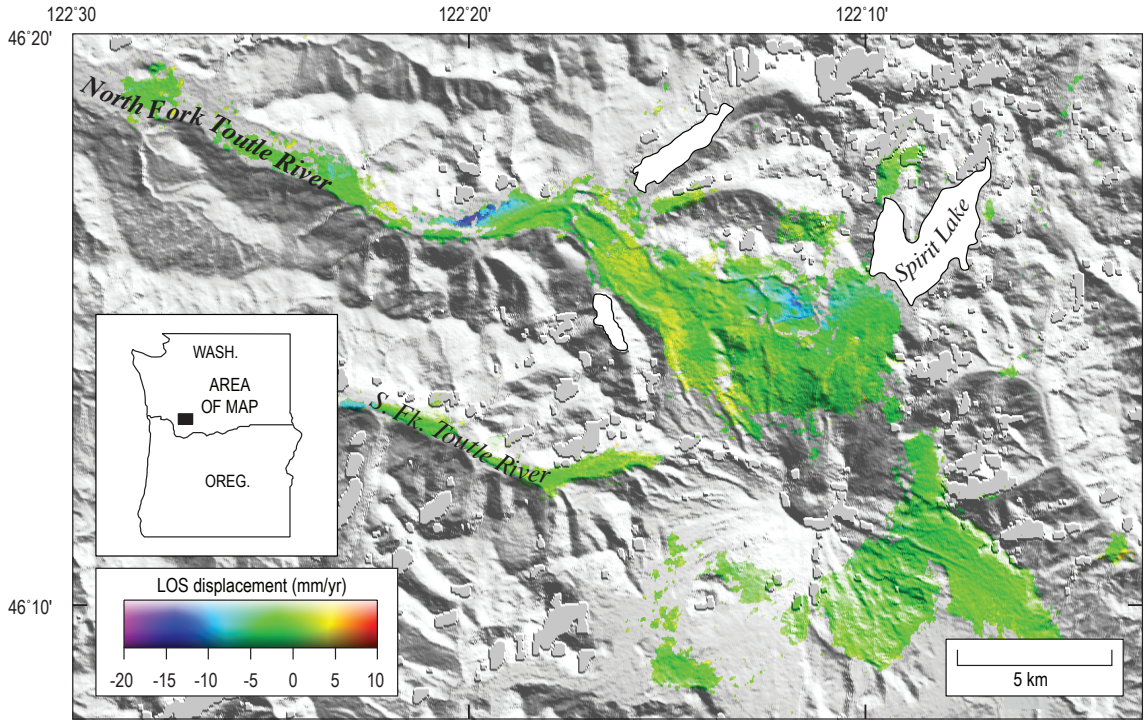

Figure 3. ERS-1/2, track 163, interferometric stack of Mount St. Helens, Washington, composed of seven interferograms spanning preeruptive 1993–2000 time period.

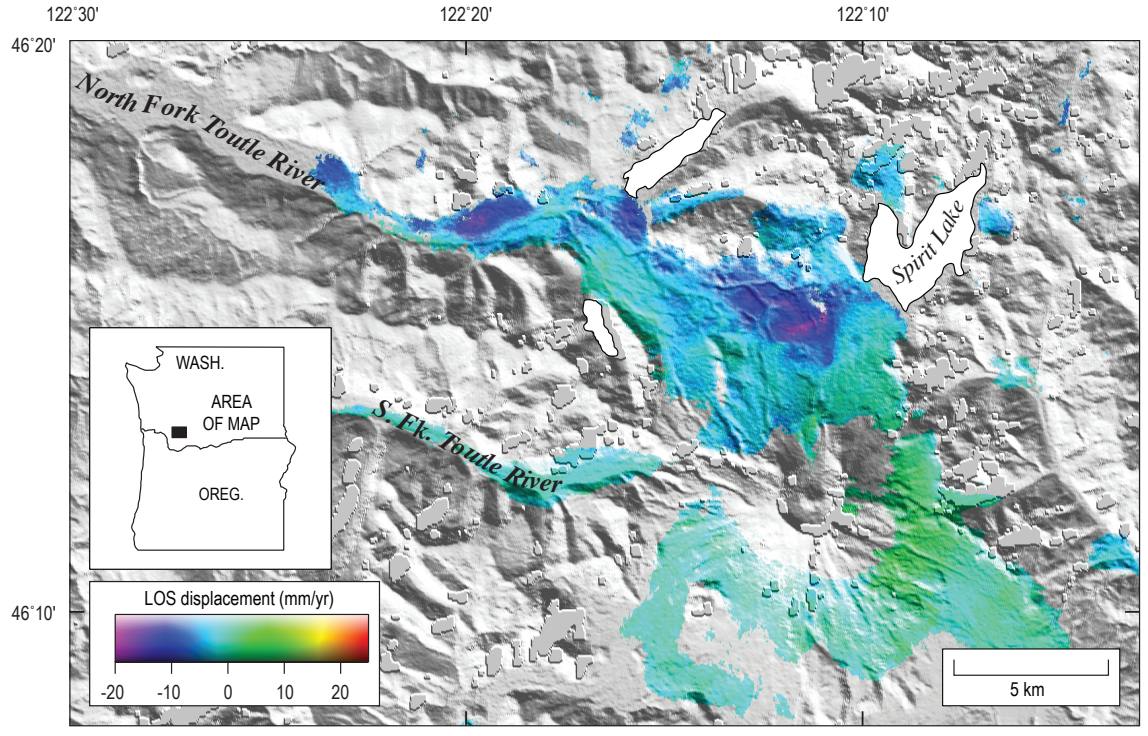

Figure 4. ERS-1/2, track 385, interferometric stack of Mount St. Helens, Washington, composed of 38 interferograms spanning preeruptive 1992–2001 time period.

slightly over the observation period, although the data are too noisy to be certain. Both regions, however, are apparent in coeruptive stacks that span 2004–5 (figs. 8–14), so neither area had ceased deforming by 2005.

Discussion

Lack of Preeruption Deformation

Dzurisin (2003) postulated that deep magma accumulation should precede volcanic unrest and eruption and might have gone undetected prior to the May 18, 1980, eruption of Mount St. Helens. He also suggested that InSAR is perhaps the best tool for detecting such deformation, as exemplified by discoveries of aseismic inflation at South Sister (Wicks and others, 2002) and Peulik (Lu and others, 2002b) volcanoes. Our results rule out surface displacements on the order of 1 cm or greater due to magma accumulation beneath Mount St. Helens between 1992 and late 2001 and between 2003 and the start of the 2004 eruption. It is unlikely that the period not covered by the InSAR stacks was the only time that displacements occurred; therefore, it is probable that no volcanowide

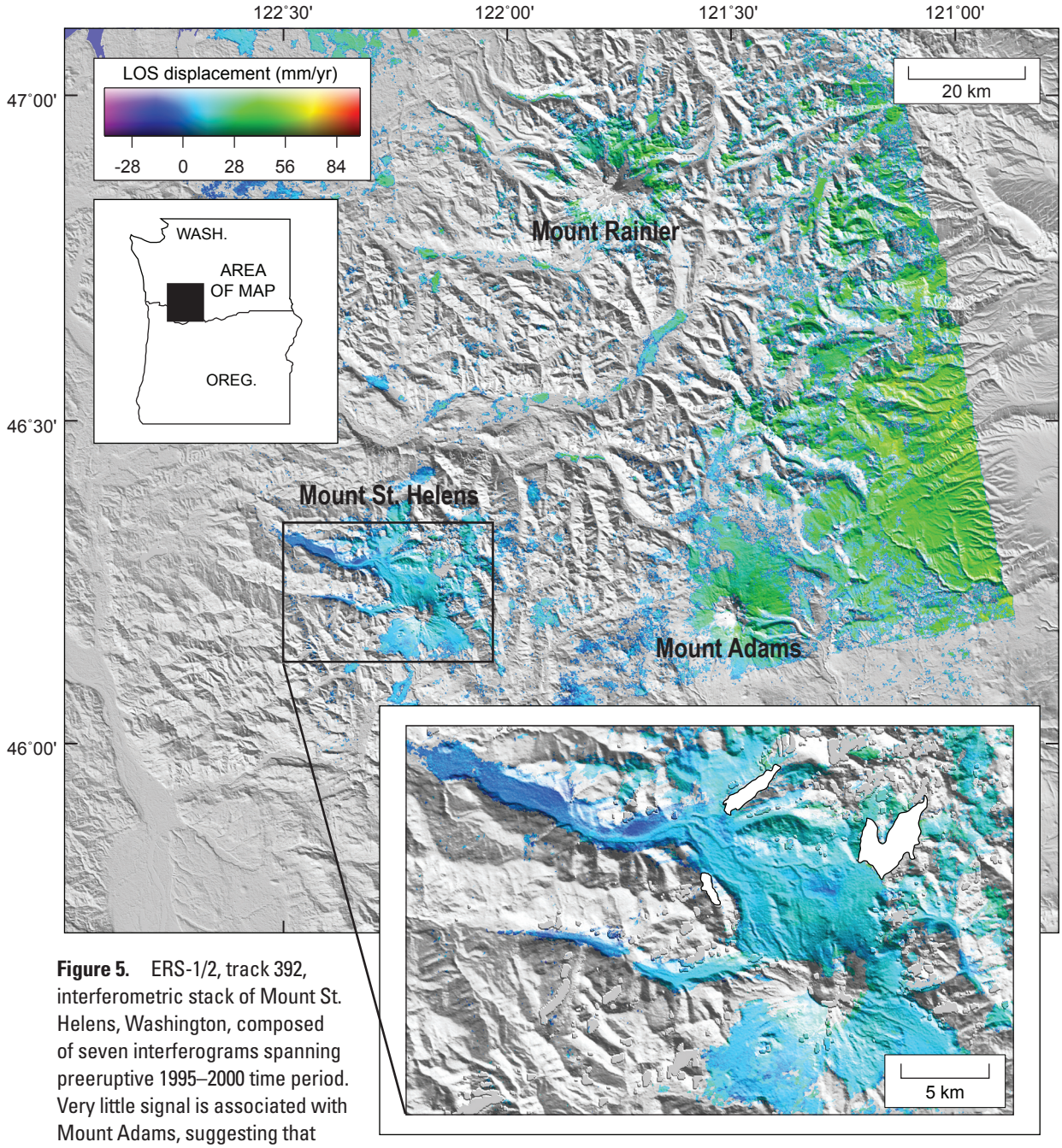

Figure 5. ERS-1/2, track 392, interferometric stack of Mount St. Helens, Washington, composed of seven interferograms spanning preeruptive 1995–2000 time period. Very little signal is associated with Mount Adams, suggesting that atmospheric artifacts are minimal.

displacements occurred during 1992–2004. How can this result be reconciled with Dzurisin's (2003) proposal?

Seismic and geodetic evidence from the late 1980s and early 1990s favor repressurization and possible resupply of the magma body located at about 6–10 km depth. Moran (1994) examined patterns of seismicity between 1987 and 1992 and concluded that the approximately 6- to 10-km-deep reservoir was being pressurized, probably by volatiles that exsolved during magma crystallization and were trapped beneath a seal in the shallow conduit. Seismicity, gas-emission events, and small explosions in 1989–91 may have been related to rupturing of this seal and escape of volatiles (Mastin, 1994). A seismic swarm in 1998 was accompanied by the emission of CO_2 (Gerlach and others, this volume, chap. 26), but whether this seismicity was related to magma migration or only the ascent of magmatic gases is unclear. Magma accumulation below 5.5 km depth is proposed by Musumeci and others (2002) to explain patterns of relocated seismicity. Lisowski and others (this volume, chap. 15) analyzed trilateration data collected in 1982 and 1991 and GPS data from 2000 and found evidence for areal dilatation between 1982 and 1991 that may indicate magma recharge. No significant changes were observed during the 1991–2000 time period. It is possible that magma was accumulating beneath Mount St. Helens only during the late 1980s and early 1990s and was manifested by deep seismicity, areal dilatation, and phreatic explosions (Mastin, 1994; Moran, 1994; Musumeci and others, 2002; Moran and others, this volume, chap. 2).

It seems that there is ample evidence for a pressure increase—either due to exsolution of volatiles, intrusion of new magma, or both—at ~6–10 km depth beneath Mount St. Helens in the years between the end of eruptive activity in 1986 and the start of the 2004 eruption. Changes in pressure or volume at this depth, if large enough, should result in displacements observable by InSAR because they would extend well outside the incoherent crater area without being overly broad or diffuse. The fact that no inflation was observed by InSAR during 1992–2004 (assuming that no deformation occurred during late 2001 to early 2003, when no InSAR data are available) suggests that either (1) the magnitude of volume increase (if magma accumulation occurred) or pressure increase (if only gas exsolution occurred) was insufficient to produce measurable surface displacements, (2) the increase in pressure or volume was accommodated by inelastic processes that did not deform the surface, or (3) the increase in pressure or volume occurred prior to 1992. Distinguishing among these mechanisms is not possible at present, although seismic and geodetic data (discussed above) that were collected after the end of the 1980–86 eruptive period and before InSAR results became available in 1992 favor option 3.

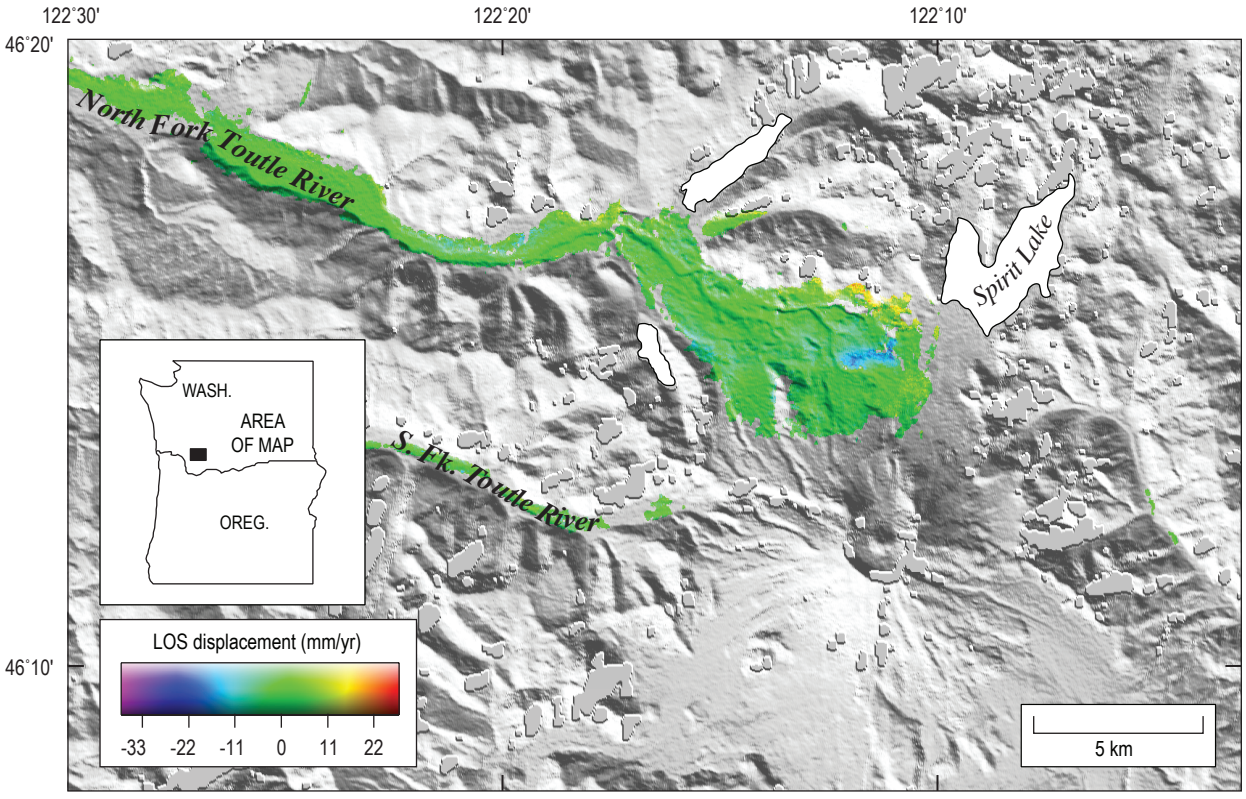

Figure 6. ENVISAT mode 2, track 156, interferometric stack of Mount St. Helens, Washington, composed of six interferograms spanning preeruptive 2003–2004 time period.

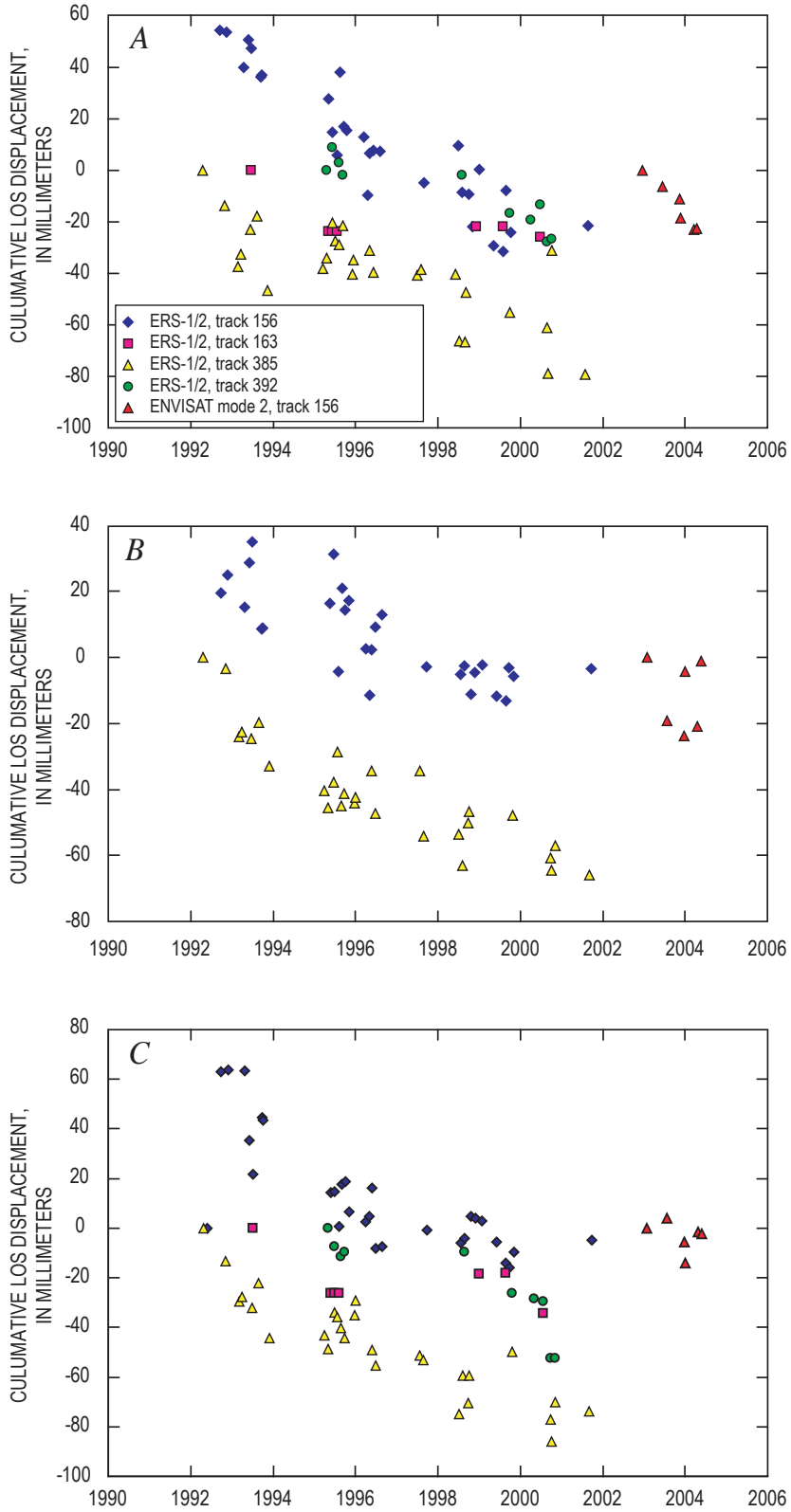

Figure 7. Time series showing line-of-sight (LOS) displacements of subsidence patches at (*A*) Johnston Ridge (site 1 in fig. 2), (*B*) Coldwater (site 2 in fig. 2), and (*C*) Elk Rock (site 3 in fig. 2). LOS displacements are relative to one another, so absolute value of Y axis is less important than changes in value over time. Note that more than 35 interferograms were used to generate time series for ERS tracks 156 and 385, whereas only 6–7 interferograms were used for ERS tracks 163 and 392, and ENVISAT track 156. Deformation rates determined from tracks with relatively few input interferograms could therefore be biased by atmospheric delay anomalies.

Subsidence Patches in the Debris-Avalanche Deposit

The origin of the localized subsidence patches on the debris-avalanche deposit is difficult to constrain and may be a result of several different processes. All three patches occur on the 1980 debris-avalanche deposit. Pyroclastic-flow deposits emplaced during explosive eruptions in 1980 bury the debris-avalanche unit at the base of Johnston Ridge near patch 1 but are not present at the other two patches (Rowley and others, 1981). The displacement patterns resemble poroelastic deformation caused by groundwater withdrawal (for example, Bawden and others, 2001), but there has been no deliberate removal of water from the debris-avalanche deposit. The subsidence has been occurring since at least 1992, and probably much longer, so subsidence mechanisms that occur on short time scales (days to months), including release of gas (Matthews and others, 2003), hydrocompaction due to rainfall (Hoblitt and others, 1985), and poroelastic deformation of the substrate (Lu and others, 2005a) cannot account for the longevity of the observed deformation and the lack of significant changes in subsidence rate over time (fig. 7). Instead, the deformation must be related to long-lived activity associated with the May 18, 1980, debris-avalanche deposit. Processes that have the potential to cause years-long subsidence of a loosely consolidated volcanic deposit like the Mount St. Helens debris-avalanche unit include cooling and contraction of an initially hot deposit (Masterlark and others, 2006), loading of a viscoelastic substrate (Briole and others, 1997; Stevens and others, 2001; Lu and others, 2005a; Masterlark and others, 2006), consolidation of a saturated or unusually dilated deposit (Major, 2000), and melting of buried ice (Branney and Gilbert, 1995; Everest and Bradwell, 2003).

The debris-avalanche deposit was emplaced onto a substrate of Tertiary volcanic rocks, with volcaniclastic sediments along river terraces of, and in, the upper part of the North Fork Toutle River valley and other drainages (Crandell, 1987; Evarts and others, 1987). The loosely consolidated debris-avalanche deposit has a volume of $2{,}500\times10^6$ m^3 and is composed mostly of cold dacite, andesite, and basalt, with probably less than 50×10^6 m^3 of the volume taken up by the hot (temperature greater than several hundred degrees Celsius) cryptodome that intruded the volcanic edifice in March–May 1980 (Voight and others, 1981; Glicken, 1996). The deposit reaches its maximum thickness, about 200 m, near the base of Johnston Ridge (but not at the exact location of the Johnston Ridge subsidence patch; Glicken, 1996). Glacial ice is thought to represent at least 100×10^6 m^3 of the volume of the unit (Brugman and Meier, 1981; Glicken, 1996). Much of this ice was buried by debris, and localized melting may have contributed to the formation of the North Fork Toutle River lahar on the afternoon of May 18, 1980 (Fairchild, 1987). Water derived from groundwater in the precollapse volcano and glacial ice incorporated into the debris avalanche amounted to approximately 250×10^6 m^3, about 12 percent of the total volume of the deposit (Glicken, 1996). A ground-water system developed in the unit following emplacement, as confirmed by numerous springs and seeps in the deposit, and seasonal changes in pond levels (J. Major, oral commun., 2006). Some parts of the debris-avalanche deposit were also saturated on emplacement, including two of the three patches of subsidence observed by InSAR (at the outlet of Coldwater Lake and below Elk Rock). The area below Elk Rock may have been the source of the May 18, 1980, North Fork Toutle River lahar (Fairchild, 1987; Glicken, 1996), and mud volcanoes caused by dewatering were observed near the outlet of Coldwater Lake in 1981 (J. Major, oral commun, 2006). In the weeks following May 18, 1980, Banks and Hoblitt (1996) measured the temperature of the deposit in shallow holes and found temperatures to be less than 100°C, with no increase in temperature below about 1.5 m. These data suggest that the maximum temperature of the deposit was no greater than boiling (Voight and others, 1981; Banks and Hoblitt, 1996), although temperatures probably varied widely depending on deposit composition (for example, shattered cryptodome versus cold volcanic edifice).

The initial emplacement temperature of the deposit would have to have been unreasonably high to cause subsidence due to cooling and contraction, as suggested by analogy with pyroclastic flows emplaced in 1986 at Augustine Volcano, Alaska. Masterlark and others (2006) used the known 3 cm/yr subsidence rate of Augustine's 1986 deposits (measured 13 years after the flows were emplaced) and the known maximum 126-m deposit thickness to model an initial temperature of 640°C. Decreasing the initial temperature to 500°C required a maximum pyroclastic-flow thickness of 336 m to produce the same subsidence rate. By analogy, the debris-avalanche deposit at Mount St. Helens would need to have an emplacement temperature of over 600°C to produce the subsidence observed by InSAR. Considering the small amount of hot cryptodome incorporated in the deposit and relatively low measured temperatures, it is unlikely that the temperature of significant volumes of the unit approached the required several hundred degrees.

Subsidence in response to a recently emplaced load occurs as the substrate relaxes viscoelastically beneath the load. The magnitude of the subsidence should be directly proportional to the size of the load and the thickness of the substrate (Briole and others, 1997). Subsidence patches on the Mount St. Helens debris-avalanche deposit, however, do not correlate with deposit thickness, although heterogeneity in pre-1980 surficial geology could still allow for subsidence due to loading. Loosely consolidated, relatively low-density sediment in and around the North Fork Toutle valley may be compacting under the load of the debris-avalanche deposit. Subsidence would occur only on parts of the debris-avalanche deposit that overlie accumulated sediment, explaining the patchiness of the subsidence and the fact that deformation occurs mostly where the unit lies near or above the buried channel and floodplains of the North Fork Toutle River. Testing this hypothesis is

difficult without additional knowledge of the thickness and extent of sedimentary deposits prior to the catastrophic debris avalanche of May 18, 1980.

Consolidation of granular deposits is a function of water content and diffusivity; compaction and subsidence occur in saturated deposits as water is removed (Major, 2000). Localized subsidence undoubtedly resulted as water seeped from saturated parts of the debris-avalanche deposit, and dewatering persisted through 2005 on the basis of springs and seeps found throughout the unit (J. Major, oral commun., 2006). Depending on the diffusivity and saturated thickness of the deposit, gravitational consolidation resulting from dewatering and diffusion of fluid pressure in excess of hydrostatic pressure could last for years, causing subsidence for decades after the deposit was emplaced (Major, 2000).

Melting of buried ice as a long-term subsidence mechanism could only occur if ice within the debris-avalanche deposit melted slowly over decades. In cold deposits (for example, the terminal moraine of a retreating glacier), buried ice can persist for hundreds of years (Everest and Bradwell, 2003). Could ice have survived more than 25 years buried in the Mount St. Helens debris-avalanche deposit? The answer depends on the deposit temperature and whether ice survived as large blocks or pulverized grains. If the entire deposit were initially about boiling (Banks and Hoblitt, 1996), there is little chance that even large blocks of ice (25–50 m in diameter) could have survived more than a few months after May 18, 1980 (Fairchild, 1987). Some parts of the debris-avalanche deposit were probably at ambient temperature, however, because much of the collapsed edifice, including most of the first landslide block, was composed of the cold outer skin of the volcano (including glacial ice; Glicken, 1996). Evidence for long-term survival of buried ice at Mount St. Helens is suggested by the discovery of subsurface ice during excavations near Spirit Lake by the U.S. Army Corps of Engineers almost 2 years after the May 18, 1980, eruption (Glicken, 1996). Slow melting of buried ice would account for the patchiness of the subsidence, as well as the lack of correlation between debris avalanche thickness and subsidence magnitude. There is, unfortunately, no way to know whether or not buried ice is the source of subsidence of the Mount St. Helens debris-avalanche deposit, but it remains a viable mechanism.

All of the possible subsidence mechanisms are asymptotic processes, meaning that subsidence rates of the debris-avalanche deposit patches should decay over time. No significant rate changes are apparent from the InSAR time series (fig. 7), so the mechanism of subsidence for the debris-avalanche deposit patches must be a long-term process, with changes in the rate of deformation requiring decades to manifest. Based on the temperature and composition of the debris-avalanche deposit and substrate, the observed patches of subsidence may be caused by differential compaction of sedimentary substrate along the buried North Fork Toutle River, gravitational consolidation of locally saturated or unusually dilated areas of the debris-avalanche deposit, or melting of buried ice. Using current knowledge, the relative contributions of these mechanisms cannot be determined; thus all three processes are viable causes for localized areas of subsidence on the May 18, 1980, debris-avalanche deposit.

Coeruptive stacks

Results

Unlike the preeruptive stacks, coeruptive stacks are inconsistent and heavily affected by atmospheric artifacts (figs. 8 through 14). The seven coeruptive stacks show all possible deformation patterns—no surface displacements, volcanowide inflation, and volcanowide deflation. Deflation of Mount St. Helens is suggested by ENVISAT mode 2, track 163 (fig. 9), ENVISAT mode 6, track 20 (fig. 12), and RADARSAT mode 2 (fig. 13). No deformation is apparent in the ENVISAT mode 2, track 156 (fig. 8), ENVISAT mode 2, track 385 (fig. 10), and ENVISAT mode 2, track 392 (fig. 11) stacks. Inflation, at least in two quadrants of the volcano, is indicated in the RADARSAT mode 5 (fig. 14) stack. These contradictory results can be reconciled by examining the character of the subsidence patch located at the base of Johnston Ridge, which was probably active during the coeruptive time period based on its persistence during the preeruptive interval and lack of decay over time (fig. 7*A*). This feature is only apparent in ENVISAT mode 2, track 163 (fig. 9), ENVISAT mode 6, track 20 (fig. 12), and the two RADARSAT beam modes (figs. 13 and 14). Stacks that do not show the subsidence patches are not sensitive to displacement rates of 2–3 cm/yr, on the same order as the expected volcanowide deflation signal measured by GPS (Lisowski and others, this volume, chap. 15).

The three interferograms that show volcanowide subsidence (figs. 9, 12, 13) are the stacks produced from at least nine input interferograms (table 1). We suspect that the averaged range changes in figures 8, 10, 11, and 14 are biased by atmospheric delay anomalies due to the limited number of interferograms used in the stacks. These stacks should not be considered for further analysis. Atmospheric delay artifacts in the stacks may also be recognized by topography-correlated fringes at presumably undeforming mountains also covered by the scenes (Beaudecel and others, 2000). Unfortunately, no mountains other than Mount St. Helens are coherent within, or covered by, the ENVISAT mode 2, track 163 (fig. 9) and ENVISAT mode 6, track 20 (fig. 12) stacks, and their quality cannot be assessed independently. Mount Adams, 60 km east of Mount St. Helens, has no associated phase-correlated topography in the RADARSAT mode 2 stack (fig. 13) which, together with the debris-avalanche subsidence patches also visible in that image, suggests that the stack is sensitive to deformation on the order of 1 cm/yr. As a result, the stack that is most representative of the coeruptive deformation state of Mount St. Helens is RADARSAT mode 2 (fig. 13). This stack suggests

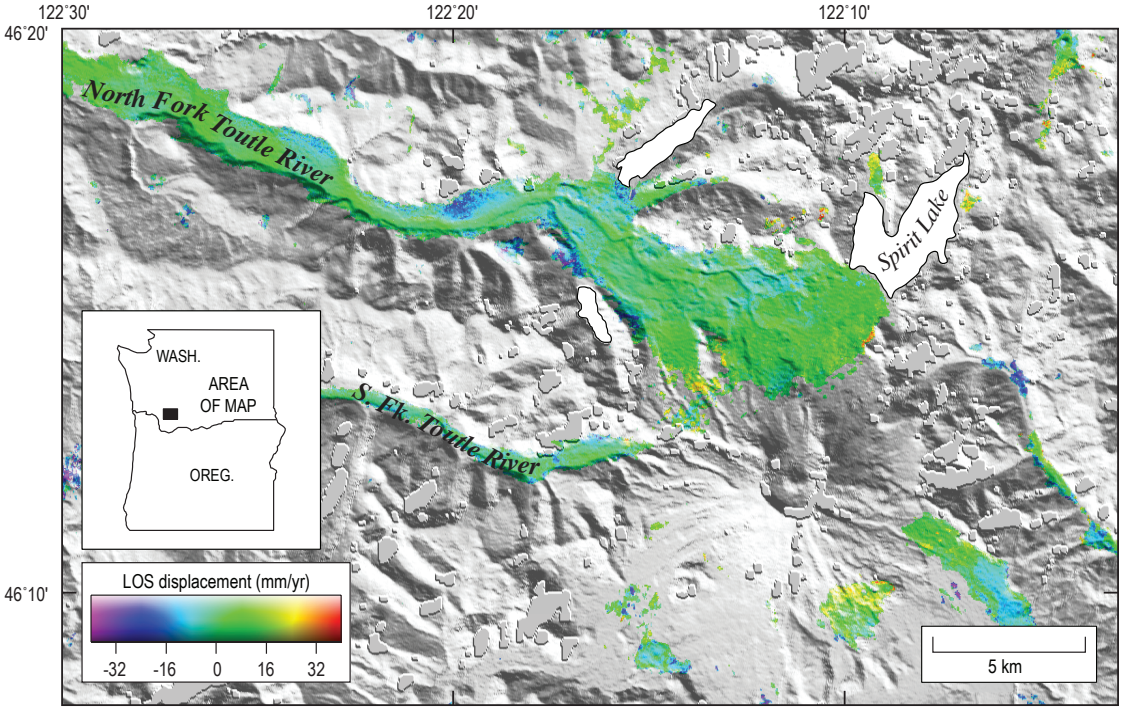

Figure 8. ENVISAT mode 2, track 156, interferometric stack of Mount St. Helens, Washington, composed of seven interferograms spanning coeruptive 2004–5 time period.

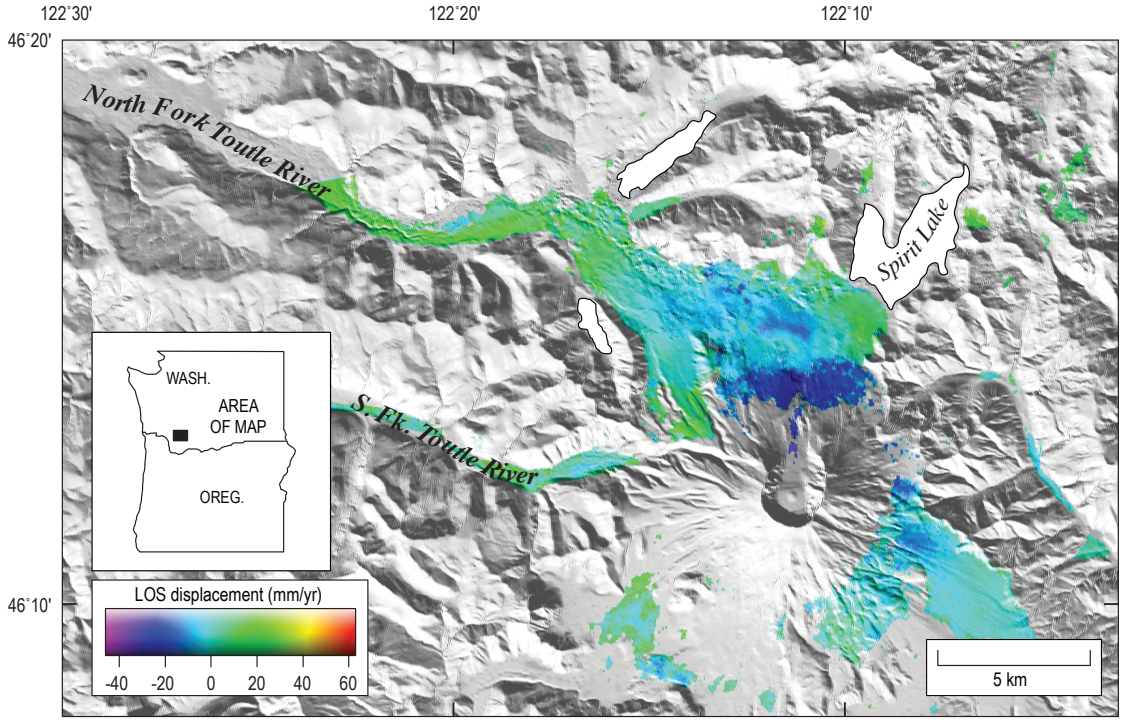

Figure 9. ENVISAT mode 2, track 163, interferometric stack of Mount St. Helens, Washington, composed of 13 interferograms spanning coeruptive 2004–5 time period.

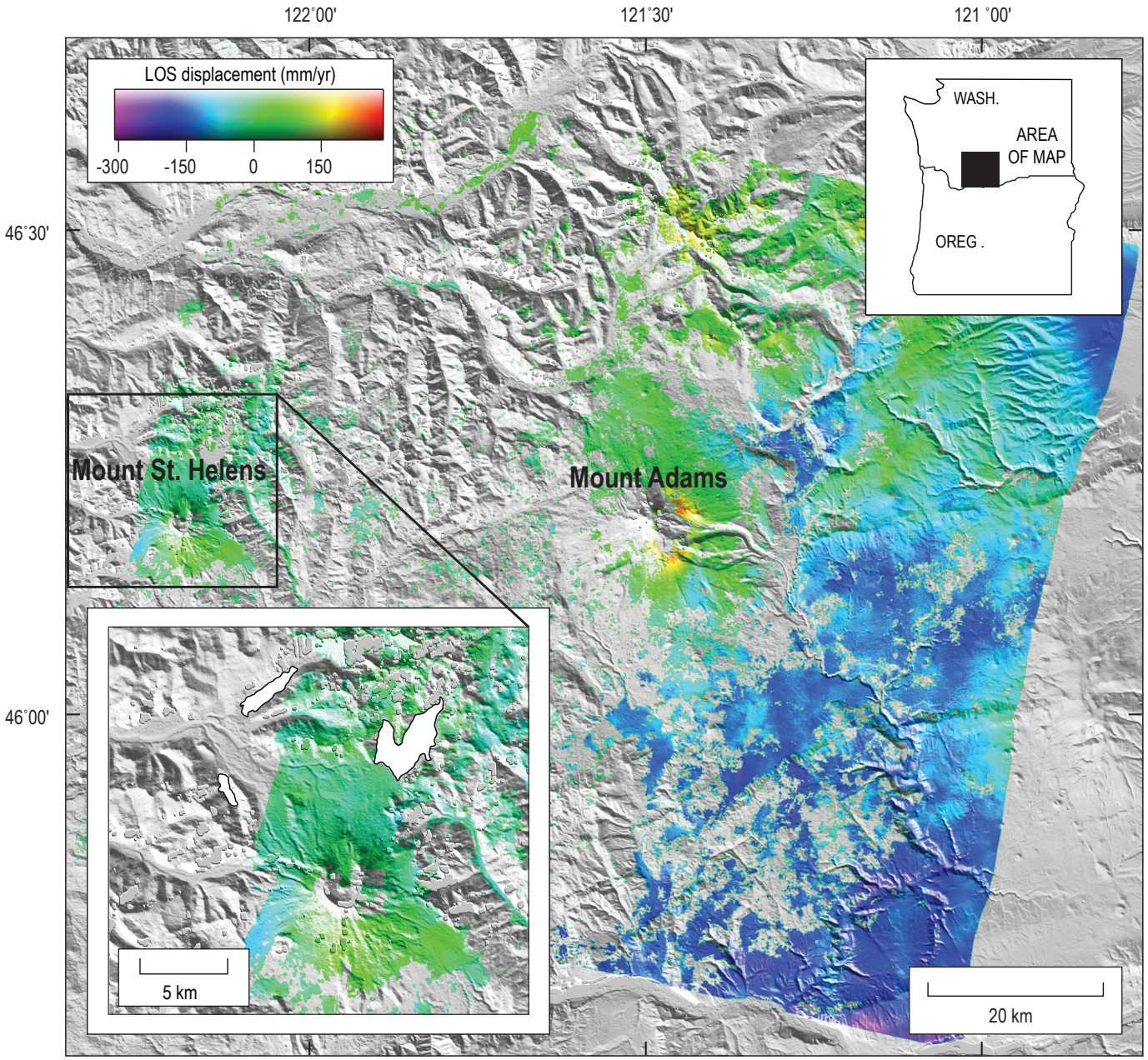

Figure 10. ENVISAT mode 2, track 385, interferometric stack of Mount St. Helens, Washington, composed of three interferograms spanning coeruptive 2004–5 time period. All three interferograms cover times of 70 days or fewer, so stacked phase has low signal-to-noise ratio and is characterized by phase that correlates with topography. This is especially apparent at Mount Adams.

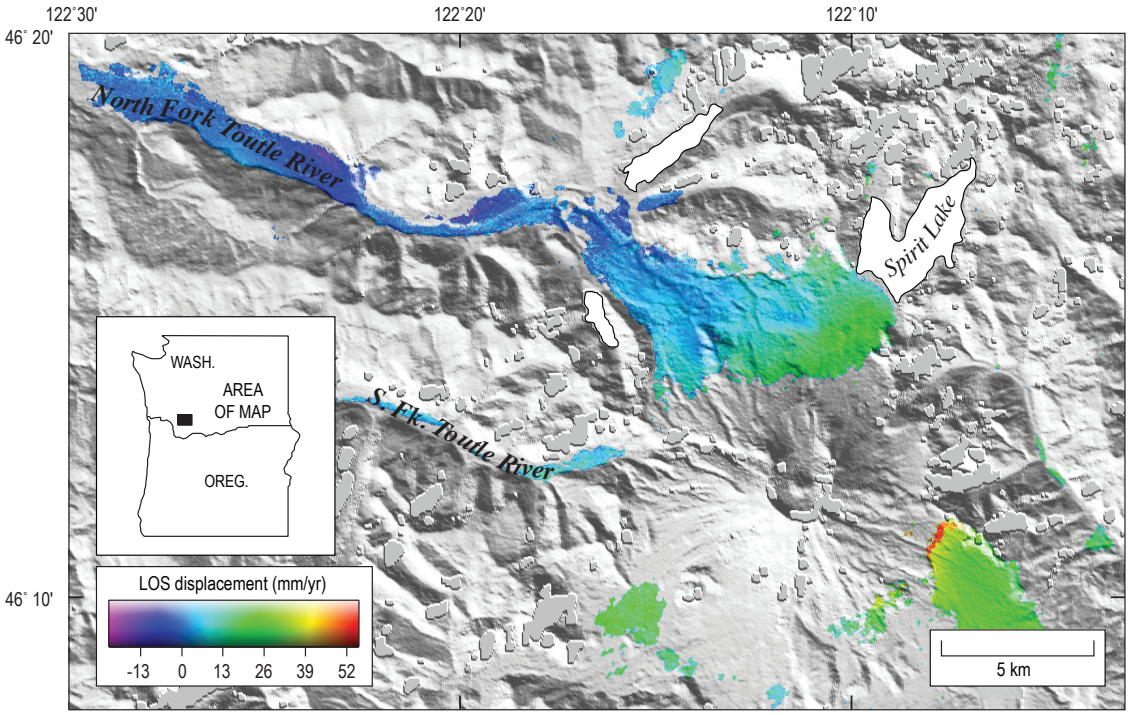

Figure 11. ENVISAT mode 2, track 392, interferometric stack of Mount St. Helens, Washington, composed of six interferograms spanning coeruptive 2004–5 time period.

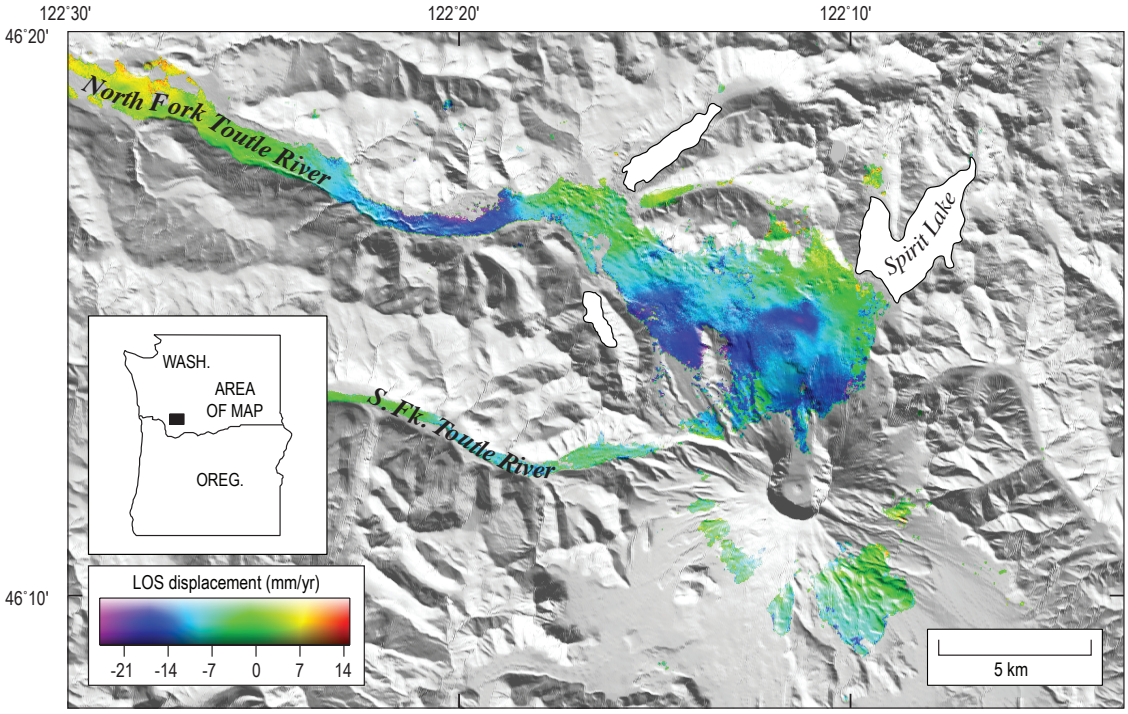

Figure 12. ENVISAT mode 6, track 20, interferometric stack of Mount St. Helens, Washington, composed of 13 interferograms spanning coeruptive 2004–5 time period.

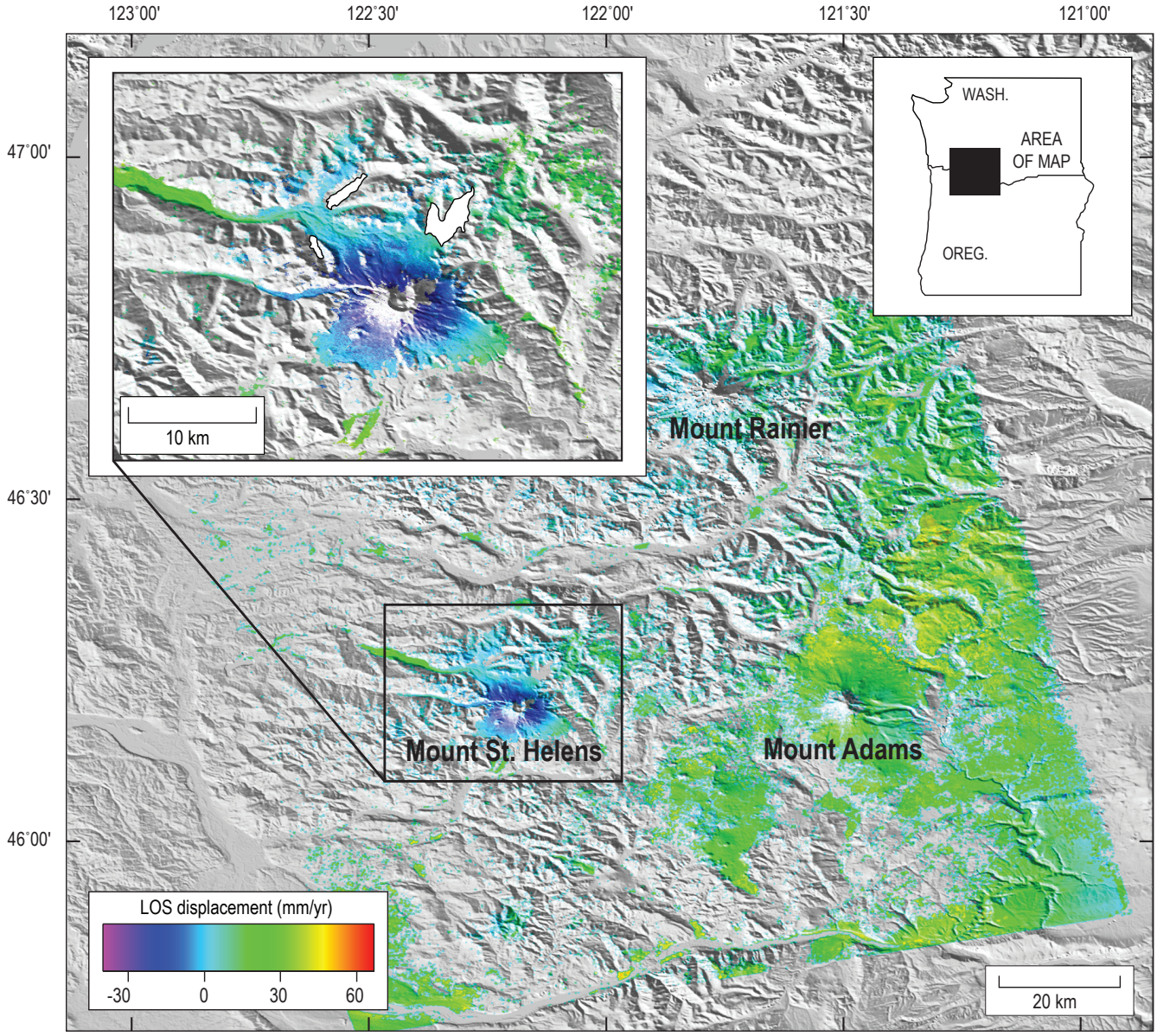

Figure 13. RADARSAT standard mode 2 ascending interferometric stack of Mount St. Helens, Washington, composed of nine interferograms spanning coeruptive 2004–5 time period. Stack clearly shows line-of-sight lengthening (subsidence) centered on Mount St. Helens which, as discussed in text, most likely reflects deformation of the ground surface. Atmospheric artifacts are probably minimized, as suggested by the lack of a significant signal associated with Mount Adams.

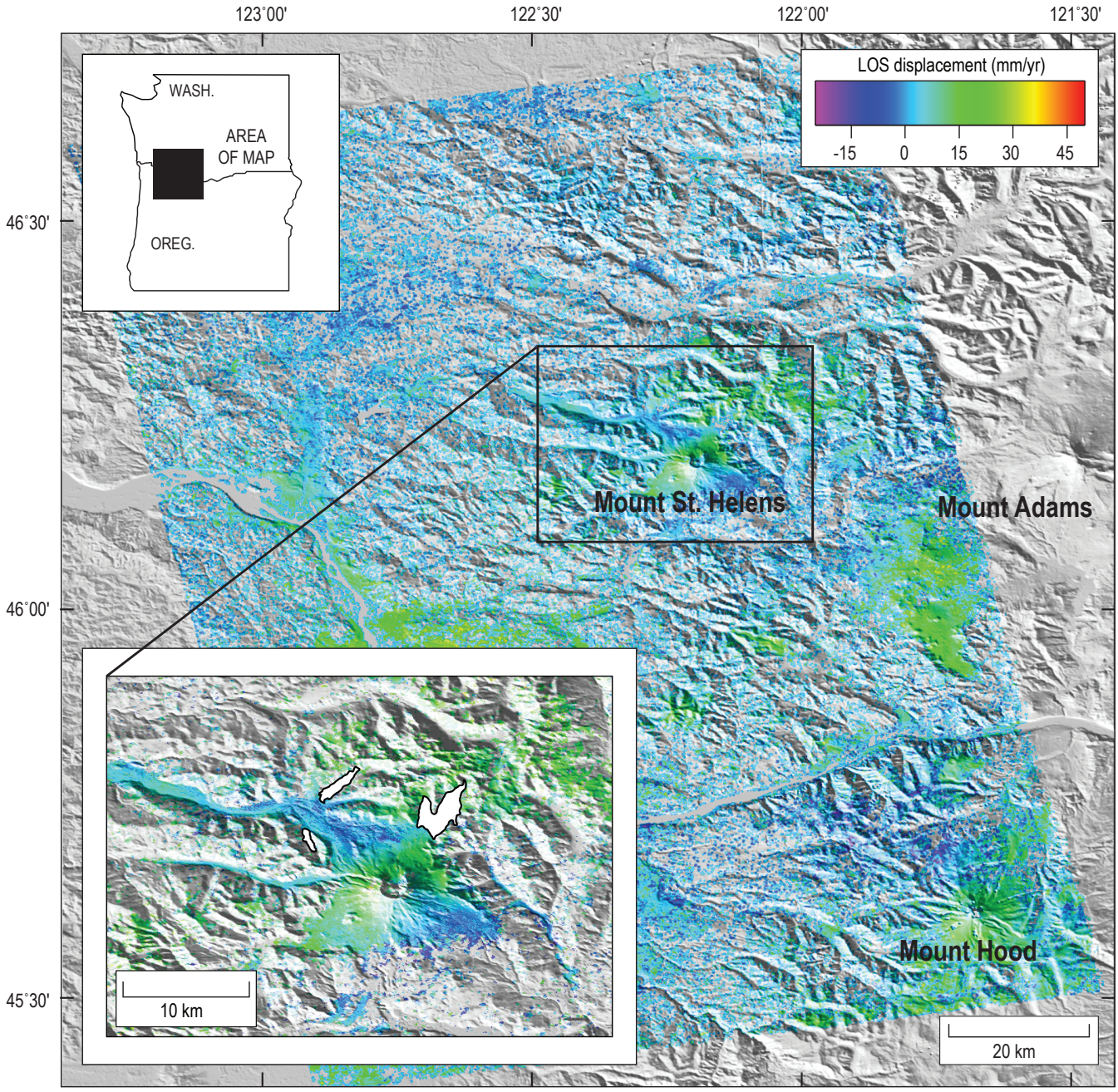

Figure 14. RADARSAT standard mode 5 ascending interferometric stack of Mount St. Helens, Washington, composed of six interferograms spanning coeruptive 2004–5 time period. Topography-correlated phase at Mount Hood suggests the presence of atmospheric artifacts in the stack.

LOS lengthening (subsidence) of at least 40–50 mm/yr centered on Mount St. Helens (the maximum is probably greater but not recoverable given the incoherence in the crater) and extends radially outwards beyond the flanks of the volcano.

Discussion

We modeled the RADARSAT mode 2 dataset (fig. 13) by inverting the LOS displacements for a buried point source of volume change (Mogi, 1958). Other types of sources (for example, an ellipsoid or circular crack) might yield a better fit to the data, but it is difficult to justify the use of more complicated source geometries in light of the limited coherence around Mount St. Helens, especially in the crater area where the deformation appears to reach a maximum. The best-fitting point source is located at a depth of 12 km directly beneath the crater of Mount St. Helens and has a volume loss of 27×10^6 m^3/yr (fig. 15). The depth compares favorably with a point source model based on GPS data (Lisowski and others, this volume, chap. 15), but it is deeper than more-complicated ellipsoidal source models (Lisowski and others, this volume, chap. 15; Mastin and others, this volume, chap. 22) and the 6–10-km-depth range for a proposed magma reservoir based on seismic data (Scandone and Malone, 1985; Barker and Malone, 1991; Moran, 1994; Musumeci and others, 2002). The greater InSAR-derived model depth is probably due to the lack of InSAR data in the crater area and the availability of only a single component of displacement from one interferometric stack.

We also modeled the data using a horizontal dislocation (Okada, 1985) constrained to uniform opening only, which approximates a sill. The best-fitting dislocation was located at a depth of 18 km, much deeper than the point source, but it had a similar volume change of about 30×10^6 m^3/yr. The difference in depths between the point source and dislocation models is unsurprising. A similar relation, for example, was found between point source and horizontal dislocation models of subsidence at Medicine Lake volcano, northern California (Dzurisin and others, 2002). The great variability in depths between the models is an indication of the strong dependence of model fits on model geometry (Delaney and McTigue, 1994). More data, especially from the crater region where displacement magnitudes are greatest, and varied look angles, which would provide additional components of displacement, are required to better constrain the geometry, volume change, and depth of the subsidence source, as well as model error estimates. Using only a single interferometric stack, results are unavoidably more ambiguous.

The modeled volume change is much smaller than the approximately 70×10^6 m^3 extruded over the first year of the eruption, as determined from analyses of digital elevation models (Schilling and others, this volume, chap. 8). Some of the difference may be explained by the fact that the stack averages the initially greater rates of subsidence and extrusion that occurred during the first few weeks of the eruption, but this is probably a minor effect. It is tempting to speculate that most of the discrepancy between modeled and extruded volumes is evidence for replenishment of the midcrustal magma reservoir by an even deeper source. Delaney and McTigue (1994), however, pointed out that the volume of injection should only equal the volume of eruption if the host rock is incompressible—clearly an unrealistic condition. They also demonstrated that modeled volume changes at depth are highly dependent on source geometry. In addition, our models assume a homogenous, isotropic, elastic rheology, which is almost certainly not the case beneath Mount St. Helens, where temperatures will be

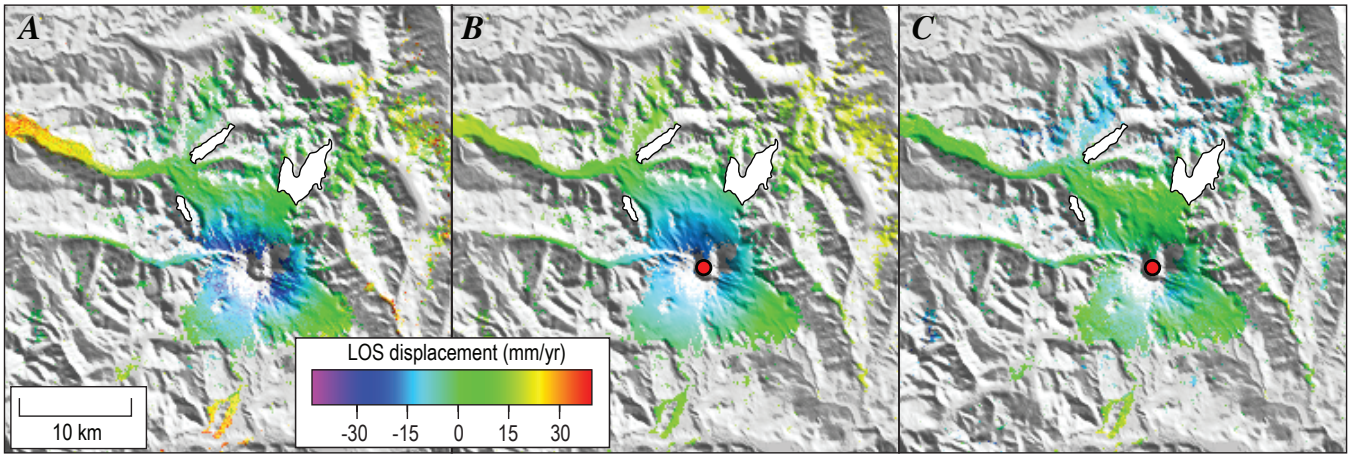

Figure 15. Observed (*A*), predicted (*B*), and residual (*C*) line-of-sight (LOS) displacements for RADARSAT standard mode 2 stack of Mount St. Helens, Washington (fig. 13), resulting from model that assumes point source of volume decrease (red circle) at depth of 12 km. LOS displacements scaled to maximize displacements around Mount St. Helens and differ from those in figure 13 for same interferogram.

elevated above the local geotherm due to the presence of the active magmatic system. Nonelastic rheologies can have a profound effect on the relation between surface deformation volume and source volume or pressure change (for example, Newman and others, 2001, 2006).

Nevertheless, it remains possible that the midcrustal magma reservoir was being replenished during the eruption, and that the discrepancy between modeled and extruded volumes was due to magma extrusion outpacing influx into the reservoir. Any surface inflation that might have resulted from recharge of the reservoir would have been masked by the greater deflation signal resulting from magma withdrawal and depressurization. Mastin and others (this volume, chap. 22) address this possibility in greater detail.

Conclusions

Interferograms from several independent tracks have been examined for signs of pre-and coeruptive deformation at Mount St. Helens. We can find no evidence for volcano-wide displacements during time periods covered by stacks of radar interferograms (1992 to late 2001 and early 2003 until the onset of eruptive activity in September 2004). Seismic and geodetic evidence suggests repressurization, and possible resupply, of the 6- to 10-km-depth magma reservoir during the late 1980s and early 1990s, but this activity did not result in surface deformation detectable by InSAR during 1992–2004. We did find several small (1–2-km-diameter) patches of subsidence on the 1980 debris-avalanche deposit, one of which was recognized previously from individual interferograms of Mount St. Helens, and attribute this deformation to viscoelastic relaxation of loosely consolidated substrate under a load, differential consolidation of the deposit, or melting of ice buried within the deposit. Tracking the continued motion of these areas will serve as input for models of the post-depositional behavior of rapidly emplaced, unconsolidated deposits.

Coeruptive interferometric stacks are dominated by atmospheric noise, and only one of the seven stacks we assembled is demonstrably sensitive to deformation on the order of 1 cm or less. This stack indicates volcanowide deflation centered on the crater of Mount St. Helens and can be modeled by a point source of volume loss at a depth of 12 km beneath the edifice. This depth is at the lower boundary of a magma reservoir inferred from seismicity before 2004.

Both the pre- and coeruptive InSAR results have important implications for magma resupply, or lack thereof, before and during the 2004 eruption. Several papers in this volume address this question from differing perspectives and reach differing conclusions (for example, Moran and others, chap. 2; Dzurisin and others, chap. 14; Lisowski and others, chap. 15; Mastin and others, chap. 22; Gerlach and others, chap. 26; Pallister and others, chap. 30). Neither InSAR nor any other single data set can resolve the issue with certainty, but the weight of evidence seems to favor at least a minor amount of magma influx or pressurization of the midcrustal magma reservoir in the years before, and perhaps during, the eruption. The InSAR results, although not directly supportive of the idea, can be reconciled with it if the preeruption changes were small enough, accommodated by inelastic processes that did not measurably deform the surface, or occurred before 1992, and if the coeruption changes reflect a net deflation of the volcano due to extrusion outpacing recharge.

It is worth noting that, in general, the RADARSAT results are more coherent than those from ERS-1/2 and ENVISAT. A possible explanation for this discrepancy is that RADARSAT's H/H polarization provides better coherence in vegetated areas than V/V, which is the standard mode for ERS-1/2 and ENVISAT. Additional investigations into this possibility are warranted, as the result may suggest that one polarization mode is preferred over others for InSAR studies.

Our work has demonstrated the importance of including numerous interferograms in stacks. Coeruption stacks with less than nine input interferograms showed no signs of deflation that is known to be occurring from GPS. That our preeruption stacks span many more years and make use of many more interferograms than the coeruption stacks is the reason for the better signal-to-noise ratio in the preeruption stacks. The addition to the coeruptive stacks of InSAR data that extend through 2006 and beyond, assuming the eruption continues, will significantly reduce the magnitude of the atmospheric noise, allowing for more detailed analysis of surface deformation and associated source mechanisms.

Acknowledgments

Summer Miller provided invaluable assistance in preparing the ERS-1/2 and ENVISAT data sets for stacking. Paul Lundgren provided code for time series analysis, which Sarah Menassian modified for use with this project. Rick Hoblitt and Don Swanson offered much-needed guidance with respect to the emplacement of the Mount St. Helens debris avalanche, and discussions with Jon Major, Dick Iverson, and Joe Walder stimulated a closer look at the subsidence patches in the debris-avalanche deposit. Jon Major's advice concerning the behavior of saturated sedimentary deposits was especially valuable. Oh-Ig Kwoun assisted with processing RADARSAT data. We are indebted to Chuck Wicks, Daniel Dzurisin, and Seth Moran for thoughtful reviews and Jane Takahashi for thorough edits. Figures 1–6 and 8–15 were made using the Generic Mapping Tools (GMT) software (Wessel and Smith, 1998). ERS-1, ERS-2, and ENVISAT SAR data are copyrighted 1992–2005 by ESA and provided by Alaska Satellite Facility (ASF) and ESA Category-1 grants 2648 and 2765. RADARSAT-1 data are copyrighted by Canadian Space Agency and were provided by ASF. We thank the ASF for supporting RADARSAT-1 data acquisitions.

References Cited

Amelung, F., Jónsson, S., Zebker, H., and Segall, P., 2000a, Widespread uplift and 'trapdoor' faulting on Galápagos volcanoes observed with radar interferometry: Nature, v. 407, no. 6807. p. 993–996.

Amelung, F., Oppenheimer, C., Segall, P., and Zebker, H., 2000b, Ground deformation near Gada 'Ale Volcano, Afar, observed by radar interferometry: Geophysical Research Letters, v. 27, no. 19, p. 3093–3096.

Banks, N.G., and Hoblitt, R.P., 1996, Direct temperature studies of the Mount St. Helens deposits, 1980–1981: U.S. Geological Survey Professional Paper 1387, 76 p.

Barker, S.E., and Malone, S.D., 1991, Magmatic system geometry at Mount St. Helens modeled from the stress field associated with posteruptive earthquakes: Journal of Geophysical Research, v. 96, no. B7, p. 11883–11894.

Bawden, G.W., Thatcher, W., Stein, R.S., Hudnit, K.W., and Peltzer, G., 2001, Tectonic contraction across Los Angeles after removal of groundwater pumping effects: Nature, v. 412, no. 6849, p. 812–815.

Beaudecel, F., Briole, P., and Froger, J.-L., 2000, Volcano-wide fringes in ERS synthetic aperture radar interferograms of Etna (1992–1998); deformation or tropospheric effect?: Journal of Geophysical Research, v. 105, no. B7, p. 16391–16402.

Berardino, P., Fornaro, G., Lanari, R., and Sansosti, E., 2002, A new algorithm for surface deformation monitoring based on small baseline differential SAR interferograms: IEEE Transactions on Geoscience and Remote Sensing, v. 40, no. 11, p. 1–10.

Bevington, P.R., and Robinson, D.K., 1992, Data reduction and error analysis for the physical sciences (2d ed.): Boston, McGraw-Hill, 328 p.

Branney, M.J., and Gilbert, J.S., 1995, Ice-melt collapse pits and associated features in the 1991 lahar deposits of Volcán Hudson, Chile—criteria to distinguish eruption-induced glacier melt: Bulletin of Volcanology, v. 57, no. 5, p. 293–302.

Briole, P., Massonnet, D., and Delacourt, C., 1997, Post-eruptive deformation associated with the 1986–87 and 1989 lava flows of Etna detected by radar interferometry: Geophysical Research Letters, v. 24, no. 1, p. 37–40.

Brugman, M.M., and Meier, M.F., 1981, Response of glaciers to the eruptions of Mount St. Helens, *in* Lipman, P.W., and Mullineaux, D.R., eds., The 1980 eruptions of Mount St. Helens, Washington: U.S. Geological Survey Professional Paper 1250, p. 743–756.

Cashman, K.V., 1988, Crystallization of Mount St. Helens 1980–1986 dacite: a quantitative textural approach: Bulletin of Volcanology, v. 50, no. 3, p. 194–209.

Cashman, K.V., 1992, Groundmass crystallization of Mount St, Helens dacite, 1980–1986; a tool for interpreting shallow magmatic processes: Contributions to Mineralogy and Petrology, v. 109, no. 4, p. 431–449, doi:10.1007/BF00306547.

Chen, C.W., and Zebker, H.A., 2001, Two-dimensional phase unwrapping with use of statistical models for cost functions in nonlinear optimization: Journal of the Optical Society of America A, v. 18, no. 2, p. 338–351.

Crandell, D.R., 1987, Deposits of pre-1980 pyroclastic flows and lahars from Mount St. Helens volcano, Washington: U.S. Geological Survey Professional Paper 1444, 91 p.

Delaney, P.T., and McTigue, D.F., 1994, Volume of magma accumulation or withdrawal estimated from surface uplift or subsidence, with application to the 1960 collapse of Kilauea Volcano: Bulletin of Volcanology, v. 56, nos. 6–7, p. 417–424.

Diefenbach, A.K., and Poland, M.P., 2003, InSAR analysis of surface deformation at Mount St. Helens, Washington [abs.]: Geological Society of America Abstracts with Programs, v. 35, no. 6, p. 562.

Dzurisin, D., 2003, A comprehensive approach to monitoring volcano deformation as a window on the eruption cycle: Reviews of Geophysics, v. 41, no. 1, 29 p., doi:1010,1029/2001RG000107.

Dzurisin D., Poland, M.P., and Bürgmann, R., 2002, Steady subsidence of Medicine Lake volcano, northern California, revealed by repeated leveling surveys: Journal of Geophysical Research, v. 107, no. B12, doi:10.1029/2001JB000893.

Dzurisin, D., Lisowski, M., Wicks, C.W., Jr., Poland, M.P., and Endo, E.T., 2006, Geodetic observations and modeling of ongoing inflation at the Three Sisters volcanic center, central Oregon Cascade Range, USA: Journal of Volcanology and Geothermal Research, v. 150, nos. 1–3, p. 35–54.

Dzurisin, D., Lisowski, M., Poland, M.P., Sherrod, D.R., and LaHusen, R.G., 2008, Constraints and conundrums resulting from ground-deformation measurements made during the 2004–2005 dome-building eruption of Mount St. Helens, Washington, chap. 14 *of* Sherrod, D.R., Scott, W.E., and Stauffer, P.H., eds., A volcano rekindled; the renewed eruption of Mount St. Helens, 2004–2006: U.S. Geological Survey Professional Paper 1750 (this volume).

Evarts, R.C., Ashley, R.P., and Smith, J.G., 1987, Geology of the Mount St. Helens area: Record of discontinuous volcanic and plutonic activity in the Cascade arc of southern Washington: Journal of Geophysical Research, v. 92, no. B10, p. 10155–10169.

Everest, J., and Bradwell, T., 2003, Buried glacier ice in southern Iceland and its wider significance: Geomorphology, v. 52, nos. 3–4, p. 347–358

Farr, T.G., and Kobrick, M., 2000, Shuttle Radar Topography Mission produces a wealth of data: Eos (American Geophysical Union Transactions), v. 81, no. 48, p. 583, 585.

Fairchild, L.H., 1987, The importance of lahar initiation processes, *in* Costa, J.E., and Wieczorek, G.F., eds., Debris flows/avalanches—processes, recognition, and mitigation: Geological Society of America Reviews in Engineering Geology 7, p. 51–61.

Fialko, Y., and Simons, M., 2001, Evidence for on-going inflation of the Socorro magma body, New Mexico, from Interferometric Synthetic Aperture Radar imaging: Geophysical Research Letters, v. 28, no. 18, p. 3549–3552.

Gerlach, T.M., McGee, K.A., and Doukas, M.P., 2008, Emission rates of CO_2, SO_2, and H_2S, scrubbing, and preeruption excess volatiles at Mount St. Helens, 2004–2005, chap. 26 *of* Sherrod, D.R., Scott, W.E., and Stauffer, P.H., eds., A volcano rekindled; the renewed eruption of Mount St. Helens, 2004–2006: U.S. Geological Survey Professional Paper 1750 (this volume).

Glicken, H., 1996, Rockslide-debris avalanche of May 18, 1980, Mount St. Helens volcano, Washington: U.S. Geological Survey Open-File Report 96–677, 90 p.

Goldstein, R.M., and Werner, C.L., 1998, Radar interferogram filtering for geophysical applications: Geophysical Research Letters, v. 25, no. 21, p. 4035–4038.

Hoblitt, R.P., Reynolds, R.L., and Larson, E.E., 1985, Suitability of nonwelded pyroclastic-flow deposits for studies of magnetic secular variation—a test based on deposits emplaced at Mount St. Helens, Washington, in 1980: Geology, v. 13, no. 4, p. 242–245.

Hooper, A., Zebker, H., Segall, P., and Kampes, B., 2004, A new method for measuring deformation on volcanoes and other natural terrains using InSAR persistent scatterers: Geophysical Research Letters, v. 31, no. 23, doi:10.1029/2004GL021737.

LaHusen, R.G., Swinford, K.J., Logan, M., and Lisowski, M., 2008, Instrumentation in remote and dangerous settings; examples using data from GPS "spider" deployments during the 2004–2005 eruption of Mount St. Helens, Washington, chap. 16 *of* Sherrod, D.R., Scott, W.E., and Stauffer, P.H., eds., A volcano rekindled; the renewed eruption of Mount St. Helens, 2004–2006: U.S. Geological Survey Professional Paper 1750 (this volume).

Lees, J.M., 1992, The magma system of Mount St. Helens; nonlinear high-resolution P-wave tomography: Journal of Volcanology and Geothermal Research, v. 53, nos. 1–4, p. 103–116.

Lisowski, M., Dzurisin, D., Endo, E.T., Iwatsubo, E.Y., and Poland, M.P., 2003, New results from a proposed PBO Cascade Volcano cluster III; post-eruptive deformation of Mount St. Helens, Washington, from EDM and GPS [abs.]: Geological Society of America Abstracts with Programs, v. 35, no. 6, p. 562.

Lisowski, M., Dzurisin, D., Denlinger, R.P., and Iwatsubo, E.Y., 2008, Analysis of GPS-measured deformation associated with the 2004–2006 dome-building eruption of Mount St. Helens, Washington, chap. 15 *of* Sherrod, D.R., Scott, W.E., and Stauffer, P.H., eds., A volcano rekindled; the renewed eruption of Mount St. Helens, 2004–2006: U.S. Geological Survey Professional Paper 1750 (this volume).

Lu, Z., Wicks, C.W., Jr., Power, J.A., and Dzurisin, D., 2000, Ground deformation associated with the March 1996 earthquake swarm at Akutan volcano, Alaska, revealed by satellite radar interferometry: Journal of Geophysical Research, v. 105, no. B9, p. 21483–21495.

Lu, Z., Power, J.A., McConnell, V.S., Wicks, C.W., Jr., and Dzurisin, D., 2002a, Preeruptive inflation and surface interferometric coherence characteristics revealed by satellite radar interferometry at Makushin Volcano, Alaska, 1993–2000: Journal of Geophysical Research, v. 107, no. B11, doi:10.1029/2001JB000970.

Lu, Z., Wicks, C.W., Jr., Dzurisin, D., Power, J.A., Moran, S.C., and Thatcher, W., 2002b, Magmatic inflation at a dormant stratovolcano; 1996–1998 activity at Mount Peulik volcano, Alaska, revealed by satellite radar interferometry: Journal of Geophysical Research, v. 107, no. B7, doi:10.1029/2001JB000471.

Lu, Z., Masterlark, T., Dzurisin, D., Rykhus, R., and Wicks, C.W., Jr., 2003a, Magma supply dynamics at Westdahl volcano, Alaska, modeled from satellite radar interferometry: Journal of Geophysical Research, v. 108, no. B7, 17 p., doi:10.1029/2002JB002311.

Lu, Z., Wicks, C.W., Jr., Dzurisin, D., Power, J., Thatcher, W., and Masterlark, T., 2003b, Interferometric Synthetic Aperture Radar studies of Alaska volcanoes: Earth Observation Magazine, v. 12, no. 3, p. 8–18.

Lu, Z., Masterlark, T., and Dzurisin, D., 2005a, Interferometric Synthetic Aperture Radar (InSAR) study of Okmok Volcano, Alaska, 1992–2003; magma supply dynamics and post-emplacement lava flow deformation: Journal of Geophysical Research, v. 110, no. B2, doi:10.01029/02004JB003148.

Lu, Z., Wicks, C.W., Jr., Kwoun, O.-I., Power, J.A., and Dzurisin, D., 2005b, Surface deformation associated with the March 1996 earthquake swarm at Akutan Island, Alaska, revealed by C-band ERS and L-band JERS radar interferometry: Canadian Journal of Remote Sensing, v. 31, no. 1, p. 7–20.

Lundgren, P., Casu, F., Manzo, M., Pepe, A., Berardino, P., Sansosti, E., and Lanari, R., 2004, Gravity and magma-induced spreading of Mount Etna Volcano revealed by satellite radar interferometry: Geophysical Research Letters, v. 31, no. 4, doi:10.01029/02003GL018736.

Major, J.J., 2000, Gravity-driven consolidation of granular slurries—implications for debris-flow deposition and deposit characteristics: Journal of Sedimentary Research, v. 70, no. 1, p. 64–83.

Masterlark, T., and Lu, Z., 2004, Transient volcano deformation sources imaged with interferometric synthetic aperture radar—application to Seguam Island, Alaska: Journal of Geophysical Research, v. 109, no. B1, doi:10.1029/2003JB002568.

Masterlark, T., Lu, Z., and Rykhus, R., 2006, Thickness distribution of a cooling pyroclastic flow deposit on Augustine Volcano, Alaska—optimization using InSAR, FEMs, and an adaptive mesh algorithm: Journal of Volcanology and Geothermal Research, v. 150, nos. 1–3, p. 186–201.

Mastin, L.G., 1994, Explosive tephra emissions at Mount St. Helens, 1989–1991; the violent escape of magmatic gas following storms?: Geological Society of America Bulletin, v. 106, no. 2, p. 175–185.

Mastin, L.G., Roeloffs, E., Beeler, N.M., and Quick, J.E., 2008, Constraints on the size, overpressure, and volatile content of the Mount St. Helens magma system from geodetic and dome-growth measurements during the 2004–2006+ eruption, chap. 22 *of* Sherrod, D.R., Scott, W.E., and Stauffer, P.H., eds., A volcano rekindled; the renewed eruption of Mount St. Helens, 2004–2006: U.S. Geological Survey Professional Paper 1750 (this volume).

Matthews, J.P., Kamata, H., Okuyama, S., Yusa, Y., and Shimizu, H., 2003, Surface height adjustments in pyroclastic-flow deposits observed at Unzen volcano by JERS-1 SAR interferometry: Journal of Volcanology and Geothermal Research, v. 125, nos. 3–4, p. 247–270.

Mogi, K., 1958, Relations between the eruptions of various volcanoes and the deformations of the ground surfaces around them: Bulletin of the Earthquake Research Institute, v. 36, no. 2, p. 99–134.

Moran, S.C., 1994, Seismicity at Mount St. Helens, 1987–1992: Evidence for repressurization of an active magmatic system: Journal of Geophysical Research, v. 99, no. B3, p. 4341–4354.

Moran, S.C., Kwoun, O.-I., Masterlark, T., and Lu, Z., 2006, On the absence of InSAR-detected volcano deformation spanning the 1995–1996 and 1999 eruptions of Shishaldin Volcano, Alaska: Journal of Volcanology and Geothermal Research, v. 150, nos. 1–3, p. 119–131.

Moran, S.C., Malone, S.D., Qamar, A.I., Thelen, W.A., Wright, A.K., and Caplan-Auerbach, J., 2008, Seismicity associated with renewed dome building at Mount St. Helens, 2004–2005, chap. 2 *of* Sherrod, D.R., Scott, W.E., and Stauffer, P.H., eds., A volcano rekindled; the renewed eruption of Mount St. Helens, 2004–2006: U.S. Geological Survey Professional Paper 1750 (this volume).

Musumeci, C., Gresta, S., and Malone, S.D., 2002, Magma system recharge of Mount St. Helens from precise relative hypocenter location of microearthquakes: Journal of Geophysical Research, v. 107, no. B10, 2264, p. ESE 16-1–ESE 16-9, doi:10.1029/2001JB000629.

Newman, A.V., Dixon, T.H., Ofoegbu, G.I., and Dixon, J.E., 2001, Geodetic and seismic constraints on recent activity at Long Valley Caldera, California; evidence for viscoelastic rheology: Journal of Volcanology and Geothermal Research, v. 105, no. 3, p. 183–206.

Newman, A.V., Dixon, T.H., and Gourmelen, N., 2006, A four-dimensional viscoelastic deformation model for Long Valley caldera, California, between 1995 and 2000: Journal of Volcanology and Geothermal Research, v. 150, nos. 1–3, p. 244–269.

Okada, Y., 1985, Surface deformation due to shear and tensile faults in a half-space: Bulletin of the Seismological Society of America, v. 75, no. 4, p. 1135–1154.

Pallister, J.S., Hoblitt, R.P., Crandell, D.R., and Mullineaux, D.R., 1992, Mount St. Helens a decade after the 1980 eruptions; magmatic models, chemical cycles, and a revised hazards assessment: Bulletin of Volcanology, v. 54, no. 2, p. 126–146, doi: 10.1007/BF00278003.

Pallister, J.S., Thornber, C.R., Cashman, K.V., Clynne, M.A., Lowers, H.A., Mandeville, C.W., Brownfield, I.K., and Meeker, G.P., 2008, Petrology of the 2004–2006 Mount St. Helens lava dome—implications for magmatic plumbing and eruption triggering, chap. 30 *of* Sherrod, D.R., Scott, W.E., and Stauffer, P.H., eds., A volcano rekindled; the renewed eruption of Mount St. Helens, 2004–2006: U.S. Geological Survey Professional Paper 1750 (this volume).

Peltzer, G., Crampé, F., Hensley, S., and Rosen, P., 2001, Transient strain accumulation and fault interaction in the Eastern California shear zone: Geology, v. 29, no. 11, p. 975–978.

Pritchard, M.E., and Simons, M., 2002, A satellite geodetic survey of large-scale deformation of volcanic centres in the central Andes: Nature, v. 418, no. 6894, p. 167–171.

Pritchard, M.E., and Simons, M., 2004a, An InSAR-based survey of volcanic deformation in the central Andes: Geochemistry, Geophysics, Geosystems, v. 5, no. 2, doi:02010.01029/02003GC000610.

Pritchard, M.E., and Simons, M., 2004b, An InSAR-based survey of volcanic deformation in the southern Andes: Geophysical Research Letters, v. 31, no. 15, doi:10.1029/2004GL020545.

Rowley, P.D., Kuntz, M.A., and MacLeod, N.S., 1981, Pyroclastic-flow deposits, *in* Lipman, P.W., and Mullineaux, D.R., eds., The 1980 eruptions of Mount St. Helens, Washington: U.S. Geological Survey Professional Paper 1250, p. 489–512.

Rutherford, M.J., Sigurdsson, H., Carey, S., and Davis, A., 1985, The May 18, 1980, eruption of Mount St. Helens—1. Melt composition and experimental phase equilibria: Journal of Geophysical Research, v. 90, no. B4, p. 2929–2947.

Scandone, R., and Malone, S.D., 1985, Magma supply, magma discharge and readjustment of the feeding system of Mount St. Helens during 1980: Journal of Volcanology and Geothermal Research, v. 23, nos. 3–4, p. 239–262, doi:10.1016/0377-0273(85)90036-8.

Schilling, S.P., Carrara, P.E., Thompson, R.A., and Iwatsubo, E.Y., 2004, Posteruption glacier development within the crater of Mount St. Helens, Washington, USA: Quaternary Research, v. 61, no. 3, p. 325–329.

Schilling, S.P., Thompson, R.A., Messerich, J.A., and Iwatsubo, E.Y., 2008, Use of digital aerophotogrammetry to determine rates of lava dome growth, Mount St. Helens, Washington, 2004–2005, chap. 8 *of* Sherrod, D.R., Scott, W.E., and Stauffer, P.H., eds., A volcano rekindled; the renewed eruption of Mount St. Helens, 2004–2006: U.S. Geological Survey Professional Paper 1750 (this volume).

Stevens, N.F., Wadge, G., Williams, C.A., Morley, J.G., Muller, J.-P., Murray, J.B., and Upton, M., 2001, Surface movements of emplaced lava flows measured by synthetic aperture radar interferometry: Journal of Geophysical Research, v. 106, no. B6, p. 11293–11313.

Voight, B., Glicken, H., Janda, R.J., and Douglass, P.M., 1981, Catastrophic rockslide avalanche of May 18, *in* Lipman, P.W., and Mullineaux, D.R., eds., The 1980 eruptions of Mount St. Helens, Washington: U.S. Geological Survey Professional Paper 1250, p. 347–377.

Wadge, G., Mattioli, G.S., and Herd, R.A., 2006, Ground deformation at Soufrière Hills Volcano, Montserrat during 1998–2000 measured by radar interferometry and GPS: Journal of Volcanology and Geothermal Research, v. 152, nos. 1–2, p. 157–173.

Walder, J.S., Schilling, S.P., Vallance, J.W., and LaHusen, R.G., 2008, Effects of lava-dome growth on the Crater Glacier of Mount St. Helens, Washington, chap. 13 *of* Sherrod, D.R., Scott, W.E., and Stauffer, P.H., eds., A volcano rekindled; the renewed eruption of Mount St. Helens, 2004–2006: U.S. Geological Survey Professional Paper 1750 (this volume).

Wessel, P., and Smith, W.H.F., 1998, New, improved version of Generic Mapping Tools released [abs.]: Eos (American Geophysical Union Transactions), v. 79, no. 47, p. 579.

Wicks, C.W., Jr., Thatcher, W., and Dzurisin, D., 1998, Migration of fluids beneath Yellowstone Caldera inferred from satellite radar interferometry: Science, v. 282, no. 5388, p. 458–462.

Wicks, C.W., Jr., Dzurisin, D., Ingebritsen, S., Thatcher, W., Lu, Z., and Iverson, J., 2002, Magmatic activity beneath the quiescent Three Sisters volcanic center, central Oregon Cascade Range, USA: Geophysical Research Letters, v. 29, no. 7, doi:10.1029/2001GL014205.

Wicks, C.W., Thatcher, W., Dzurisin, D., and Svarc, J., 2006, Uplift, thermal unrest, and magma intrusion at Yellowstone caldera: Nature, v. 440, no. 7080, p. 72–75, doi:10.1038/nature04507.

Wright, T., Parsons, B., and Fielding, E., 2001, Measurement of interseismic strain accumulation across the North Anatolian Fault by satellite radar interferometry: Geophysical Research Letters, v. 28, no. 10, p. 2117–2120.

Wright, T.J., Parsons, B., England, P.C., and Fielding, E.J., 2004, InSAR observations of low slip rates on the major faults of western Tibet: Science, v. 305, no. 5681, p. 236–239.

Zebker, H.A., Amelung, F., and Jonsson, S., 2000, Remote sensing of volcano surface and internal processes using radar interferometry, *in* Mouginis-Mark, P.J., Crisp, J.A., and Fink, J.H., eds., Remote sensing of active volcanism: Washington, D.C., American Geophysical Union Geophysical Monograph 116, p. 179–205.